



HAL
open science

Understanding and Optimisation of transport mechanisms in Perovskite on Silicon Heterojunction Tandem Solar Cells

Apolline Puaud

► **To cite this version:**

Apolline Puaud. Understanding and Optimisation of transport mechanisms in Perovskite on Silicon Heterojunction Tandem Solar Cells. Material chemistry. Université Grenoble Alpes [2020-..], 2021. English. NNT: 2021GRALI074 . tel-03462780

HAL Id: tel-03462780

<https://theses.hal.science/tel-03462780v1>

Submitted on 2 Dec 2021

HAL is a multi-disciplinary open access archive for the deposit and dissemination of scientific research documents, whether they are published or not. The documents may come from teaching and research institutions in France or abroad, or from public or private research centers.

L'archive ouverte pluridisciplinaire **HAL**, est destinée au dépôt et à la diffusion de documents scientifiques de niveau recherche, publiés ou non, émanant des établissements d'enseignement et de recherche français ou étrangers, des laboratoires publics ou privés.

THÈSE

Pour obtenir le grade de

DOCTEUR DE L'UNIVERSITE GRENOBLE ALPES

Spécialité : 2MGE : Matériaux, Mécanique, Génie Civil,
Électrochimie

Arrêté ministériel : 25 mai 2016

Présentée par

Apolline PUAUD

Thèse dirigée par **Anis JOUINI**, et codirigée par **Delfina MUNOZ**,
Docteure Ingénieure de Recherche, CEA et **Muriel MATHERON**,
Ingénieure de Recherche HDR, CEA

préparée au sein du **Laboratoire des cellules à Hétérojonction (LPH)**,
au **Département des Technologies Solaires (DTS)** du **Commissariat**
à l'énergie atomique et aux énergies alternatives (CEA), à l'**Institut**
National de l'Énergie Solaire (INES)
dans l'**École Doctorale I-MEP2 - Ingénierie – Matériaux, Mécanique,**
Environnement, Énergétique, Procédés, Production

Compréhension et Optimisation des mécanismes de transport dans les cellules Tandem Pérovskite sur Hétérojonction de Silicium

Understanding and Optimisation of transport mechanisms in Perovskite on Silicon Heterojunction Tandem Solar Cells

Thèse soutenue publiquement le **2 septembre 2021**,
devant le jury composé de :

Monsieur Anis JOUINI Ingénieur HDR, CEA INES	Directeur de thèse
Monsieur Pere ROCA I CABARROCAS Professeur des Universités, École Polytechnique	Rapporteur
Monsieur Joaquim PUIGDOLLERS GONZALEZ Professeur, Universitat Politècnica de Catalunya	Rapporteur
Monsieur David MUÑOZ-ROJAS Directeur de recherche, CNRS délégation Alpes	Président
Monsieur Bertrand PAVIET-SALOMON Ingénieur docteur, CSEM Neuchâtel	Examineur
Madame Carmen JIMENEZ AREVALO Docteure Ingénieure de Recherche, CNRS délégation Alpes	Invitée
Monsieur Lars KORTE Docteur Ingénieur de Recherche, HZB Berlin	Invité



RÉSUMÉ

Les rendements record des cellules solaires en silicium à simple-jonction se rapprochent de leur limite théorique. Dans ce contexte, les tandems monolithiques Pérovskite sur silicium sont un excellent choix pour atteindre plus de 30 % d'efficacité et être intégrés en module, avec peu de développement supplémentaire. Ces cellules solaires tandem, avec cellule inférieure à hétérojonction de silicium (SHJ), ont démontré des rendements allant jusqu'à 29 %, sur de petites surfaces (1 cm^2), au cours des dernières années. Pour développer ce type de technologie, la jonction entre les deux sous-cellules est une composante clé. En effet, les deux sous-cellules sont connectées en série par cette jonction, nommée jonction de recombinaison, qui doit permettre aux porteurs de charge de se recombiner, sans entraîner de pertes optiques ou électriques supplémentaires.

Les objectifs de cette Thèse sont d'étudier les mécanismes de transport dans les jonctions de recombinaison, au sein des cellules solaires tandem Pérovskite sur SHJ, afin de définir des méthodes de développement et d'optimisation de ces jonctions. Dans cette Thèse, nous proposons et mettons en place des méthodes de caractérisation des jonctions de recombinaison, pour préparer leur intégration dans les dispositifs tandem. Tout d'abord, nous avons développé une jonction tunnel en silicium microcristallin, déposée par PECVD à basse température ($200 \text{ }^\circ\text{C}$), afin de préserver la cellule inférieure. Ensuite, les couches de silicium microcristallin développées ont été caractérisées et nous avons validé qu'elles présentent les conditions requises pour former une jonction tunnel permettant une recombinaison efficace des porteurs de charge. De plus, nous avons observé une augmentation de la durée de vie des porteurs minoritaires, ce qui démontre que les couches développées améliorent la passivation chimique et l'effet de champ des cellules inférieures SHJ. Nous avons également fabriqué des cellules solaires SHJ avec l'ajout de la jonction $\mu\text{c-Si:H}$ (n^+/p^+) développée, nous n'avons observé aucune résistance série supplémentaire et nous avons mesuré des courbes I-V de forme classique, ne présentant pas de forme en S. La jonction de recombinaison développée n'a donc pas d'influence négative sur la cellule inférieure SHJ.

Deuxièmement, nous nous sommes concentrés sur la caractérisation électrique des jonctions de recombinaison, sans produire une cellule tandem entière. Nous avons établi différentes structures de test dans le but de caractériser électriquement les jonctions de recombinaison. Nous avons ensuite utilisé la jonction $\mu\text{c-Si:H}$ (n^+/p^+), développée précédemment, comme exemple de jonction pour étudier les différentes structures de test et discuter de leur fonctionnement. Finalement, nous avons proposé différentes structures et méthodes de caractérisation électrique, adaptées à différentes jonctions de recombinaison, et nous avons présenté leur potentiel et leurs limitations.

Troisièmement, nous avons ensuite étudié l'influence des jonctions de recombinaison sur les cellules solaires tandem Pérovskite/SHJ, mais également l'impact de ces jonctions sur la cellule supérieure à base de Pérovskite. En vue de choisir l'architecture tandem la plus efficace, nous avons réalisé des simulations optiques des cellules solaires tandem, avec différentes jonctions de recombinaison. Nous avons également développé des structures de test permettant d'étudier la cellule supérieure Pérovskite, au moyen de caractérisations électriques et structurales, en fonction de la jonction de recombinaison utilisée. Pour finir, nous avons présenté l'intégration de la jonction tunnel développée en dispositif tandem et discuté des perspectives d'amélioration.

MOTS CLÉS:

Cellules Solaires à base de Pérovskite
Cellules Solaires Tandem
Hétérojonction de Silicium
Jonction de Recombinaison
Jonction Tunnel
Silicium Microcristallin
Tandem Pérovskite sur Silicium

ABSTRACT

Silicon based single-junction solar cells record efficiencies are getting closer to their theoretical limit. In this context, monolithic Perovskite on silicon tandem solar cells are an excellent choice to achieve more than 30 % efficiency and to be integrated into modules, without much further development. Such tandem solar cells with a silicon heterojunction (SHJ) bottom-cell have demonstrated efficiencies up to 29 %, on small surfaces (1 cm²), in the past few years. To develop this type of devices, the junction between the two subcells is a key feature. Indeed, the two subcells are connected in series by this junction, named recombination junction, which must allow the charge carriers to recombine, without causing additional optical or electrical losses.

The objectives of this work are to investigate the transport mechanisms in the recombination junction, within Perovskite on SHJ tandem solar cells, in order to define methods for the development and optimisation of several recombination junctions. In this work, we propose and implement methods for the characterisation of recombination junctions, in order to prepare their integration in tandem devices.

First, we developed a tunnel junction in microcrystalline silicon, deposited by PECVD at low temperature (200 °C), to preserve the SHJ bottom-cell. Then, the developed microcrystalline silicon layers were characterised and we validated that they have the requirements to form an efficient tunnel recombination junction. Moreover, we observed an increase of minority carrier lifetime, demonstrating that the developed layers improve the chemical passivation and field effect of SHJ solar cells. Furthermore, we made SHJ solar cells, with the addition of the developed $\mu\text{-Si:H}$ (n^+/p^+) junction, observed no additional series resistance and measured conventionally shaped I-V curves, without S-shape. Thus, the developed recombination junction does not negatively influence the SHJ bottom-cell.

Secondly, we focused on the electrical characterisation of the recombination junctions, without producing an entire tandem solar cell. We established different test-structures with the aim of electrically characterising the recombination junctions. Then, we used the previously developed $\mu\text{-Si:H}$ (n^+/p^+) junction as an example to study the different test-structures and discuss their operation. Finally, we proposed different structures and electrical characterisation methods, suitable for different recombination junctions, and presented their potential and limitations.

Thirdly, we studied the influence of recombination junctions on Perovskite/SHJ tandem solar cells, but also the impact of these junctions on the Perovskite-based top-cell. For this purpose, we have performed optical simulations of tandem solar cells with different recombination junctions. We also developed test-structures to investigate on the Perovskite top-cell, through electrical and structural characterisations, depending on the recombination junction used. To conclude, we presented the integration of the developed tunnel junction in a tandem device and discussed further improvements and perspectives.

KEY WORDS:

Microcrystalline Silicon
Perovskite on Silicon Tandem
Perovskite Solar Cells
Recombination Junction
Silicon Heterojunction
Tandem Solar Cells
Tunnel Junction

ACKNOWLEDGMENTS

Je tiens premièrement à remercier le CEA Liten, plus particulièrement le Département des Technologies Solaires, pour le financement de ces travaux de Thèse.

Je souhaite ensuite remercier Pere Roca I Cabarrocas et Joaquin Puigdollers Gonzalez, rapporteurs de ces travaux, pour avoir pris le temps de lire mon travail. Merci également à David Muñoz-Rojas et Bertrand Paviet Salomon, examinateurs de ces travaux, d'avoir accepté de faire partie de mon jury de Thèse. Et merci à Carmen Jimenez Arevalo et Lars Korte pour s'être intéressés à ces travaux, en tant qu'invités. Merci à tous les six pour votre attention et vos commentaires constructifs.

Un grand merci à mon directeur de Thèse, Anis Jouini et également à Charles Roux et Solenn Berson pour m'avoir fait confiance et permis d'effectuer cette Thèse sur un sujet déjà très important pour moi, dans ce cadre exceptionnel qu'est l'INES. Merci d'avoir accepté ma candidature.

Merci encore à Anis Jouini pour avoir assumé son rôle et pris le temps de diriger cette Thèse malgré ses autres responsabilités.

Je ne vous remercierai jamais assez mais un énorme merci à Delfina Muñoz et Muriel Matheron pour tout ce que vous m'avez apporté. Delfi, merci pour avoir respecté mon indépendance tout en étant toujours présente si besoin, autant « solairement » parlant que personnellement. Je t'admire énormément pour réussir à trouver 72h dans une seule journée. Muriel, merci pour ta bienveillance constante (qualité rare), ton écoute et ton calme à toute épreuve. Ce fut vraiment un plaisir de travailler avec vous.

Je tiens également à remercier Bernard Cassini, ancien chef du Service SMCP et Charles Roux, nouveau chef du Service SCPV mais surtout ancien chef du laboratoire LHET. Merci à vous deux d'avoir toujours été disponibles et à l'écoute. Merci également à Christine Mir pour avoir géré le côté administratif des conférences/déplacements.

Un immense merci à toute l'équipe du LHET (nouvellement LPH) pour votre bonne humeur et votre soutien quotidien. Merci à la team PECVD, Julien, Julie et Laëtitia pour les journées passées sur (ou dans) l'Hélia et merci beaucoup à AnSo pour les discussions microcristallin ! Merci aussi aux teams PVD et sérig. pour l'aide lors de mes lots pénibles et merci Mathieu pour les supers mesures I-V. Merci également aux teams maintenance et WET, toujours dispos pour aider et/ou rigoler. Merci à Fabien et Adrien pour l'accueil aux réunions Planning et PI et pour la gestion des lots. Enfin, merci beaucoup à Anthony pour ta positivité et pour être toujours là quand on en a besoin et merci à Martin, Wilfried et Jordi pour leurs conseils et discussions enrichissantes !

Merci à toute l'équipe Tandem : Solenn, Olivier, Nathalie, Carine, Perrine et Elise pour votre motivation à faire des tandems à 30% malgré toutes les « intempéries » !

Je remercie également tous ceux qui ont su rendre les journées à Restaura moins « blanches » : Fred, Raf, Charles, Caroline et tous les autres. Et merci à tous les « plus ou moins jeunes » pour vos rires à l'INES et ailleurs : Son, Daniel, Thibault, Félix, Marine, Ravi, Julien, Audrey, Antoine, Camille, Mylène, Joël, Baptiste, Emmanuel, Pierre...

Merci à Sénami pour avoir été une super stagiaire, j'espère que ta Thèse te plaira.

Merci à Pia pour ton sourire à toute épreuve et ton apprentissage hyper rapide du français qui m'a permis, j'espère, de te transmettre une bonne partie de ce que j'ai appris, bon courage pour la suite, tu es entre de bonnes mains.

Un énorme merci également à Laurie-Lou pour toutes les galères qu'on a traversées à l'INES et au CSEM, mais aussi les super discussions, interrogations et solutions... et les crêpes !

Merci à Thien-Phap Nguyen sans qui je n'aurai jamais découvert le monde fabuleux des cellules solaires à base de Pérovskite.

Merci à tous ceux qui ont été à mes côtés pendant ces quatre années compliquées. Merci la team cerceau pour les tractions « avec le sourire ». Merci les poules d'eau et les anciens Grenoblois pour tous ces moments de joie et de détente. Merci Pauline, la meilleure kiné, pour m'avoir supportée presque quotidiennement, c'est grâce à toi que ma jambe est comme neuve aujourd'hui. Merci Maxime et Maël d'être toujours présent pour moi. Merci Maryse, Christophe, Alex, Sy' et Denis de m'avoir accueillie et supportée. Merci à mes frères, sœurs, neveux et nièces pour vos photos et colis surprises qui remontent le moral malgré la distance.

Je voudrai aussi remercier les deux personnes qui me soutiennent (et/ou me supportent) au quotidien. Merci à ma bouillotte boudeuse favorite, Noumie, cette Thèse n'aurait pas été écrite sans tes ronronnements et tes câlins (et tes pas sur le clavier...). Et merci Docteur Léo pour ta patience, tes conseils, tes relectures et tout le reste.

Enfin, merci à mes parents pour votre amour. Cette Thèse est pour vous, vous qui avez toujours fait de votre mieux pour moi. J'espère partager avec vous encore longtemps. Je vous aime.

CONTENTS

RÉSUMÉ	3
ABSTRACT	5
ACKNOWLEDGMENTS	7
CONTENTS	9
ACRONYMS AND ABBREVIATIONS	11
LIST OF TABLES	14
LIST OF FIGURES	15
I. GENERAL INTRODUCTION	20
I.1. CONTEXT	20
I.2. MOTIVATION AND OBJECTIVES	22
I.3. APPROACH	23
II. STATE-OF-THE-ART	24
II.1. TANDEM SOLAR CELLS	25
II.2. SILICON HETEROJUNCTION SOLAR CELLS	28
II.3. PEROVSKITE ON SILICON HETEROJUNCTION TANDEM SOLAR CELLS	31
<i>II.3.1. Introduction</i>	31
<i>II.3.2. Review Before 2018</i>	33
<i>II.3.3. 2018-2020 Timeline</i>	35
II.4. RECOMBINATION JUNCTIONS	41
<i>II.4.1. Highly Doped Tunnel Junction</i>	41
<i>II.4.2. Transparent Conductive Oxide as Recombination Layer</i>	42
<i>II.4.3. Recombination Junctions in Perovskite/SHJ Tandem</i>	42
II.5. CHAPTER OUTLOOK	43
III. MATERIALS AND METHODS	44
III.1. FABRICATION PROCESSES	45
<i>III.1.1. Substrate cleaning</i>	45
<i>III.1.2. Plasma-enhanced CVD</i>	46
III.1.2.a. Industrial Tool	46
III.1.2.b. Development Tool	46
<i>III.1.3. Transparent Conductive Oxide Deposition</i>	47
<i>III.1.4. Metallisation</i>	48
III.1.4.a. Electron-beam Evaporation	49
III.1.4.b. Thermal Evaporation	49
III.1.4.c. Screen-Printing	50
<i>III.1.5. Laser Cutting</i>	50
<i>III.1.6. Perovskite Solar Cell</i>	50
<i>III.1.7. Example of a Tandem Solar cell Fabrication Process</i>	52
III.2. LAYER CHARACTERISATION METHODS	52
<i>III.2.1. Ellipsometry</i>	52
III.2.1.a. Ellipsometry Measurements	53
III.2.1.b. Fitting Models	53
<i>III.2.2. Spectrophotometry</i>	54
<i>III.2.3. Raman spectroscopy</i>	54
<i>III.2.4. Four-terminal Sensing</i>	55
<i>III.2.5. Hall Effect Measurements</i>	56
<i>III.2.6. Thin-film's Activation Energy</i>	57
<i>III.2.7. Contact Resistances Measurements</i>	57
<i>III.2.8. Scanning and Transmission Electron Microscopy</i>	58
III.2.8.a. SEM Measurements	58

III.2.8.b. STEM-EDX Measurements	58
III.2.9. Confocal Microscopy	58
III.2.10. X-ray Diffraction	59
III.3. SOLAR CELLS CHARACTERISATION	59
III.3.1. Lifetime Measurements	59
III.3.2. Suns- V_{oc} Measurements	60
III.3.3. Quantum Efficiency Measurements	60
III.3.4. Current-Voltage Measurements	61
III.3.4.a. Solar Cells J-V curves	61
III.3.4.b. Temperature-Dependent Dark I-V	62
III.4. OPTICAL SIMULATION	63
III.4.1. Software Presentation: CROWM	63
III.4.2. Optical Indexes Extraction Method	63
III.5. CHAPTER CONCLUSION	64
IV. MICROCRYSTALLINE SILICON TUNNEL JUNCTION FOR PIN TANDEM SOLAR CELLS	65
IV.1. INTRODUCTION	66
IV.2. MICROCRYSTALLINE SILICON LAYERS DEVELOPMENT	66
IV.2.1. PECVD Parameters	68
IV.2.2. Growth and Microcrystalline Phase	72
IV.2.3. Microcrystalline Silicon layers properties	74
IV.3. INTEGRATION OF MICROCRYSTALLINE SILICON ON SHJ SOLAR CELLS	75
IV.3.1. Bulk Passivation Improvement	75
IV.3.2. Rear Emitter SHJ Solar Cells with Front-side N-Type Microcrystalline Silicon	77
IV.3.3. Standard Emitter SHJ Solar Cells with Back-side Microcrystalline Silicon Tunnel Junction	79
IV.4. CHAPTER CONCLUSION	82
V. WAYS TO CHARACTERISE RECOMBINATION JUNCTIONS FOR PEROVSKITE ON SILICON TANDEM SOLAR CELLS	83
V.1. INTRODUCTION	84
V.2. TUNNEL RECOMBINATION JUNCTION AS TUNNEL DIODE	85
V.2.1. Test-Structures for Tunnel Junctions Measurements	85
V.2.2. Tunnel Diode Behaviour	90
V.2.3. Conclusion	93
V.3. TRANSPORT MECHANISMS INSIGHT IN NPN JUNCTIONS	95
V.4. CHARACTERISATION OF RECOMBINATION JUNCTIONS	102
V.5. CHAPTER CONCLUSION	105
VI. TOWARDS PEROVSKITE ON SILICON HETEROJUNCTION TANDEM SOLAR CELLS INTEGRATION	107
VI.1. INTRODUCTION	108
VI.2. OPTICAL ANALYSIS OF RECOMBINATION JUNCTIONS IN PK/SHJ TANDEM SOLAR CELLS	109
VI.2.1. Transparent Conductive Oxides	109
VI.2.2. Microcrystalline Silicon Tunnel Junction	113
VI.2.3. Conclusion	117
VI.3. INVESTIGATION OF THE RECOMBINATION JUNCTIONS INFLUENCE ON THE PEROVSKITE TOP-CELL	117
VI.4. TANDEM SOLAR CELLS INTEGRATION	124
VI.5. CHAPTER CONCLUSION	126
VII. CONCLUSION AND PERSPECTIVES	128
SCIENTIFIC CONTRIBUTION	132
REFERENCES	133
APPENDICES	145
Appendix A. Chemically polished silicon wafers study for large-area printed PK	145
Appendix B. Passivation degradation after e-beam evaporation of silver electrodes	147
Appendix C. Investigation of shunt issues in PK/SHJ tandem solar cells	148
RÉSUMÉ ÉTENDU	151

ACRONYMS AND ABBREVIATIONS

(i)	Intrinsic
(n)	N-Type
(p)	P-Type
:H	Hydrogenated
μc-Si	Microcrystalline Silicon
2T	Two-Terminal
4T	Four-Terminal
A	Absorptance
AA	Aperture Area
AFM	Atomic Force Microscopy
Ag	Silver
Al	Aluminium
AM	Air Mass
Ar	Argon
ARC	Anti-Reflection Coating
a-Si	Amorphous Silicon
Au	Gold
AZO	Aluminium Doped Zinc Oxide
B2BT	Band-to-band Tunnelling
B₂H₆	Diborane
Br	Bromine
C₇H₈	Toluene
CB	Conduction Band
CH₃CN	Acetonitrile
CMP	Chemical-Mechanical Polishing
Cs	Cesium
c-Si	Crystalline Silicon
CVD	Chemical vapour Deposition
CZ	Czochralski
DMF	Dimethylformamide
DMSO	Dimethyl Sulfoxide
DSP	Double-Side Polishing/Polished
E_a	Activation Energy
E_c	Conduction Band Energy
EDX	Energy Dispersive X-ray Spectroscopy
E_f	Fermi Level
E_{fn}	Electron quasi-Fermi Level
E_{fp}	Hole quasi-Fermi Level
E_g	Band-gap Energy
EQE	External Quantum Efficiency
ETL	Electron Transport Layer

ETM	Electron Transport Material
E_v	Valence Band Energy
FA	Formamidinium
FAI	Formamidinium Iodide
FF	Fill Factor
FIB	Focused Ion Beam
FZ	Float-Zone
GaAs	Gallium Arsenide
H_2	Dihydrogen
HTL	Hole Transport Layer
HTM	Hole Transport Material
I	Iodine
IBC	Interdigitated Back Contact
iFF	Implied Fill Factor
In_2O_3	Indium Oxide
IR	Infrared
I_{sc}	Short-circuit Current
ITO	Indium Tin Oxide
iV_{oc}	Implied Open-circuit Voltage
IZO	Indium Zinc Oxide
J_{mpp}	Current Density at the Maximum Power Point
J_{sc}	Short-circuit Current Density
LCOE	Levelized Cost Of Energy/Electricity
Li-TFSI	Lithium bis-Trifluoromethanesulfonimide
M2	156.75 mm x 156.75 mm wafer
MA	Methylammonium
MAI	Methylammonium iodide
MoO_x	Molybdenum oxide
MPP	Maximum Power Point
N_2	Nitrogen
nc-Si	Nanocrystalline Silicon
NIP	Device Architecture where the N-type layer is deposited first
O_2	Dioxygen
Pb	Lead
$PbBr_2$	Lead Bromide
$PbCl_2$	Lead Chloride
PbI_2	Lead Iodide
PCE	Power Conversion Efficiency
Pd	Palladium
PECVD	Plasma-Enhanced Chemical Vapor Deposition
PERC	Passivated Emitter and Rear Contact
PERL	Passivated Emitter and Rear Locally diffused
pFF	Pseudo Fill Factor
PH_3	Phosphine
PIN	Device Architecture where the P-type layer is deposited first

PK	Perovskite
poly-Si	Polycrystalline Silicon
PTAA	Poly(TriAryl Amine)
PVD	Physical Vapour Deposition
R	Reflectance
R&D	Research and Development
R_c	Contact Resistance
RF	Radio Frequency
RJ	Recombination Junction
R_s	Series Resistance
R_{sheet}	Sheet Resistance
R_{shunt}	Shunt Resistance
R_{tot}	Total Reflectance
SAM	Self Assembled Monolayer
SCCM	Standard Cubic Centimetres per Minute
SDR	Saw Damage Removal
SE	Spectroscopic Ellipsometry
SEM	Scanning Electron Microscopy/Microscope
SHJ	Silicon Heterojunction
SiH₄	Silane
SiO₂	Silicon Dioxide
SnO₂	Tin(IV) Oxide
STEM	Scanning Transmission Electron Microscopy/Microscope
T	Transmittance
TAT	Trap-Assisted Tunnelling
TBP	TertioButylPyridine
TCO	Transparent Conductive/Conducting Oxide
TiO₂	Titanium Dioxide
TJ	Tunnel Junction
TLM	Transfer Length Method
TMO	Transition Metal Oxide
TOPCon	Tunnel Oxide Passivated Contact
UV	Ultraviolet
VB	Valence Band
V_{mpp}	Voltage at the Maximum Power Point
V_{oc}	Open-circuit Voltage
XRD	X-Ray Diffraction
X_{μc-Si}	Microcrystalline Phase Fraction
Δn	Excess Minority Carrier Density
δp	Penetration Depth
η	Efficiency
λ	Wavelength
ρ_c	Contact Resistivity
σ	Conductivity (lateral conductivity)
τ_{eff}	Effective Minority Carrier Lifetime

LIST OF TABLES

Table II.1-1 Main advantages and disadvantages of the tandem solar cell configurations presented in Figure II.1-1	26
Table II.3-1 Timeline (publication date) of the Perovskite/SHJ tandem solar cells, from January 2018 to December 2020.....	40
Table III.1-1 Definitions of the notations for hydrogenated thin-film silicon materials used in this work (adapted from [127]).....	47
Table III.1-2 Table of the tools used for the ITO layers deposition with the substrates type and ITO's thicknesses.....	48
Table III.1-3 Details of the metallisation used for the different substrates of this work.....	48
Table III.1-4 Details of the solution prepared for Perovskite solar cells.....	51
Table III.2-1 Summary of the fitting models for each studied material.....	53
Table IV.2-1 PECVD chamber parameters used for the deposition of the $\mu\text{c-Si:H}$ layers.....	68
Table IV.2-2 Gas flow ratios and deposition times of the developed $\mu\text{c-Si:H}$ layers.....	70
Table IV.2-3 E_a of the developed microcrystalline silicon layers.....	75
Table IV.3-1 Minority carrier lifetime at $10^{15} \Delta n \text{ cm}^{-3}$ and corresponding iV_{oc} and iFF	76
Table IV.3-2 Average minority carrier lifetime at $10^{15} \Delta n \text{ cm}^{-3}$ and corresponding iV_{oc} and iFF for both solar cells batches.....	77
Table V.2-1 Definition, objectives and simplified circuit diagrams of the proposed test-structures.....	86
Table V.2-2 Reminder of the objectives of each test-structures and notes about the obtained results.....	94
Table V.3-1 Thicknesses and average microcrystalline phase fractions of the tunnel junctions, extracted by SE and Raman spectroscopy.....	96
Table VI.2-1 Thicknesses of the different layers used in optical simulations with a varying ITO thickness.....	109
Table VI.2-2 Thicknesses of the different layers used in optical simulations with current-matching condition.....	110
Table VI.2-3 J_{sc} in each subcell and R_{tot} obtained with optical simulations for the devices of Figure VI.2-3 . The presented PCE are calculated assuming $FF = 75\%$ and $V_{oc} = 1.8 \text{ V}$	113
Table VI.2-4 Thicknesses of the different layers used in optical simulations with current-matching condition.....	114
Table VI.2-5 J_{sc} in each subcell and R_{tot} obtained with optical simulations for the devices of Figure VI.2-6 . The presented PCE are calculated assuming $FF = 75\%$ and $V_{oc} = 1.8 \text{ V}$	115
Table VI.3-1 J-V parameters of the studied devices a) and b) from Figure VI.3-1 obtained with I-V measurements (3 samples of each device), after a shading correction on the J_{sc} (the shading induce by the metallisation is different for each sample, a correction is applied to compare the devices with the same active area).....	119
Table VI.4-1 J-V parameters of PIN PK/SHJ tandem solar cells, with the developed $\mu\text{c-Si:H}$ (n^+/p^+) junction (see Figure IV.1-1), extracted from I-V measurements with two different HTM (PEDOTS:PSS and a SAM), without shading correction on the J_{sc}	125

LIST OF FIGURES

Figure I.1-1 Evolution of global mean surface temperature (GMST) over the period of instrumental observations. Reproduced from the IPCC <i>Global Warming of 1.5 °C</i> report [1], <i>Framing and Context</i> chapter, Figure 1.2, P.57.	20
Figure I.1-2 One and two-diode models of solar cells.....	21
Figure I.1-3 Solar photovoltaic world cumulative installed capacity and annual additions in Gigawatts from 2010 to 2020.....	22
Figure II.1-1 Drawing of the main existing tandem solar cell configurations; a) Mechanically stacked, 4-terminal tandem solar cell; b) Monolithic, 2-terminal tandem solar cell; c) Optical spectral splitting, 4-terminal tandem solar cell.	25
Figure II.1-2 One-diode model of a monolithic tandem solar cell.	26
Figure II.1-3 Band diagrams of a a) NIP single-junction solar cell and a b) NIP tandem solar cell, at V_{oc} . E_{fn} and E_{fp} are respectively the electron and hole quasi-Fermi levels in the materials.....	27
Figure II.2-1 Drawing of notable c-Si solar cells with their respective efficiency. a) <i>Bell Labs</i> solar cell; b) <i>Hoffman Electronics</i> ; c) and d) <i>Comsat Labs</i> ; e), f), g) <i>UNSW</i> ; h) First measured at 24.7 %, then at 25 %, <i>UNSW</i> ; i) <i>Fraunhofer ISE</i>	28
Figure II.2-2 a) First SHJ solar cell with an intrinsic thin layer developed by <i>Sanyo</i> ; b) Standard emitter SHJ with an efficiency of 25.1 % presented by <i>KANEKA</i> in 2015; c) SHJ solar cells produced in the CEA-INES pilot-line.	29
Figure II.2-3 a) 2D drawing of a (100) N-type crystalline silicon; b) 2D drawing of an intrinsic amorphous silicon; c) 2D drawing of the heterojunction a-Si:H (i)/c-Si (n). Dangling bonds are represented in red lines and excess electrons in yellow circles.....	30
Figure II.2-4 Band diagram of a SHJ solar cell in the configuration illustrated Figure II.2-2 c) , without the metallisation.....	30
Figure II.3-1 a) Structure of a Perovskite crystal with the formula ABX_3 , often named a one-cation Perovskite; b) Structure of a double-cation Perovskite, as used in this work.	31
Figure II.3-2 a) Planar NIP Perovskite solar cell; b) Planar PIN Perovskite solar cell; c) Mesoporous NIP Perovskite solar cell; d) Mesoporous PIN Perovskite solar cell.....	32
Figure II.3-3 Chart of the highest confirmed efficiencies of c-Si solar cells, by the <i>National Renewable Energy Laboratory-NREL</i> (04/01/2021).	33
Figure II.3-4 2T tandem solar cells structures showed in the literature, with their respective efficiency, active area and date of publication.	35
Figure II.3-5 Chart of the highest confirmed efficiencies of emerging solar cells, by the <i>NREL</i> (04/01/2021, https://www.nrel.gov/pv/cell-efficiency.html).	36
Figure II.4-1 I-V Curve (in orange) of a tunnel diode in the dark and the different current contributions (dashed lines: tunnel current J_T in green, excess current J_X in yellow and thermal current J_{Th} in blue). Peak current (I_P) and Valley current (I_V) are also represented.	41
Figure II.4-2 Drawing of the band diagrams at each cross on the tunnel diode I-V curve in Figure II.4-1 . The purple dashed lines represent the quasi-Fermi levels.....	42
Figure III.1-1 SEM front and cross-section images (III.2.8.a) of an n-type CZ (100) commercial wafer “as-cut”, after the SDR step and after the pyramidal texturing process.	45
Figure III.1-2 Drawing of a PECVD process chamber.....	46
Figure III.1-3 Simplified picture of the PECVD <i>Jusung</i> tool.	47
Figure III.1-4 Sketch of an electron-beam evaporation chamber.....	49

Figure III.1-5 Drawing of the synthesis of a Perovskite layer by the anti-solvent, spin-coating method employed.....	51
Figure III.1-6 Summary of the fabrication process of a tandem solar cell.....	52
Figure III.2-1 Drawing of the polarisation modulation ellipsometer.	53
Figure III.2-2 Details of the detector compartment of the spectrophotometer.	54
Figure III.2-3 Example of a Raman spectrum measured on a microcrystalline layer on glass. The three peaks used for the decorrelation are highlighted.....	55
Figure III.2-4 Drawing of the 4-point probe R_{sheet} measurement.....	56
Figure III.2-5 Sketch of the charge separation during the Hall Effect measurement. ...	56
Figure III.2-6 a) Cross-section sketch of a TLM sample used to investigate the electron contact in SHJ solar cells. b) Example of a TLM plot after measuring the resistances R_x for increasing the electrode spacing d_x	57
Figure III.3-1 Drawing of the lifetime measurement setup.....	60
Figure III.3-2 Dark J-V Curve in red and Light J-V Curve in blue of a solar cell.	62
Figure III.3-3 Sketch of the Cryostat tool.....	62
Figure III.4-1 Optical indexes extraction protocol applied for Perovskite solar cell materials, in a NIP single-junction.....	64
Figure IV.1-1 PIN Perovskite on SHJ tandem solar cell with a microcrystalline silicon tunnel junction.	66
Figure IV.2-1 a) N-type $\mu\text{-Si:H}$ layer on a quartz-glass substrate; b) P-type $\mu\text{-Si:H}$ layer on a quartz-glass substrate; c) $\mu\text{-Si:H}$ (n^+/p^+) junction on a quartz-glass substrate. d) IN/IN DSP Isotype (N-type) and symmetrical precursors on FZ DSP wafer; e) IN/IP DSP SHJ precursors on FZ DSP wafer. f) IN/IN M2 Isotype (N-type) and symmetrical precursors on CZ textured wafer; g) IN/IP M2 SHJ precursors on CZ textured wafer. .	67
Figure IV.2-2 a) SE fitting model used for the microcrystalline silicon layers deposited on quartz-glass substrate; b) SE fitting model used for the microcrystalline silicon layers deposited on IN/IN DSP precursors.	68
Figure IV.2-3 Pseudodielectric function, $\epsilon = \epsilon_r + i(\epsilon_i)$, of the materials used in the fitting model, solid lines for the microcrystalline silicon, dashed lines for pure crystalline silicon and dotted lines for amorphous silicon.....	68
Figure IV.2-4 Pseudodielectric function of $\mu\text{-Si:H}$ (n^+) layer by varying the deposition time, on IN/IN DSP substrate on the left and on quartz-glass substrate on the right. ϵ_i in circle dots and solid lines and ϵ_r in square dots and dashed lines.	69
Figure IV.2-5 Thickness and $X_{\mu\text{-Si}}$ extracted from the fitted pseudodielectric function curves for the $\mu\text{-Si:H}$ (n^+) layer, according to the deposition time.	70
Figure IV.2-6 Pseudodielectric function of the $\mu\text{-Si:H}$ (n^+)/ $\mu\text{-Si:H}$ (p^+) junction by varying the deposition time of the $\mu\text{-Si:H}$ (p^+) layer, on IN/IN DSP substrate on the left and on quartz-glass substrate on the right. ϵ_i in circle dots and solid lines and ϵ_r in square dots and dashed lines.....	71
Figure IV.2-7 Thickness and $X_{\mu\text{-Si}}$ extracted from the fitted pseudodielectric function curves for the $\mu\text{-Si:H}$ (n^+)/ $\mu\text{-Si:H}$ (p^+) junction, according to the deposition time of the $\mu\text{-Si:H}$ (p^+) layer.	71
Figure IV.2-8 Percentage of microcrystalline phase obtained by SE and Raman spectroscopy for $\mu\text{-Si:H}$ (n^+), $\mu\text{-Si:H}$ (n^+/p^+) and $\mu\text{-Si:H}$ (p^+) on IN/IN DSP substrates (respectively $n+$, $n+/p+$ and $p+$) and on quartz-glass substrates (respectively a) , b) and c)	72
Figure IV.2-9 Raman spectrum of the microcrystalline silicon layers deposited on quartz-glass substrates. With a 442 nm laser on the left ($\delta p \approx 50$ nm) and a 325 nm laser on the right ($\delta p \approx 8$ nm).	73
Figure IV.2-10 STEM image of the $\mu\text{-Si:H}$ (n^+/p^+) junction on a IN/IN DSP substrate.73	

Figure IV.2-11 STEM image of the $\mu\text{-Si:H}$ (n^+/p^+) junction on a IN/IN DSP substrate with a drawing of the microcrystallites (without distinction of the crystalline planes).	73
Figure IV.2-12 R_{sheet} and lateral conductivity obtained in this work with four-terminal sensing measurements on quartz-glass reference substrates (35 deposition processes for $\mu\text{-Si:H}$ (n^+), 29 for $\mu\text{-Si:H}$ (p^+) and 32 for the PN junction).....	74
Figure IV.2-13 Absorptance of the developed microcrystalline silicon layers.....	75
Figure IV.3-1 Minority carrier lifetimes of M2 textured precursors (IN/IN M2 on the left and IN/IP M2 on the right). Precursors in yellow dots, with $\mu\text{-Si:H}$ (n^+) on the top in red and with the PN junction on the top in blue.....	76
Figure IV.3-2 Minority carrier lifetimes at $10^{15} \Delta n \text{ cm}^{-3}$ measured during all of this work on several precursors.....	77
Figure IV.3-3 J_{sc} (on the left) and V_{oc} (on the right) extracted from I-V measurements of total cell area.....	78
Figure IV.3-4 PCE extracted from I-V measurements of total cell area.....	78
Figure IV.3-5 EQE of the best cells of each batch.....	79
Figure IV.3-6 FF extracted from I-V measurements of total cell area and pFF obtained with Suns- V_{oc} measurements on the left. Calculated R_s of the solar cells on the right....	79
Figure IV.3-7 a) Standard emitter SHJ solar cells as references; b) Standard emitter SHJ solar cells with the $\mu\text{-Si:H}$ (n^+) layer at the back-side; c) Standard emitter SHJ solar cells with the $\mu\text{-Si:H}$ (n^+/p^+) junction at the back-side.....	80
Figure IV.3-8 J_{sc} , V_{oc} and FF extracted from I-V measurements of total cell area, pFF obtained with Suns- V_{oc} measurements and calculated R_s of the solar cells.....	80
Figure IV.3-9 PCE extracted from I-V measurements of total cell area.....	81
Figure IV.3-10 Measured I-V curves of the three batches.....	81
Figure V.1-1 Usual test-structures used to characterise highly doped tunnel junctions and tunnel diodes. a) For transversal I-V measurements and b) for lateral I-V measurements.....	84
Figure V.2-1 Test-structures proposed in this part for transversal dark I-V measurements.....	85
Figure V.2-2 Simplified circuit diagrams for the proposed test-structures.....	86
Figure V.2-3 J-V curves measured in the dark and structure of the “SHJ devices version” of test-structure g) (6 devices).....	87
Figure V.2-4 J-V curves measured in the dark and structure of the “SHJ devices version” of test-structure d) (3 devices).....	88
Figure V.2-5 Fabrication steps of the small test-structures, regardless of the starting substrate.....	88
Figure V.2-6 I-V curves measured in the dark of double-side textured small test-structures g) . The inset shows the curves at low voltage bias and the linear fitting curve.....	89
Figure V.2-7 Temperature dependent I-V curves, measured in the dark, of double-side textured test-structures a) (dotted lines), b) (dashed lines) and c) (solid lines).....	90
Figure V.2-8 Temperature dependent I-V curves, measured in the dark, of double-side textured test-structures d) (dotted lines) and f) (solid lines) made with e-beam evaporation metallisation.....	91
Figure V.2-9 Temperature dependent I-V curves, measured in the dark, of double-side textured test-structures d) (dotted lines), e) (dashed lines) and f) (solid lines) made with thermal evaporation metallisation.....	92
Figure V.2-10 Temperature dependent I-V curves, measured in the dark, of double-side textured test-structures d) made with thermal evaporation metallisation.....	92
Figure V.3-1 Test-structure a) (Figure V.2-1) and its adjusted simplified circuit diagram.....	95

Figure V.3-2 Simplified band diagrams of the front-side stack of test-structures with a microcrystalline silicon tunnel junction and a TCO. At forward bias (regarding the $\mu\text{c-Si:H}$ (n^+/p^+) tunnel junction) in the left and at reverse bias (regarding the $\mu\text{c-Si:H}$ (n^+/p^+) tunnel junction) in the right.....	95
Figure V.3-3 Test-structures used in the experiment, based on test-structures d) , e) and f) from Figure V.2-1 . The circuit diagram of the test-structures separated in three resistances (R_{front} for the studied front stack, R_{bulk} for the substrate and R_{back} for the Ohmic back-side) is also presented.	96
Figure V.3-4 Contact resistivity, ρ_c , from 200 K to 350 K calculated for both Ohmic back-sides. Batch-1 in green and Batch-2 in blue.....	97
Figure V.3-5 I-V curves from 200 K to 350 K of structures b) (on the left) and d) (on the right), with the tunnel junction $\mu\text{c-Si:H}$ (n^+/p^+) ① and the AZO layer, from Batch-2. ...	98
Figure V.3-6 R_{front} and ρ_c calculated for structures b) with the $\mu\text{c-Si:H}$ (n^+) ① layer and the ITO layers (one on the left and the other on the right), from Batch-2. Measured I-V curves are presented in insets.	98
Figure V.3-7 R_{front} and ρ_c calculated for structures d) with the tunnel junction $\mu\text{c-Si:H}$ (n^+/p^+) ① and the ITO layers (one on the left and the other on the right, as in Figure V.3-6), from Batch-2. Measured I-V curves are presented in insets.	99
Figure V.3-8 I-V curves from 200 K to 350 K of structure e) with the tunnel junction $\mu\text{c-Si:H}$ (n^+/p^+) ①, from Batch-2. Corresponding R_{front} are plot in inset.	100
Figure V.3-9 I-V curves from 200 K to 350 K of structure e) with the tunnel junction $\mu\text{c-Si:H}$ (n^+/p^+) ③, from Batch-1. Corresponding R_{front} are plot in inset.	101
Figure V.3-10 Elemental EDX depth (nm) profile and corresponding STEM image of a cross section at the centre of the Al electrode of structure e) with the tunnel junction $\mu\text{c-Si:H}$ (n^+/p^+) ①, from batch-2.....	101
Figure V.3-11 STEM-EDX elemental mapping of a cross section at the centre of the Al electrode of structure e) with the tunnel junction $\mu\text{c-Si:H}$ (n^+/p^+) ①, from batch-2...102	102
Figure V.4-1 Contact resistivity, ρ_c , from 300 K to 350 K, of the two presented stacks, extracted from transversal I-V measurements (see part V.3).....	103
Figure V.4-2 Structures used to investigate the thin ITO recombination layer forming a recombination junction with the a-Si:H (p) layer of the SHJ bottom-cell in NIP tandem cells. a) Symmetrical and isotype (P-type) structures with thick a-Si:H (p) layers (20 nm), b) Isotype (P-type) structures with the front a-Si:H layers of the SHJ NIP bottom-cell, structures c) are the same as structures b) but with the thin ITO RJ layer and structures d) are the same as structures c) but with a thick ITO layer.....	103
Figure V.4-3 Minority carrier lifetimes at $10^{15} \Delta n \text{ cm}^{-3}$ of structures a) , b) , c) and d) (Figure V.4-2) without metallisation, as-dep (1), after the annealing under nitrogen (2) or after the annealing under air (3). Annealing: one hour on a hot-plate at 100 °C.	104
Figure V.4-4 R_{front} of structures a) , b) , c) and d) (Figure V.4-2), as-dep (1) and after the annealing under air (3).....	105
Figure V.5-1 Defined test-structures for transversal dark I-V measurements of recombination junctions. a) For PIN tandem solar cells and b) for NIP tandem solar cells.	105
Figure VI.2-1 Current losses due to the parasitic absorption of the RJ ITO, depending on its thickness. In black for a PIN architecture and in red for a NIP architecture.....	110
Figure VI.2-2 Simulated absorption and corresponding current in each subcell (top-cell in red and bottom-cell in blue). The EQE is presented in dashed lines and the losses by reflection in purple. NIP architecture on the left and PIN architecture on the right.	111
Figure VI.2-3 PK/SHJ tandem solar cell structures with a thin ITO at the junction between both subcells and the thicknesses used for optical simulations. a) Reference	

devices for NIP and PIN architectures. b) Device where the ITO replace the a-Si:H (n) layer. c) Device where the ITO replace the SnO ₂ layer.....	111
Figure VI.2-4 Simulated absorption of each subcell (top-cell in red and bottom-cell in blue) and 1-R _{tot} obtained by optical simulations, as a function of texturing and architecture (NIP in black and PIN in green) for each studied device (Figure VI.2-3).	112
Figure VI.2-5 Simulated absorption and corresponding current in each subcell (top-cell in red and bottom-cell in blue). The EQE is presented in dashed lines and the losses by reflection in purple. NIP architecture on the left and PIN architecture on the right.	113
Figure VI.2-6 PK/SHJ tandem solar cell structures with a microcrystalline silicon-based tunnel junction and the thicknesses used for optical simulations. a) Reference devices for NIP and PIN architectures. b) Devices where a highly doped $\mu\text{-Si:H}$ layer forms a recombination junction with one of the charges transport layer of the top-cell. c) Devices where a highly doped $\mu\text{-Si:H}$ layer acts as a charges transport layer (ETL or HTL)....	114
Figure VI.2-7 Simulated absorption of each subcell (top-cell in red and bottom-cell in blue) and 1-R _{tot} (in black) obtained by optical simulations, as a function of texturing and architecture, for each studied device (Figure VI.2-6).	116
Figure VI.3-1 a) “Tandem-like” device with a thin ITO layer as the RJ, b) “Tandem-like” device with a thick ITO layer (70 nm) as the RJ and the corresponding circuit diagram of these devices (using the one-diode model for the Perovskite top-cell).	118
Figure VI.3-2 J-V curves in the left and EQE spectra in the right of the studied devices a) (in orange) and b) (in blue) from Figure VI.3-1 .	118
Figure VI.3-3 Substrates used to investigate the Perovskite layer: a Ref on commercial glass substrate (as the Perovskite single-junction solar cells), a) Simplified version of the “tandem-like” device with a thin ITO layer, b) “tandem-like” substrate with a thick ITO layer and c) “tandem-like” substrate with a $\mu\text{-Si:H}$ (n ⁺) layer instead of an ITO.....	119
Figure VI.3-4 SEM images (III.2.8.a) of the Perovskite layer deposited on the substrates presented in Figure VI.3-3	120
Figure VI.3-5 X-ray diffraction patterns (Bragg-Brentano geometry, Co source, see part (III.2.10) of the Perovskite layer deposited on the substrates presented Figure VI.3-3 . The inset table shows the area ratios of low angle PbI ₂ and Perovskite diffraction peaks.	121
Figure VI.3-6 “tandem-like” devices with different junctions between the Perovskite top-cell and the N-type bottom-stack.	121
Figure VI.3-7 J-V curves of the “tandem-like” devices from Figure VI.3-6 (2 or 3 samples per device type). A zoom is presented in inset to more easily differentiate the curves.	122
Figure VI.3-8 J-V parameters of the “tandem-like” devices from Figure VI.3-6 obtained with I-V measurements, after a shading correction on the J _{sc} (the shading induce by the metallisation is different for each sample, a correction is applied to compare the devices with the same active area).	123
Figure VI.3-9 R _{tot} of the devices from Figure VI.3-6 , measured by spectrophotometry in solid lines and obtained with optical simulations in dashed lines. On the right, a zoom is done to have a better view of each curve, from 600 nm to 1000 nm.	124
Figure VI.4-1 J-V curves of PIN PK/SHJ tandem solar cells, with the developed $\mu\text{-Si:H}$ (n ⁺ /p ⁺) junction (Figure IV.1-1), with two different HTM and different pretreatment duration: a) 3 min UV/O ₃ and PEDOT:PSS; b) , c) and d) 5 min UV/O ₃ and PEDOT:PSS; e) 5 min UV/O ₃ and a SAM (2-PACz) HTM,.....	126
Figure VI.5-1 “tandem-like” devices to measure the Perovskite top-cell processed in tandem conditions (a) for NIP architecture and b) for PIN architecture).	127

I. GENERAL INTRODUCTION

I.1. Context

This work takes place in the context of the climate crisis, presenting photovoltaics as an essential part of the possible solution/remediation.

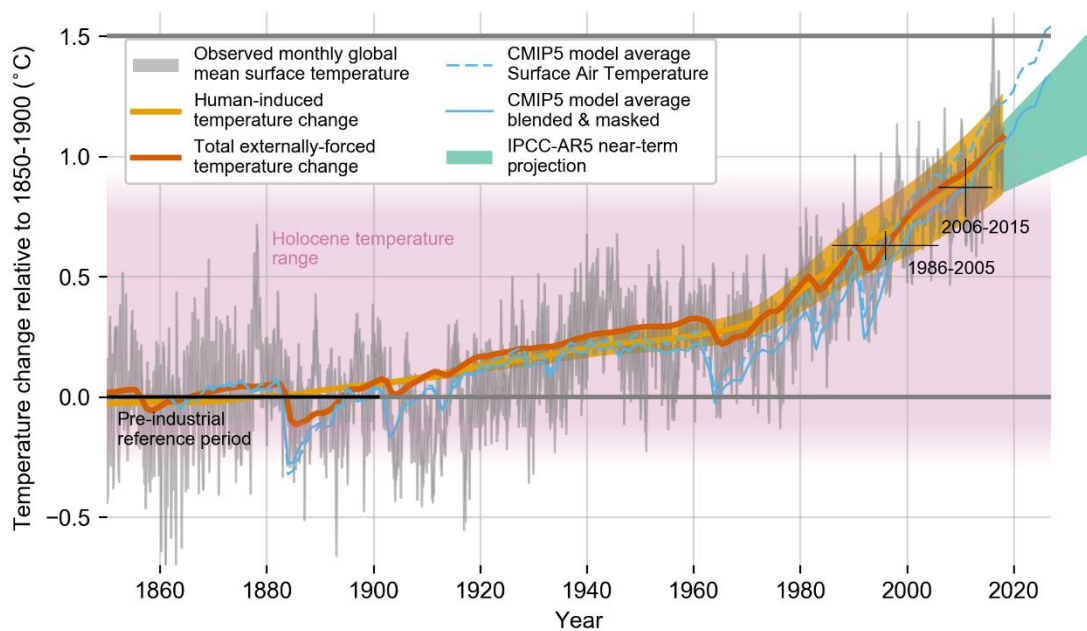


Figure I.1-1 Evolution of global mean surface temperature (GMST) over the period of instrumental observations. Reproduced from the IPCC *Global Warming of 1.5 °C* report [1], *Framing and Context* chapter, Figure 1.2, P.57.

The climate change ([1], [2]), illustrated with the temperature change in **Figure I.1-1**, leads us to rethink our greenhouse gas emissions. Indeed, it is now clear that the climate crisis is “man-made” and it keeps getting worse (because of overproduction / overconsumption due to our societies). Our way of consuming and producing must therefore change. This change necessarily involves the reduction of the CO₂ level in the atmosphere (which is undoubtedly linked to the rise in temperatures

presented in **Figure I.1-1** [3]). Thus, this leads to scenarios including renewable energy sources, comprising photovoltaic energy ([4], [5]).

The photovoltaic energy is produced by devices named solar cells, thanks to the photovoltaic effect demonstrated by E. Becquerel in 1839 [6]. In fact, when a semiconductor material absorbs light (depending on its bandgap), the absorbed photons give energy to electrons and create so-called electron-hole pairs. If there are electrodes at both sides of the material and a difference in electrochemical potential at these terminals, the electron-hole pairs tend to be separated and the charges move toward the electrodes (electrons on one side and holes on the other). This results in a potential difference (V) and an electric current density (J), respectively named V_{oc} when the current is zero (open-circuit conditions) and J_{sc} when the voltage is zero (short-circuit conditions).

According to its functioning principle, a solar cell is usually modelled by a one-diode model or a two-diode model, presented in **Figure I.1-2**. The corresponding equations under illumination are equation (I. 1-1) for the one-diode model and equation (I. 1-2) for the two-diode model.

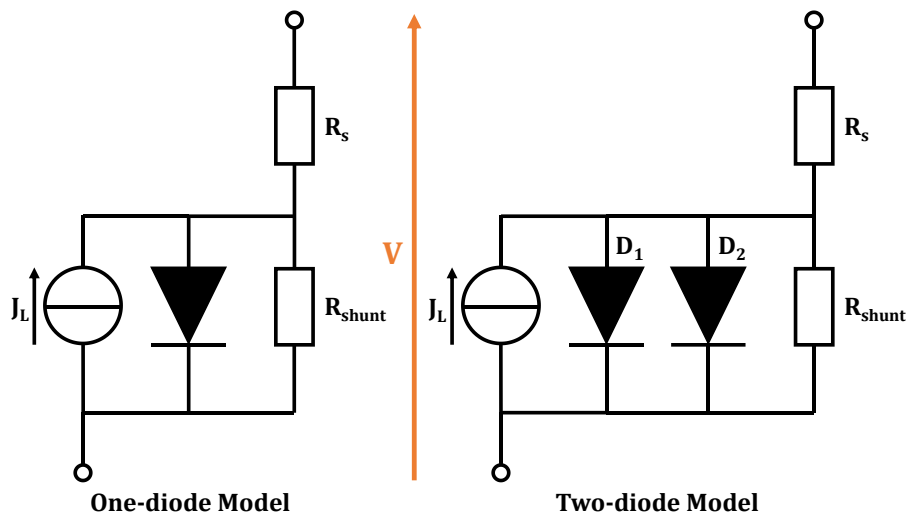


Figure I.1-2 One and two-diode models of solar cells.

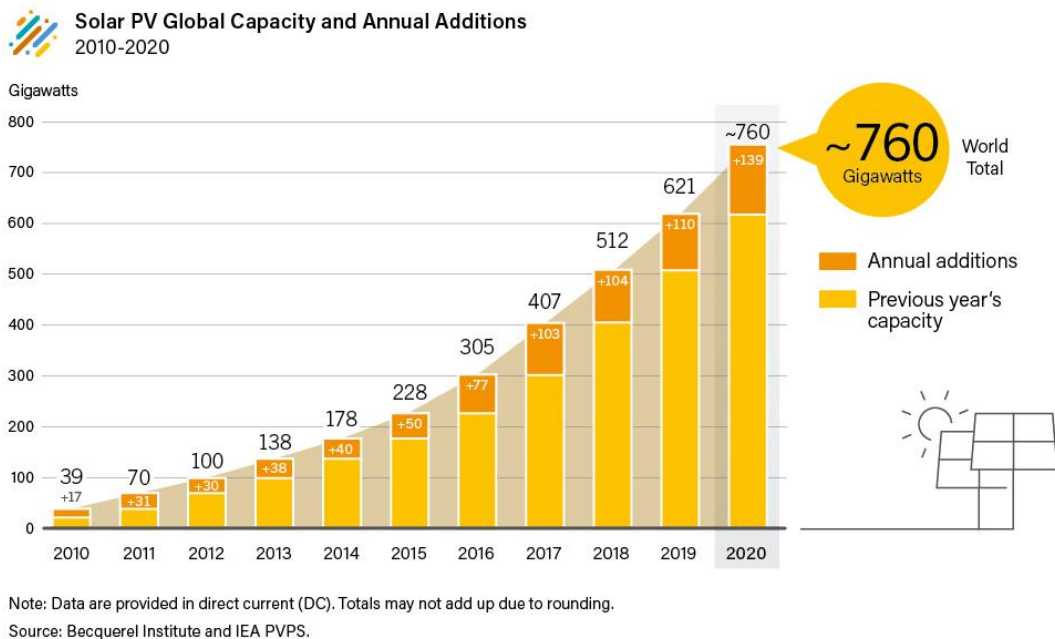
$$J = J_L - J_0 \cdot \left(\exp\left(\frac{V + J \cdot R_s}{n \cdot k \cdot T / q}\right) - 1 \right) - \frac{V + J \cdot R_s}{R_{shunt}} \quad (\text{I. 1-1})$$

$$J = J_L - J_{01} \cdot \left(\exp\left(\frac{V + J \cdot R_s}{n_1 \cdot k \cdot T / q}\right) - 1 \right) - J_{02} \cdot \left(\exp\left(\frac{V + J \cdot R_s}{n_2 \cdot k \cdot T / q}\right) - 1 \right) - \frac{V + J \cdot R_s}{R_{shunt}} \quad (\text{I. 1-2})$$

Where k is the Boltzmann constant, q is the elementary charge, T is the temperature, J_L is the current density generated under illumination, R_s is the series resistance of the solar cell, R_{shunt} is the shunt resistance, n , n_1 and n_2 are the ideality factors of the diodes and J_0 , J_{01} and J_{02} are the saturation currents of the diodes.

Since the discovery of this effect, the photovoltaic research and industry have grown fast. Spatial applications were the first drivers for silicon photovoltaic technology development in the 1950s. Then, terrestrial applications came on the front scene. At the start of this work (end of 2017), the cumulative installed solar photovoltaic capacity exceeded 400 GW and it reached 760 GW at the end of 2020 (see **Figure I.1-3** from [7]). This global capacity is estimated to exceed 1000 GW over the next 2 years [8]. The key

factor of this increase is a drop in production costs [9], associated with an increase in solar cells efficiencies. This work is part of this race, by proposing studies of development and understanding of a promising high efficiency and potentially low-cost solar cell technology.



REN21 RENEWABLES 2021 GLOBAL STATUS REPORT

Figure I.1-3 Solar photovoltaic world cumulative installed capacity and annual additions in Gigawatts from 2010 to 2020.

Indeed, the solar photovoltaic world market share is dominated by high temperature crystalline silicon solar cells, such as PERC, PERL or TOPCon (see part II.2 for more details), but Si-based tandem technologies should enter the market in the next 5 years [9]. Tandem technologies allow a more efficient use of the energy of absorbed photons, combining two solar cells composed of absorber materials with different bandgaps (splitting of the solar spectrum, see part II.1). Moreover, these technologies have higher theoretical efficiency limit [10]. Si-based tandem technologies consist in a silicon-based bottom-cell associated with a top-cell in a material with a larger bandgap. From an economic perspective, the addition of this top-cell must be as inexpensive as possible. **Therefore, this work focuses on Perovskite on silicon heterojunction tandem solar cell, a technology able to surpass the current industrial PCE while limiting the production costs increase.**

I.2. Motivation and objectives

With this context favourable to photovoltaic technologies, the motivations presented below led to the establishment of this work.

From 2015 to 2017, some proofs of concept of PK/SHJ tandem solar cells were presented in the literature ([11]–[15], see part II.3.2 for more details). These devices, involving the series connection of a Perovskite solar cell and a SHJ solar cell, have thus demonstrated PCE exceeding 20 %, on small surfaces, rivalling the silicon single-junction efficiencies. Moreover, several types of architecture (NIP and PIN), texturing (polished/polished, polished/textured and textured/textured) and recombination junctions (TCO and highly doped PN junction) have been proposed in

experiments and simulations. Furthermore, those early studies also showed that it is essential to reduce losses to increase the efficiencies, whether optical (due to parasitic absorption of the different layers) or related to the charges transport, in particular in the recombination junction (RJ).

However, even if this RJ between the two subcells seems a key factor, the published studies did not dwell on this subject. In fact, they demonstrated the viability of an ITO layer and a highly doped silicon PN junction in the proofs of concept but without proposing any prospects for characterisation and improvement. This justifies this work, which consists in **characterising, understanding and optimising the recombination junction between the subcells**, by developing adapted methods.

Therefore, the objectives of this work are as follow:

- Development of a highly doped silicon tunnel junction suitable for 2T PK/SHJ tandem solar cells,
- Implementation of characterisation methods to optimise the recombination junctions,
- Understanding the transport mechanisms in 2T PK/SHJ tandem solar cells and the influence of their RJ.

I.3. Approach

In this last part of the general introduction, we describe the approach carried out to achieve the objectives of this work.

In chapter II, we present the basics of tandem solar cells and recombination junctions as well as the state-of-the-art of PK/SHJ tandem solar cells. Then, in chapter III, we detail the fabrication processes and the characterisation methods used along this work.

In order to study the two types (previously presented) of RJ during this work, we developed a highly doped silicon PN junction, based on microcrystalline silicon. In chapter IV, we present the development of this RJ for PK/SHJ tandem solar cells in the PIN architecture. Moreover, we detail the microcrystalline silicon layers characterisation and optimisation. In conclusion, we discuss the integration of these layers into SHJ solar cells and their viability for tandem solar cells.

Then, towards the understanding of the transport mechanisms and the optimisation of the RJ, we investigated, set up and discussed ways to characterise electrically the RJ in chapter V. Furthermore, we present advantages and limitations of these characterisation methods, depending of the RJ type and the experimental potential limitations.

Finally, to investigate the influence of the RJ in PK/SHJ tandem solar cells and allow its pairing with the Perovskite top-cell, we perform optical simulations in chapter VI. Moreover, we develop and present an innovative “tandem-like” device that could be very useful in the understanding, development and optimisation of the PK/SHJ tandem solar cells. To conclude, we present the integration of the developed microcrystalline silicon junction in PK/SHJ tandem solar cells and discuss further improvements.

II. STATE-OF-THE-ART

This chapter presents the state-of-the-art of Perovskite/SHJ tandem solar cells and is articulated in four parts. The first part presents a brief history and the basics of tandem solar cells. The second part is an overview of c-Si solar cells and a presentation of SHJ solar cells. Then, the third part describes the recent arrival of Perovskite and Perovskite/SHJ tandem solar cell as a major field of interest in the photovoltaic community. To conclude, the fourth part focuses on the recombination junction, a key part of tandem solar cells that is deeply studied in this work. This chapter not only shows a review of the state-of-the-art technology at the beginning of this work, but also a follow-up of the major advances, in this quickly evolving field of research, during these three years.

II.1. Tandem Solar Cells

In this part, we shortly introduce the history of tandem solar cells. Then, we discuss the tandem main configurations, and to conclude we explain the operation of a monolithic tandem solar cell.

After the observation of the photovoltaic effect by E. Becquerel in 1839 [6], the first solar cells elaborated were single-junction solar cells [16]. That is to say that it comes down to an absorber material of N-type or P-type (or even intrinsic) in contact with a layer of the opposite type, forming a PN junction (or a PIN device). In the 1970s, in order to improve the efficiency limit of existing solar cells, the idea of tandem and multi-junction solar cells was proposed [17]. During this period, two possibilities were considered for tandem solar cells: “stacked cells” or a splitting approach [18], represented respectively in **Figure II.1-1 b)** and **c)**. **Figure II.1-1** shows the three main tandem configurations and **Table II.1-1** presents their advantages and disadvantages. In this work, we only studied monolithic tandem solar cell (**Figure II.1-1 b)**), mainly for its ease of implementation in module and its lower cost. The first monolithic (or two-terminal) tandem solar cell, was made of AlGaAs/GaAs, in 1978, by S. M. Bedair *et al.* [19] using a heavily doped tunnel junction between the two subcells.

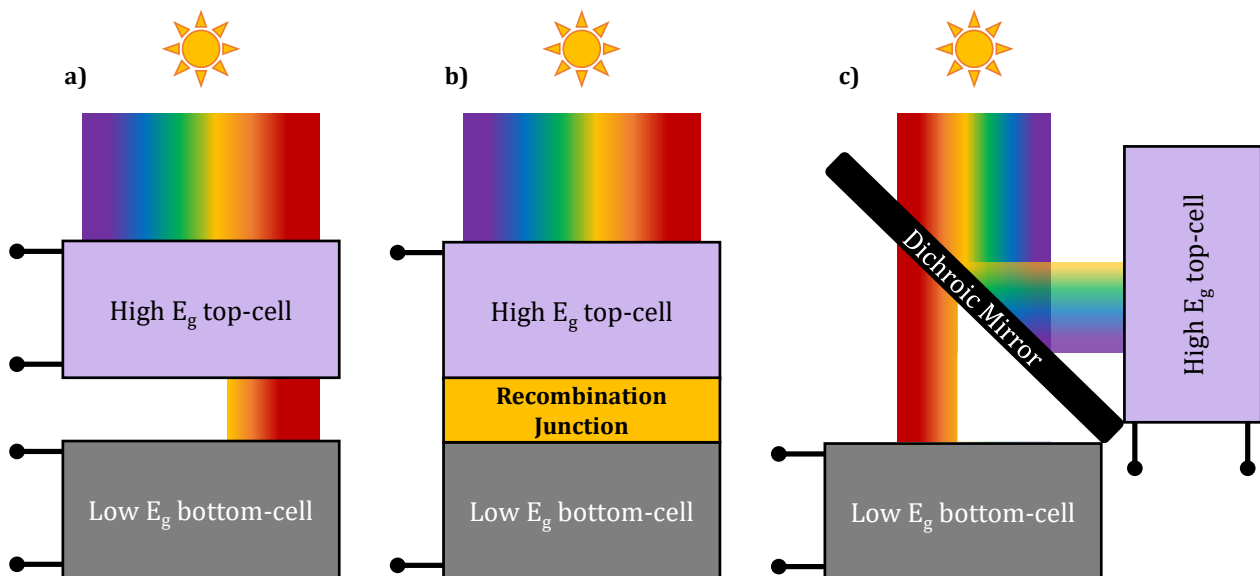


Figure II.1-1 Drawing of the main existing tandem solar cell configurations; **a)** Mechanically stacked, 4-terminal tandem solar cell; **b)** Monolithic, 2-terminal tandem solar cell; **c)** Optical spectral splitting, 4-terminal tandem solar cell.

A monolithic (2T) tandem solar cell is a superposition of two subcells separated by a recombination junction (II.4) or designed such that their superposition forms a recombination junction. The two subcells are connected in series, thus the current density of the tandem is the minimum current density between those of the subcells, equation (II.1-1). Thus, a current matching between the two subcells leads to the maximum potential current in the 2T tandem solar cell and therefore to a better efficiency. Moreover, in the case of an ideal 2T tandem solar cell, the open-circuit voltage of the tandem is the addition of the subcells open-circuit voltages, equation (II.1-2). In reality, the recombination junction often induces an additional resistance in the system, R_{Junction} in **Figure II.1-2**, which leads to losses in the tandem V_{oc} [20].

$$I_{sc,tandem} = \text{minimum}\{I_{sc,top-cell}; I_{sc,bottom-cell}\} \quad (\text{II. 1-1})$$

$$V_{oc,tandem} = V_{oc,top-cell} + V_{oc,bottom-cell} \quad (\text{II. 1-2})$$

Tandem	Advantages	Disadvantages
Mechanically stacked (Figure II.1-1 a))	<ul style="list-style-type: none"> Easy implementation (subcells fabricated and optimised independently) Separate MPP and tracking systems Low sensitivity to spectral variations and top-cell's bandgap [21] 	<ul style="list-style-type: none"> Four electrodes and at least three must be transparent Doubled power electronics in module and systems
Monolithic (Figure II.1-1 b))	<ul style="list-style-type: none"> Only one electrode must be transparent (two for bifacial devices) Same module architecture as single-junction solar cells 	<ul style="list-style-type: none"> Current matching between the two subcells Technical manufacturing constraints (thermal budget, surface state...) Sensitivity to spectral variations and top-cell's bandgap [21]
Splitting system (Figure II.1-1 c))	<ul style="list-style-type: none"> Standard solar cells can be used Separate MPP and tracking systems 	<ul style="list-style-type: none"> Doubled power electronics in module and systems Expensive optical components

Table II.1-1 Main advantages and disadvantages of the tandem solar cell configurations presented in **Figure II.1-1**.

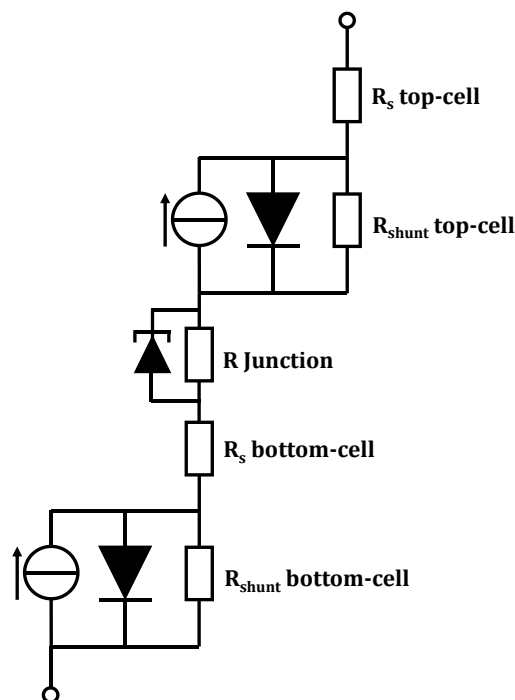


Figure II.1-2 One-diode model of a monolithic tandem solar cell.

Figure II.1-3 illustrates an example of band diagrams of single-junction and 2T tandem solar cell, with an N-type substrate, in the standard emitter configuration (named NIP in this work, in order to correlate with Perovskite solar cells nomination, the intrinsic (I) part is not presented here but the principle is the same as with only NP junctions). In an ideal single-junction solar cell under illumination, we can assume that the holes move to the P-type side while the electrons move to the N-type side. If we connect the two electrodes (or terminals) of the solar cell, carriers will flow in a closed circuit and recombine at the interface between the P-type side material and the electrode. In this configuration, the observed current, J_{sc} , is called photocurrent. In an ideal 2T tandem solar cell, the same operation happens in each subcell but there are two zones where the carriers will recombine: at the interface between the P-type side material and the electrode (front-side in the NIP configuration presented **Figure II.1-3 b**) and in the recombination junction between the two subcells. This is why the tandem J_{sc} cannot exceed the minimum J_{sc} between the subcells.

As for a single-junction solar cell, the V_{oc} is dependent of the quasi-Fermi levels shown in **Figure II.1-3** ($V_{ext} = \frac{1}{q} \cdot (E_{fn} - E_{fp})$, where q is the elementary charge and V_{ext} is the potential between the two terminals of the solar cell; at V_{oc} : $V_{ext} = V_{oc}$). If the recombination junction is not optimised, the tandem solar cell will not operate at its full potential. The recombination junction is therefore one of the most important part of the development of tandem solar cells, a focus on it will be done in part II.4.

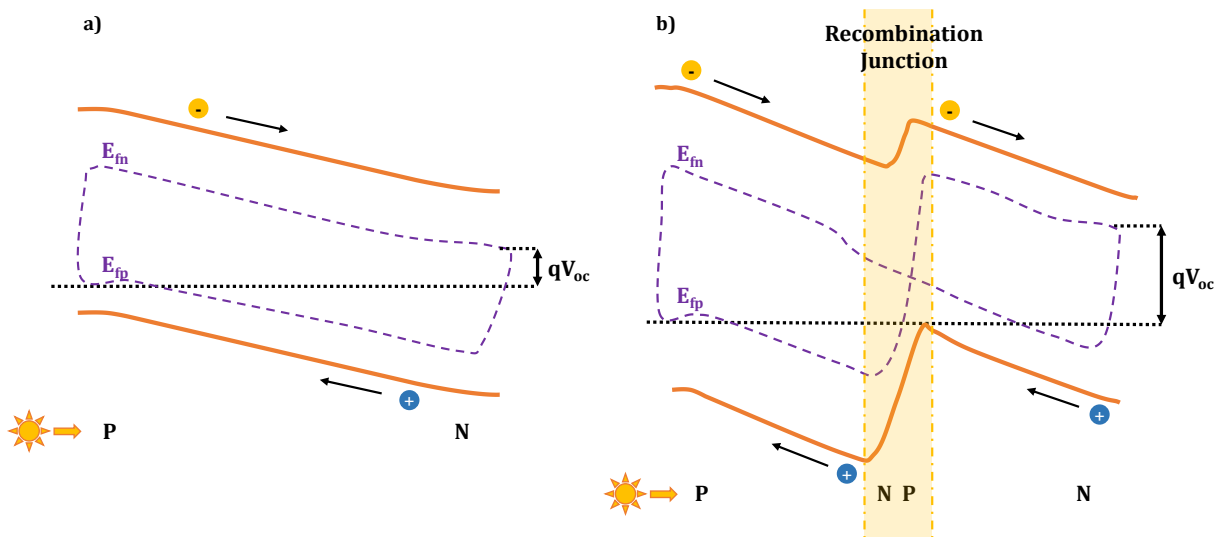


Figure II.1-3 Band diagrams of a **a)** NIP single-junction solar cell and a **b)** NIP tandem solar cell, at V_{oc} . E_{fn} and E_{fp} are respectively the electron and hole quasi-Fermi levels in the materials.

In this work, we did not study multi-junction solar cells with more than two subcells but the operation theory is the same by adding other subcells and there is always a recombination junction between each subcell. In fact, the more subcells there are, the higher the theoretical efficiency limit is [10], [22]–[24]. In 2020, J. F. Geist *et al.* presented a six-junctions solar cell with an efficiency of 39.2 % under 1 sun (47.1 % under 143 suns concentration) [25], which is very promising but using very expensive III-V materials. Consequently, the vast majority of these technologies are only used for space applications, where the ratio performance/cost is not a key issue. This is not the case for terrestrial applications for massive deployment of the photovoltaic, where tandem or multi-junction solar cells need to demonstrate the lowest LCOE possible to be competitive with silicon-based technologies.

II.2. Silicon Heterojunction Solar Cells

After presenting the working principle of tandem solar cells in the previous part, in this section, we relate the history of crystalline silicon solar cells to SHJ cells, as we know them today. Then, we describe in more details the different components of SHJ solar cells.

Figure II.2-1 shows the evolution of the structure of high temperature crystalline silicon solar cells. In the 1940s, *Bell Labs* discovered that crystalline silicon presents very good properties for photovoltaic applications [26], [27]. In 1957, they presented a solar cell on N-type crystalline silicon base with a thin P-type layer, **Figure II.2-1 a)**, which exceeded 10 % efficiency [16]. In order to produce solar cells for space applications, P-type c-Si (less sensitive to radiation) quickly replaced the N-type as base for the solar cells and an anti-reflection coating was added to improve optical properties, as well as a front-side metallisation grid, **Figure II.2-1 b)**[28]. In the 1970s, *Comsat corporation* improved the efficiencies with lowly resistive wafer, highly doped back-side, **Figure II.2-1 c)** and front-side texturing, **Figure II.2-1 d)** [29]. Then, the *University of New South Wales (UNSW)*, in Sydney, added a passivation layer (SiO_2) and reached 18 % efficiency with their Metal Insulator NP junction (MINP), **Figure II.2-1 e)**. In 1988, they exceeded 20 % efficiency with their Passivated Emitter Solar Cell (PESC), **Figure II.2-1 f)**, by using inverse pyramid structure and partially direct Metal/emitter contact. Then, with a local ($n+$) doping in the emitter and a partially opened passivation layer at the back-side, their PERC structure, **Figure II.2-1 g)**, reached 22.6 % efficiency in 1989 [30].

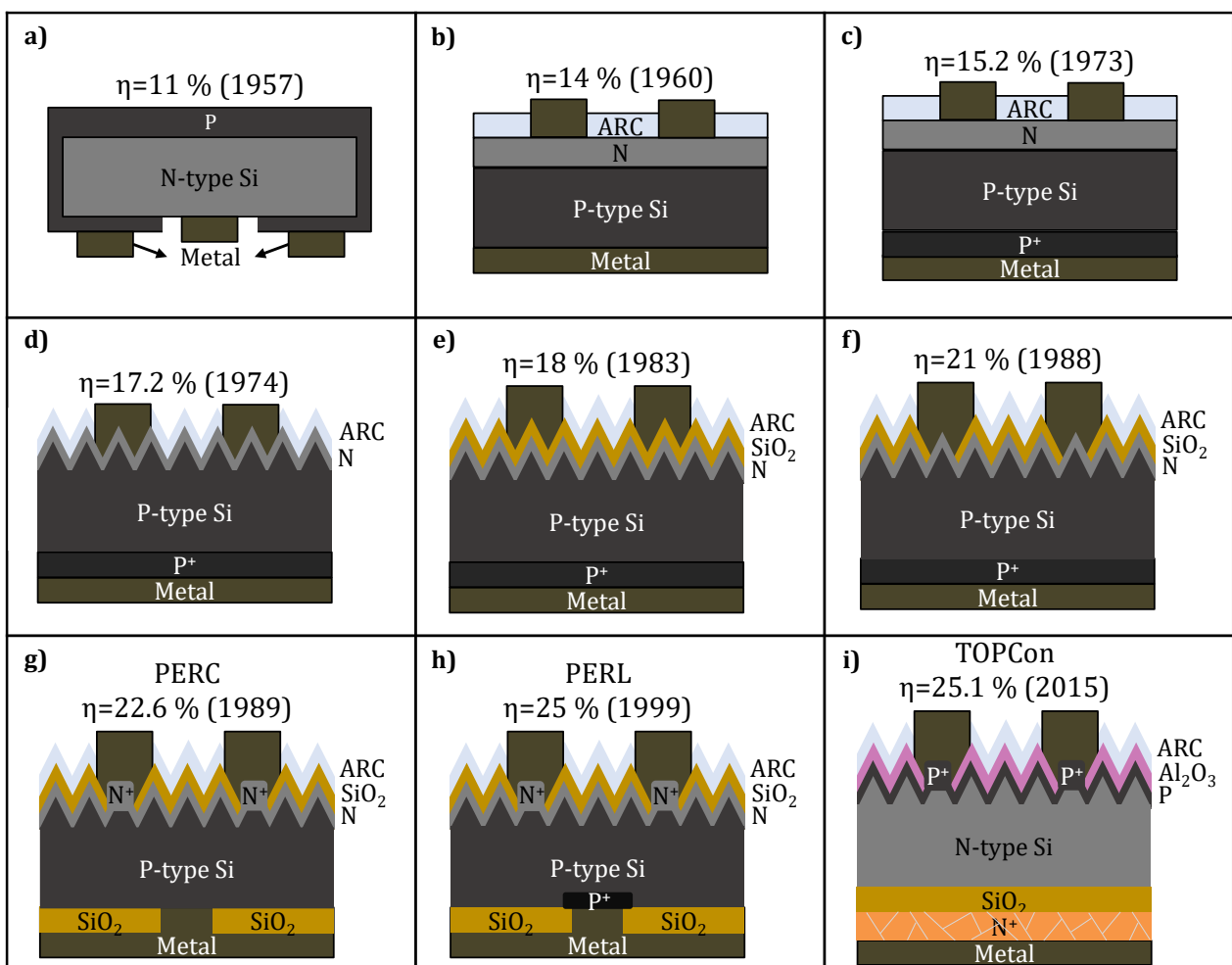


Figure II.2-1 Drawing of notable c-Si solar cells with their respective efficiency. **a)** *Bell Labs* solar cell; **b)** *Hoffman Electronics*; **c)** and **d)** *Comsat Labs*; **e)**, **f)**, **g)** *UNSW*; **h)** First measured at 24.7 %, then at 25 %, *UNSW*; **i)** *Fraunhofer ISE*.

Continuing their momentum, they reached the 25 % efficiency 10 years later with the PERL structure, thanks to a local (p⁺) doping at the back-side, **Figure II.2-1 h** [31]. Fifteen years later, the Fraunhofer ISE developed the TOPCon structure on N-type wafers, **Figure II.2-1 i**), using a passivating tunnel oxide and a (n⁺) poly-Si at the back-side [32]. Since then, more and more solar cells with passivated contacts, made with high temperature process, have appeared [33], and became a hot topic in research. In parallel, low temperature surface passivation using hydrogenated amorphous silicon and forming a heterojunction with the crystalline silicon were developed [34]. In 1990, *Sanyo Electric Co.* presented the first SHJ solar cell using an a-Si:H (i) passivation layer, named HIT (Heterojunction with Intrinsic Thin-layer)[35]. In 1992, they exceeded 18 % efficiency with a heterostructure contact at the rear side, **Figure II.2-2 a**) [36]. With further optimisations, they reached 24.7 % efficiency in 2013 with a very thin wafer (98 μm) [37]. Shortly afterwards, *KANEKA Corporation* exceeded certified 25 % efficiency on large area, **Figure II.2-2 b**) [38], [39]. This efficiency record was the best for front-rear contacted SHJ solar cells until the *Hanergy Group* achieved 25.11 % efficiency in total area (M2 wafer) for a bifacial (with a metallisation grid at the back-side instead of a full surface metallisation) solar cell, in 2019 [40]. **Figure II.2-2 c**) shows the bifacial SHJ solar cells produced in the pilot-line at the CEA-INES and the best efficiencies reached. The best efficiencies for crystalline silicon solar cells are not obtained with front-rear contacted configuration but with IBC configuration (**Figure II.2-1 a**) for example), with passivated contacts at low temperature [41] or at high temperature [42]. The IBC configuration allows higher current thanks to a larger active area (no metallisation on the front-side). Tandem solar cells with an IBC bottom-cell are 3T (3-Terminal) structures. This work is focused on the front-rear contacted configuration to make 2T tandem solar cells, thus we do not detail more IBC solar cells here.

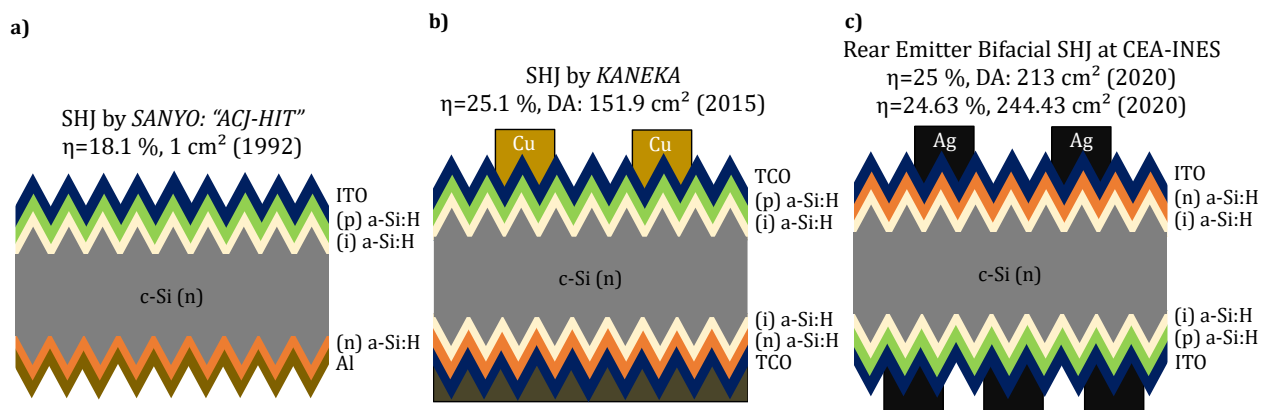


Figure II.2-2 a) First SHJ solar cell with an intrinsic thin layer developed by *Sanyo*; **b)** Standard emitter SHJ with an efficiency of 25.1 % presented by *KANEKA* in 2015; **c)** SHJ solar cells produced in the CEA-INES pilot-line.

The CEA-INES SHJ solar cells are composed of an N-type crystalline silicon wafer, with pyramidal texturing. Then, very thin intrinsic or low-doped hydrogenated amorphous silicon layers are deposited by PECVD at low temperature, around 200 °C, to passivate the wafer and improve the V_{oc} . **Figure II.2-3** shows the 2D structure of c-Si (n) and a-Si:H (i) materials and the heterojunction formed between them. The addition of hydrogen during the PECVD process greatly reduces dangling bonds in the material, which reduces defects and therefore unwanted recombination.

On top of each a-Si:H (i) layers, doped thin layers are also deposited by PECVD at low temperature, a-Si:H (n) on the front-side and a-Si:H (p) on the back-side, for a rear emitter SHJ solar cell, and the opposite for a standard emitter SHJ solar cell. They act as selective layers to extract the charge carriers. Then, ITO layers are deposited by PVD on the doped a-Si:H layers. These ITO layers have a high lateral conductivity to transport

the charge carriers to the metallisation and they are optically optimised (front-side and back-side ITO are often different). ITO layers act as anti-reflection layers and play a role in the selective contacts. For example, the back-side ITO forms a recombination junction with the P-type amorphous layer (**Figure II.2-4**).

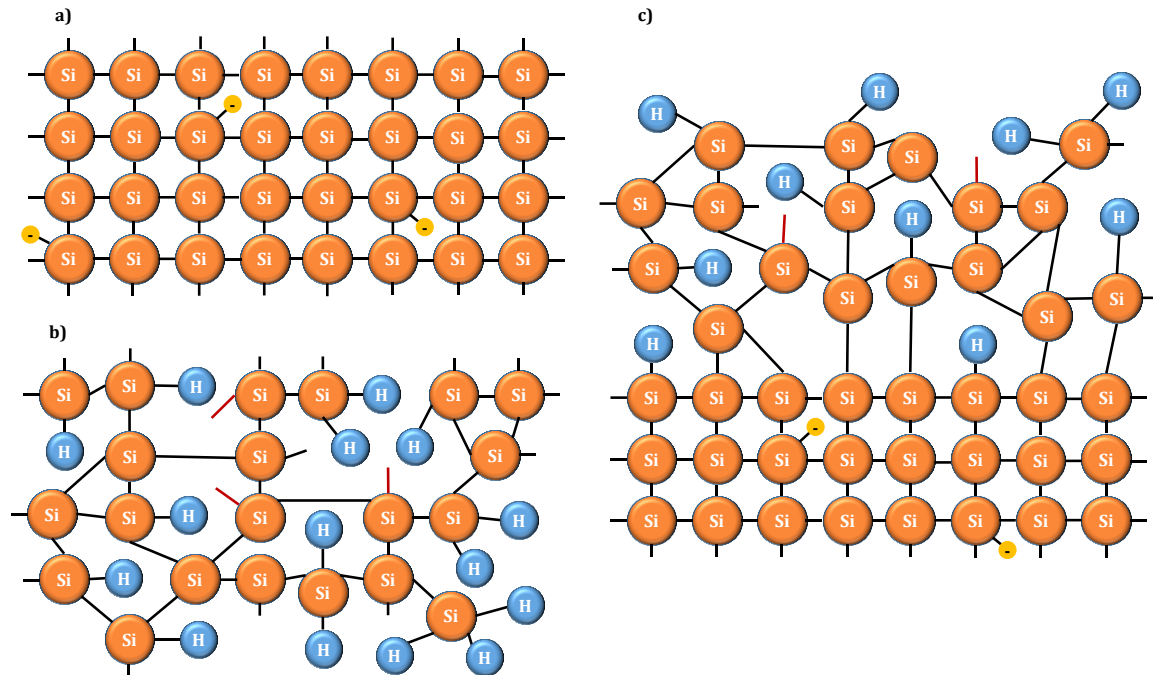


Figure II.2-3 **a)** 2D drawing of a (100) N-type crystalline silicon; **b)** 2D drawing of an intrinsic amorphous silicon; **c)** 2D drawing of the heterojunction a-Si:H (i)/c-Si (n). Dangling bonds are represented in red lines and excess electrons in yellow circles.

Finally, the solar cells are metallised with silver pastes deposited by screen-printing and annealed at a temperature around 200 °C, depending on the screen-printing paste used. During this annealing, the screen-printing paste is cured and ITO layers are crystallised, which improves their electrical properties and contact with other layers.

With the chemical passivation and the high field effect induced by the amorphous layers, SHJ solar cells can reach higher V_{oc} (exceeding 750 mV with thin wafers, [43]) than other silicon solar cells. On the other hand, amorphous silicon and ITO layers induce parasitic absorption that can reduce the J_{sc} . There are possibilities to counter this: some materials such as nanocrystalline silicon ([40], [44]–[47]) or TMOs ([48]–[55]) can replace the amorphous layers and other TCOs ([56]–[59]) can be used instead of the ITO. However, in

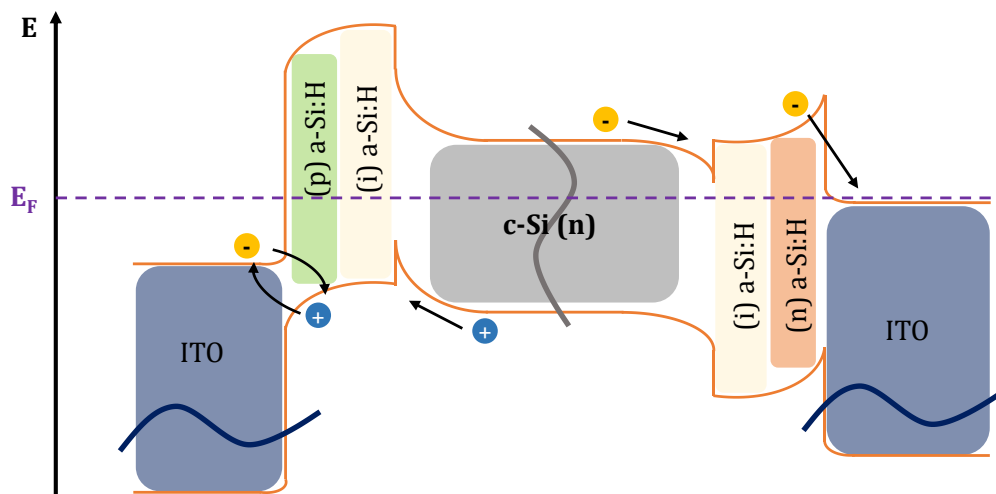


Figure II.2-4 Band diagram of a SHJ solar cell in the configuration illustrated **Figure II.2-2 c)**, without the metallisation.

a context of industrialisation, SHJ solar cells, as presented in **Figure II.2-2 c)**, remain the most common configuration. **Figure II.2-4** shows an example of the band diagram of this type of SHJ solar cells (band bending changes with bandgaps, work functions and electron affinities).

II.3. Perovskite on Silicon Heterojunction Tandem Solar Cells

After the presentation of tandem and SHJ solar cells, in this part we join the both. First, we introduce the idea of Perovskite on SHJ tandem solar cells and explain the interest in this technology. Then, we review the advancement of this technology before the start of this work. To conclude, we present a timeline of the main advances in Perovskite/SHJ tandem solar cells that took place during the three years of this work.

II.3.1. Introduction

Discovered in 1839 in the Urals, by Lev A. Perovski, the crystalline structural minerals named Perovskite have become among the most promising materials in the field of photovoltaics. In 1994, D. Mitzi *et al.* showed that organic lead-halide Perovskite behave as metal-semiconductor transitions [60]. In addition, the 2D to 3D transition changes the electronic properties and reduces the bandgap. As a narrow bandgap is necessary in the field of solar cells, research in this field is then increased. In 2009, A. Kojima *et al.* used a 3D Perovskite ($\text{CH}_3\text{NH}_3\text{PbX}_3$) as an hybrid organic/inorganic sensitizer in dye-sensitized solar cells (with photosensitive pigments) [61]. They observed that the absorption of this Perovskite on a nanocrystalline surface (TiO_2) produces a photocurrent, allowing for PCE of 3 to 4 %. However, they also noted that the use of a liquid electrolyte causes the Perovskite to decompose in contact with it, due to solubilisation in the liquid electrolyte, thus the photovoltaic effect was unstable. In 2012, by replacing the liquid electrolyte by an organic HTM (spiro-OMeTAD), two teams managed to obtain efficiencies around 10 % using different structures, both stable [62], [63]. Thereafter, the improvements multiplied and the number of publications about Perovskite solar cells exploded [64]. In 2015, the best certified efficiency had already exceeded 20 % [65]. The current best certified PCE was obtained in 2020 and exceeds 25 % on small scale (active area $\leq 1 \text{ cm}^2$) [66].

The structure of a Perovskite crystal is cubic and composed of three sites (A, B and X in **Figure II.3-1**) corresponding to the location of the different components according to the type of Perovskite used. For example, a Perovskite crystal of the $\text{CH}_3\text{NH}_3\text{PbI}_3$ type is formed this way: CH_3NH_3^+ in A-site, Pb^{2+} in B-site and I^- in X-site. The large range of

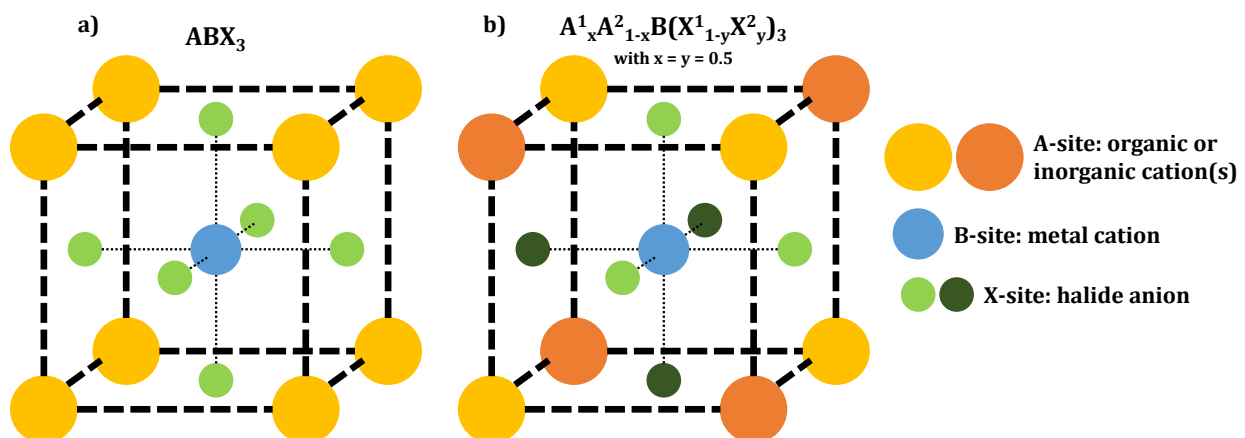


Figure II.3-1 a) Structure of a Perovskite crystal with the formula ABX_3 , often named a one-cation Perovskite; **b)** Structure of a double-cation Perovskite, as used in this work.

material components accessible for Perovskite crystal make it possible to tune its composition according to needs. For example, to modify the bandgap of the Perovskite, it is possible to change the cation in the A-site, to add some Sn with the Pb in the B-site or to modify the Br/I ratio in the X-site.

To obtain a solar cell, the Perovskite is combined with other materials and acts as an intrinsic absorber. Usually, the Perovskite layer is placed between an ETM and a HTM, which are in contact with electrodes. There are two possible structure for a Perovskite solar cell, planar (flat interfaces, **Figure II.3-2 a)** and **c)**) or mesoporous (use of porous materials, often semiconductor oxides whose mesopores are filled with the Perovskite, **Figure II.3-2 c)** and **d)**). Usually, when the ETM is deposited first, the solar cell architecture is named NIP and when the HTM is deposited first, the architecture is named PIN, we use the same convention for tandem solar cells architectures. In this work, we used planar top-cells with PTAA as the HTM and SnO₂ as the ETM.

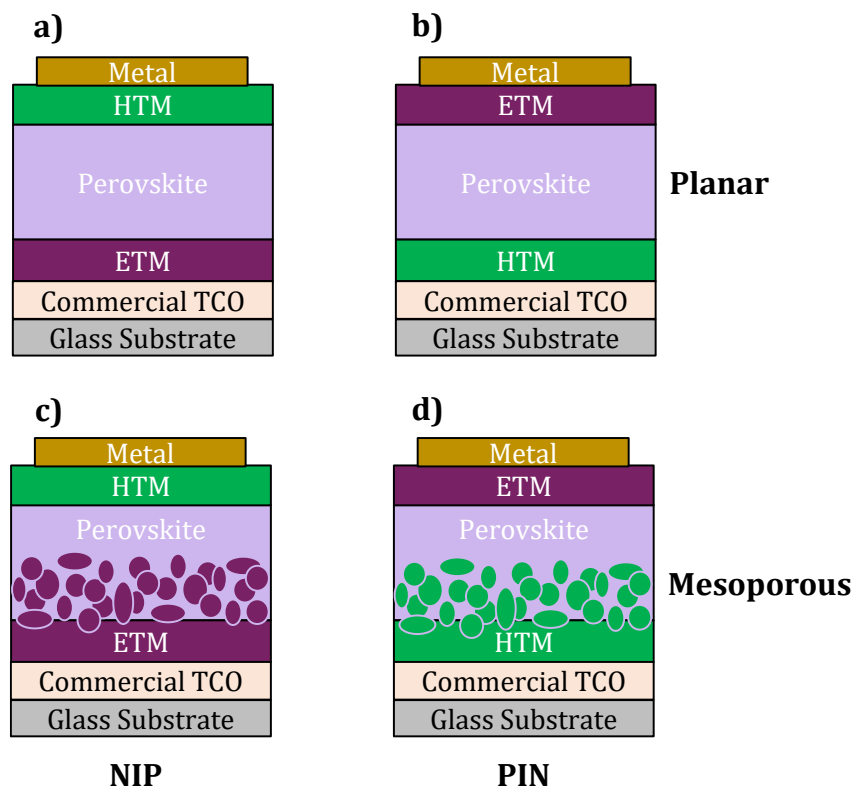


Figure II.3-2 a) Planar NIP Perovskite solar cell; **b)** Planar PIN Perovskite solar cell; **c)** Mesoporous NIP Perovskite solar cell; **d)** Mesoporous PIN Perovskite solar cell.

To sum up, Perovskite materials are abundant, low cost to process and can reach high efficiencies ([67], [68]) thanks to a strong absorption with steep absorption edge [69], good charge separation (low exciton binding energy) and charge transport (large diffusion lengths, low effective masses...). That makes them very attractive in the field of photovoltaic where the main goal is reducing costs while increasing efficiencies. Moreover, the possibility to control the bandgap of these materials allows us to use them in multijunction solar cells, even in all-Perovskite multijunction solar cells [70]–[76]. Crystalline silicon, already dominating the high efficiency photovoltaic market and having a small gap (1.12 eV), appears to be an excellent partner for Perovskite materials. In fact, by adding a Perovskite solar cell, using potentially low-cost techniques, on a conventional c-Si based solar cell, we may obtain a monolithic tandem possibly exceeding 40 % efficiency [17]. Moreover, the technologies in modules and in photovoltaic installations do not have to be modified much. Still, major efforts need to be deployed to upscale Perovskite solar cells and improve their stability.

The choice of a SHJ bottom-cell to form a tandem solar cell with a Perovskite top-cell is not random. In fact, SHJ solar cells present many advantages:

- Perovskite solar cells are usually deposited on top of a TCO layer and SHJ solar cells have a TCO layer on the front-side. Moreover, TCOs work well as recombination junction in organic tandem solar cells which are composed of similar ETM and HTM [77]–[79].
- SHJ solar cells reached efficiencies exceeding 25 % and have higher V_{oc} (over 740 mV) than other c-Si solar cells, even under low light (as it is the case in tandem solar cells).
- The parasitic absorption of amorphous layers in the visible range, which is one of the main defects of SHJ solar cells compared to other c-Si cells, does not impact the J_{sc} in tandem solar cells.
- Low temperature processes used in SHJ solar cells (PVD and metallisation) can be used on Perovskite/SHJ tandem solar cells unlike high temperature processes which can degrade the Perovskite.
- SHJ solar cells fabrication process was demonstrated to be cost effective [80].

Moreover, with the stagnation of the c-Si solar cells (presented in part II.2) efficiencies, illustrated in **Figure II.3-3**, the fast increase of the Perovskite solar cells efficiencies (**Figure II.3-5**) and the market entry of SHJ solar cells, this type of tandem solar cells appears very promising.

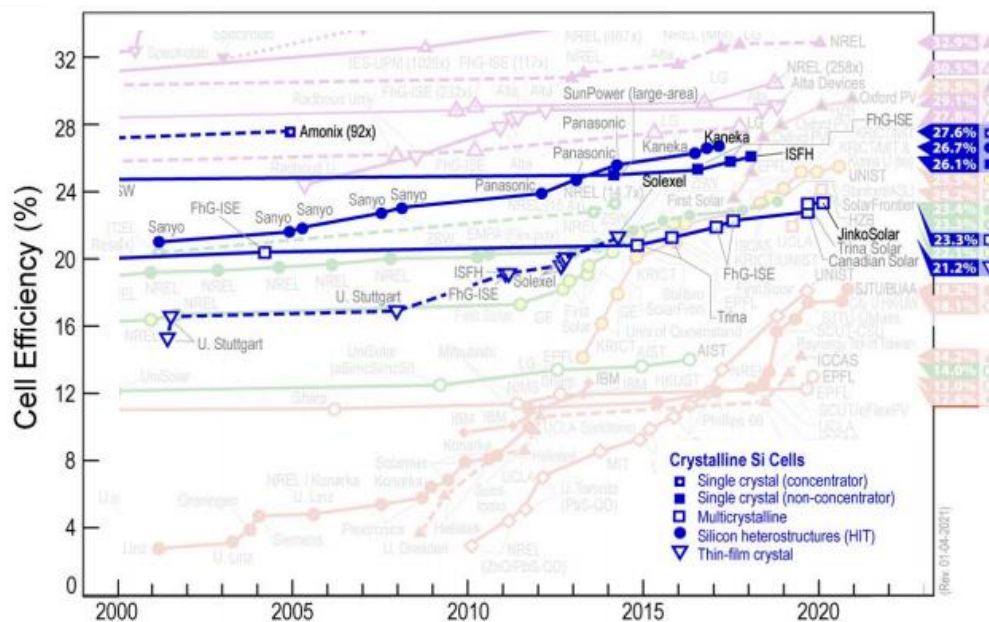


Figure II.3-3 Chart of the highest confirmed efficiencies of c-Si solar cells, by the *National Renewable Energy Laboratory-NREL* (04/01/2021).

II.3.2. Review Before 2018

In 2013, H. Snaith presented the concept of a monolithic Perovskite/SHJ tandem solar cell [81]. However, the first Perovskite/Silicon tandem was a 4T solar cell, presented in 2014 by P. Löper *et al.*, with 13.4 % efficiency [82]. They used a standard emitter SHJ solar cell (**Figure II.2-2 b**) as the bottom-cell and a mesoporous NIP Perovskite solar cell (**Figure II.3-2 c**) as the top-cell with a metal-free MoO_x/ITO transparent electrode. Then, J. P. Mailoa *et al.* published in February 2015 the first experimental 2T Perovskite/Silicon tandem, with 1 cm^2 area, **Figure II.3-4 a**) [83]. They

did not use a SHJ bottom cell but an N-type wafer, with a textured back-side and a flat front-side, with highly doped emitter and back surface field. They deposited a poly-Si (n⁺) layer on top of the emitter to form a tunnel recombination junction. This proof of concept reached 13.7 % efficiency, despite a large current mismatch between the two subcells.

In October 2015, S. Albrecht *et al.* presented the first Perovskite/SHJ tandem, using a thick (80 nm) patterned ITO layer as the recombination layer and a totally flat substrate, **Figure II.3-4 b)** [11]. They developed a planar semi-transparent Perovskite top-cell with SnO₂ as HTM and a MoO_x/ITO front transparent electrode. Using a Lithium Fluoride antireflective layer, they reached 18.1 % efficiency. Later, in December 2015, J. Werner *et al.* exceeded 19 % efficiency with a 1.22 cm² area flat tandem solar cell, **Figure II.3-4 c)**, [12]. Then, in July 2016, they presented the same architecture with a textured back-side and reached 20.5 % efficiency for 1.43 cm² active area [84]. In October 2016, *Oxford PV* showed a 4 cm² area tandem exceeding 21 % efficiency, **Figure II.3-4 d)** [85]. In this presentation, they also discussed the commercial challenges of this technology and presented the industrial potential of 2T Perovskite/SHJ tandem solar cells.

In November 2016, J. Werner *et al.* reached 16 % efficiency, with an aperture area of 1.43 cm², using an Aluminium Back-Surface-Field bottom-cell, a mesoporous Perovskite top-cell and a Zinc tin oxide (ZTO) recombination layer, **Figure II.3-4 e)** [86]. They investigated the impact of the ZTO layer thickness and found a strong influence of this layer on the device optics. Therefore, they highlighted the fact that optical modelling is necessary to optimise layers thicknesses and optical properties (as refractive indexes). The next year, K. A. Bush *et al.* presented a new best efficiency of 23.6 %, stable more than 30 min under illumination, on 1 cm² area, using a textured back-side and a mainstream ITO recombination layer, **Figure II.3-4 f)** [14]. In the same work, they studied the top-cell stability in ambient conditions and showed that with a great encapsulation, the Perovskite can be stable.

In October 2017, F. Sahli *et al.* demonstrated a nc-Si:H tunnel junction, to replace the commonly used TCO recombination layer, on top of a SHJ bottom-cell and reached 21.2 % efficiency (1.43 cm² AA) with their tandem solar cell, **Figure II.3-4 g)** [13]. In the same work, they presented the up-scalability of this type of tandem by obtaining an efficiency of 18 % with a 12.96 cm² aperture area, despite an important current mismatch. The same month, Y. Wu *et al.* obtained 22.5 % efficiency on 1 cm² area with a new silicon-homojunction bottom-cell, again associated to a mesoporous Perovskite top-cell, **Figure II.3-4 h)** [87]. With a textured back-side, a 40 nm ITO recombination layer and a great current-matching (17.8 mA/cm² in the top-cell and 17.6 mA/cm² in the bottom-cell) they demonstrated a new tandem architecture concept. By using a bottom-cell capable of withstanding a high-temperature annealing, the top-cell can be composed of the commonly used mesoporous TiO₂ (**Figure II.3-4 a), e), h)**). However, a SHJ bottom-cell offers the highest V_{oc} and efficiencies obtained. To conclude this short review, R. Fan *et al.* presented a Perovskite/SHJ tandem, **Figure II.3-4 i)** [15], exceeding 20 % efficiency on a very small area. They investigated several Perovskite bandgaps and obtained increasing V_{oc} and J_{sc} by increasing the bandgap from 1.55 eV to 1.69 eV, thanks to a better current-matching.

All the tandem solar cells presented in **Figure II.3-4** have small areas, compared to usual c-Si solar cells, and present a flat front-side substrate. This is explained by the Perovskite deposition method used (the spin-coating, described in part **III.1.6**) which needs a smooth surface to be homogeneous and the intrinsic lower stage of development of this technology. This method was used because it is widespread in research labs. The consequence is that best efficiencies were obtained with this process in single-junction

Perovskite solar cell. Nevertheless, as a proof of concept for industrialisation, other deposition methods ([88]) should be used to obtain a large-area Perovskite/Silicon tandem solar cell. However, these tandem solar cells demonstrate the great potential of this 2T technology with efficiencies rising from 13.7 % to 23.6 % in just two years. Moreover, this illustrates a large number of possible improvements, in both subcells but especially in the recombination junction.

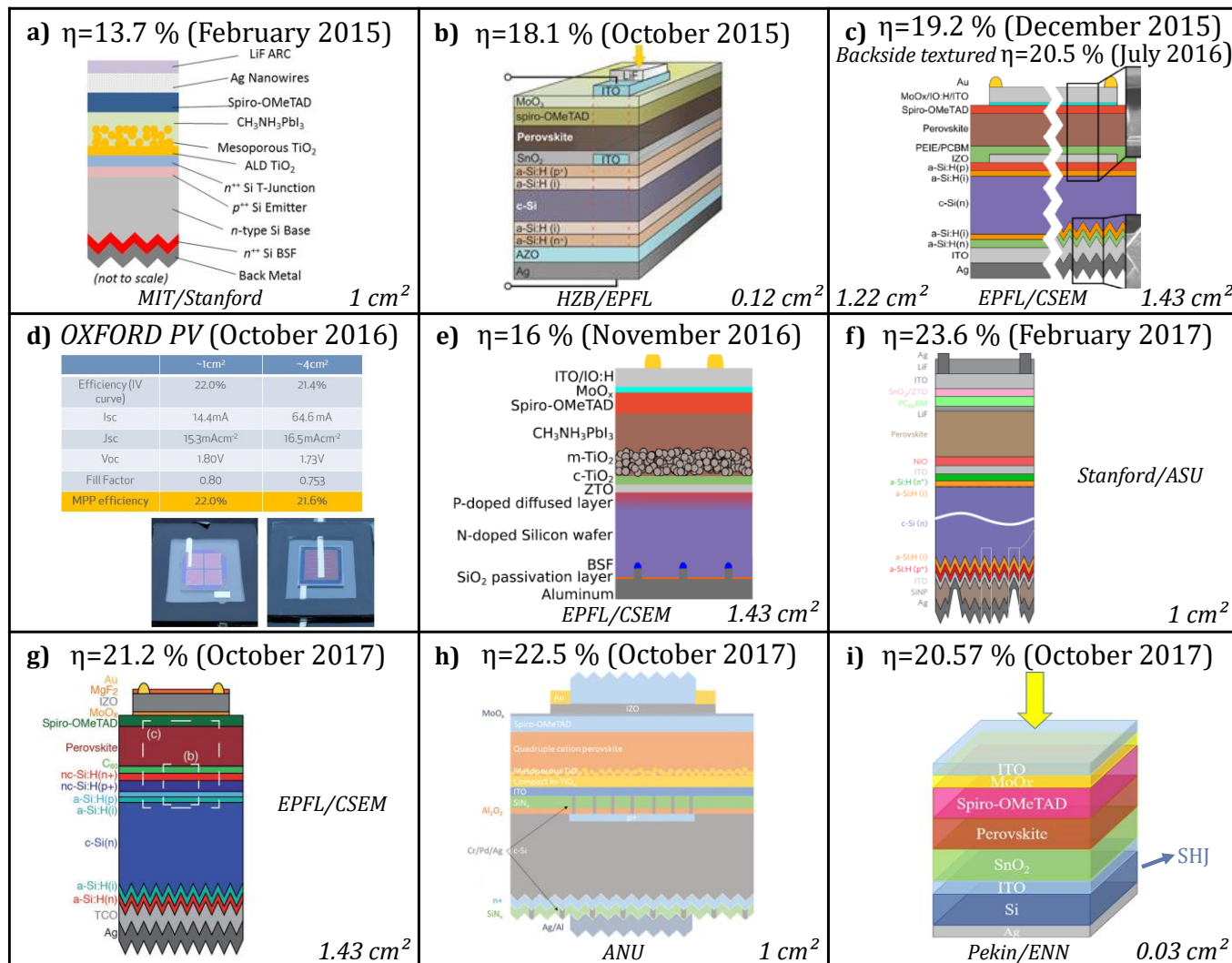


Figure II.3-4 2T tandem solar cells structures showed in the literature, with their respective efficiency, active area and date of publication.

Figure II.3-4 shows all the existing monolithic Perovskite on Silicon tandem solar cells at the start of this work. In parallel, several 4T tandem solar cells were presented in the literature using semi-transparent Perovskite top-cell and SHJ bottom-cell with efficiencies already exceeding 26 % in 2017 [89]. However, as presented in part II.1, 2T tandem solar cells seem much more suitable for a large commercialisation.

II.3.3. 2018-2020 Timeline

Table II.3-1 shows the advances of the Perovskite/SHJ tandem solar cells, from the beginning of this work to the end of 2020. Tandem architectures and the obtained PCE are presented, as well as the recombination junction used and the key points of those tandem devices. We can observe a large variety of architectures, materials and techniques, with efficiencies exceeding 20 % and even exceeding the record efficiency for c-Si single-junction solar cell, 26.7 % (**Figure II.3-3**).

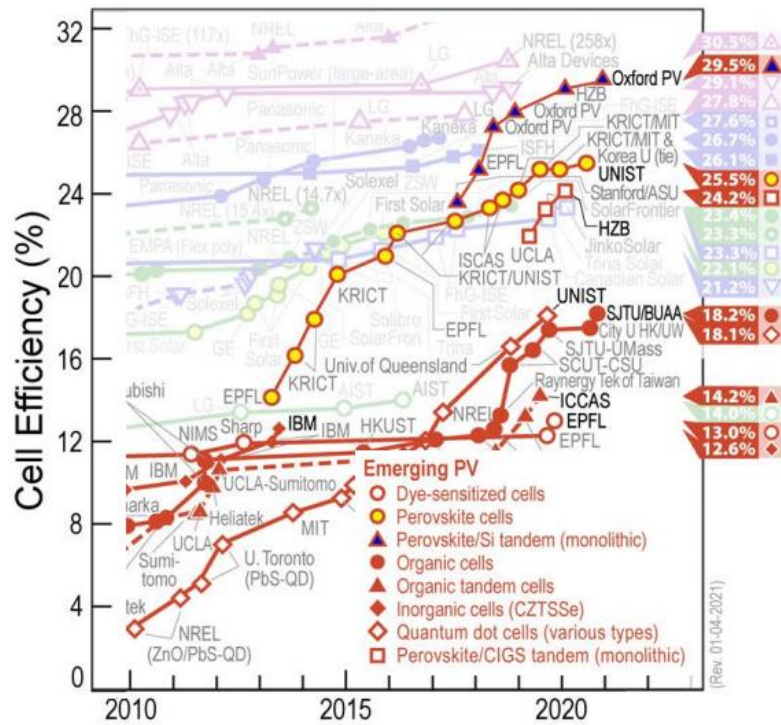


Figure II.3-5 Chart of the highest confirmed efficiencies of emerging solar cells, by the NREL (04/01/2021, <https://www.nrel.gov/pv/cell-efficiency.html>).

NREL's best efficiencies chart, **Figure II.3-5**, presents the evolution of 2T Perovskite/Silicon tandem solar cells highest efficiencies (blue triangles). Even if OXFORD PV has obtained half of these highest efficiencies; they are not presented in **Table II.3-1** because they do not communicate the corresponding architectures. They reached 29.52 % efficiency in December 2020, which is currently the best-certified efficiency for PK/SHJ tandem solar cells [90]. Moreover, it is worth to mention that, they already work on the deployment of the technology in mass production and already communicated efficiencies exceeding 25 %, for industrial large-area tandem solar cells on M2 wafers (244.43 cm²).

Comments on evolution over the 2018-2020 timeline (**Table II.3-1**):

- The progress in efficiency is due to a better light management and integration of new materials: light management foils, index-matching layers, PK with adapted bandgap, more transparent recombination junctions, thin and efficient charge transport layers (SAM)...
- There is no more mesoporous Perovskite structure and TiO₂ ETM.
- We observe a large progress in Perovskite processing, using photovoltaic industry relevant techniques (blade-coating...), even on textured wafers.

2019 January

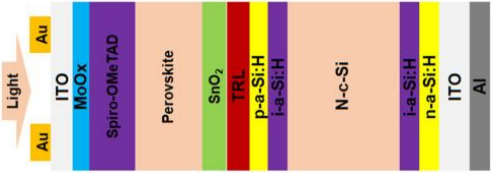
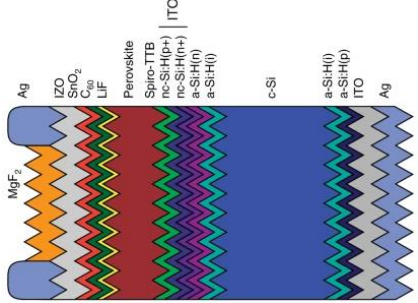
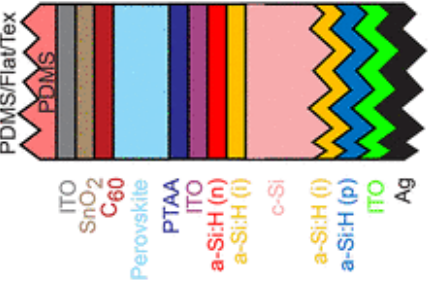
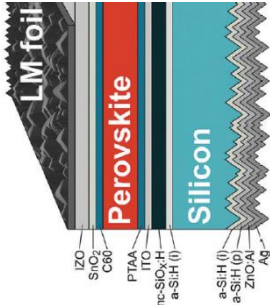
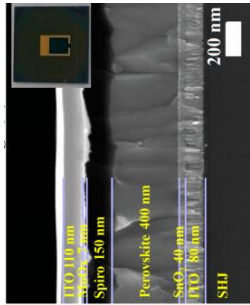
October

August

June

March

2018

<p>Structures</p>					
<p>PCE (%)</p>	<p>16.86 % (Forward)</p>	<p>25.24 % (Stabilised)</p>	<p>25.0 %</p>	<p>25.4 % (Forward)</p>	<p>20.43 % (Reverse)</p>
<p>Recombination Junction</p>	<p>ITO 80 nm</p>	<p>nc-Si:H (n⁺) / nc-Si:H :H (p⁺) ≈ 50 nm</p>	<p>ITO 20 nm</p>	<p>ITO 20 nm</p>	<p>ITO 80 nm</p>
<p>Area</p>	<p>1 cm² AA</p>	<p>1.42 cm² AA</p>	<p>1 cm² Active area</p>	<p>0.77 cm² AA</p>	<p>0.13 cm² Active area</p>
<p>Key Points</p>	<ul style="list-style-type: none"> ▪ $\eta = 18.81\%$ for 0.13 cm² AA ▪ Optimisation of the front MoO_x/ITO electrode 	<ul style="list-style-type: none"> ▪ Double-side textured device – Perovskite deposited with 2-step method (co-evaporation, then spin-coating) 	<ul style="list-style-type: none"> ▪ PDMS scattering layer (Reducing Reflection) & thinner top ITO ▪ PK A & X-site ratios tuned (increasing V_{oc}) 	<ul style="list-style-type: none"> ▪ Textured Light Management (LM) foil ▪ Optical optimisation of the bottom-cell: nc-SiO_x:H (n) as selective layer [92] 	<ul style="list-style-type: none"> ▪ V_{oc} up to 1.83 V (Highest published) - high τ_{eff} for the SHJ bottom-cell & Cs-doped Perovskite
<p>References</p>	<p>Nankai Univ. (China) [96]</p>	<p>EPFL/CSEM [95]</p>	<p>Stanford/ASU [94]</p>	<p>HZB [93]</p>	<p>Nankai Univ. (China) [91]</p>

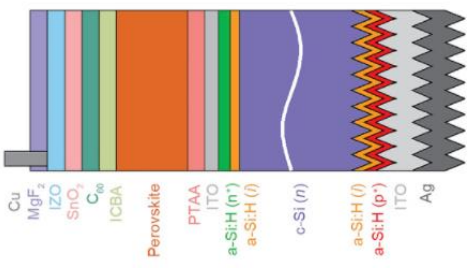
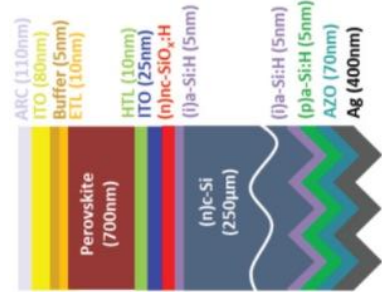
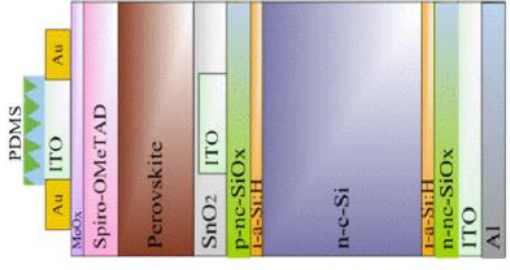
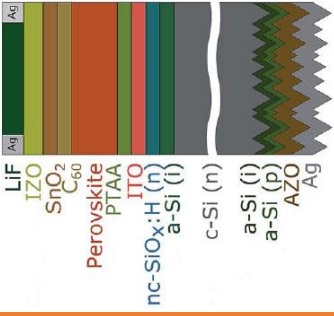
2019

January

February

April

May

	January	February	April	May
Structures				
PCE (%)	25.4 %	25.2 % (Stabilised)	21.93 %	26 % (Stabilised)
Recombination Junction	ITO 20 nm	ITO 25 nm	ITO 40 nm	ITO 20 nm
Area	0.42 cm ²	1.1 cm ² AA	<i>Not Specified</i>	0.77 cm ² Active area
Key Points	<ul style="list-style-type: none"> ■ Cu/IZO front electrode ■ Perovskite I/Br ratio optimisation to increase the J_{sc} 	<ul style="list-style-type: none"> ■ Minimised reflectance losses: 110 nm nc-SiO_x:H (n) with a refractive index of 2.6 at 800 nm / 25 nm ITO 	<ul style="list-style-type: none"> ■ Inverted pyramidally-textured PDMS foil as ARC ■ nc-SiO_x selective layers instead of amorphous silicon 	<ul style="list-style-type: none"> ■ Thicknesses adjustment: IZO, Perovskite, nc-SiO_x:H ■ Top contact (IZO/LiF) optimised
References	<i>U. Nebraska, U. N Carolina, ASU [101]</i>	<i>HZB/Oxford PV [100]</i>	<i>Nankai Univ. (China), TU Delft [99]</i>	<i>HZB [97]</i>

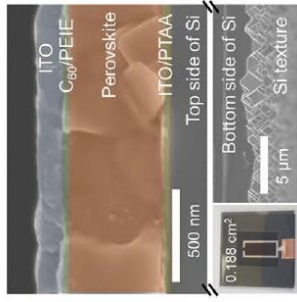
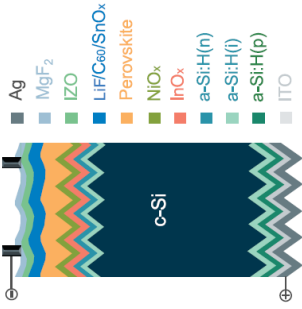
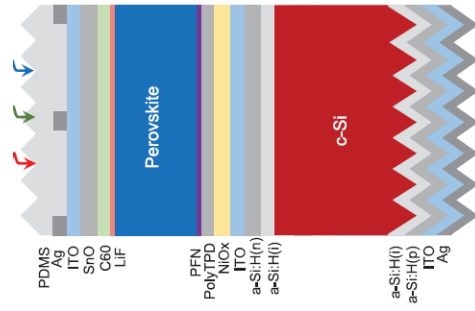
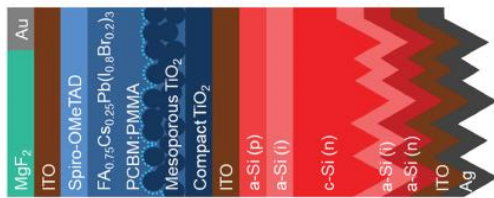
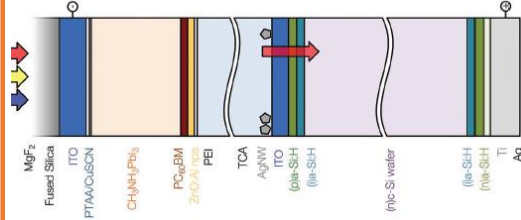
2019

August

November

2020 March

Structures



PCE (%)

21.0 %

21.6 % (Stabilised)

27.13 % (Stabilised)

25.7 % (Stabilised)

26.7 % (Stabilised)

Recombination Junction

Laminated (ITO/Ag nanowires/Transparent Conductive Adhesive)

ITO 80 nm

ITO 20 nm/
NiO_x 20 nm

InO_x 15 nm

ITO 20 nm

Area

0.104 cm² Active area

0.25 cm² Active area

1 cm² Active area

0.83 cm² AA

0.188 cm² AA

Key Points

- Independently processed subcells interconnected with a lamination step using a doped PEDOT:PSS as lowly resistive TCA

- Optimised wide bandgap (1.7 eV) mesoporous Perovskite top-cell
- V_{oc} up to 1.85 V (Highest published)

- Bi-layer recombination junction ITO/NiO_x
- Optimised triple-halide (Cl, Br, I) Perovskite, 1.67 eV

- Spin-coated PK on textured SHJ cell
- Stabled after 400 hours at 85 °C in the dark (≈ 40 % relative humidity)

- η = 26.2 % for 1 cm² Active area
- Optimised PK with long-term stability under light illumination

References

FAU, KAUST, Harvard Univ., HZB [106]

Fraunhofer [105]

Colorado, Stanford, NREL, ASU [104]

Toronto Univ., KAUST, NREL [103]

KAIST, Seoul Univ., NREL, Colorado [102]

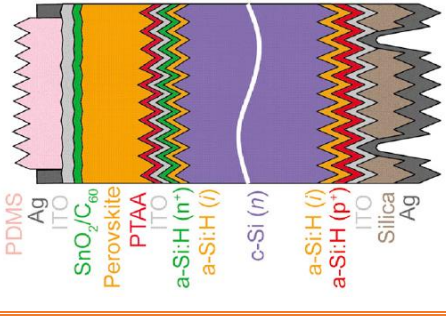
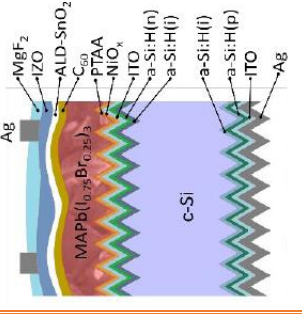
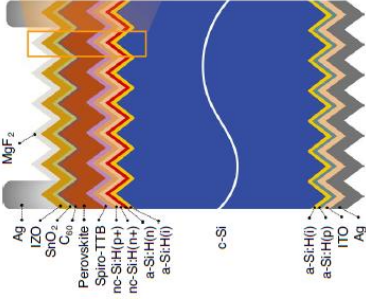
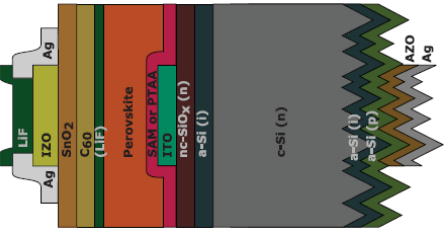
2020	April	May	August	September	December
Structures					
PCE (%)	26.1 % (Stabilised)	25.1 % (Stabilised)	24.05 % (Stabilised)	25 % (Stabilised)	29.15 % (Stabilised)
RJ	ITO 20 nm	ITO 80 nm	ITO 15 nm	nc-Si:H (n ⁺)/ nc-Si:H (p ⁺)	ITO 20 nm
Area	0.4225 cm ² Active area	0.25 cm ² Active area	1 cm ² Active area	0.8317 cm ²	1.064 cm ²
Key Points	<ul style="list-style-type: none"> Blade-coated PK on sub-micrometer textured bottom-cell with an industrialisable process 	<ul style="list-style-type: none"> Optimised wide bandgap (1.68 eV) planar PK top-cell FF up to 80 % Improvement after 5 months storage 	<ul style="list-style-type: none"> Single-step slot-die-coated PK on textured bottom-cell New PCE record for a slot-die-coated PK solar cell: η = 21.8 % 	<ul style="list-style-type: none"> Highest achieved J_{sc}: 19.8 mA/cm² 	<ul style="list-style-type: none"> Self-Assembled Monolayer (SAM) as HTM to improve passivation, charge extraction and the FF (up to 80 %)
References	ASU [111]	Fraunhofer/HZB [110]	KAUST, Toronto Univ. [109]	KAUST [108]	HZB [107]

Table II.3-1 Timeline (publication date) of the Perovskite/SHJ tandem solar cells, from January 2018 to December 2020.

II.4. Recombination Junctions

In this part, we provide an insight into the recombination junctions in tandem solar cells. First, by presenting the several possibilities and their mechanisms and secondly, by focusing on the case of Perovskite on SHJ tandem solar cells.

The recombination junction between the two subcells is a key part of a tandem solar cell because it is essential for its operation. As introduced in part II.1, this junction ensures the correct series connection of the subcells. It must allow all generated electrons in the top-cell and all generated holes in the bottom-cell to recombine, in the NIP case presented in **Figure II.1-3 b)**, or the reverse for the PIN architecture. Therefore, the following requirements are necessary for a RJ:

- Optically transparent, in the IR region, to minimise parasitic absorption and maximise the absorption in the bottom-cell,
- Adapted optical indexes to reduce the reflection (optical matching between the layers),
- Active dopant concentrations and layer thicknesses sufficient to produce high built-in voltages across both subcells [112],
- Avoid a counter-diode creation to preserve an efficient tunnelling transport and prevent V_{oc} losses,
- High concentration of localised states to serve as hopping centres and increase the recombination probability.

The RJ of the first multi-junction solar cells were composed of a highly doped tunnel junction, presented in the following part II.4.1. Currently, TCO are also used to play this role, particularly in organic or Perovskite multi-junction solar cells, presented part II.4.2.

II.4.1. Highly Doped Tunnel Junction

Highly doped tunnel junctions are similar to tunnel diodes, they are composed of a PN junction with a narrow space charge region. In 1958, L. Esaki discovered that diode with highly doped narrow PN junctions could present a negative resistance region in their I-V curve [113]. This type of diode was then named tunnel diode or Esaki diode.

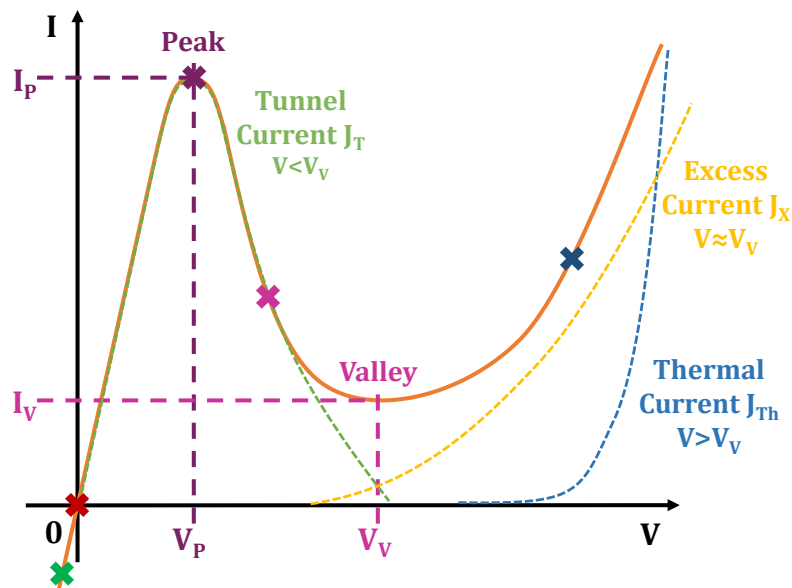


Figure II.4-1 I-V Curve (in orange) of a tunnel diode in the dark and the different current contributions (dashed lines: tunnel current J_T in green, excess current J_X in yellow and thermal current J_{Th} in blue). Peak current (I_P) and Valley current (I_V) are also represented.

A negative resistance means that the current decreases when the voltage increases. This phenomenon is observable in **Figure II.4-1**, from the peak to the valley the resistance of the junction is negative. **Figure II.4-2** shows a drawing of the energy diagrams at each step of the tunnel diode I-V curve presented in **Figure II.4-1**. At reverse bias, electrons tunnel through the narrow space charge region from the valence band of the P-type layer to the conduction band of the N-type layer. At zero bias, the CB of the N-type layer and the VB of the P-type are nearly at the same energy level, the junction is at thermal equilibrium. Then, by applying a small voltage, electrons in the CB of the N-type layer tunnel to the empty states of the VB in the P-type layer until $V=V_P$, when the tunnel current is maximum. Next, when the applied voltage is further increased, the bands start to be misaligned and the tunnel current decreases, until the valley, where it drops to zero. At higher voltages the junction operates as a normal diode, thermionic emission becomes the main transport mechanism.

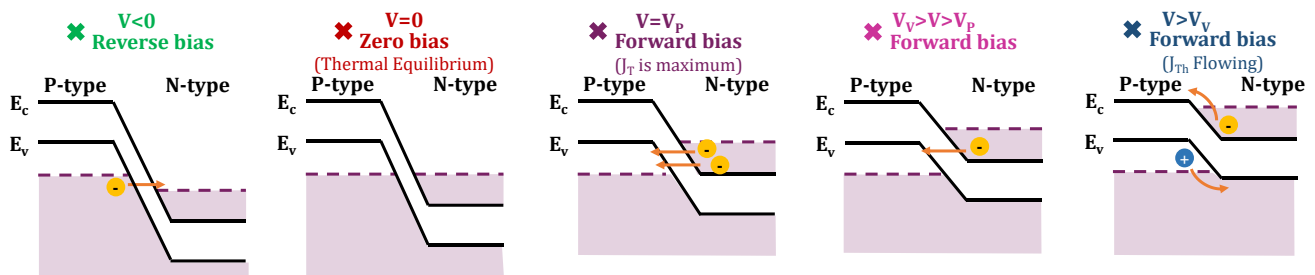


Figure II.4-2 Drawing of the band diagrams at each cross on the tunnel diode I-V curve in **Figure II.4-1**. The purple dashed lines represent the quasi-Fermi levels.

In the case of a RJ in a tandem solar cell, charges recombine continuously in the junction. In fact, free charge carriers are coming from the subcells and the band alignment stay in the tunnel current regime (voltage bias at the junction is near zero).

Highly doped tunnel junctions are the main RJ used in multi-junction solar cells composed of III-V materials (possibly with germanium or silicon) and all-silicon multi-junction (as micromorph solar cells).

II.4.2. Transparent Conductive Oxide as Recombination Layer

Tunnel junction can be quite easily obtained by modifying the doping of inorganic crystalline materials. By contrast, it seems more complicated to make in organic multi-junction solar cells. Therefore, the first organic tandem solar cells used very small clusters (layer with a thickness less than 1 nm) of silver or gold as charge recombination sites between the subcells [78], [114]. Then, to improve the stability of these devices and their absorption, TCO layers were used instead of a metal [79]. Currently, organic or Perovskite based multi-junction solar cells use TCO, mixed TCO/Metal layers or direct contact between ETL and HTL as RJ [74], [78], [115], [116].

The N-type TCO layers used have many localised states that permit recombination by trap-assisted tunnelling and band-to-band tunnelling with the HTL. The charge transport mechanisms are the same as at the recombination interface a-Si:H (p)/ITO in SHJ solar cells, described in the literature [117]–[120].

II.4.3. Recombination Junctions in Perovskite/SHJ Tandem

We have explained the two most used possibilities of RJ in the previous parts. In this part **II.4.3**, we present the recombination junctions used in Perovskite/SHJ tandem solar cells, already mentioned in **Table II.3-1**. The first used junction in this type

of device was composed of a thin ITO layer (**Figure II.3-4 b**)), it is currently the most widely used junction. In fact, as SHJ solar cells usually feature ITO layers, on the front and back-sides, and Perovskite solar cells are often deposited on an ITO layer, using it as the junction between the subcells seems like an obvious choice.

Nevertheless, thin ITO layers have bad refractive indexes matching with a-Si:H layers to be optically optimised for these tandem cells. The refractive indexes variation are too high and this can lead to significant reflection losses. To counter this, *Helmholtz-Zentrum Berlin (HZB)* adapted the bottom-cell by using a nc-SiO_x:H layer instead of an a-Si:H layer as the selective layer in contact with the ITO. The refractive index, n , of this nc-SiO_x:H layer can be tuned with a variation of the PECVD parameters. They performed some optical simulations and experiments to find the best refractive index and thickness combination, depending on the other layers of the tandem cell and the wafer texturing ([92], [100], [121]). Furthermore, they subsequently also adapted the top-cell to optimise the junction between the ITO layer and the HTL. They developed self-assembled monolayer (SAM) as the hole extraction/transport layer, which allowed them to improve the tandem cells FF and reach 29.15 % efficiency [107].

Otherwise, F. Sahli *et al.* presented a nanocrystalline silicon tunnel junction to avoid the parasitic absorption and the possible shunt paths due to the high lateral conductivity of ITO layers [13]. They used this type of junction in NIP and PIN tandem cells, and also in fully textured tandem solar cells and demonstrated that this type of highly doped tunnel junction works well [95]. In fact, nanocrystalline silicon layers are more transparent in the infrared range than thin ITO layers and present a better refractive index matching with the adjacent layers. Moreover, nc-Si:H layers are deposited in a PECVD tool, as the a-Si:H layers.

Contrary to some other Perovskite/Silicon tandem solar cells ([122], [123]), there has not yet been a direct junction between the two subcells presented for Perovskite/SHJ tandem cells, but it is a possibility to explore (see simplified devices in the part VI.2).

II.5. Chapter Outlook

This chapter II is a short presentation of the State-of-the-Art of the Perovskite/SHJ tandem solar cell technology. As these tandems combine several technologies and mechanisms, this chapter is not exhaustive but contains all the necessary information to follow this work. Finally, we present a brief overview of the starting point of this work at the CEA-INES in 2018.

At the start of this work, SHJ solar cells had already exceeded 25 % efficiency (part II.2) and more and more investment was being made in this technology (*Panasonic, HEVEL, ENEL, Hanergy...* [124]). The CEA-INES was producing SHJ solar cells, on M2 size wafers, with an average efficiency of 22 %, in its pilot-line (part III.1). In parallel, the CEA-INES team was working on Perovskite solar cells and already obtained 18 % on 3 mm² area and 12.4 % efficiency with a mini-module of 8 cm² area. A proof of concept of a tandem solar cell combining these two technologies has been done in 2017, on a fully flat (CMP) substrate, using a thin ITO layer as the RJ. This proof of concept has presented a good addition of the tensions, with a V_{oc} exceeding 1.5 V. One of the key topics identified to improve the device was the recombination junction, which was the least known feature of this tandem solar cell technology. This work started here, with the objective to understand and improve the RJ.

III. MATERIALS AND METHODS

In chapter II we have reviewed the State-of-the-Art closely related with this work, and explained the initial conditions of this Thesis. In this chapter, we focus on the fabrication process of the solar cells and test-structures used. All process steps are described and the different deposition tools are presented. Structural, chemical and electrical characterisation methods are explained, as well as the employed optical simulation software. Some specific methods developed or improved during this work are more detailed in the next chapters.

III.1. Fabrication Processes

This first part is dedicated to the different fabrication steps of the devices and test-structures, from the silicon wafer preparation to the complete solar cells metallisation. An example of the process used to make a tandem solar cell, with the steps previously detailed is also described.

III.1.1. Substrate cleaning

For different research purposes, we have chosen two types of c-Si wafers:

- Commercial N-type FZ (100) DSP (CMP) wafers, most often used for microelectronics applications, with a resistivity between 1 and 5 $\Omega\cdot\text{cm}$ and a thickness between 260 and 300 μm , 4-inch size. Most of the time we used those mirror-polished wafers for layer characterisation, but also for tandem solar cells or “tandem-like” devices (part VI.3). We cleaned those wafers with a wet-chemical process using hydrogen fluoride (HF) and hydrochloric acid (HCl) to remove native oxide and potential surface contaminants before other fabrication steps.
- Commercial N-type CZ (100) “as-cut” wafers with a resistivity between 0.5 and 1.5 $\Omega\cdot\text{cm}$ and a thickness around 180 μm , M2 size. Those wafers are mostly used to make textured substrates for SHJ solar cells or test-structures. We first placed them into a KOH-based (potassium hydroxide) solution for SDR and pyramidal texturing in an industrial “wet bench” *Akrion* tool. Thanks to an anisotropic chemical reaction due to the KOH, we then obtain double-side textured wafers with random pyramids (sides are oriented according to the (111) plane and the bases of the pyramids are in the (100) plane), **Figure III.1-1** shows SEM images of the surfaces along the process. Next, textured wafers are placed into an O_3 -HF solution and then plunged into a HF-last step [125] to deoxidise the surface.

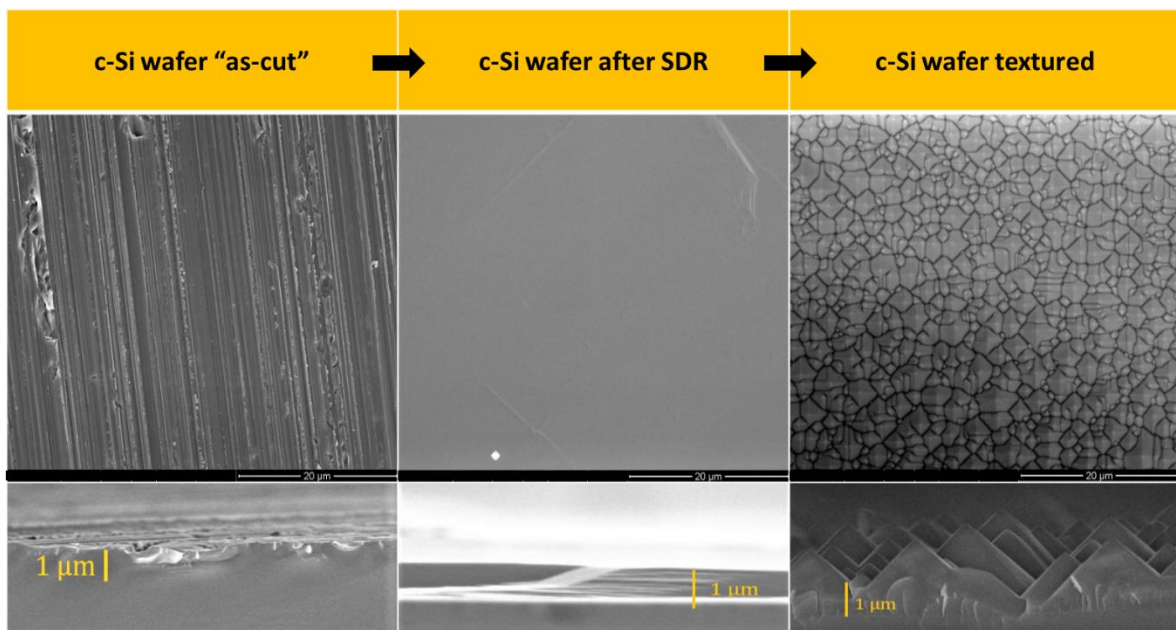


Figure III.1-1 SEM front and cross-section images (III.2.8.a) of an n-type CZ (100) commercial wafer “as-cut”, after the SDR step and after the pyramidal texturing process.

III.1.2. Plasma-enhanced CVD

Plasma-enhanced CVD is the most used technique in SHJ solar cells to perform the deposition of the amorphous silicon layers. At the industrial scale, this method allows to obtain uniform and reproducible depositions at high throughputs with a high quality passivation. We used two different tools, an industrial tool (III.1.2.a) for the deposition of the amorphous silicon layers and a development tool (III.1.2.b), mainly for the development and deposition of microcrystalline silicon layers.

III.1.2.a. Industrial Tool

After the substrate preparation, wafers are loaded into a PECVD industrial tool from *Meyer Burger*. This tool is composed of RF plasma parallel plate reactors with a protecting box around the process chamber and a 13.56 MHz RF source, to minimise plasma damage and improve uniformity. All amorphous silicon layers (intrinsic, N-type and P-type) used in this work were deposited in this tool, using recipes optimised for an industrial line production of SHJ solar cells, in the CEA-INES pilot-line (capacity of 2400 wafers per hour). M2 wafers are loaded with automation on the tray, under N₂ atmosphere in a “loading chamber”, whereas we loaded manually the 4-inch wafers under air atmosphere. When all substrates are placed on the tray, the tray is loaded into a process chamber; **Figure III.1-2** shows a simple PECVD process chamber (RF planar capacitor) for large area deposition. The process chamber is coated beforehand according to the type of layer to be made.

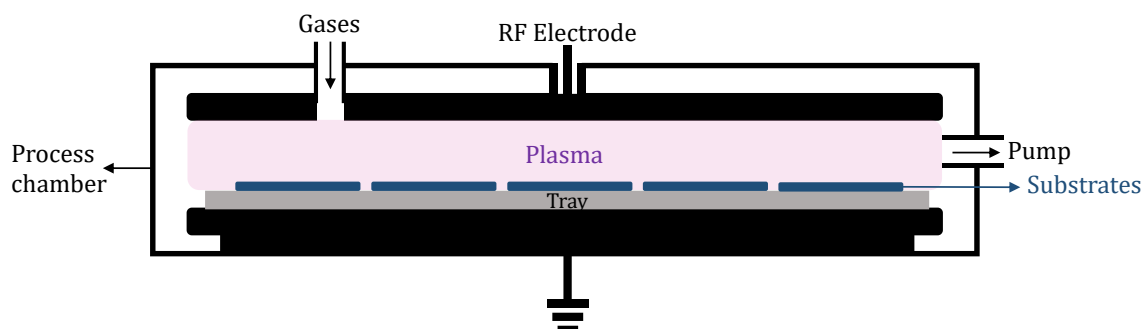


Figure III.1-2 Drawing of a PECVD process chamber.

The amorphous silicon layers deposition process is performed at 200 °C (trays are maintained at 200 °C even outside the process chamber) using SiH₄ and H₂ gases. To obtain an a-Si:H (n) layer a PH₃ gas is added and respectively a B₂H₆ gas is added for a-Si:H (p). In the plasma, gases are decomposed and ionised, some ionised species bind to the atoms on the surface of the substrates by a chemical reaction and start forming an amorphous layer. During the growth of the layer, the substrate temperature and the deposition rate are keys to control defect density and the hydrogen content [126], they are carefully monitored.

III.1.2.b. Development Tool

In this work, we use several forms of hydrogenated thin-film silicon materials deposited by PECVD, to clarify the notation we employ the same as Ruud E.I. Schropp [127], presented in **Table III.1-1**. This notation may be different from that used in the recent literature but it is employed throughout this work.

Materials	Phases	Feature size
a-Si:H	Single phase: amorphous	none
In the literature, the notation " nc-Si:H " is sometimes employed	2 phases: amorphous and crystalline	< 10 nm crystals
μc-Si:H	2 phases: amorphous and crystalline	< 20 nm crystals
poly-Si:H	Single phase: crystalline with grain boundaries	> 20 nm crystals

Table III.1-1 Definitions of the notations for hydrogenated thin-film silicon materials used in this work (adapted from [127]).

We used a R&D tool from *Jusung* to develop different microcrystalline silicon layers (part IV.2). **Figure III.1-3** shows a simplified representation of the tool, which is composed of separated P-type and N-type process chambers, equipped with 13.56 MHz RF sources and maintained at 220 °C. Substrates are placed on the tray manually, under air atmosphere and then the tray is loaded into the loading chamber. The loading chamber is next placed under vacuum. When a sufficient vacuum is reached, the tray and the substrates are heated at 230 °C during 120 seconds and then moved into the adequate process chamber. Microcrystalline silicon layers are deposited using the same gases as amorphous silicon layers (PH₃ for N-type and B₂H₆ for P-type) but different parameters are used, especially the gas flow ratio H_2/SiH_4 and the RF power. The optimisation of those parameters is presented in details in part IV.2.1.

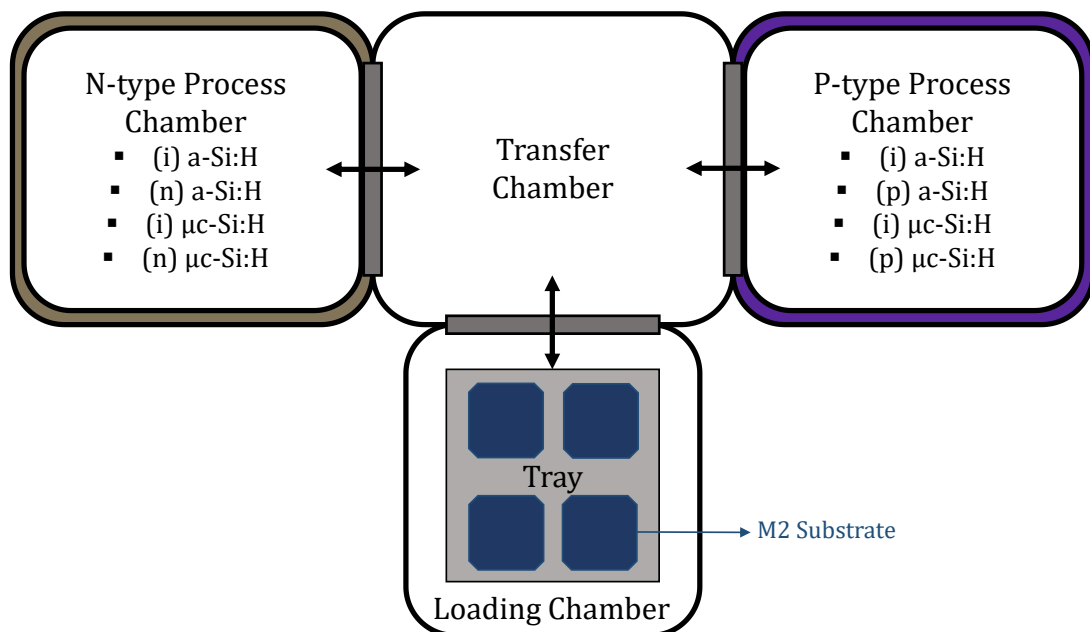


Figure III.1-3 Simplified picture of the PECVD *Jusung* tool.

III.1.3. Transparent Conductive Oxide Deposition

TCO layers are essential in SHJ and tandem structures to improve lateral carrier collection and optical properties for enhanced efficiency. Usually, they are deposited by sputtering-PVD, and the most common among them is Indium Tin Oxide (ITO). In sputtering process, Ar⁺ ions are bombarded on a target composed of the needed elements (In₂O₃ and SnO₂ to obtain an ITO layer for example). Contrary to the PECVD, during the physical vapour deposition, the layer is formed on the substrate thanks to a mechanical grip. In most cases, a compromise is done between the optical and electrical

properties, by varying the oxygen flow. In fact, the conductivity tends to be better with less oxygen but to be the most transparent a lot of oxygen is needed [128]. Moreover, the temperature of the substrate, the tin proportion in the target and the power of the process are also important factors to obtain good material properties, while degrading as little as possible the previous layers on the substrate.

Tool used	Substrates type	ITO's thickness (on polished surface)
Meyer Burger (industrial)	<ul style="list-style-type: none"> ▪ Tandem and “tandem-like” (see part VI.3) precursors ▪ SHJ solar cells 	<ul style="list-style-type: none"> • 70 nm • 100 nm • < 30 nm
Jusung (R&D)	<ul style="list-style-type: none"> ▪ Test-structures for TJ, chapter V (ITO deposition around 200 °C) ▪ Front-side of tandem and “tandem-like” (VI.3) samples (ITO deposition at ambient temperature) 	<ul style="list-style-type: none"> • 100 nm • 200 nm

Table III.1-2 Table of the tools used for the ITO layers deposition with the substrates type and ITO's thicknesses.

We used two different PVD tools according to the substrates and the previous layers, details are presented in **Table III.1-2**. Standard recipes for SHJ and tandem cells were systematically used without specific development. More details about the deposited ITO layers are presented in the following chapters (V and VI).

III.1.4. Metallisation

For charge carrier collection and electrical measurements of test-structures and solar cells, a metallisation step is needed after the TCO deposition. We used three different metallisation techniques for this last step. **Table III.1-3** presents the technique used according to each type of device.

Substrates type	Technique	Metal and Tool	Pattern
SHJ solar cells	Screen-Printing (III.1.4.c)	Ag Industrial tool (on the CEA-INES pilot-line)	5-busbars, bifacial
Tandem and “tandem-like” (VI.3)	Thermal Evaporation (III.1.4.b)	Ag – <i>Vinci</i> tool Au – <i>Riber</i> tool	Back-side: full surface Front-side: one busbar designed for a 3 cm x 3 cm aperture area
Test-structures for TJ (V)	Electron-beam Evaporation (III.1.4.a) Thermal Evaporation (III.1.4.b)	Ag – <i>Oerlikon</i> tool Ag – <i>Vinci</i> tool	Back-side: full surface (with edges exclusion) Front-side: circular electrodes

Table III.1-3 Details of the metallisation used for the different substrates of this work.

III.1.4.a. Electron-beam Evaporation

Electron-beam evaporation was used to deposit silver electrodes on test-structures in an *Oerlikon* tool. We chose this technique because it is easy to set-up for small substrates (5 cm x 5 cm) and permits a more precise masking of the samples than with sputtering. **Figure III.1-4** represents an e-beam evaporation chamber. The chamber is placed under high vacuum after the installation of the substrates on the holder and the source material in the crucible. Then, an electron-beam is projected on the source material to transform it into a gaseous phase. In contact with an object (everything solid in the chamber) atoms in the gas precipitate into solid form. Thanks to a quartz crystal the thickness is monitored during the process. Most of the time the substrate holder is placed into rotation during the deposition and a shutter controls the start and the end of the process.

We performed full surface evaporation on the back-side of 5 cm x 5 cm samples. Those samples were placed into a holder masking the edges to avoid lateral shunts. Moreover, for the front-side of those samples we used a mask to obtain circular patterns (part V.2.1). We chose to deposit 400 nm of silver in order to perform probes measurements without piercing the metallisation.

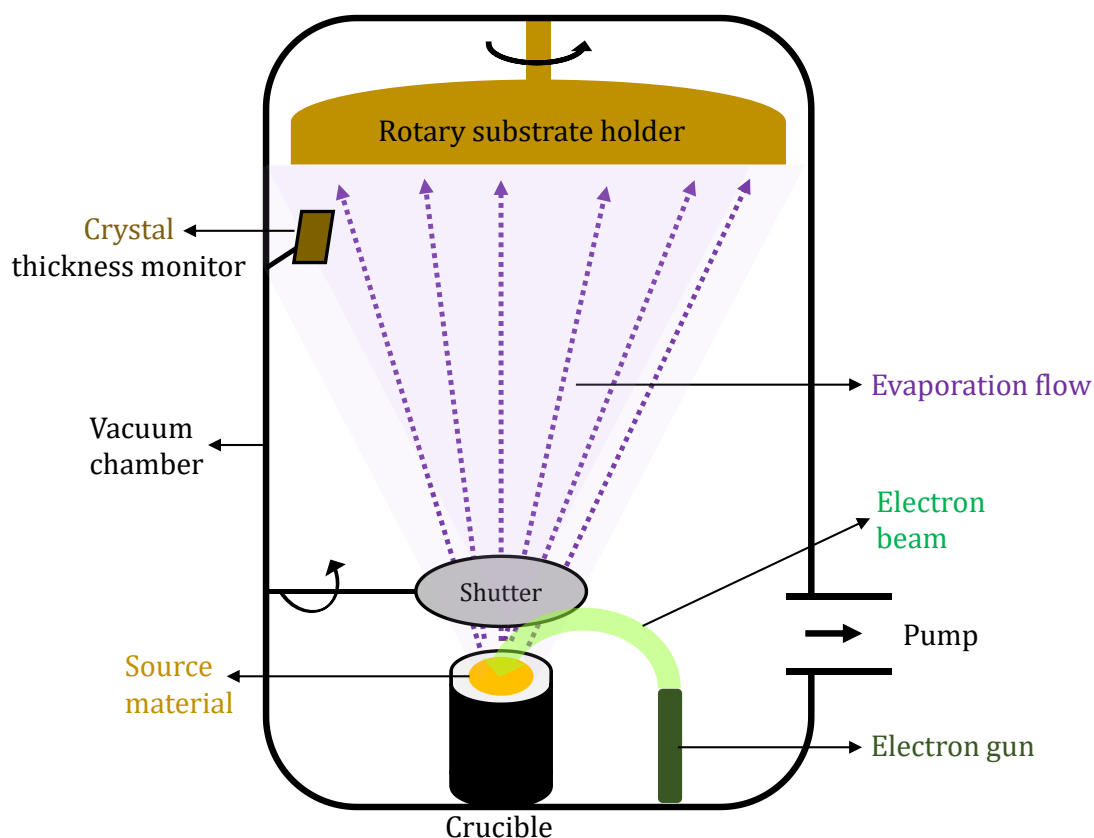


Figure III.1-4 Sketch of an electron-beam evaporation chamber.

III.1.4.b. Thermal Evaporation

As e-beam evaporation gives high-energy evaporated material, some samples can be damaged, for example, in SHJ solar cells the minority carrier lifetime is usually reduced. To avoid this possible damage, we used thermal evaporation for tandem and “tandem-like” solar cells (chapter VI) and also for some test-structures (chapter V).

Thermal evaporation is a PVD method very close to e-beam evaporation: instead of an electron gun there is a heater (a hot resistance or a thermal filament for example) near the crucible. The heat transforms the source material into a gaseous phase and the rest

of the process is mostly the same as with an e-beam but the evaporated material has less energy. We used this method on all FZ DSP wafers, for 5 cm x 5 cm or smaller samples. Contrary to e-beam evaporation, we deposited only 200 nm of metal to reduce the deposition time and prevent a possible overheating.

III.1.4.c. Screen-Printing

Screen-printing is the main used metallisation method in the solar cells industry, mainly for its high throughput. SHJ solar cells done during this work were screen-printed using the industrial tool of the CEA-INES pilot-line with a 5-busbars design. The silver paste used is optimised for this type of solar cells and needs a low temperature annealing [43], [125]. Therefore, the last fabrication step for SHJ solar cells is then a curing around 200 °C for up to 30 minutes [124].

III.1.5. Laser Cutting

In this work, some of the test-structures, tandem solar cells and “tandem-like” samples are done on 5 cm x 5 cm substrates. M2 textured wafers are manually cut after the PECVD process with the help of a diamond tip. Otherwise, for more precision and speed, 4-inch wafers are cut using a laser cutting machine, according to a defined design. We used a 1064 nm IR laser made by *Rofin*. Process recipes (intensity, frequency and speed) are adapted to reduce the laser damage in the wafers edge to suppress non-desired recombination or parasitic losses.

III.1.6. Perovskite Solar Cell

First step into the Perovskite solar cell deposition is the preparation of the solutions, presented in **Table III.1-4**. Then, less than 30 minutes before the deposition, the substrate is placed into a chamber to receive a UV/O₃ treatment during 30 minutes, to clean the surface and make it more hydrophilic. Next, the substrate is placed into a glovebox, under nitrogen, containing a spin-coater.

Solutions	Active Materials / Solvents	Shaking / Rest
MAI	<ul style="list-style-type: none"> ▪ MAI (powder) ▪ DMF (solvent) 	Agitated for 3h minimum
MAPbI _{3-x} Cl _x (Perovskite one-cation)	<ul style="list-style-type: none"> ▪ MAI (solution) ▪ PbCl₂ (powder) ▪ DMF (solvent) 	Agitated for 4h
FAPbI ₃	<ul style="list-style-type: none"> ▪ FAI (powder) ▪ PbI₂ (powder) ▪ DMF (solvent) ▪ DMSO (solvent) 	Agitated for 12h minimum at 40 °C
PbBr ₂	<ul style="list-style-type: none"> ▪ PbBr₂ (powder) ▪ DMF (solvent) ▪ DMSO (solvent) 	Agitated for 12h minimum at 40 °C
CsI	<ul style="list-style-type: none"> ▪ CsI (powder) 	Agitated until dissolution of the CsI

	<ul style="list-style-type: none"> ▪ DMSO (solvent) 	
Cs_xFA_{1-x}Pb(I_{1-y}Br_y)₃ (Perovskite double-cation)	<ul style="list-style-type: none"> ▪ FAPbI₃ (solution) ▪ PbBr₂ (solution) ▪ CsI (solution) 	Prepared 30 minutes before the layer deposition
SnO₂	<ul style="list-style-type: none"> ▪ Commercial solution diluted in EDI 	
Li-TFSI	<ul style="list-style-type: none"> ▪ Li-TFSI (powder) ▪ CH₃CN (solvent) 	Agitated until dissolution of the Li-TFSI
PTAA	<ul style="list-style-type: none"> ▪ PTAA (powder) ▪ C₇H₈ (solvent) ▪ Li-TFSI (solution) ▪ TBP (solvent) 	→ Agitated until dissolution of the PTAA → Agitated for 12h minimum at 65 °C → Rest 2h minimum before the layer deposition

Table III.1-4 Details of the solution prepared for Perovskite solar cells.

We used Perovskite solar cells in the NIP configuration, thus the ETL is deposited first. The SnO₂ (the ETM that we used in Perovskite solar cells) solution is spin-coated on the substrate which is then annealed during 1 min at 80 °C. Then, Perovskite thin-film can be made by a lot of deposition techniques, separated in two categories: solution-based deposition (spin-coating, slot-die coating [129], spray coating [130], inkjet printing [131]...) or vapour-based deposition (thermal evaporation [132], CVD [133], [134], flash evaporation [135], vapour-assisted solution processing [136]...) [88], [137]. In this work, one of the most popular deposition method is performed, the spin-coating technique, with an anti-solvent step, illustrated in **Figure III.1-5**. After the annealing and the Perovskite layer crystallisation, the HTM (the PTAA), is spin-coated on the Perovskite layer. Each used spin-coating recipes had already been optimised and no specific development was done on the Perovskite solar cells deposition during this work.

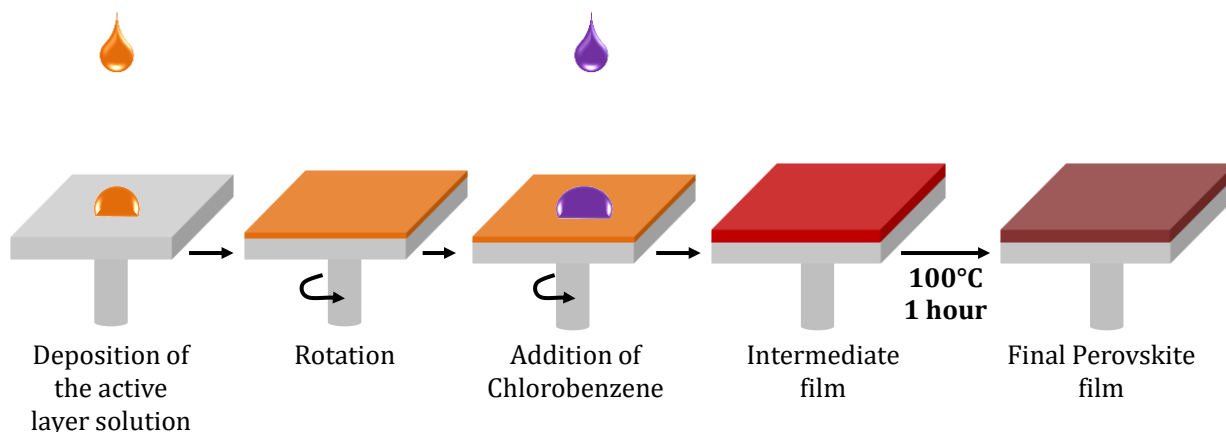


Figure III.1-5 Drawing of the synthesis of a Perovskite layer by the anti-solvent, spin-coating method employed.

III.1.7. Example of a Tandem Solar cell Fabrication Process

Figure III.1-6 shows an example of the full fabrication process for a NIP tandem with the steps previously detailed.

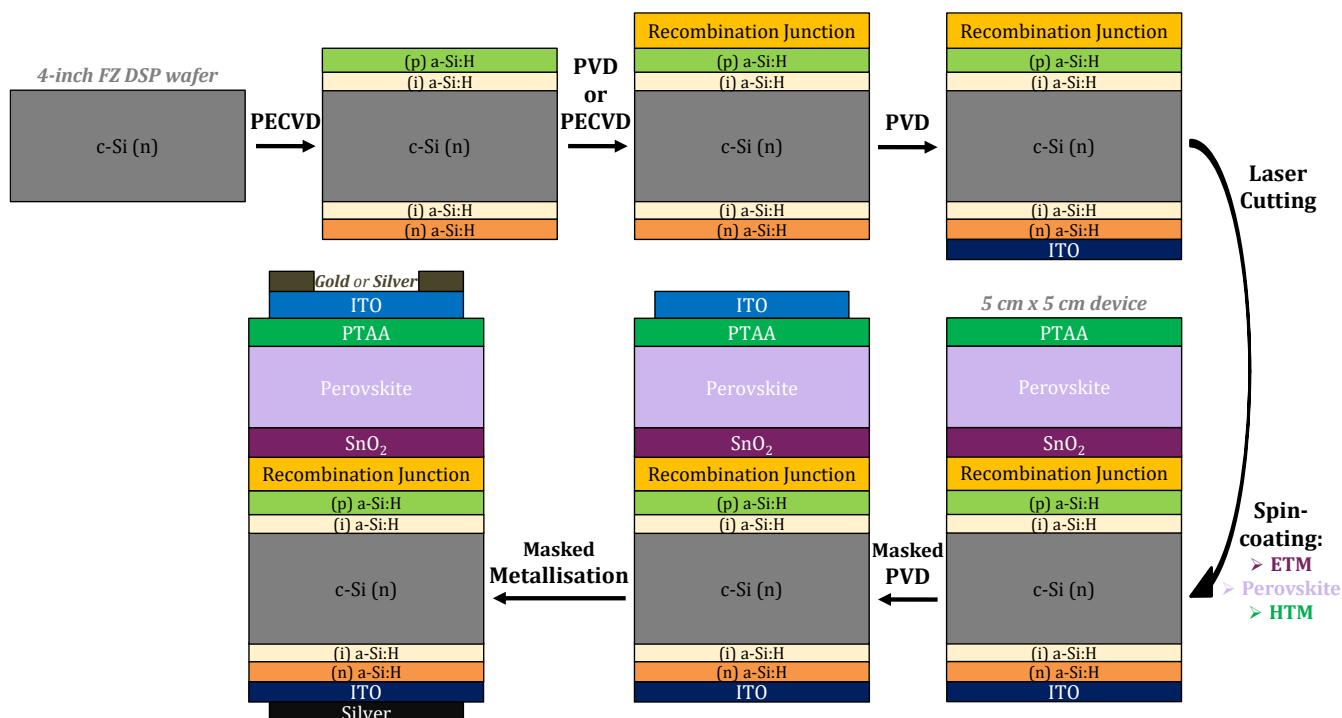


Figure III.1-6 Summary of the fabrication process of a tandem solar cell.

III.2. Layer Characterisation Methods

In this second part, we present the structural, chemical and electrical characterisation methods used on a single layer or on a stack of layers, deposited as described in part III.1.

III.2.1. Ellipsometry

Spectroscopic Ellipsometry (SE) is a method often used in the solar cells industry to control the thicknesses, uniformity and reproducibility. SE measures the modification in state of polarisation of a polarised light after reflection on the studied sample. This modification is evaluated by the two ellipsometric angles, Ψ ($\tan\Psi$ is the amplitude ratio upon reflection) and Δ (is the change in phase shift), which are the measured parameters [138]. Then, with an appropriate modelling, samples parameters can be extracted. This characterisation method is non-destructive and adapted to determine thicknesses and optical properties of thin-films, but also other properties such as crystallinity or the layer uniformity. In next chapters, the presented ellipsometry diagrams show the measured complex dielectric function (equation (III. 2-1)) of the studied sample, as function of the wavelength (λ).

$$\varepsilon(\lambda) = \sin^2 \phi_0 + \sin^2 \phi_0 \cdot \tan^2 \phi_0 \cdot \left(\frac{1 - \tan \Psi(\lambda) \cdot e^{i\Delta(\lambda)}}{1 + \tan \Psi(\lambda) \cdot e^{i\Delta(\lambda)}} \right)^2 = \varepsilon_r(\lambda) + i\varepsilon_i(\lambda) \quad (\text{III. 2-1})$$

where ϕ_0 is the angle of incidence of the polarised light.

III.2.1.a. Ellipsometry Measurements

We performed ellipsometry measurements on many samples, using quartz-glass substrates or commercial CMP (100) c-Si wafers to avoid any roughness to obtain a proper signal.

For the measurements, we used a Polarisation Modulation ellipsometer (*UVISEL* from *HORIBA Jobin Yvon*), as described in **Figure III.2-1** and the data were analysed with the software *DeltaPsi2*. With this equipment, the incidence angle can be adapted, according to the studied samples, to find the incidence angle for which the values of Ψ and Δ are the most sensitive. In this work, we mostly used $\phi_0=70^\circ$.

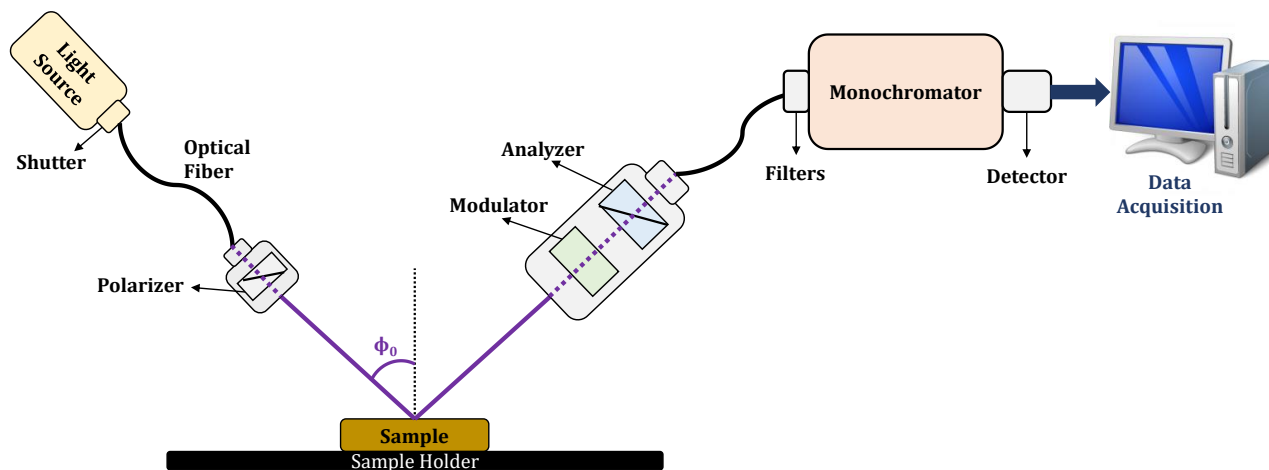


Figure III.2-1 Drawing of the polarisation modulation ellipsometer.

The sample is placed on the holder and its positioning is adjusted with an autocollimator. The incidence angle and the spectral range are chosen, then the measurement starts. After the data acquisition, a model adapted to the sample is used to fit the data (III.2.1.b) and obtain the structural and optical parameters.

III.2.1.b. Fitting Models

We characterise several materials with SE measurements, the employed fitting models are gathered in **Table III.2-1**. Each model was developed and optimised according to our experimental materials. For samples with a c-Si substrate, we used an infinite c-Si substrate in the model, whereas for samples on quartz-glass, the substrate in the model is an infinite void and the first layer is the quartz-glass with a fixed thickness of 1 mm. We adapted the fitting ranges according to the quality of the measured signal, depending on the studied materials.

Materials	Fitting Model	Fitting Range
a-Si:H	Tauc-Lorentz [20][21]	From 1.5 eV to 4.7 eV
μ c-Si:H	<i>Detailed in IV.2</i>	From 1.5 eV to 4.7 eV
ITO	Drude & 2*Lorentz [141][142]	From 1 eV to 4.2 eV
SnO ₂	Lorentz [143]	From 1.5 eV to 4 eV
Perovskite	Triple New Amorphous [144]	From 1.5 eV to 4 eV
PTAA	New Amorphous [144]	From 1.5 eV to 4 eV

Table III.2-1 Summary of the fitting models for each studied material.

III.2.2. Spectrophotometry

In solar cells, optical properties of materials are very important to optimise the efficiencies. A simple way to characterise those optical parameters is spectrophotometry. We used a spectrophotometer operating in UV, visible and IR spectral ranges (from 280 nm to 2450 nm), from *PerkinElmer*, to measure the transmittance and the reflectance of our samples. In our case, we only made measurements in the absorption range of the studied solar cells, from 300 nm to 1200 nm. We performed reflectance measurements on samples with glass or silicon substrate and transmittance measurements on quartz-glass substrates.

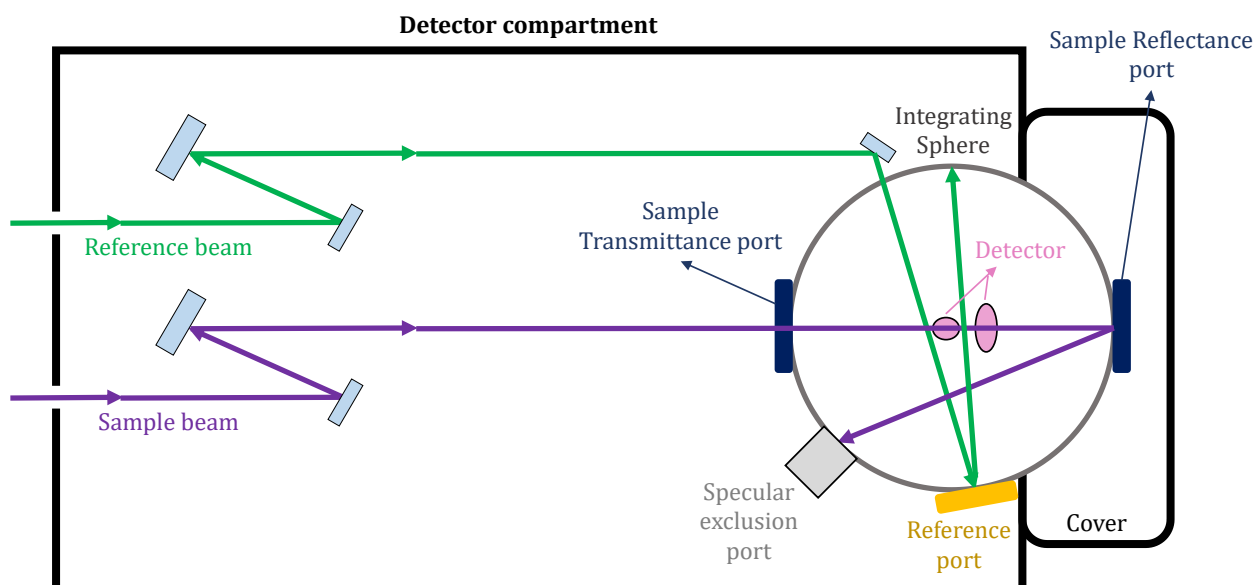


Figure III.2-2 Details of the detector compartment of the spectrophotometer.

The spectrophotometer is composed of two radiation sources with an optical system to forward them to the detector compartment. **Figure III.2-2** shows the details of this compartment. The specular exclusion port can be used to measure only the diffuse reflectance of a sample instead of total reflectance. In fact, in this work we sometimes used the diffuse reflectance as an indication of the sample roughness (see [Appendix A](#)).

After the transmittance and the reflectance measurements every 10 nm, we calculated the absorptance with equation (III. 2-2):

$$A = 100 - R - T \quad (\text{III. 2-2})$$

III.2.3. Raman spectroscopy

The Raman Effect is a molecular vibration that causes a variation in polarisability and thus the deformation of orbitals. The sample is illuminated with a light beam of a chosen frequency, there are absorption, transmission, reflection or scattering of photons. The majority of the scattering is elastic, therefore of the same frequency as that of the laser but a small part is inelastic, following the Raman Effect, it is this one that we study in Raman spectroscopy.

In order to complete the characterisation performed with spectroscopic ellipsometry and spectrophotometry, we did Raman spectroscopy on microcrystalline silicon layers on glass and on c-Si substrate (part [IV.2.2](#)). Our goal was to characterise the crystallinity of those layers. Thus, we used a 325-nm laser to characterise the layer's surface

($\delta p \approx 8$ nm) and a 442-nm laser to look more deeply ($\delta p \approx 50$ nm). We used an *InVia* Raman spectrometer, from *Renishaw*, to perform those measurements.

We decorrelated the obtained Raman spectra in three peaks (**Figure III.2-3**): 480 cm^{-1} for the amorphous phase, 520 cm^{-1} for crystalline silicon, and 507 cm^{-1} for the mix-phase (small grains). Then, the microcrystalline phase fraction, $X_{\mu\text{c-Si}}$, was calculated using equation (III. 2-3), adapted from [145]:

$$X_{\mu\text{c-Si}} = \frac{I_{520} + I_{507}}{I_{520} + I_{507} + \sigma I_{480}} \quad (\text{III. 2-3})$$

where σ is the ratio of the integrated Raman cross-section for amorphous to microcrystalline silicon (we assumed $\sigma = 1$ according to the layers thicknesses which induce small crystallite sizes, [145], [146]). I_{520} , I_{507} , and I_{480} are the integrated intensities of the previous cited Raman peaks.

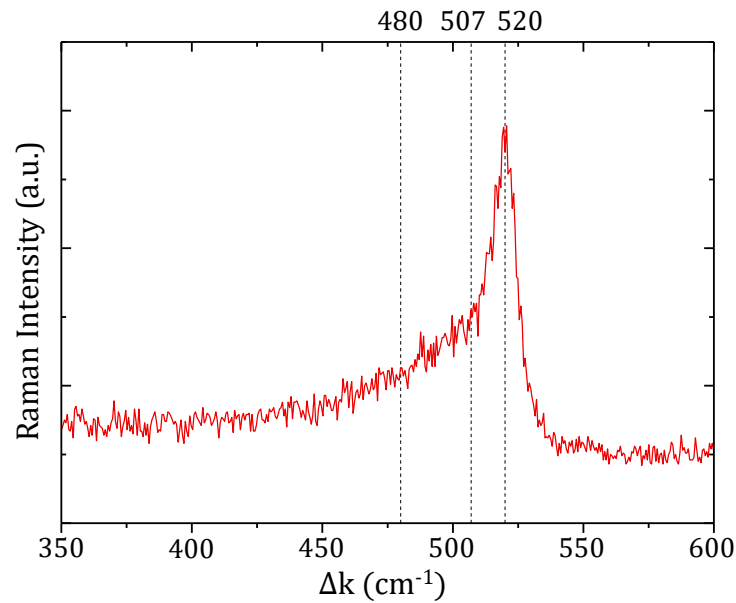


Figure III.2-3 Example of a Raman spectrum measured on a microcrystalline layer on glass. The three peaks used for the decorrelation are highlighted.

III.2.4. Four-terminal Sensing

In photovoltaic, the sheet resistance and the conductivity of a material are very important parameters and their measurement is usual to characterise thin-films. In this work, 4-point probe measurement were performed in a *Napson* tool to determine these parameters, for several thin-films deposited on quartz-glass substrates. The tool is composed of a substrate holder and a probe holder, several probes can be used with different weights applied on them to optimise the measure with the type of the sample. The probe, in grey on **Figure III.2-4**, has four small probes in line, separated from each other by the distance S , the inner probes are linked to a voltmeter (V) and the outer probes are linked to a current source (I). With this configuration, the R_{sheet} is calculated with equation (III. 2-4):

$$R_{\text{sheet}} = \frac{V}{I} \frac{\pi}{\ln 2} \Omega \text{ per Square} \quad (\text{III. 2-4})$$

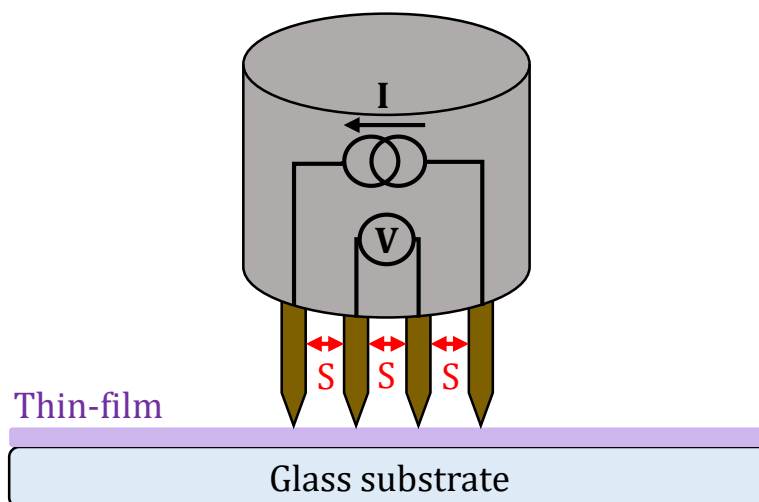


Figure III.2-4 Drawing of the 4-point probe R_{sheet} measurement.

Thereby, with the thickness t of the thin-film extracted by SE measurements, we can obtain the thin-film conductivity, σ , with equation (III. 2-5):

$$\sigma = \frac{1}{t \cdot R_{sheet}} \quad (\text{III. 2-5})$$

III.2.5. Hall Effect Measurements

The conductivity obtained with 4-point probe measurements could be impacted on very thin layers by a possible penetration in the layer by the probes. To validate the 4-terminal sensing results on thin microcrystalline silicon layers, we performed conductivity measurements coupling the van der Pauw method and the Hall effect [147]. The used tool is a *HMS5000 Ecopia* including a permanent magnet with a 30 mm diameter.

The same samples on square glass substrate as for 4-terminal sensing measurements are put into the tool and a probe is placed at each corner. The thin-film thickness is negligible compared to the sample length and width so, by applying a current I and a perpendicular magnetic field B , free carriers are deviated by a Lorentz force. Holes and electrons are led on opposite sides, as illustrated in **Figure III.2-5**. This charge separation results in a potential difference, named Hall voltage V_H . Without magnetic field and knowing the thin-film's thickness t (extracted by SE), the conductivity is determined with equation (III. 2-6):

$$\sigma = \frac{I}{V_H \cdot d} \quad (\text{III. 2-6})$$

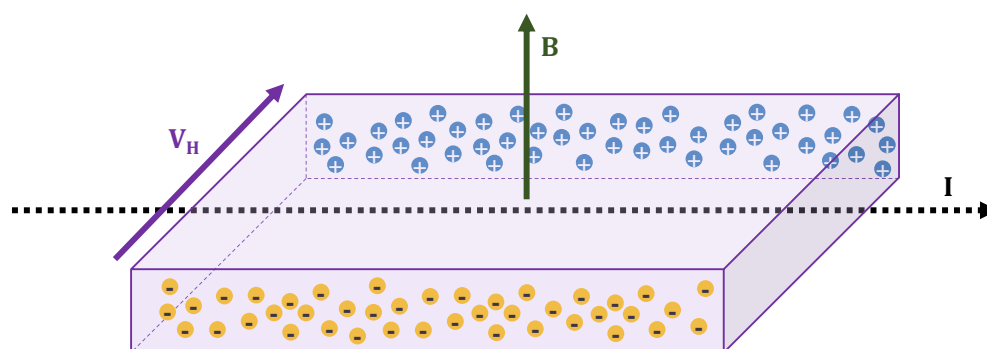


Figure III.2-5 Sketch of the charge separation during the Hall Effect measurement.

III.2.6. Thin-film's Activation Energy

The activation energy, E_a , provides details of the energy levels in a thin-film, it can be interpreted as the energy needed by a charge carrier to achieve conduction ($E_c - E_F$ or $E_F - E_v$, [148]). Activation energies of microcrystalline silicon layers on glass were extracted from dark I-V measurements with temperature variation. Aluminium electrodes are deposited on the thin-films by thermal evaporation. Then, we measure the current in the dark by applying a voltage between the electrodes at a monitored temperature. The conductivity is obtained from the resistance extracted with the I-V measurements (using the Ohm's law), using equation (III. 2-7):

$$\sigma = \frac{1}{R} \frac{L}{t \cdot w} \quad (\text{III. 2-7})$$

where t is the layer thickness, w is the electrodes length (8 mm in our case) and L the electrodes spacing (1 mm in our case).

Then, the activation energy is extracted with an Arrhenius slope using equation (III. 2-8):

$$\sigma = A \cdot e^{\frac{-E_a}{K_b \cdot T}} \quad (\text{III. 2-8})$$

where A is a constant, K_b is the Boltzmann's constant and T is the temperature in Kelvin.

III.2.7. Contact Resistances Measurements

The contact resistance between two materials is an important factor in solar cells. In fact, in SHJ solar cells, the contact resistances is the main contribution to the total R_s of the solar cell and reduces its efficiency [149].

We determined contact resistances with our own method, presented in details in chapter IV, using transversal I-V measurements. In order to validate this method, we compared the obtained values with those obtained with the well-known TLM, adapted to SHJ solar cells and multi-layer systems [150], at CEA-INES by L. Basset *et al.* [149].

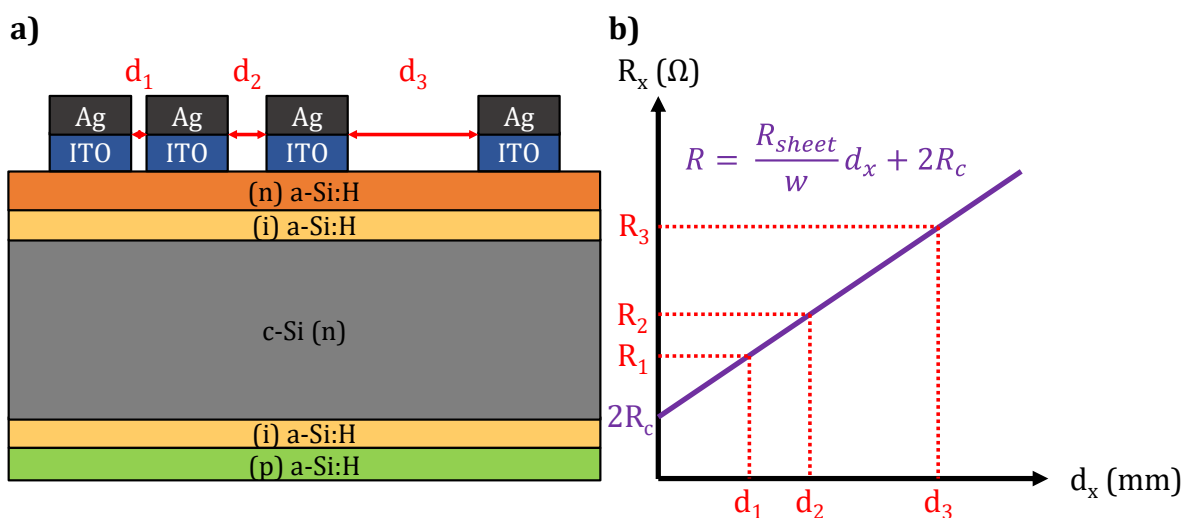


Figure III.2-6 a) Cross-section sketch of a TLM sample used to investigate the electron contact in SHJ solar cells. **b)** Example of a TLM plot after measuring the resistances R_x for increasing the electrode spacing d_x .

TLM is performed on patterned samples with rectangular electrodes, an example in cross-section in the electrodes width is illustrated in **Figure III.2-6 a)**. Resistances R_x are extracted from I-V measurements between two electrodes, using the Ohm's law. Then,

R_x is plotted as function of the electrodes spacing, d_x , and R_c is extracted from the equation of the obtained line, shown in **Figure III.2-6 b**), where w is the electrodes length. The contact resistivity, ρ_c is then obtained with equations (III. 2-9) and (III. 2-10), where L_t is the transfer length.

$$R_c = R_{sheet} \cdot \frac{L_t}{W} \cdot \coth\left(\frac{L}{L_t}\right) \quad (\text{III. 2-9})$$

$$\rho_c = R_{sheet} \cdot L_t^2 \quad (\text{III. 2-10})$$

III.2.8. Scanning and Transmission Electron Microscopy

III.2.8.a. SEM Measurements

Scanning electron microscopy is a characterisation method commonly used in many fields. SEM uses a focused e-beam to scan the surface of a sample and obtain images that contain information about the composition and the topography of this sample. We performed SEM measurements in front and cross-section view (e.g. **Figure III.1-1**) on manually cut silicon substrates for several applications in this work. Measurements were done under high vacuum in a *Nova NanoSEM 630*, from *FEI Company*, and the equipment settings were adapted according to what we wanted to observe.

III.2.8.b. STEM-EDX Measurements

Scanning transmission electron microscope is a transmission electron microscope with a mapping possibility and often equipped with additional detectors, useful for analytical techniques, as the EDX in our case. STEM is often used in the solar cells development to characterise the nanoscale structure of materials. Moreover, energy dispersive X-ray spectroscopy is used in a STEM to obtain an elemental mapping of samples (e.g. **Figure V.3-11**). To perform STEM-EDX measurements, the samples have been prepared with focused ion beam, in a *ZEISS 750* tool, to obtain very small cross-section. Samples had been previously coated with a thick mixture of Platinum and Carbon to protect the section during the FIB cut-out. After the FIB cross-section preparation, STEM-EDX measurements were performed under high vacuum in a *Tecnai Osiris* tool, from *FEI Company*.

III.2.9. Confocal Microscopy

Confocal microscopy is very useful to obtain the topography of samples surfaces and have an idea of their roughness. For example, confocal microscopy is used to characterise the metallisation lines (done by screen-printing) on SHJ solar cells. In this work, a *Sensofar* confocal microscope is used to obtain optical and topography images of the samples surface at a larger scale than with the previous techniques (III.2.8).

With this technique, images do not contain out-of-focus information contrary to other standard fluorescence microscopy. During the measurements, a vertical scan is done to obtain images of different focal planes, then the software, *SensoScan* in this work, provides topography images after a 3D reconstruction. These topography images were useful to determine if we can use the spin-coating deposition method (III.1.6) on chemically polished wafers (see **Appendix A**).

III.2.10. X-ray Diffraction

X-ray diffraction is a characterisation technique used on materials to study their crystallographic structure and some chemical and physical properties. XRD is usually employed to investigate the Perovskite material [151]. A Cobalt tube is used to produce X-rays, these X-rays are diffracted according of the crystal lattice of the sample and a detector measures the diffracted X-rays. The source and the detector are moving around the sample in a so-called Bragg-Brentano geometry, thus the obtained diffractograms (of the measured X-rays intensity) are as function of the detector angle.

We performed XRD measurements, in an *Aeris* tool (from *Panalytical*), on Perovskite layers coated on several substrates. The goal was to compare the Perovskite crystallisation according to its underlying layers. Diffractograms analysis are presented in part VI.3.

III.3. Solar Cells Characterisation

After the material optical, electrical and structural characterisation, we also characterised the electrical properties of final devices, as SHJ solar cells (in parts IV.3 and V.2.1), tandem and “tandem-like” solar cells (see chapter VI) and tests-structures for TJ (in chapter V). This part explains the different methods employed.

III.3.1. Lifetime Measurements

Effective minority carrier lifetime and implied parameters (iV_{oc} and iFF) are very important to improve solar cells efficiencies, as they give information on the devices quality. We performed those measurements by photoconductance decay, with a *WCT-120 Sinton* tool, illustrated in **Figure III.3-1**, very common in the solar cells industry. This type of measurement is contactless and averages over a defined circular area of 40 mm diameter (at the centre of the sample). The sample is placed on a holder that contains a coil connected to a computer. During the measurement, a flash illumination causes the generation of extra electron-hole pairs in the sample. The sample conductance increases and is measured. Then, the photoconductance, named $\Delta\sigma$, is obtained by subtracting the dark conductance to the conductance under illumination. This photoconductance is linked with the excess minority carrier density (Δn) by the equation (III. 3-1), where μ_n and μ_p are respectively the electrons and holes mobility. The reference permits to obtain the carrier generation rate, G , to calculate the effective lifetime, τ_{eff} , with equation (III. 3-2).

$$\Delta n = \frac{\Delta\sigma}{q(\mu_n + \mu_p)} \quad (\text{III. 3-1})$$

$$\tau_{eff} = \frac{\Delta n}{G - \frac{d\Delta n}{dt}} \quad (\text{III. 3-2})$$

In this work, we made the measurements in the transient regime as our samples feature very high carrier lifetimes. The flash is very brief thus the generation G is considered negligible compared to the second term, thus equation (III. 3-2) becomes equation (III. 3-3).

$$\tau_{eff} = \frac{\Delta n}{-\frac{d\Delta n}{dt}} \quad (\text{III. 3-3})$$

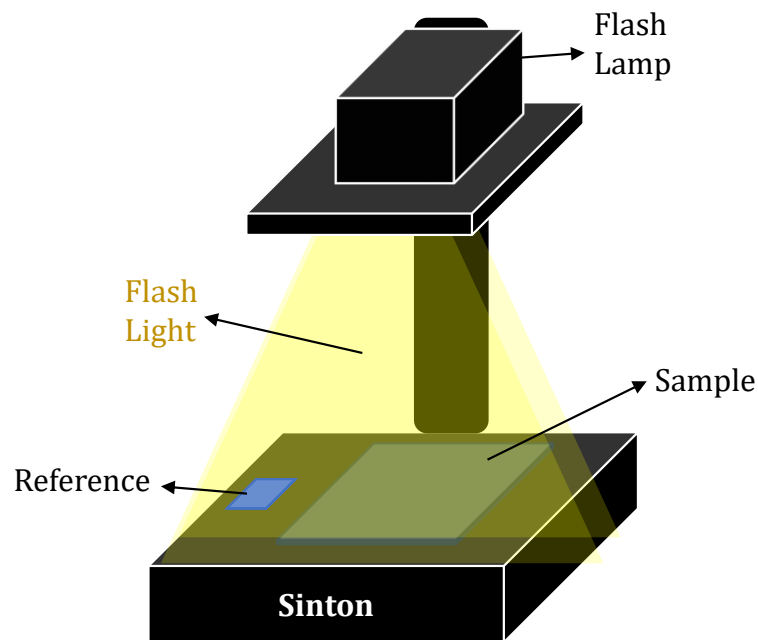


Figure III.3-1 Drawing of the lifetime measurement setup.

τ_{eff} is usually used as an indicator of the bulk's surface passivation quality and often measured on isotype symmetrical samples without metallisation (after PECVD or PVD).

III.3.2. Suns- V_{oc} Measurements

Suns- V_{oc} measurements are done on metallised solar cells, contrary to lifetime measurements, to obtain a “pseudo J-V Curve”. The Suns- V_{oc} setup, from *Sinton*, is very similar to the *WCT-120 Sinton* tool [152], presented in **Figure III.3-1**. The sample is placed on the tool and a probe is put on a busbar. The illumination intensity is varied, thus J_{sc} and V_{oc} are varying too and each couple of $J_{\text{sc}}-V_{\text{oc}}$ is plotted in the “pseudo J-V Curve”. In our Suns- V_{oc} tool, the J_{sc} is not measured but a reference solar cell is used to monitor the illumination intensity, which allows to obtain the same curve. This “pseudo J-V Curve” is not impacted by the R_s because there is no current at V_{oc} and the curve is flat at J_{sc} (if the R_s is not very large, which is the case with the solar cells studied in this work).

We can extract a “pseudo FF”, pFF, from the “pseudo J-V Curve” and a fast and easy way to obtain the R_s of a solar cell is by comparing the measured FF and the measured pFF, with equation (III. 3-4) [153].

$$R_s = (pFF - FF) \cdot \frac{J_{\text{sc}} \cdot V_{\text{oc}}}{J_{\text{mpp}}^2} \quad (\text{III. 3-4})$$

III.3.3. Quantum Efficiency Measurements

The External Quantum Efficiency of a solar cell is defined as the ratio between the number of charge carriers collected at the contacts and the number of incident photons. In this work, EQE measurements were performed on complete devices, in a self-made tool, with a 150 W Xenon lamp spectrally filtered by a monochromator. The measurements were performed from 300 nm to 1200 nm. For each wavelength λ , the current density collected by the solar cell, J_c , for an applied voltage, is measured, as well as the incident power, P_{in} . The EQE is then calculated with equation(III. 3-5):

$$EQE(\lambda) = \frac{1}{q} \cdot \frac{hc}{\lambda} \cdot \frac{J_c(\lambda)}{P_{in}(\lambda)} \quad (\text{III. 3-5})$$

where q is the electronic charge, h is the Planck's constant and c is the speed of light in a vacuum atmosphere.

By performing spectrophotometry measurements on the solar cell to obtain its reflectance R , the Internal Quantum Efficiency (IQE) can be determined with equation (III. 3-6). The IQE allows to overcome reflectance and transmittance of the solar cells, it is defined as the ratio between the number of charge carriers collected and the number of absorbed photons.

$$IQE(\lambda) = \frac{EQE(\lambda)}{1 - R(\lambda)} \quad (\text{III. 3-6})$$

III.3.4. Current-Voltage Measurements

III.3.4.a. Solar Cells J-V curves

We performed Light J-V measurements of solar cells under AM1.5G standard conditions using two different AAA solar simulators, previously calibrated with reference cells:

- For bifacial M2 SHJ solar cells, a J-V tester of the CEA-INES pilot-line, from *Chroma*, was used. The busbars are contacted on both sides of the cell with arrays of pins.
- Otherwise, tandem and “tandem-like” (chapter VI) solar cells (5 cm x 5 cm) were measured using two force-sense probes placed on the only busbar, in a self-made tool. For these measurements, edges of the cell are masked and only an area of 8.45 cm² is illuminated. Several curves are measured, the illumination is continuous and a J-V curve is done every 10 to 15 seconds.

With light J-V curves, we can extract the four main parameters of a solar cell:

- J_{sc} : current density when the voltage is zero, usually the largest current density which may be obtained from the solar cell
- V_{oc} : the voltage when the current is zero, often considered as the maximum voltage available from the solar cell
- FF: the ratio of the maximum power from the solar cell to the product of V_{oc} and J_{sc} , equation (III. 3-7)

$$FF = \frac{V_{mpp} \cdot J_{mpp}}{V_{oc} \cdot J_{sc}} \quad (\text{III. 3-7})$$

- PCE or efficiency, η : the fraction of the incident power, P_{in} , which is converted to electricity, determined with equation (III. 3-8)

$$\eta = \frac{V_{oc} \cdot J_{sc} \cdot FF}{P_{in}} \quad (\text{III. 3-8})$$

Dark I-V measurements were performed using the same tools but without the light source and with a black box around the sample holder. An example of light J-V curve, in blue, and dark J-V curve, in red, is shown in **Figure III.3-2**.

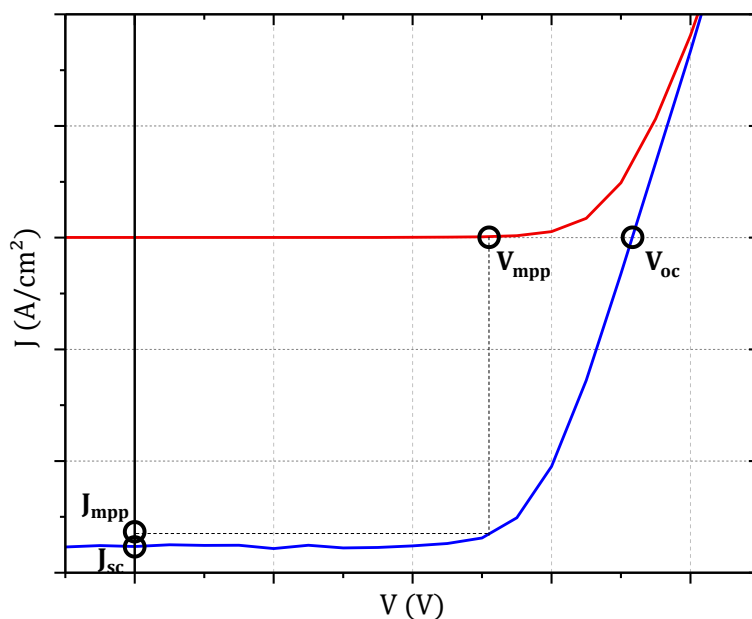


Figure III.3-2 Dark J-V Curve in red and Light J-V Curve in blue of a solar cell.

III.3.4.b. Temperature-Dependent Dark I-V

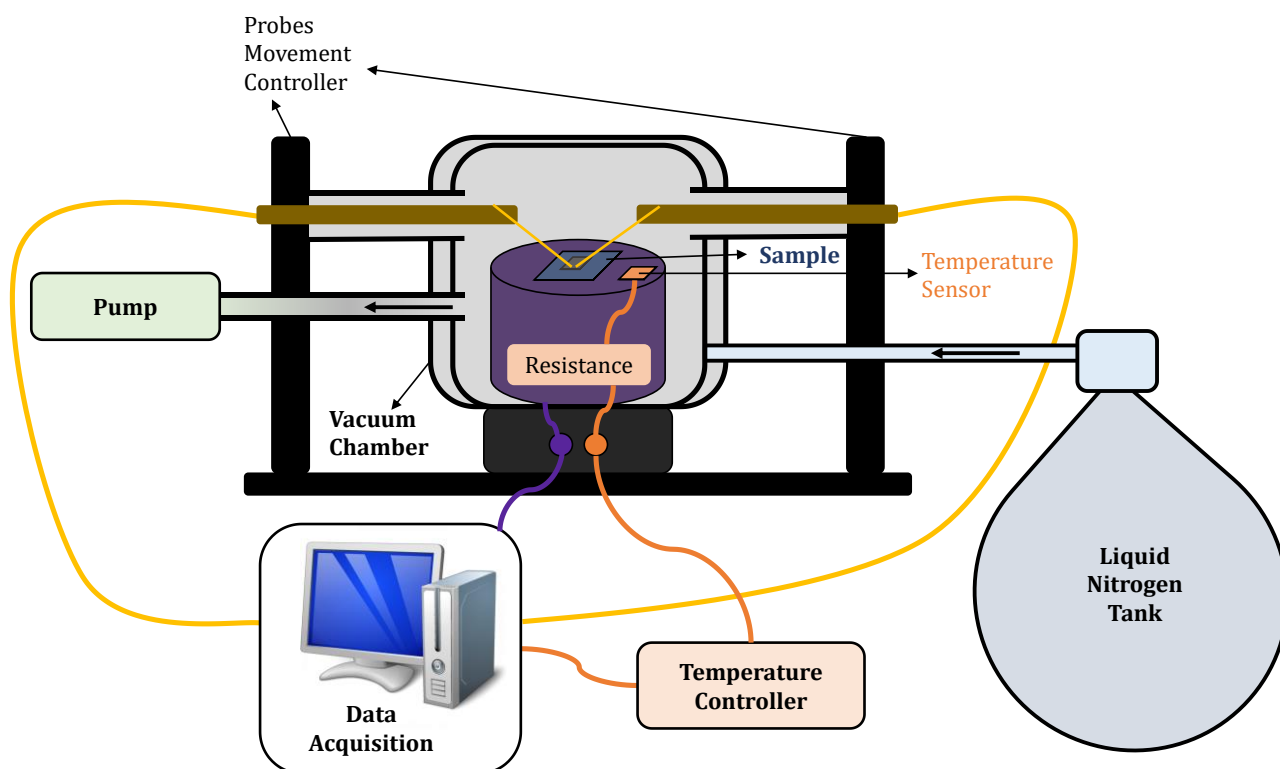


Figure III.3-3 Sketch of the Cryostat tool.

Dark I-V measurements at variable temperature were performed in the Cryostat tool presented in **Figure III.3-3**. The sample is put in the tool and the chamber is placed under vacuum. Controllers are then used to place the probes on the chosen

electrode. The probes and the chuck are connected to a measurement station *Keithley 4200*. A *Temperature Controller 9700* is connected to the measurement station and a temperature sensor. A resistance (50 Ω) in the chuck is used to heat the sample and a tank of liquid nitrogen is connected to the vacuum chamber to cool the sample. Thanks to the full installation, we can measure the current during a voltage sweep at a precise temperature.

In this work, the Cryostat tool was used to perform transversal measurements, using two probes (Force-Sense) on the front-side electrode of the sample and with the back-side metallisation in direct contact with the chuck. More details about these measurements are presented in chapter V.

III.4. Optical Simulation

To conclude this chapter, this part presents the software used in this work to perform optical simulations and the method implemented to extract the optical properties needed for these simulations.

III.4.1. Software Presentation: CROWM

In this work, we performed optical simulations using the software CROWM (Combined Ray Optics / Wave Optics Model), provided by the *Laboratory of Photovoltaics and Optoelectronics, University of Ljubljana* [154]. All the simulations were done under the solar spectrum at AM1.5G (1 sun), with 100 incident rays, from 310 to 1200 nm (10 nm step). In the software, we enter the structure of the simulated device, layer by layer and the optical indexes (n and k parameters) of each layer as input parameters. Moreover, AFM images are also used as input parameters to define layers surface state (polished or textured).

After the simulation, the output data are the total reflectance and the total transmittance of the simulated device and the absorptance of each layer, as function of the wavelength. Simulated J_{sc} are extracted from absorptance data with the equation (III. 4-1):

$$J_{sc} = \frac{q}{hc} \int P_{spc}(\lambda) \cdot A_{layer}(\lambda) \cdot \lambda \cdot d\lambda \quad (\text{III. 4-1})$$

where h is the Planck's constant, c is the speed of light in a vacuum atmosphere and P_{spc} is the power of the input solar spectrum.

This calculated J_{sc} represents the expected generated photocurrent in absorber layers, assuming that all the absorbed photons contribute to the generation. Moreover, for non-absorber layers, it represents the expected losses due to the parasitic absorption.

III.4.2. Optical Indexes Extraction Method

In order to obtain optical simulations as close as possible to our experimental devices, we extracted the optical indexes of each simulated layer from ellipsometry measurements and validated them with the following protocol:

- Deposition of single layer (of known thickness, previously measured by mechanical profilometry) and stacked layers such as solar cells
- Ellipsometric measurement at three different incident angles (50 °, 60 ° and 70 °) of each sample (III.2.1.a)

- Spectrophotometric reflectance and transmittance measurements and absorbance extraction, on the same samples (see part III.2.2)
- Creation of ellipsometric models specific to each layer (especially for Perovskite solar cell materials)
- Validation of the models by fitting curves
- Extraction of optical indexes with DeltaPsi2 (III.2.1.a)
- Optical simulation with the obtained optical indexes
- Comparison, for optical indexes validation, of measured R, T, A values and data obtained with the simulations

This protocol is illustrated in **Figure III.4-1** with the example of the Perovskite solar cell materials, in a NIP single-junction.

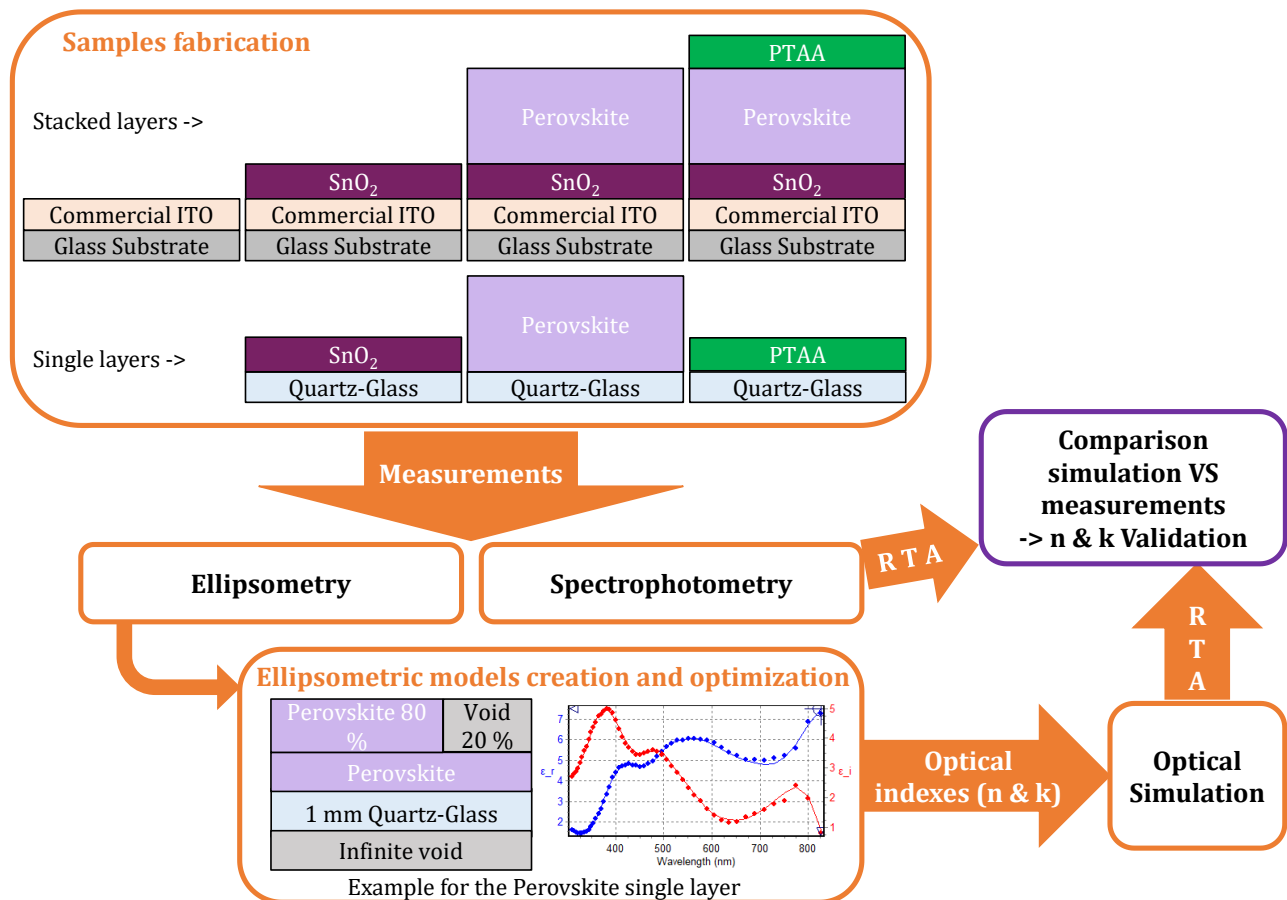


Figure III.4-1 Optical indexes extraction protocol applied for Perovskite solar cell materials, in a NIP single-junction.

Optical simulations are presented in part VI.2. They were used all over this work to optimise materials thicknesses and compare different possible layers. Moreover, they were useful to correlate measured J_{sc} with parasitic absorption and highlight which layer or material need to be optimised or modified.

III.5. Chapter Conclusion

In this chapter III, we have explained the fabrication processes of our samples and presented the techniques used to characterise the materials and the solar cells. We also described the optical simulation software and detailed our optical indexes extraction method. In the following chapters, these methods are cited and not again detailed.

IV. MICROCRYSTALLINE SILICON TUNNEL JUNCTION FOR PIN TANDEM SOLAR CELLS

In the previous chapters, we have presented the state-of-the-art of Perovskite on silicon heterojunction monolithic tandem solar cells and the characterisation and fabrication methods used in this work. In this chapter, we present the development of a microcrystalline silicon tunnel junction to act as recombination junction in PIN Perovskite/SHJ tandem devices. First, we present the choice of the PECVD parameters and the layers characterisation and optimisation. Then, we integrate the developed layers in SHJ solar cells and analyse the results. Finally, we discuss whether the developed junction is ready for integration into a tandem solar cell or if further characterisations are required.

IV.1. Introduction

As presented in part II.4.1, highly doped tunnel junctions can be used as recombination junction in tandem solar cells. This junction should be thin, transparent and conductive enough for the charge carriers to recombine. In addition, with a SHJ bottom cell, tunnel junction layers should not degrade the a-Si:H layers and interfaces, which are very sensitive to temperature steps. In this context, microcrystalline silicon that could be processed at low-temperature (≤ 200 °C) seems to be a good choice. It also presents some advantages compared to other recombination junctions, as transparent conductive oxides. In fact, microcrystalline silicon layers tend to be more transparent in the IR range and have optical indexes more adapted [155]. Moreover, this type of junction performed well in several multijunction solar cells [95], [156]–[158] and have all the required qualities. For example, F. Sahli *et al.* demonstrated a Perovskite/SHJ tandem solar cell with a nanocrystalline silicon tunnel junction at low temperature (< 200 °C) in both standard (NIP) and rear emitter (PIN) configurations [13], [95].

The CEA-INES pilot-line produces rear emitter SHJ solar cells and the record efficiency for a Perovskite/SHJ tandem was obtained in the PIN configuration (**Figure II.3-4 f**). Thus, we chose to start developing a tunnel junction in microcrystalline silicon, deposited at low temperature to preserve the SHJ bottom-cell, in the PIN configuration, as represented in **Figure IV.1-1**. In this work, the $\mu\text{c-Si:H}$ layers were deposited in the PECVD development tool (III.1.2.b)) on top of a-Si:H layers deposited in the PECVD industrial tool (III.1.2.a) but, in an industrial fabrication process for tandem devices the same tool could be used for both.

In this chapter, the tunnel junction is developed to be integrated on a polished substrate to allow the deposition of the Perovskite top-cell by spin-coating. The deposition time of this junction is then adapted to conserve similar thicknesses in the results and studies presented on textured surfaces.

The main objective of this chapter IV is to present the development and the characterisations done to obtain a microcrystalline silicon tunnel junction ready for its integration in tandem solar cells. Some parts of this chapter were published in [159]. Moreover, the reproducibility of this recombination junction throughout the duration of this work is also discussed. Therefore, in the following chapters, this recombination junction is used in several presented experiments but its characteristics are not presented again.

IV.2. Microcrystalline Silicon Layers Development

In this part, the PECVD process conditions used for the deposition of the $\mu\text{c-Si:H}$ layers are explained, as well as their impact on the properties of the deposited layers. Then, these layers are extensively characterised and their properties are presented.

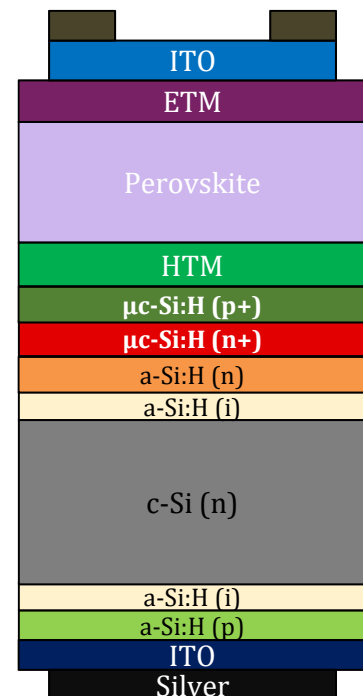


Figure IV.1-1 PIN Perovskite on SHJ tandem solar cell with a microcrystalline silicon tunnel junction.

Figure IV.2-1 shows the main samples used in this chapter. Moreover, for each $\mu\text{c-Si:H}$ layer deposited in this work, a quartz-glass substrate and a IN/IN DSP precursor (Figure IV.2-1 d)) are used as references to control the layer properties.

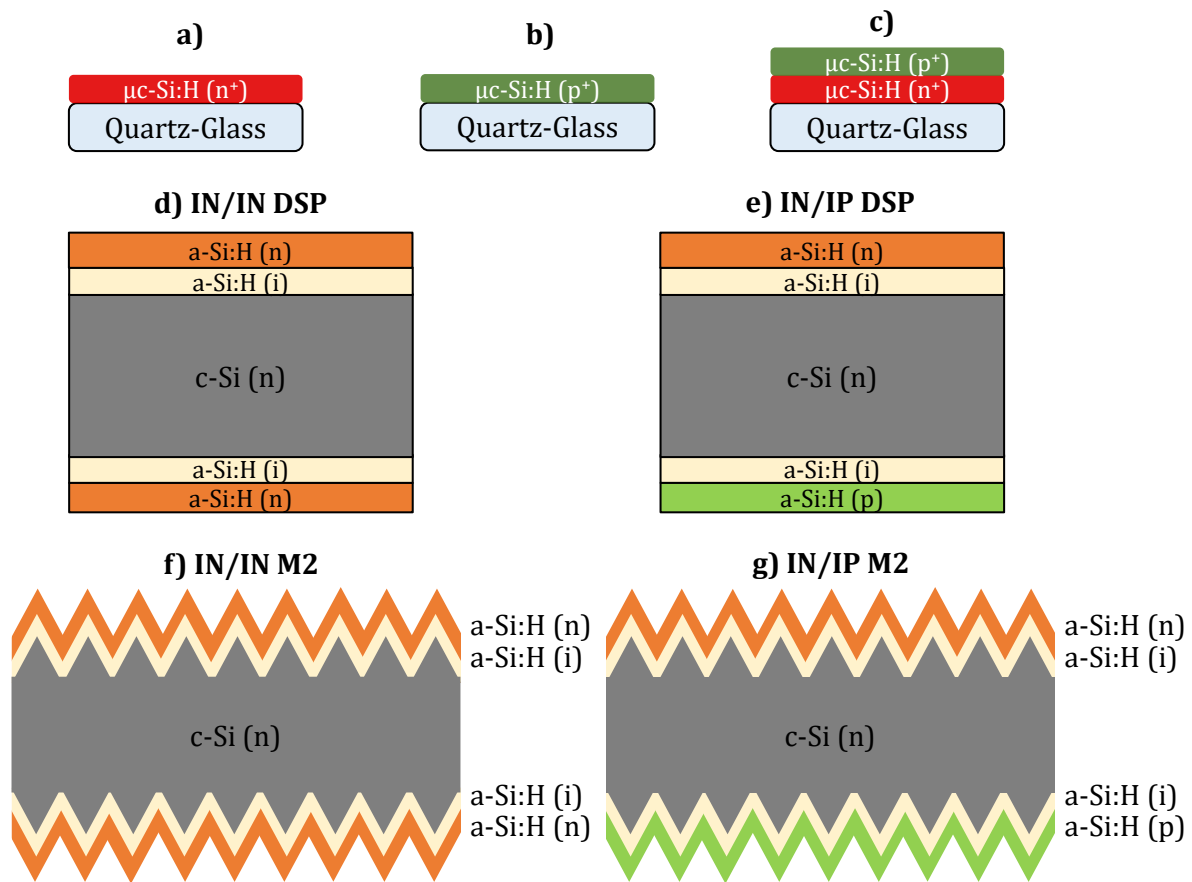


Figure IV.2-1 a) N-type $\mu\text{c-Si:H}$ layer on a quartz-glass substrate; b) P-type $\mu\text{c-Si:H}$ layer on a quartz-glass substrate; c) $\mu\text{c-Si:H}$ (n^+/p^+) junction on a quartz-glass substrate. d) IN/IN DSP Isotype (N-type) and symmetrical precursors on FZ DSP wafer; e) IN/IP DSP SHJ precursors on FZ DSP wafer. f) IN/IN M2 Isotype (N-type) and symmetrical precursors on CZ textured wafer; g) IN/IP M2 SHJ precursors on CZ textured wafer.

For the layers development, we used spectroscopic ellipsometry (see III.2.1) and four-terminal sensing (see III.2.4) as the reference characterisation methods. SE measurements were fitted with a model assuming a mixture of $\mu\text{c-Si:H}$, a-Si:H and void (for the layer roughness, applying the Bruggeman's Effective Medium Approximations [160]), as presented in Figure IV.2-2. The fitting process determined the layers thicknesses and the microcrystalline phase fraction ($X_{\mu\text{c-Si}}$) percentages. The pseudodielectric functions of the different materials used in this model are shown in Figure IV.2-3. The $\mu\text{c-Si:H}$ material is based on small grains polysilicon material and represents the microcrystalline phase of the layer.

Four-terminal sensing measurements were performed to control the R_{sheet} and the lateral conductivity, σ , of the layers deposited on quartz-glass substrates, more details are presented in part IV.2.3. The characterisations performed on quartz-glass substrates are not directly representative of the layer in a final tandem device. However, we used them as reference to investigate the reproducibility of the PECVD recipes and to compare several process conditions. Similarly, as the growth of the $\mu\text{c-Si:H}$ layers is different on quartz-glass and on amorphous silicon ([161]), the values of R_{sheet} and σ are probably a little different in the studied devices.

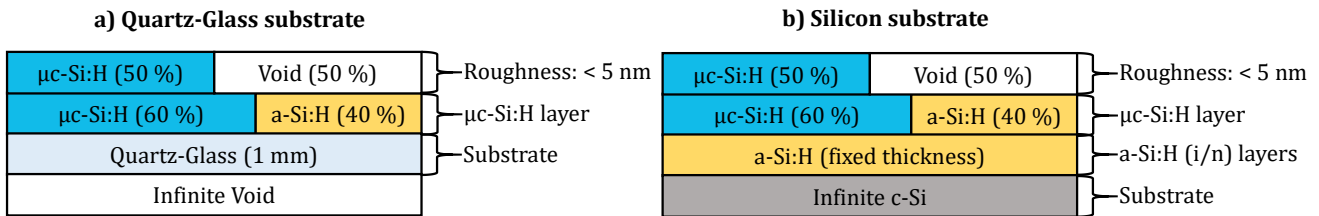


Figure IV.2-2 a) SE fitting model used for the microcrystalline silicon layers deposited on quartz-glass substrate; b) SE fitting model used for the microcrystalline silicon layers deposited on IN/IN DSP precursors.

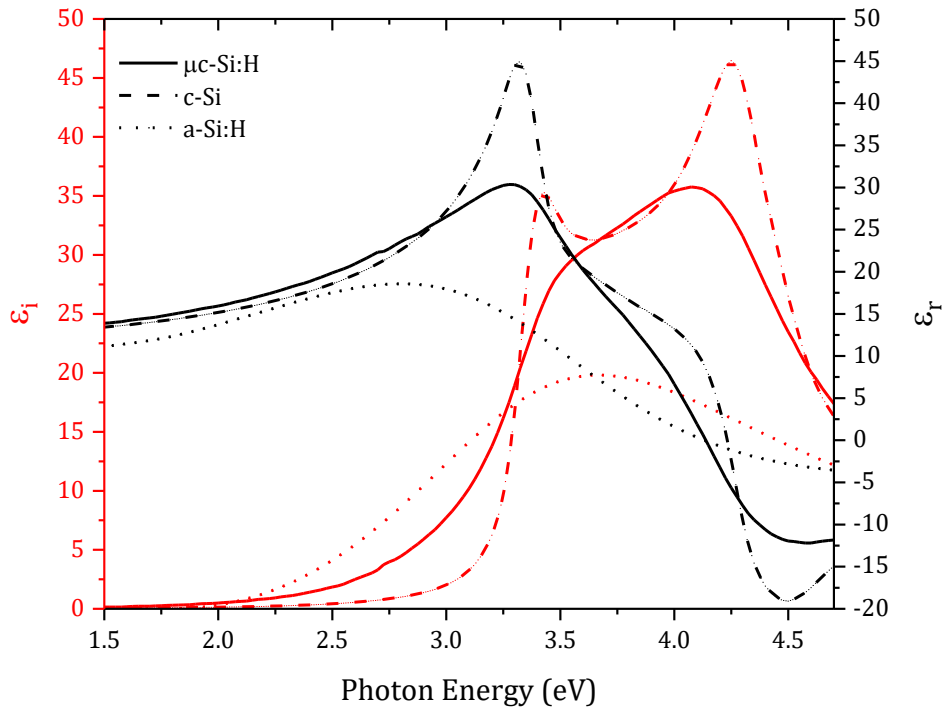


Figure IV.2-3 Pseudodielectric function, $\epsilon = \epsilon_r + i(\epsilon_i)$, of the materials used in the fitting model, solid lines for the microcrystalline silicon, dashed lines for pure crystalline silicon and dotted lines for amorphous silicon.

IV.2.1. PECVD Parameters

In 2011, a study was performed in the development tool to define the best chamber pressure, RF power, susceptor speed and susceptor position to deposit microcrystalline silicon. For this work, we used those parameters, presented in **Table IV.2-1**, as a starting point for the development. The chamber pressure is high but the plasma is stable and no powder ([162], [163]) was observed on the tray neither on the substrates. Moreover, a great uniformity is obtained when several reference samples are placed all over the tray. However, this may impact the surface roughness of the layers which is not an issue for this work (the layers then being covered by wet deposition methods). The RF power is also high, in order to increase the deposition rate which tends to be very low for microcrystalline silicon ([126]). The susceptor position and speed are adjusted to increase the deposition rate and improve the deposition uniformity.

Chamber Pressure (Torr)	RF Power (Watt)	Susceptor Speed (mm/sec)	Susceptor Position (mm)
9	1100	3	21

Table IV.2-1 PECVD chamber parameters used for the deposition of the $\mu\text{c-Si:H}$ layers.

First, we created a coating recipe to prepare the trays and the chambers before the $\mu\text{-Si:H}$ layers deposition. This coating recipe only uses H_2 and SiH_4 gases, to deposit intrinsic material on the tray and the process chamber. Moreover, this recipe is composed of two deposition cycles of 300 s. In order to obtain microcrystalline layers with a high density of states, to enhance recombination (see part II.4), we used a very high hydrogen content ([127], [164], [165]). Thus, the gas flow ratio R , defined in equation (IV. 2-1), with SiH_4 and H_2 the gas flow rates in sccm, is very low (hydrogen gas flow \gg silane gas flow): $R = 0.0025$.

$$R = \frac{\text{SiH}_4}{\text{SiH}_4 + \text{H}_2} \quad (\text{IV. 2-1})$$

Secondly, we deposited N-type layers on quartz glass and IN/IN DSP substrates by varying the deposition time, with the same $R = 0.0025$ ratio and a R_N gas flow ratio fixed at 1, defined in equation (IV. 2-2), with SiH_4 and PH_3 the gas flow rates in sccm.

$$R_N = \frac{\text{PH}_3}{\text{SiH}_4} \quad (\text{IV. 2-2})$$

The samples were then characterised with SE and four-terminal sensing measurement, as explained previously.

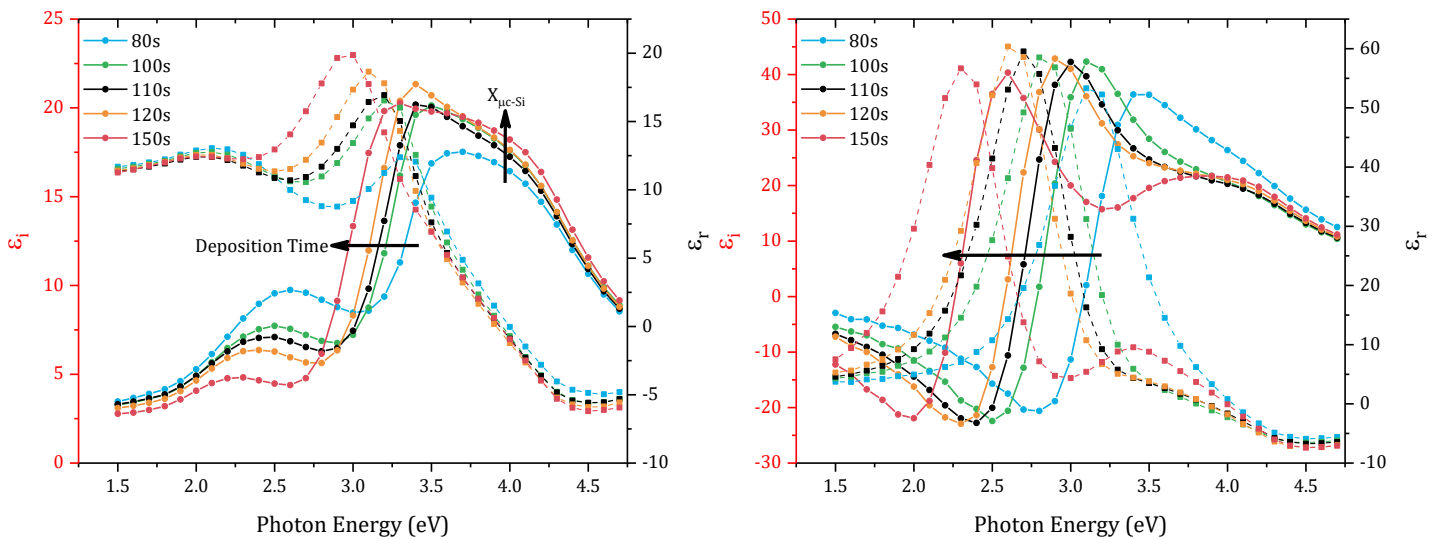


Figure IV.2-4 Pseudodielectric function of $\mu\text{-Si:H}$ (n^+) layer by varying the deposition time, on IN/IN DSP substrate on the left and on quartz-glass substrate on the right. ϵ_i in circle dots and solid lines and ϵ_r in square dots and dashed lines.

Figure IV.2-4 presents the measured pseudodielectric functions for a deposition time from 80 s to 150 s. When the deposition time increases, we observed a shift of the real part to the left and an increase of the $X_{\mu\text{-Si}}$. In order to form a thin (from 40 to 55 nm) tunnel recombination junction, the objective was to obtain highly conductive layers from 20 to 25 nm each. We extracted the layers thicknesses and the microcrystalline phase fraction percentages from SE measurements for each deposition time, the results are shown in **Figure IV.2-5**. As expected looking at the pseudodielectric functions, the thickness and the $X_{\mu\text{-Si}}$ of the $\mu\text{-Si:H}$ (n^+) increase with the deposition time. Therefore, we then used a deposition time of 100 s to have the highest $X_{\mu\text{-Si}}$ (greater than 50 % according to the SE fitted curves) for a layer thinner than 25 nm. Then, we fixed the deposition time at 100 s and varied the R_N gas flow ratio. We observed that the $X_{\mu\text{-Si}}$ decreases if R_N increases but does not increase if R_N decreases. Thus, we fixed $R_N = 1$ because it seemed to be the best agreement in terms of $X_{\mu\text{-Si}}$ and conductivity.

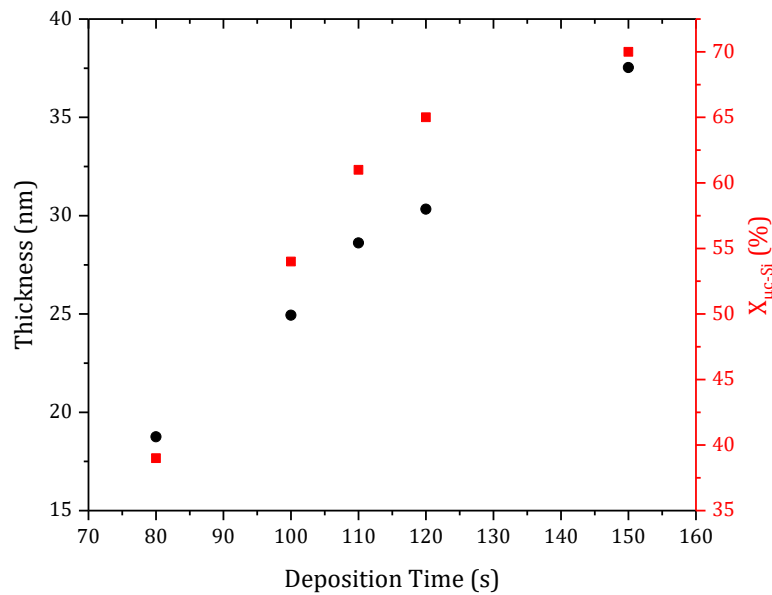


Figure IV.2-5 Thickness and $X_{\mu\text{c-Si}}$ extracted from the fitted pseudodielectric function curves for the $\mu\text{c-Si:H}$ (n^+) layer, according to the deposition time.

To further characterise this $\mu\text{c-Si:H}$ (n^+) layer, we then deposited the layer (with the parameters presented in **Table IV.2-2**) on a known poly-Si (p^+) layer and performed electrochemical capacitance-voltage measurements (ECV). We chose to do this on a poly-Si (p^+) layer because this type of measurement did not work on IN/IN DSP substrate and we assumed that even if the growth of the layer can be different, the doping profile should be very similar. We obtained active dopants concentration between 2.10^{20} and 4.10^{20} at/cm^3 throughout the layer thickness, which is high enough to have a degenerated material and build a tunnel junction [166].

Moreover, R_{sheet} measured with four-terminal sensing on quartz-glass samples were very reproducible and resulted in lateral conductivity around 10 S/cm. This conductivity is high for thin silicon layers and altogether low enough to avoid shunt problems in the future tandem device ([13], [167]).

In order to build the tunnel junction, we did similar experiments with a P-type layer deposited on top of the previously developed $\mu\text{c-Si:H}$ (n^+) layer. We used the same R_P ratio and a R_P gas flow ratio fixed at 1, defined in equation (IV. 2-3), with SiH_4 and B_2H_6 the gas flow rates in sccm.

$$R_P = \frac{B_2H_6}{SiH_4} \quad (\text{IV. 2-3})$$

We observed that R_{sheet} of $\mu\text{c-Si:H}$ (p^+) layers on quartz-glass substrate were high and very variable from sample to sample, sometimes not measurable. Thus, we increased R_P from 1 to 1.2 in order to increase the active dopant concentration and decrease the R_{sheet} . The obtained results were much more promising, with more homogeneous R_{sheet} around 400 $\text{k}\Omega/\square$. By increasing again R_P , the $X_{\mu\text{c-Si}}$ started decreasing. Thus, we fixed R_P at 1.2 and varied the deposition time of this P-type layer to obtain a NP junction about 50 nm thick.

$\mu\text{c-Si:H}$ Layer	R	R_N or R_P	Deposition Time
N-type	0.0025	1	100 s
P-type	0.0025	1.2	80 s

Table IV.2-2 Gas flow ratios and deposition times of the developed $\mu\text{c-Si:H}$ layers.

Figure IV.2-6 shows the measured pseudodielectric functions of the NP junction for a deposition time of the $\mu\text{-Si:H}$ (p^+) layer from 50 s to 80 s and **Figure IV.2-7** presents the corresponding thickness and $X_{\mu\text{-Si}}$. The extracted $X_{\mu\text{-Si}}$ seems strongly dependent of the layers thickness, as for the N-type layer, this is discussed in the following part (IV.2.2). Therefore, we chose to use a deposition time of 80 s for the P-type layer on polished substrate, for the rest of this work. This results in a PN junction with a thickness of 50 ± 5 (roughness) nm with a $X_{\mu\text{-Si}}$ exceeding 70% on IN/IN DSP substrates.

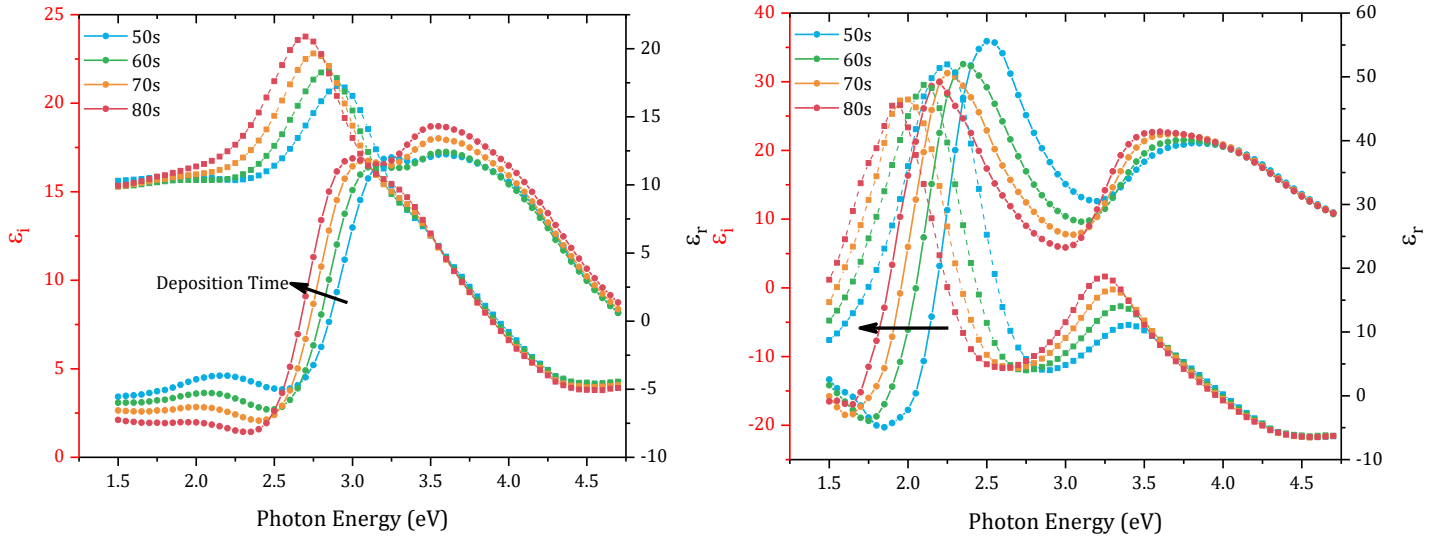


Figure IV.2-6 Pseudodielectric function of the $\mu\text{-Si:H}$ (n^+)/ $\mu\text{-Si:H}$ (p^+) junction by varying the deposition time of the $\mu\text{-Si:H}$ (p^+) layer, on IN/IN DSP substrate on the left and on quartz-glass substrate on the right. ϵ_1 in circle dots and solid lines and ϵ_2 in square dots and dashed lines.

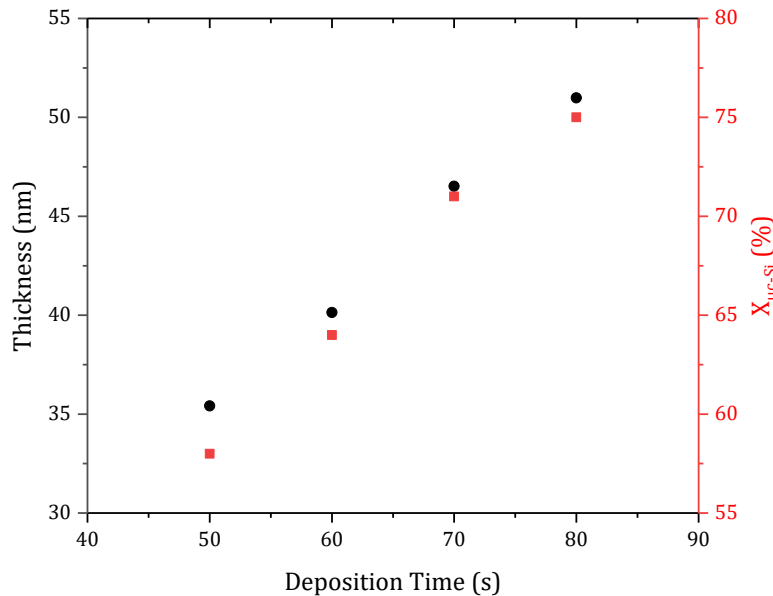


Figure IV.2-7 Thickness and $X_{\mu\text{-Si}}$ extracted from the fitted pseudodielectric function curves for the $\mu\text{-Si:H}$ (n^+)/ $\mu\text{-Si:H}$ (p^+) junction, according to the deposition time of the $\mu\text{-Si:H}$ (p^+) layer.

IV.2.2. Growth and Microcrystalline Phase

In order to further investigate the developed $\mu\text{-Si:H}$ layers, we performed Raman spectroscopy measurements (III.2.3) to confirm the percentage of microcrystalline phase obtained by SE (III.2.1). **Figure IV.2-8** demonstrates that the $X_{\mu\text{-Si}}$ extracted by Raman spectroscopy and SE are consistent, especially for the layers on quartz-glass substrates (a), b) and c)). In fact, the differences observed between the two techniques are mainly explained by the fact that SE probes the entire stack, no matter its thickness, contrary to Raman spectroscopy. Moreover, the $X_{\mu\text{-Si}}$ obtained by SE does not include the rough surface of the layers, neither the amorphous layers below. Thus, the $X_{\mu\text{-Si}}$ measured by Raman spectroscopy with the 325 nm laser ($\delta p \approx 8$ nm) is almost the same for the P-type layer and the n^+/p^+ stack, because only the front P-type layer is measured. However, for the samples measured with the 442 nm laser ($\delta p \approx 50$ nm), the obtained results are different, which shows that they are dependent of the laser penetration depth. This explains why the $X_{\mu\text{-Si}}$ is lower than with SE for samples on IN/IN DSP substrates. In fact, with the $\mu\text{-Si:H}$ (n^+/p^+) junction (n^+/p^+ in the **Figure IV.2-8**), the laser penetrates to the a-Si:H layers and for the layers n^+ and p^+ the laser penetrates to the c-Si bulk.

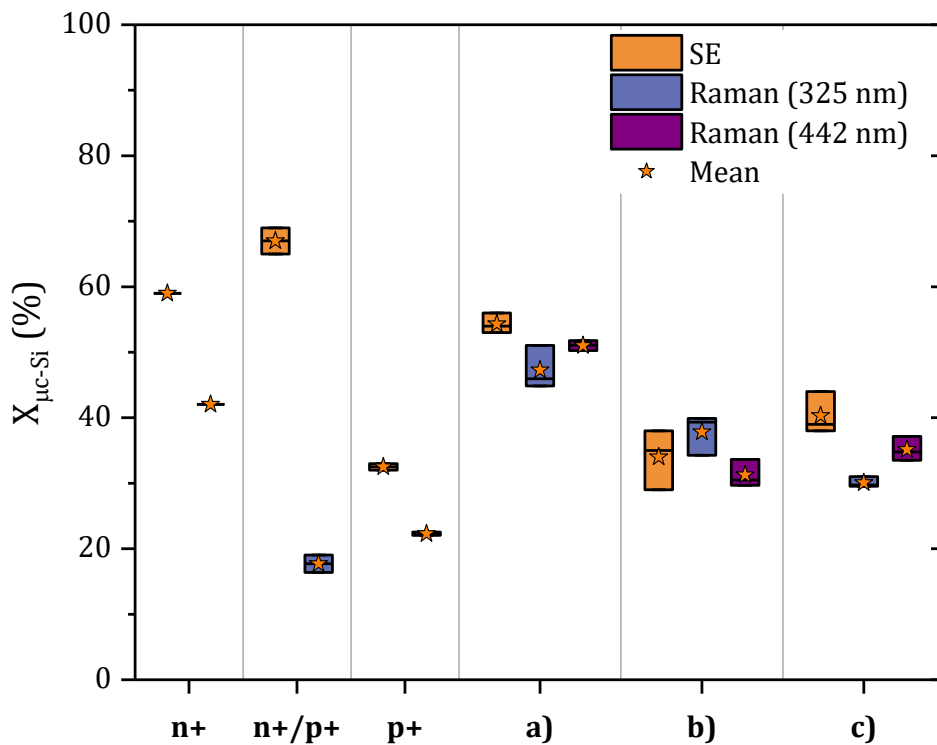


Figure IV.2-8 Percentage of microcrystalline phase obtained by SE and Raman spectroscopy for $\mu\text{-Si:H}$ (n^+), $\mu\text{-Si:H}$ (n^+/p^+) and $\mu\text{-Si:H}$ (p^+) on IN/IN DSP substrates (respectively n^+ , n^+/p^+ and p^+) and on quartz-glass substrates (respectively a), b) and c)).

Figure IV.2-9 shows the measured Raman spectra on quartz-glass substrates (III.2.3). With the 442 nm laser $\delta p \approx 50$ nm (on the left), the curves (three for each type of sample) of the same layers overlap, this demonstrates a good deposition uniformity. With the 325 nm laser $\delta p \approx 8$ nm, (on the right), the curves are also very similar for the same layers but there are some differences due to the roughness of the surface and the surface degradation of the layers (oxidation, scratching...).

We previously mentioned that the growth of a microcrystalline silicon layer is different on quartz-glass and on amorphous silicon (IN/IN DSP substrates). This is also observable in **Figure IV.2-8** because on a-Si:H layers the $X_{\mu\text{-Si}}$ increases with the thickness whereas

this is not always the case on quartz-glass. This is explained by the fact that the $\mu\text{-Si:H}$ layer, while growing, interacts with the surface of the substrate, especially if it is an a-Si:H layer ([126], [168]). Interactions with the plasma at the substrates surface, during the deposition process, change the incubation and nucleation of the $\mu\text{-Si:H}$ layers. Moreover, the a-Si:H are also modified, especially the a-Si:H (n) which acts as the incubation layer for the $\mu\text{-Si:H}$ layers growth. However, we think that the hydrogen flux is too high for the deposition on quartz-glass, which leads to a $X_{\mu\text{-Si}}$ limited by the bombardment during the deposition process at steady-state. Thus, the $X_{\mu\text{-Si}}$ does not increase with the thickness, unlike the IN/IN DSP substrates, which do not seem to be affected.

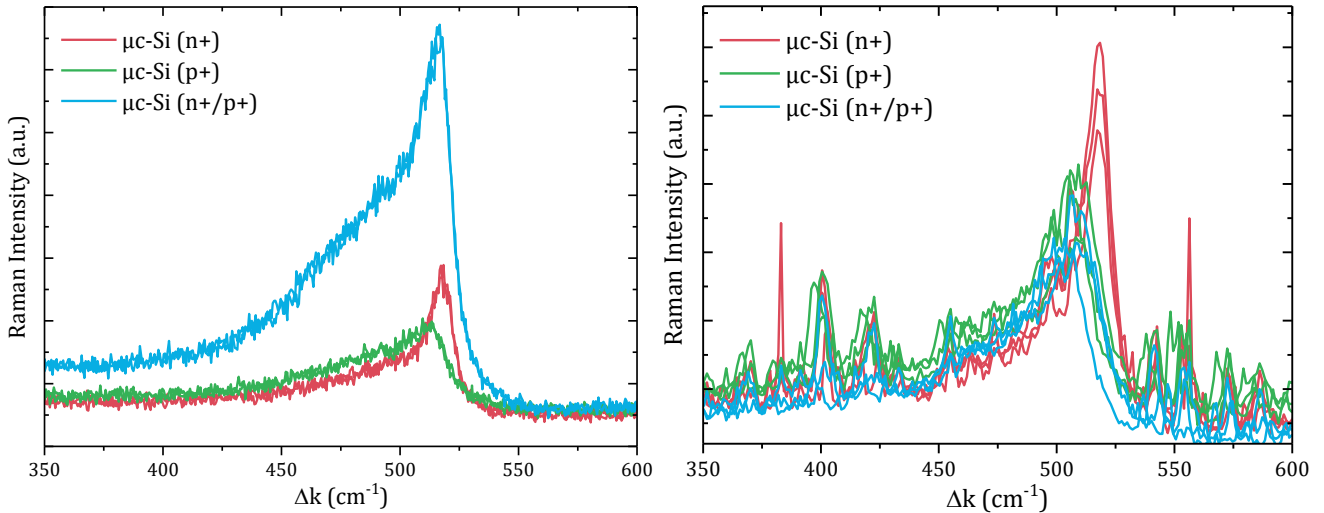


Figure IV.2-9 Raman spectrum of the microcrystalline silicon layers deposited on quartz-glass substrates. With a 442 nm laser on the left ($\delta p \approx 50$ nm) and a 325 nm laser on the right ($\delta p \approx 8$ nm).

Figure IV.2-10 is a STEM image (III.2.8.b) of the developed $\mu\text{-Si:H}$ (n⁺/p⁺) junction (covered by a thin ITO) on an IN/IN DSP substrate. The thickness of the junction is well consistent with the SE measurements. Moreover, this seems to confirm that the a-Si:H (n) layer really acts as an incubation layer. In fact, it is difficult to distinguish the a-Si:H (n) layer from the $\mu\text{-Si:H}$ (n⁺) layer as the nucleation of the microcrystallites starts above the a-Si:H (i) layer (see **Figure IV.2-11**).

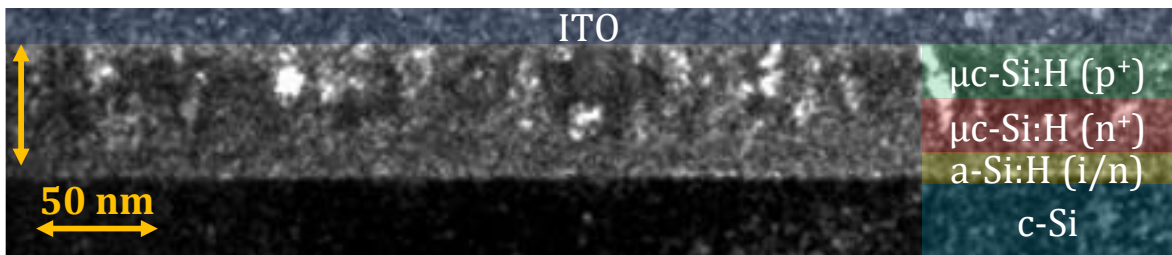


Figure IV.2-10 STEM image of the $\mu\text{-Si:H}$ (n⁺/p⁺) junction on a IN/IN DSP substrate.

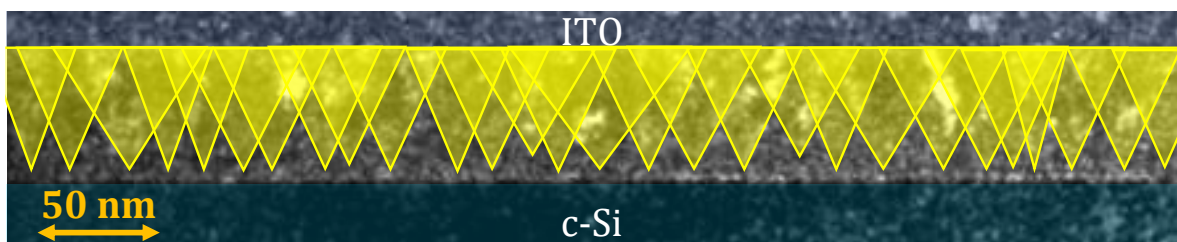


Figure IV.2-11 STEM image of the $\mu\text{-Si:H}$ (n⁺/p⁺) junction on a IN/IN DSP substrate with a drawing of the microcrystallites (without distinction of the crystalline planes).

IV.2.3. Microcrystalline Silicon layers properties

In the previous parts, we developed microcrystalline silicon layers to form a highly doped tunnel junction in Perovskite/SHJ tandem solar cells and validated the following requirements (see part II.4):

- Thin layers: PN junction between 45 and 55 nm (SE and STEM),
- High concentration of localised states due to high hydrogen content,
- $X_{\mu\text{-Si}}$ which permits high vertical conductivity, and lateral conductivity not high enough to cause shunt issues in a tandem device,
- Active dopant concentration in the order of 10^{20} at/cm².

Furthermore, we also performed Hall Effect measurements (III.2.5) on the samples on quartz-glass substrates (Figure IV.2-1 a), b) and c)) to confirm the σ values obtained with four-terminal sensing measurements. As the layers are thin, we needed to confirm that the R_{sheet} values were not impacted by a possible degradation (penetration/flattening) of the layers by the probes. For each measured layer, the same R_{sheet} and σ were obtained with Hall Effect measurements. Thus, the four-terminal sensing method is well adapted to quickly characterise the $\mu\text{-Si:H}$ layers on quartz-glass. Figure IV.2-12 shows all the obtained values during this work (for around 30 samples in each cases). The R_{sheet} values are uniform for the N-type layer and the PN junction, which leads to average lateral conductivities of 12.5 S/cm and 7.7 S/cm respectively. For the P-type layer, the R_{sheet} values are more variable but the lateral conductivities are between 0.25 and 3 S/cm, which is very high for a P-type thin silicon layer. Finally, the developed $\mu\text{-Si:H}$ layers have σ values more than four orders of magnitude higher than doped amorphous silicon used in SHJ cells [169]. Overall, we observe a very good reproducibility of the quartz-glass reference samples (also with SE measurements).

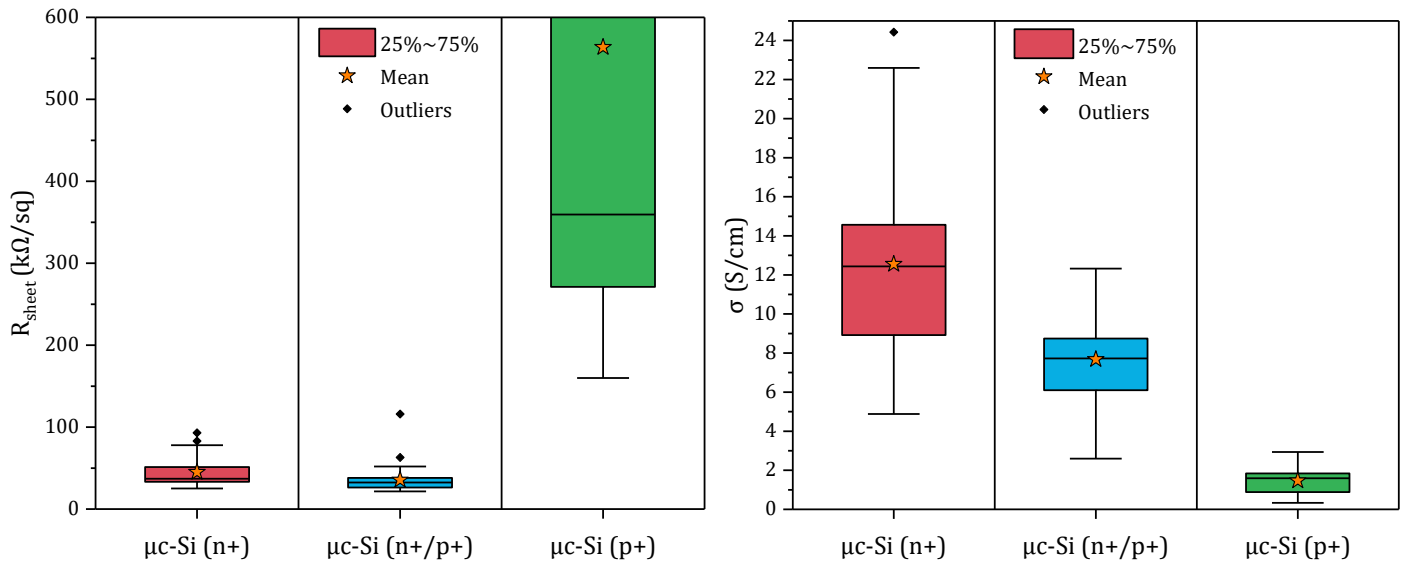


Figure IV.2-12 R_{sheet} and lateral conductivity obtained in this work with four-terminal sensing measurements on quartz-glass reference substrates (35 deposition processes for $\mu\text{-Si:H (n+)}$, 29 for $\mu\text{-Si:H (p+)}$ and 32 for the PN junction).

The activation energy of the developed layers was measured with the method described in part III.2.6. The calculated values are presented in Table IV.2-3, they are very low compared to a-Si:H layers ([118]), which should improve the charge carriers conduction and thus enhance the recombination in the $\mu\text{-Si:H (n+/p+)}$ junction. This should also

reduce the barriers at the interface with the other layers and thus reduce the contact resistivity ([117], [118], [170]).

Layer	$\mu\text{-Si:H (n}^+)$	$\mu\text{-Si:H (p}^+)$
E_a (meV)	26 ± 1	30 ± 1

Table IV.2-3 E_a of the developed microcrystalline silicon layers.

Moreover, we obtained the absorptance of the developed layers with spectrophotometry measurements (III.2.2), Figure IV.2-13. The layers are almost fully transparent between 800 nm and 1200 nm ($\mathcal{A} < 2\%$). Thus, the absorption in the SHJ bottom-cell is very little impacted in the tandem configuration.

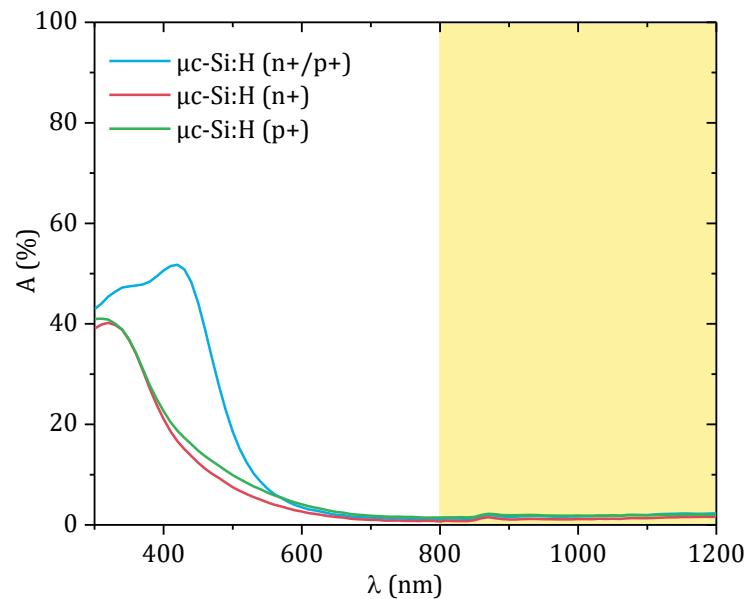


Figure IV.2-13 Absorptance of the developed microcrystalline silicon layers.

IV.3. Integration of Microcrystalline Silicon on SHJ Solar Cells

In this part, the developed $\mu\text{-Si:H}$ layers are integrated in SHJ devices and their impact is discussed to confirm their suitability for integration in PK/SHJ tandem solar cells.

IV.3.1. Bulk Passivation Improvement

Before integrating the developed junction in a tandem device, it remains to verify that it has no negative impact on the SHJ bottom-cell.

First, we performed minority carrier lifetime measurements (III.3.1) after the PECVD process, on M2 textured precursors (Figure IV.2-1 f) and g)), after the layers development. Figure IV.3-1 and Table IV.3-1 demonstrate an improvement of the passivation for symmetric precursors (IN/IN) with the addition of the $\mu\text{-Si:H}$ layers. In fact, the lifetime is more than doubled with the $\mu\text{-Si:H (n}^+/\text{p}^+)$ junction. We believe that this improvement is induced by the high level of hydrogen during the deposition, which penetrates in the a-Si:H layers and passivates silicon dangling bonds (see Figure II.2-3). Moreover, the high conductivity of the $\mu\text{-Si:H}$ layers compared to a-Si:H layers increases the field effect.

For the SHJ precursors (IN/IP), the addition of the $\mu\text{-Si:H}$ layers is a bit beneficial but less observable. In fact, the gain cannot be as high as with IN/IN precursors because of

the limitation induced by the rear emitter (P-type a-Si:H layer). However, we observed an implied V_{oc} improvement.

Samples	iV_{oc} (mV)	Lifetime at $10^{15} \Delta n$ cm^{-3} (μs)	iFF (%)
IN/IN M2	/	1790	81.2
IN/IN M2 + μc -Si:H (n^+)	/	3720	83.9
IN/IN M2 + μc -Si:H (n^+/p^+)	/	4240	84.4
IN/IP M2	732	1630	84.3
IN/IP M2 + μc -Si:H (n^+)	735	1940	84.6
IN/IP M2 + μc -Si:H (n^+/p^+)	735	1880	84.5

Table IV.3-1 Minority carrier lifetime at $10^{15} \Delta n \text{ cm}^{-3}$ and corresponding iV_{oc} and iFF.

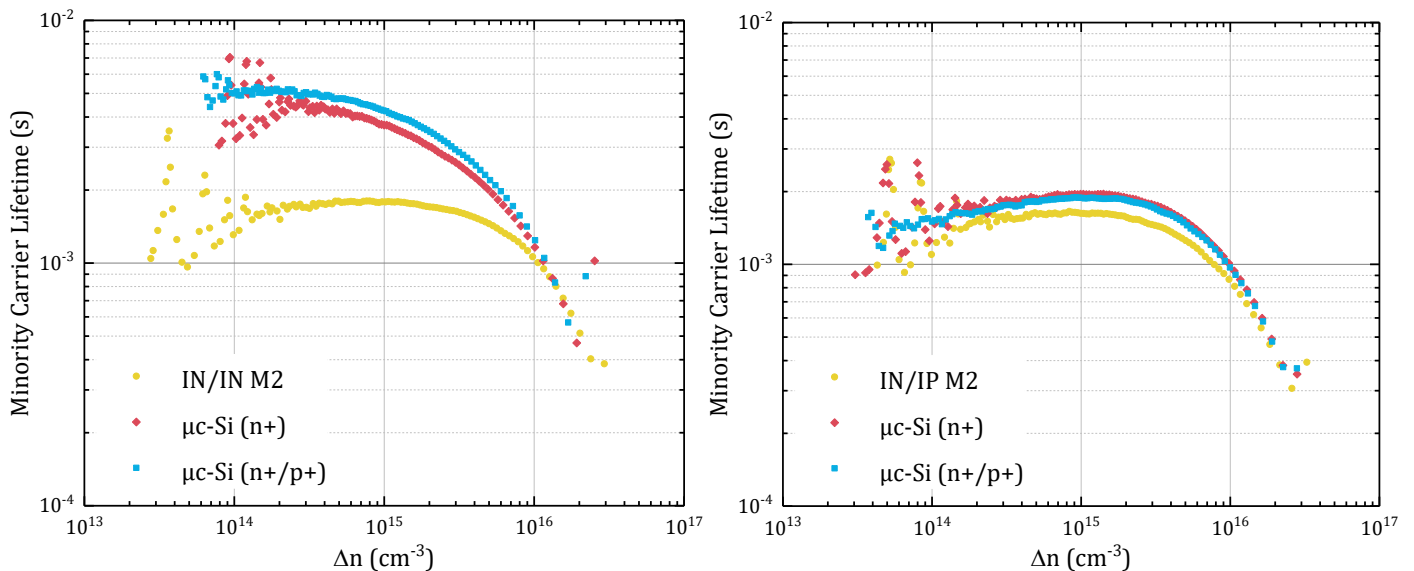


Figure IV.3-1 Minority carrier lifetimes of M2 textured precursors (IN/IN M2 on the left and IN/IP M2 on the right). Precursors in yellow dots, with μc -Si:H (n^+) on the top in red and with the PN junction on the top in blue.

Figure IV.3-2 shows all the minority carrier lifetimes measured during this work. This confirms what we observed in Figure IV.3-1 and Table IV.3-1. In fact, it is not very observable on Figure IV.3-2, but for each experiment done during this work the μc -Si:H layers deposition increases the minority carrier lifetime. This increase is all the more important if the minority carrier lifetime of the precursor is not very high. Thus, the hydrogen diffusion heals the precursors. Furthermore, we also observed that the lifetime improvement is stable over time. Indeed, after one month under nitrogen, the minority carrier lifetime of the samples remains the same.

Finally, by using a PECVD process at low temperature, the deposition process of μc -Si:H layers did not degrade the SHJ precursors. Moreover, the bulk passivation is improved by the high hydrogen content and not degraded by the μc -Si:H layers growth. Thus, this confirms that the a-Si:H (i) layer are not negatively affected by the μc -Si:H layers growth and only the a-Si:H (n) layer acts as an incubation layer. In conclusion, adding the microcrystalline silicon tunnel junction tends to improve the precursors by a better chemical passivation and increased field effect.

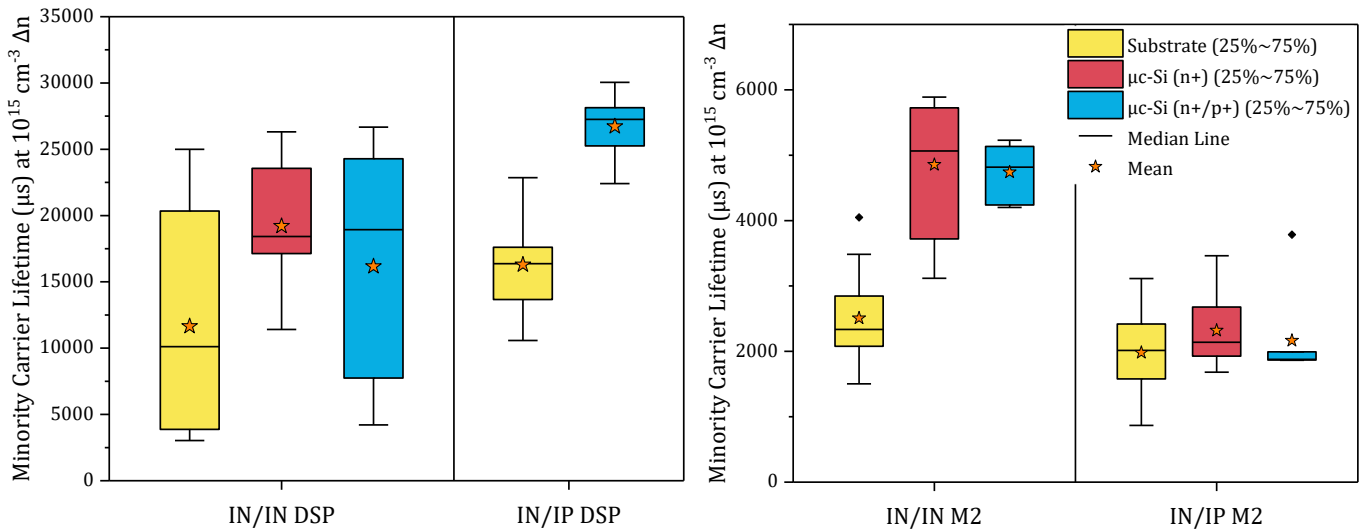


Figure IV.3-2 Minority carrier lifetimes at $10^{15} \Delta n \text{ cm}^{-3}$ measured during all of this work on several precursors.

IV.3.2. Rear Emitter SHJ Solar Cells with Front-side N-Type Microcrystalline Silicon

In order to verify the previous conclusion, we made two batches of ten SHJ solar cells, one classical rear emitter (*REF* batch, see **Figure II.2-2 c**) and one with the N-type $\mu\text{c-Si:H}$ layer on top of the amorphous one ($\mu\text{c-Si:H}$ (n^+) batch). The two batches endured exactly the same fabrication and characterisation processes, except the $\mu\text{c-Si:H}$ (n^+) layer deposition for the $\mu\text{c-Si:H}$ (n^+) batch. Post-PECVD, minority carrier lifetime measurements, presented **Table IV.3-2**, show better average implied parameters ($i\text{FF}$ and iV_{oc}) and an increased lifetime for the $\mu\text{c-Si:H}$ (n^+) batch. This validates an improvement of the passivation, with the addition of the $\mu\text{c-Si:H}$ (n^+) layer.

Batch	iV_{oc} (mV)	Lifetime at $10^{15} \Delta n \text{ cm}^{-3}$ (μs)	$i\text{FF}$ (%)
<i>REF</i>	732.9 ± 1.4	2600 ± 370	84.09 ± 0.35
$\mu\text{c-Si:H}$ (n^+)	733.8 ± 1.4	2900 ± 340	84.19 ± 0.35

Table IV.3-2 Average minority carrier lifetime at $10^{15} \Delta n \text{ cm}^{-3}$ and corresponding iV_{oc} and $i\text{FF}$ for both solar cells batches.

Then, both solar cell batches were measured in the same conditions (AM1.5G standard conditions) with a J-V tester of the CEA-INES pilot-line (**III.3.4.a**). In **Figure IV.3-3**, we observe no significant difference between the two batches in term of V_{oc} . In fact, the best V_{oc} are in the *REF* batch but the worst too and the average V_{oc} are equal for the two batches. However, there is a non-negligible but expected loss in current by the addition of the $\mu\text{c-Si:H}$ (n^+) layer due to parasitic absorption in the visible range (see **Figure IV.2-13**). Therefore, the current loss of 1.2 mA/cm^2 induces an average loss in efficiency of 0.5% presented in **Figure IV.3-4**. In order to confirm that this loss in J_{sc} only occurs in the visible range, we performed spectral response measurements (**III.3.3**), the measured EQE are shown in **Figure IV.3-5**. We observed that the loss occurs between 300 and 700 nm and that there is no visible difference between the batches after 800 nm. In conclusion, this current loss is not a problem in PK/SHJ tandem solar cells application because the Perovskite top-cell fully absorbs in the visible range.

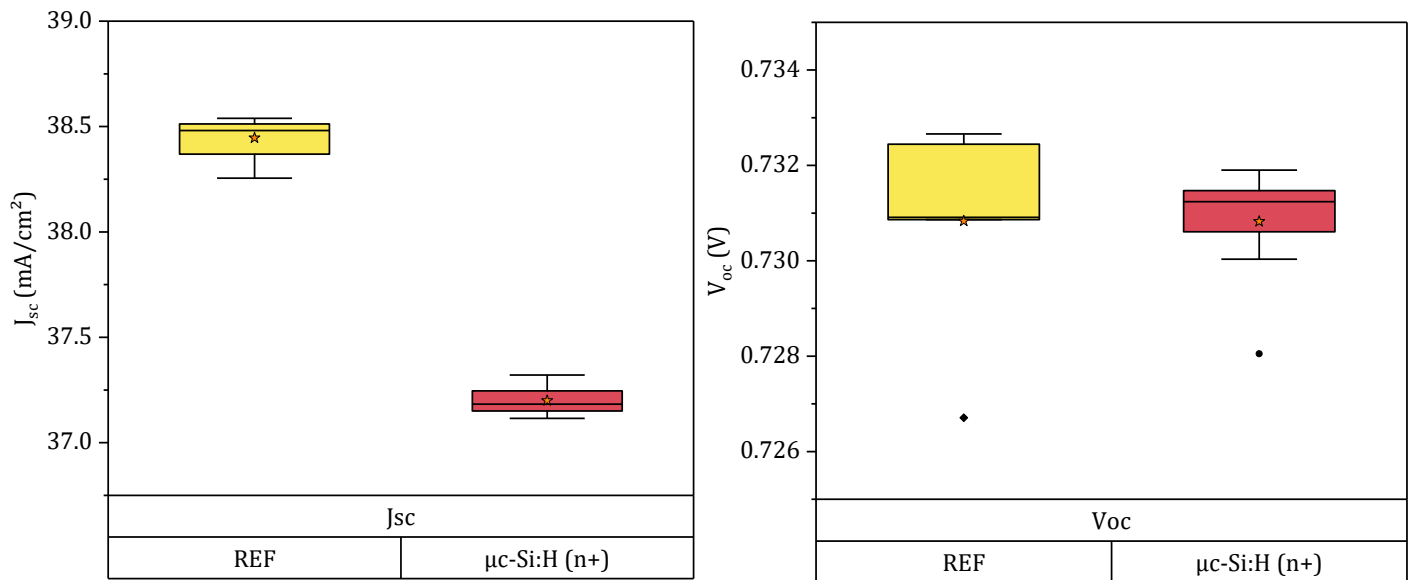


Figure IV.3-3 J_{sc} (on the left) and V_{oc} (on the right) extracted from I-V measurements of total cell area.

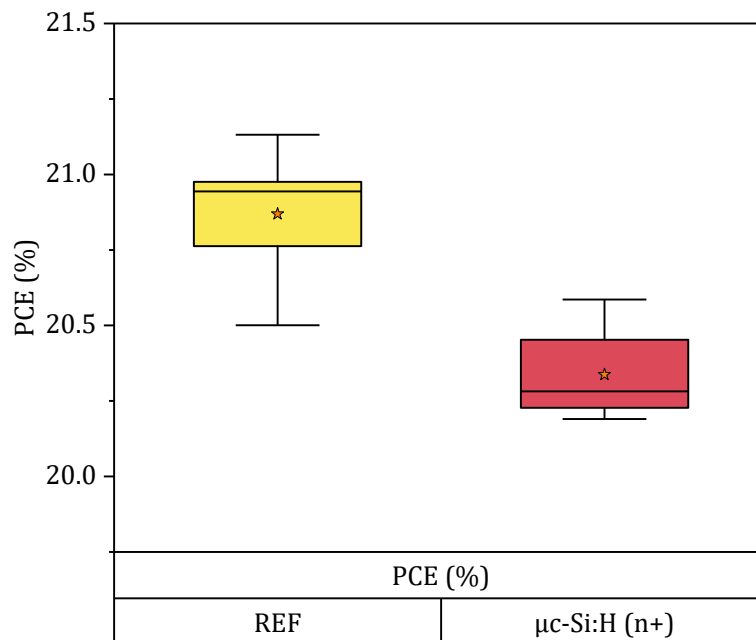


Figure IV.3-4 PCE extracted from I-V measurements of total cell area.

Figure IV.3-6 presents the pFF and FF of the solar cells and the R_s calculated with the method presented part III.3.2. Better FF are obtained for the $\mu\text{c-Si:H (n+)}$ batch, more than 0.5% in average. In fact, this is explained by the better passivation but also by lower series resistance. This also tends to prove that the addition of the $\mu\text{c-Si:H (n+)}$ layer reduces the contact resistivity with the other layers. For example, the contact with the ITO, as G. Nogay *et al.* already observed [46]. Moreover, some other experiments were done with the same type of batches, varying the front-side TCO, and the same results were observed. No matter what front TCO is used, the FF is improved and the R_s decreased with the $\mu\text{c-Si:H (n+)}$ on the a-Si:H (n) one.

Finally, we confirmed that adding a $\mu\text{c-Si:H (n+)}$ layer on top of SHJ solar cells do not induce undesirable effect, except a current loss in the visible range, which is not an issue for tandem application.

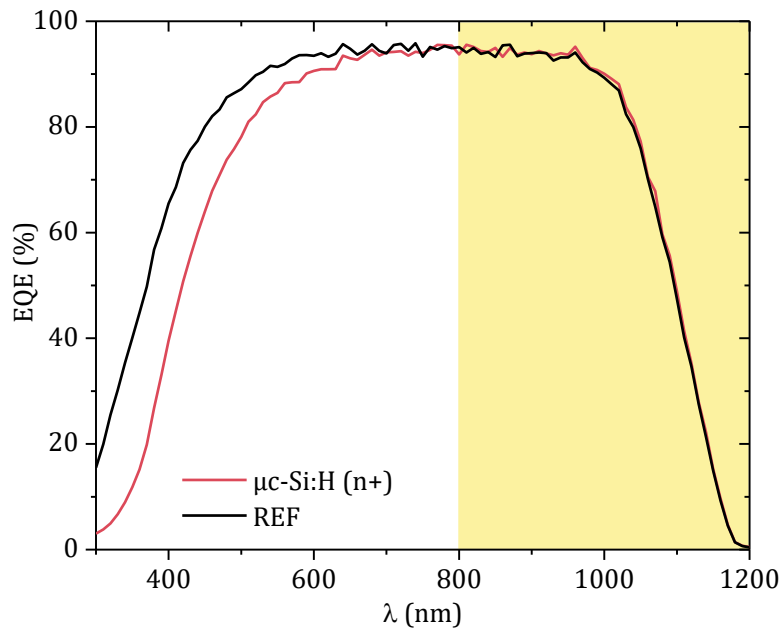


Figure IV.3-5 EQE of the best cells of each batch.

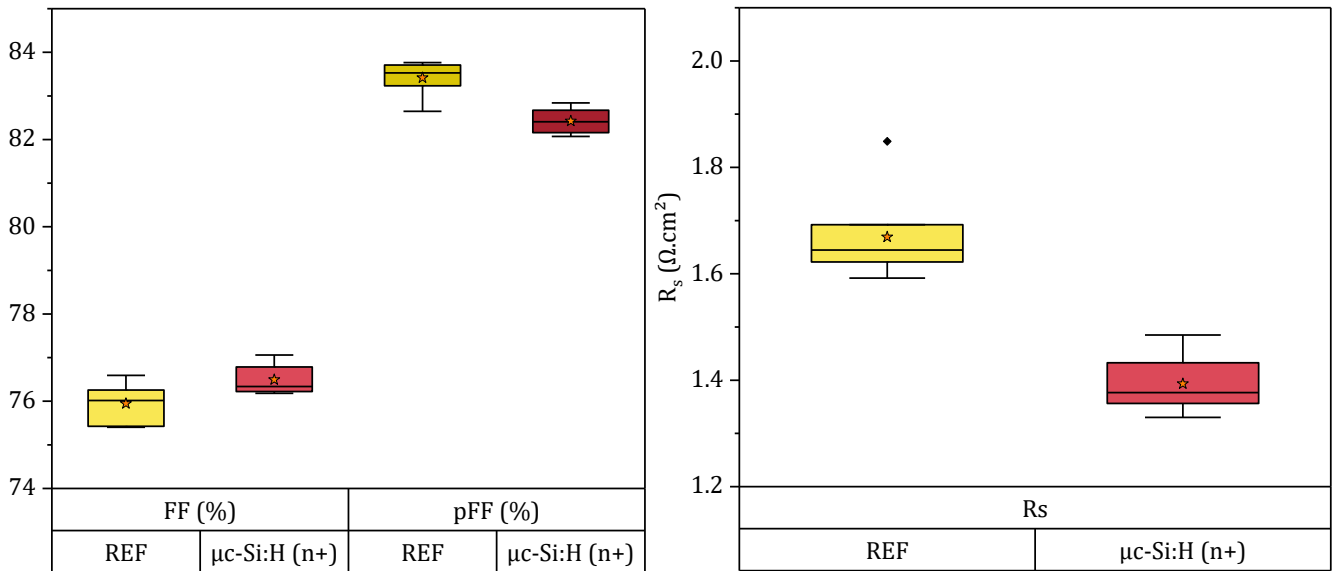


Figure IV.3-6 FF extracted from I-V measurements of total cell area and pFF obtained with Suns- V_{oc} measurements on the left. Calculated R_s of the solar cells on the right.

IV.3.3. Standard Emitter SHJ Solar Cells with Back-side Microcrystalline Silicon Tunnel Junction

In the previous part, we demonstrated that the $\mu\text{c-Si:H (n}^+)$ layer does not have a negative impact on the SHJ bottom-cell. In this part, we made standard emitter SHJ solar cells with the addition of the developed $\mu\text{c-Si:H}$ layers at the back-side of the devices. The goal of this study is to investigate the influence of the $\mu\text{c-Si:H}$ layers without the current loss. In fact, we want to verify that the full PN junction does not induce additional R_s and does not result in I-V curves with an S-shape. In fact, an S-shape can be observed if there is an accumulation of the charge carriers at the junction, for example.

Figure IV.3-7 shows the three types of SHJ solar cells in this study. As they are standard emitter solar cells, the front ITO is deposited with edge exclusion to avoid shunts.

Moreover, the thicknesses of the amorphous layers were optimised for the rear emitter configuration and were not adapted for standard emitter solar cells. Thus, the J_{sc} are lower than in the previous part (IV.3.2).

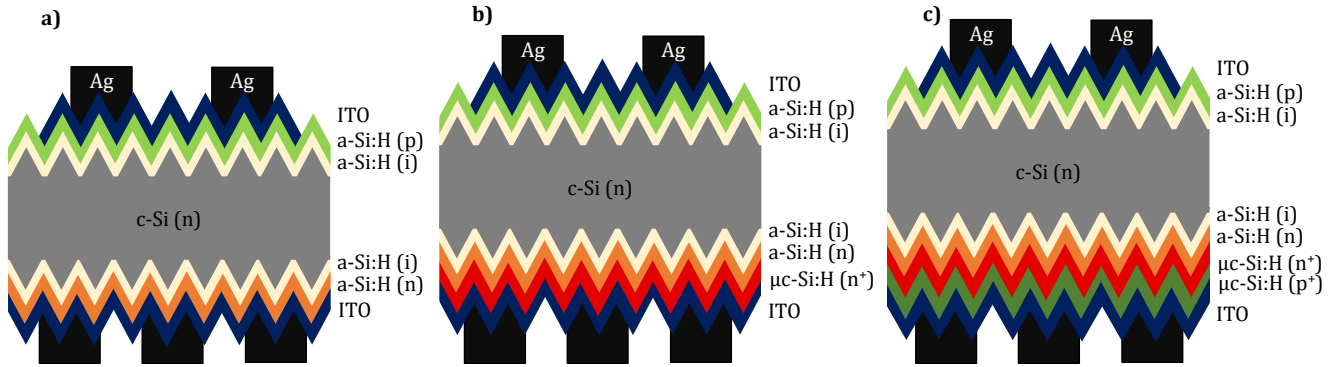


Figure IV.3-7 a) Standard emitter SHJ solar cells as references; b) Standard emitter SHJ solar cells with the $\mu\text{c-Si:H (n}^+)$ layer at the back-side; c) Standard emitter SHJ solar cells with the $\mu\text{c-Si:H (n}^+/\text{p}^+)$ junction at the back-side.

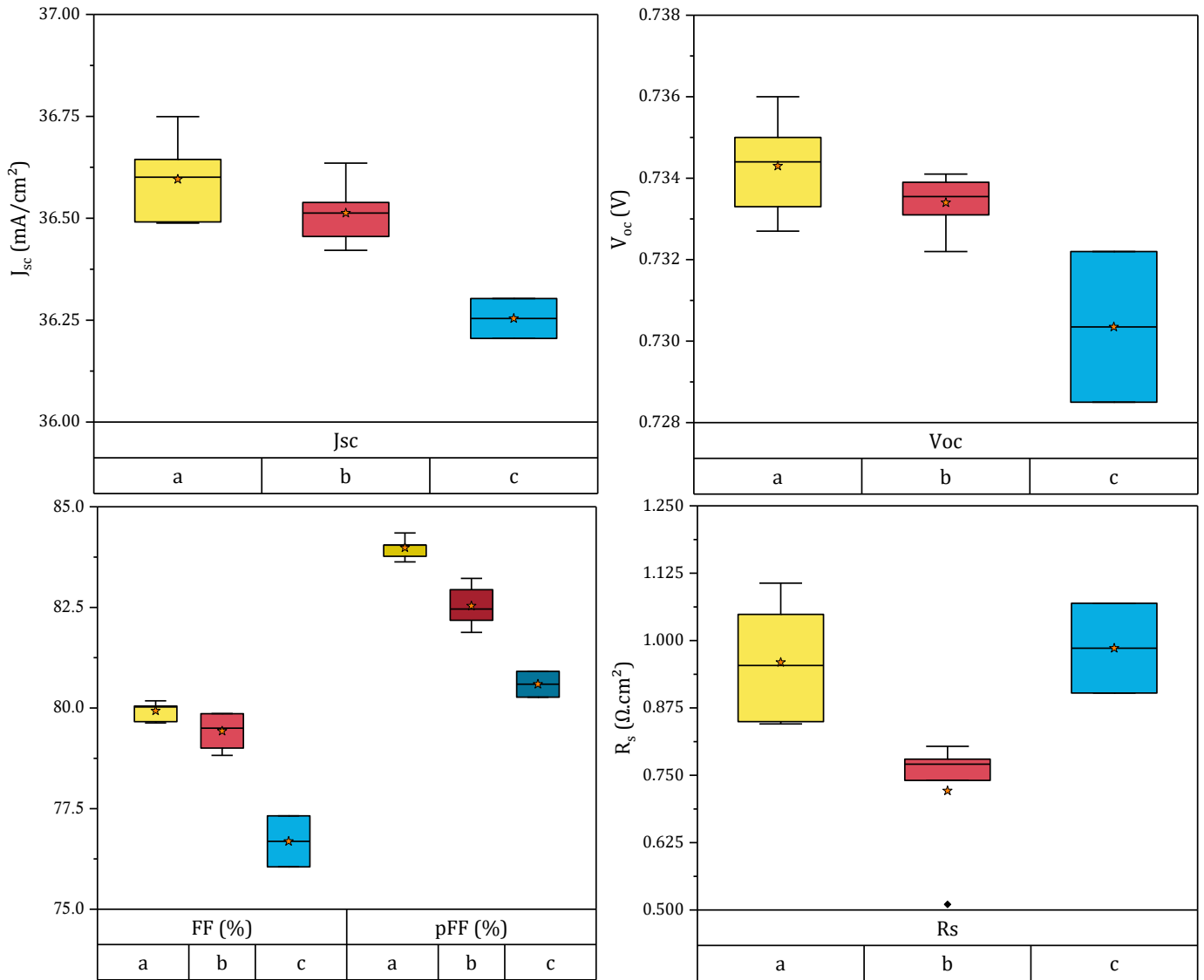


Figure IV.3-8 J_{sc} , V_{oc} and FF extracted from I-V measurements of total cell area, pFF obtained with Suns- V_{oc} measurements and calculated R_s of the solar cells.

Unlike the batches of the previous part, the three batches of this study (a, b and c, respectively for the devices **a)**, **b)** and **c)** of **Figure IV.3-7)** did not endure exactly the same fabrication and characterisation processes. In fact, the reference solar cells, a, were less exposed to the air than the batches b and c. This could explain why the reference batch is a little better than the batch b, contrary to the previous experiments. However, **Figure IV.3-8)** demonstrates that the series resistances are really lower for the batch b.

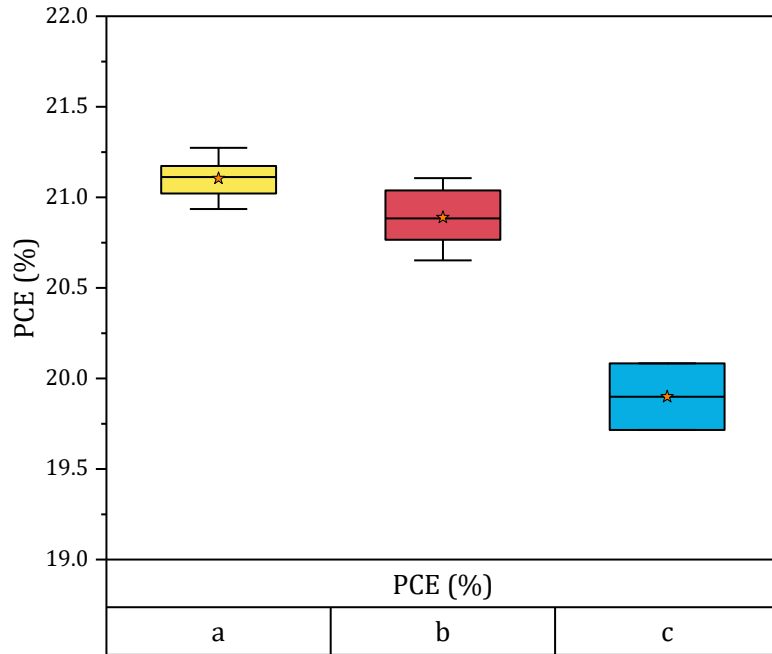


Figure IV.3-9 PCE extracted from I-V measurements of total cell area.

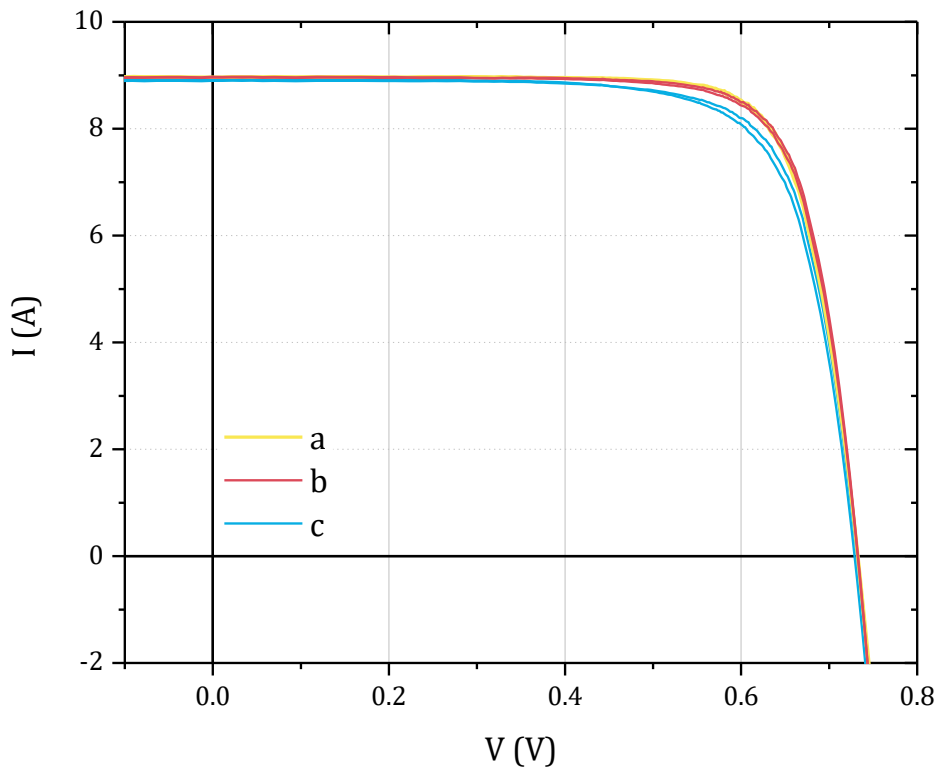


Figure IV.3-10 Measured I-V curves of the three batches.

Nevertheless, in **Figure IV.3-8)** and **Figure IV.3-9)**, the batch c with the $\mu\text{c-Si:H}$ (n^+/p^+) junction performed worse than the two other batches. Yet, the series resistances are

nearly the same for the batch a and c, which confirms that the $\mu\text{-Si:H (n}^+/\text{p}^+)$ junction does not induce additional high R_s . Moreover, the I-V parameters obtained for the batch c are impacted by the P-type layer in the electron contact, especially by the $\mu\text{-Si:H (p}^+)/\text{ITO}$ interface. In fact, in the batch c, the electron contact is composed of a NPN junction, which induces transport mechanisms much more complex than the classical electron contact in SHJ solar cells, this is discussed in more details in part V.3. Finally, in the PK/SHJ tandem configuration (**Figure IV.1-1**), the $\mu\text{-Si:H (n}^+/\text{p}^+)$ junction is not in direct contact with an ITO layer thus such issues should not be observed.

Figure IV.3-10 shows several I-V curves of the three batches. For the batch c, the curves have an usual shape, as the other batches, no S-shape is observed, which is very promising for the tandem application [171]. In conclusion, the developed microcrystalline silicon tunnel junction seems well optimised to be used as the recombination junction in Perovskite/SHJ tandem solar cells.

IV.4. Chapter Conclusion

In this chapter IV, we have developed a $\mu\text{-Si:H (n}^+/\text{p}^+)$ junction in order to use it as a highly doped tunnel junction allowing the charge carriers to recombine in a tandem solar cell. This junction is integrated on top of a SHJ solar cell, for monolithic tandem applications. We characterised the microcrystalline silicon layers and validated that they have the requirements to form an efficient tunnel recombination junction. On top of that, we observed an increase of minority carrier lifetime which demonstrates that the $\mu\text{-Si:H}$ layers improve the SHJ solar cells chemical passivation and field effect. Moreover, the $\mu\text{-Si:H (n}^+/\text{p}^+)$ junction is nearly transparent in the IR range, which therefore little affects the absorption of the SHJ bottom-cell in the tandem configuration. Finally, we made SHJ solar cells with the addition of the $\mu\text{-Si:H (n}^+/\text{p}^+)$ junction and observed that no additional R_s is created and that the I-V curves do not show an S-shape.

To conclude, the developed $\mu\text{-Si:H (n}^+/\text{p}^+)$ junction has all the structural, optical and electrical requirements to fulfil its role of recombination junction. In the next chapters, we discuss further possible electrical characterisations on recombination junction to compare this $\mu\text{-Si:H (n}^+/\text{p}^+)$ junction with other possible choices. Moreover, we investigate the influence of this $\mu\text{-Si:H (n}^+/\text{p}^+)$ junction on the Perovskite top-cell before integrating it into a complete Perovskite/SHJ tandem solar cell.

V. WAYS TO CHARACTERISE RECOMBINATION JUNCTIONS FOR PEROVSKITE ON SILICON TANDEM SOLAR CELLS

In chapter [IV](#), we presented the development of a highly doped microcrystalline silicon PN junction, a relevant candidate for a recombination junction in Perovskite/SHJ tandem solar cells. The $\mu\text{c-Si:H}$ developed layers were characterised with several methods and we concluded that they fulfil the requirements to form a highly doped tunnel junction (see part [II.4.1](#)). In this chapter, we investigate the electrical performance of such a junction. To this end, we discuss and set up electrical characterisation methods for recombination junctions, in order to optimise and compare several recombination junctions before their implementation in tandem solar cells.

V.1. Introduction

In the previous chapter IV, we developed a highly doped tunnel junction with microcrystalline silicon layers. Moreover, we added this junction to the electron contact of SHJ solar cells to study its impact on the bottom-cell, as it had already been presented in the literature [171]–[173]. In part II.4.1, we explained that highly doped tunnel junctions are very similar to tunnel diodes and can be assimilated as tunnel diodes for electrical measurements. In this chapter, in order to have more insights into recombination mechanisms, we propose and discuss several ways to characterise the developed $\mu\text{-Si:H}$ (n^+/p^+) junction and other RJ, by assimilating them to tunnel diodes.

Highly doped tunnel junctions for multi-junction solar cells have been characterised several times in the literature. For example, usual GaAs based tunnel junctions were often isolated on a substrate with electrodes at front and back-sides to obtain characteristic I-V curves of tunnel diodes (**Figure II.4-1**) [174]–[176]. Sometimes, other samples with electrodes only at the front, for lateral I-V measurements, were used, but the principle remains the same [177]. Similarly, such test-structures were used for diffusion doped silicon tunnel junctions [173], [178]–[180] as for silicon tunnel diodes [181]. **Figure V.1-1** shows the test-structures conventionally used to perform I-V measurements on tunnel junctions.

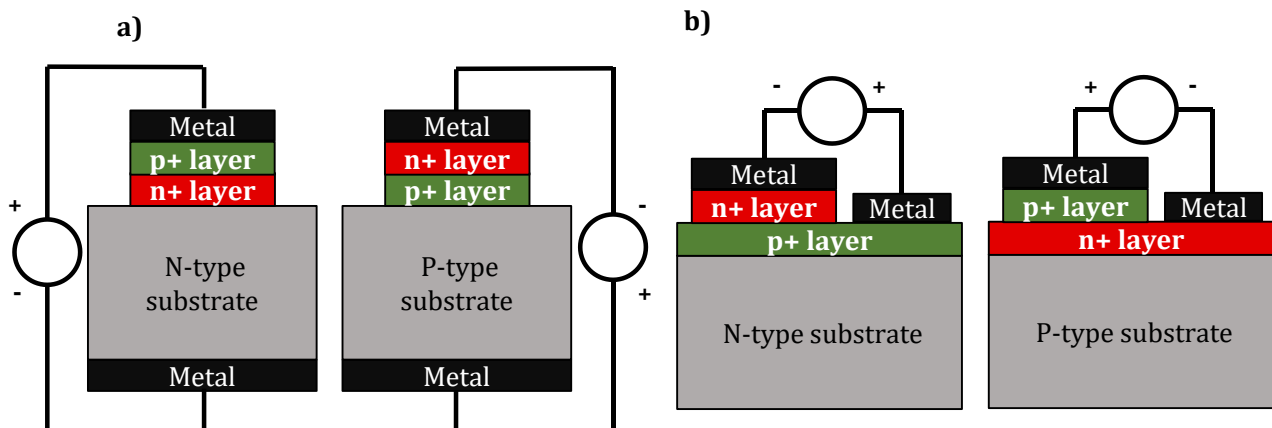


Figure V.1-1 Usual test-structures used to characterise highly doped tunnel junctions and tunnel diodes. **a)** For transversal I-V measurements and **b)** for lateral I-V measurements.

In our case, the aim is to define a test-structure where the tunnel junction can be as close as in the tandem solar cell, as did G. J. Bauhuis *et al.* and J. Kim *et al.* [182], [183]. Thus, to achieve the same layer growth, we have to keep the same substrate as in the final device, and also the subjacent a-Si:H layers.

In literature, some groups also performed electrical simulations of the tunnel junctions, for example M. Baudrit *et al.* [175], [184], and obtained good agreement with experimental measurements. However, in this work, we did not perform electrical simulations. The main reason is that the used materials for recombination junction in Perovskite/SHJ tandem solar cells are dependent on the substrate and it is hard to describe them in details for electrical simulations. Thus, electrical measurements seemed more appropriate for this kind of materials (microcrystalline silicon, TCO, TMO, organic HTM/ETM...) than simulations.

The main objective of this chapter is to develop electrical characterisation methods for the recombination junctions in Perovskite/SHJ tandem solar cells. These methods should

be easier to implement than the full tandem solar cells fabrication and measurements and, at the same time, be representative of the final device behaviour.

V.2. Tunnel Recombination Junction as Tunnel Diode

In this part, we propose several test-structures to characterise the microcrystalline silicon tunnel junction, presented in the previous chapter IV, with dark I-V measurements.

V.2.1. Test-Structures for Tunnel Junctions Measurements

The objective of this part is to define useful test-structures to characterise electrically the developed tunnel junction (see chapter IV) and other highly doped tunnel junctions for PK/SHJ tandem cells. As explained previously, we want to characterise the tunnel junctions as close as they are in the tandem solar cells.

First, we have to keep the substrate and the layers preceding the junction, namely, a-Si:H (i)/a-Si:H (n). Secondly, we look for test-structures simpler than the tandem solar cell itself, in order to isolate the tunnel junctions from other solar cell behaviour. Therefore, test-structures for transversal I-V measurements seem much easier to set up than those for lateral I-V measurements (**Figure V.1-1 b**).

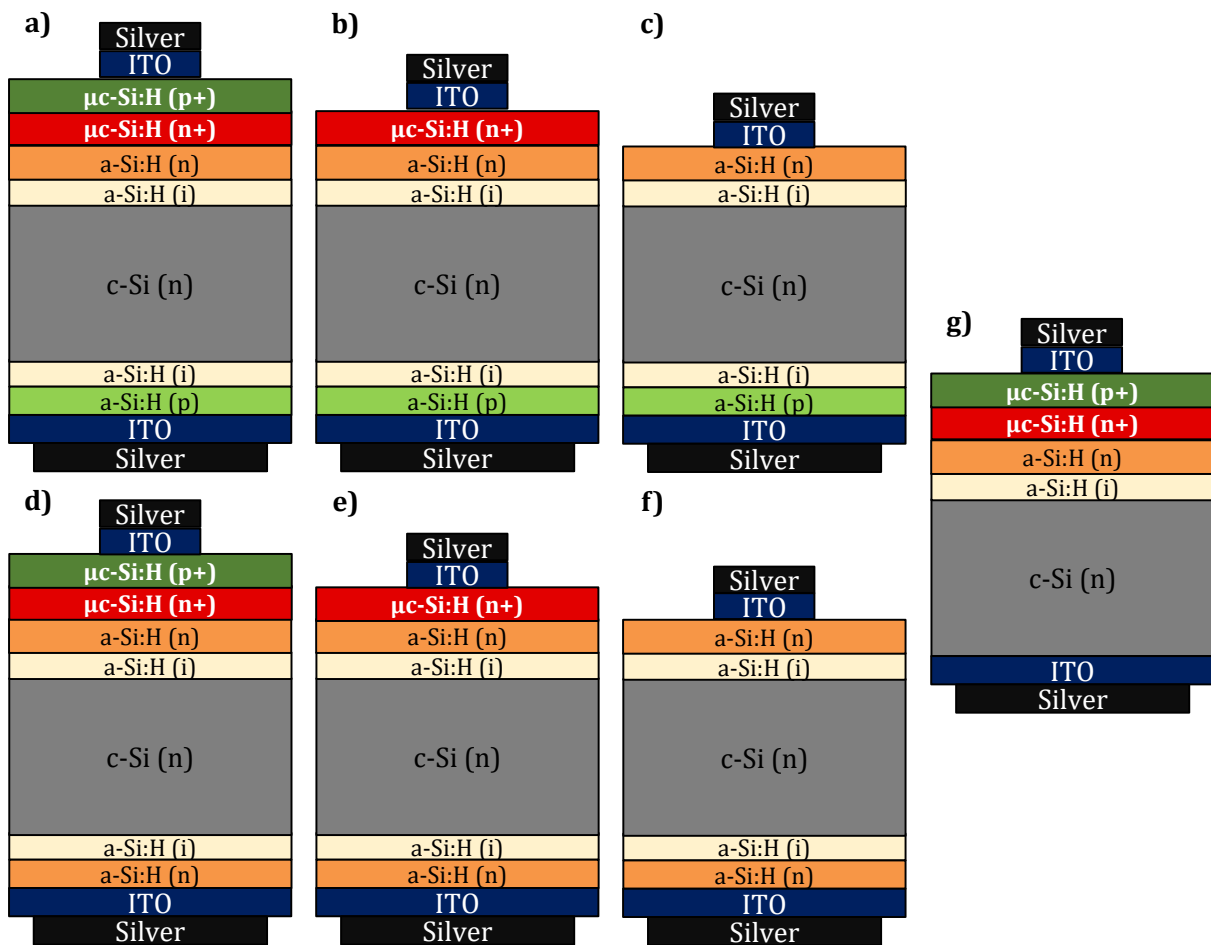


Figure V.2-1 Test-structures proposed in this part for transversal dark I-V measurements.

Taking into account all these considerations and the available equipment and methods (see chapter III), we defined the test-structures presented in **Figure V.2-1**.

These test-structures are composed of the usual SHJ solar cell materials, as the amorphous layers and the ITO/Silver electrodes with the addition of the layers composing the tunnel junction ($\mu\text{c-Si:H}$ in our case). **Table V.2-1** presents the main objective of each test-structure.

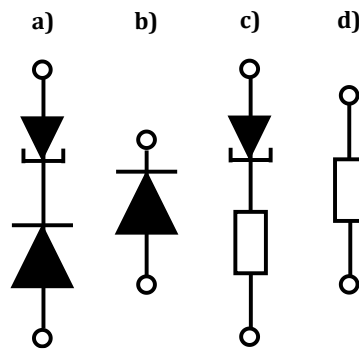


Figure V.2-2 Simplified circuit diagrams for the proposed test-structures.

Test-Structure	Remarks	Objective	Simplified Circuit Diagram
Figure V.2-1 a)	SHJ solar cell with the tunnel junction	To investigate the impact of the tunnel junction on the SHJ cell (see IV.3)	Figure V.2-2 a)
Figure V.2-1 b)	SHJ solar cell with the N-type layer of the tunnel junction	To compare to structure a) : to investigate the impact of the P-type layer (additional R_s ?)	Figure V.2-2 b)
Figure V.2-1 c)	SHJ solar cell	Reference for a) and b) structures	Figure V.2-2 b)
Figure V.2-1 d)	Figure V.2-1 f) with the tunnel junction on the front-side	Alternative to structure g) to measure the I-V curve of the tunnel junction	Figure V.2-2 c)
Figure V.2-1 e)	Isotype with the N-type layer of the tunnel junction	To compare this isotype structure with structure d) (second reference)	Figure V.2-2 d)
Figure V.2-1 f)	Symmetrical and isotype	Reference for d) and e) structures	Figure V.2-2 d)
Figure V.2-1 g)	Tunnel junction on the substrate	To measure the I-V curve of the tunnel junction	Figure V.2-2 c)

Table V.2-1 Definition, objectives and simplified circuit diagrams of the proposed test-structures.

First, we made structures **a)**, **d)** and **g)** in their “SHJ devices version”, that is to say on commercial N-type CZ, fully textured, M2 size wafers, with industrial screen-printing metallisation (III.1.4.c). These devices were then measured in light and in dark with the J-V tester of the CEA-INES pilot-line. For structure **a)** (**Figure V.2-1**), the obtained results are similar to those presented in the parts IV.3.2 and IV.3.3. A current loss is observed because of the junction on the front-side but the V_{oc} and the FF remain in the order of

magnitude of SHJ solar cells. Moreover, possible shunt problems or S-shape are not observed, neither in light nor in dark I-V measurements. Furthermore, the R_s remains negligible (less than $1.5 \Omega \cdot \text{cm}^2$) for the tandem application.

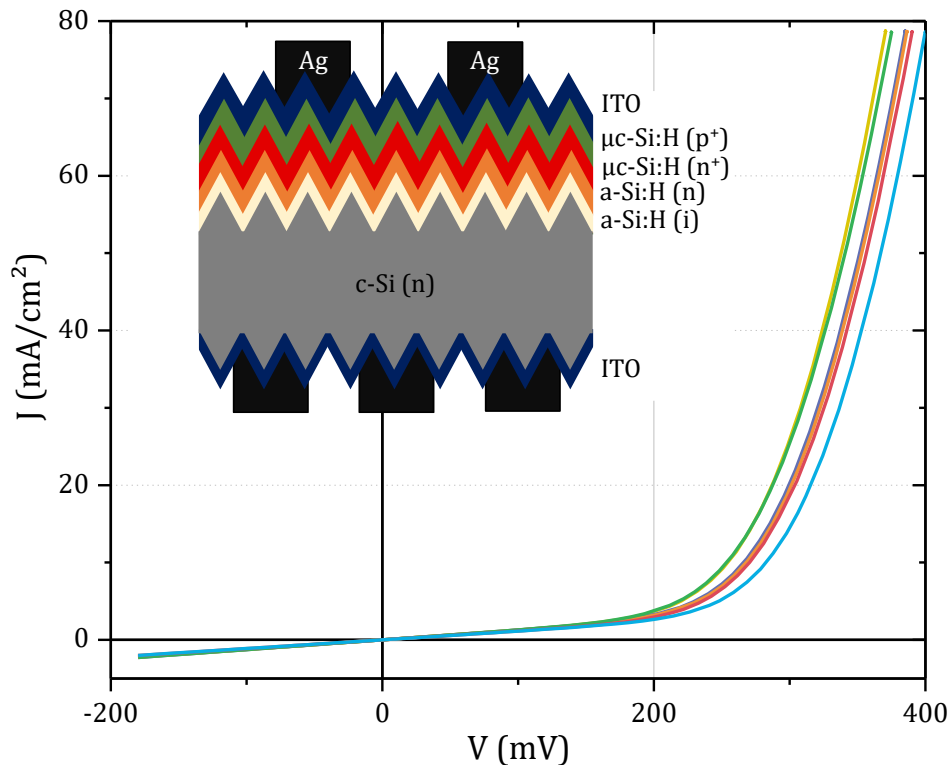


Figure V.2-3 J-V curves measured in the dark and structure of the “SHJ devices version” of test-structure **g**) (6 devices).

Figure V.2-3 shows the measured dark J-V curves of the test-structures composed of the $\mu\text{c-Si:H}$ (n^+/p^+) tunnel junction on the substrate (test-structure **g**). We observed a diode behaviour with shunt issues, in contrast with test-structures **a**). By fitting the J-V curves with the two-diode model (see **Figure I.1-2**, part **I.1**), we obtained R_{shunt} under $500 \text{ Ohm} \cdot \text{cm}^2$ for all samples, despite the edge exclusion. However, series resistances are all less than $1 \text{ Ohm} \cdot \text{cm}^2$, which is positive but these values may have been reduced due to the large shunts. Thus, obtained R_s are not necessarily representative of those of test-structure **g**) (**Figure V.2-1**). A diode behaviour was expected, considering the studied structure, but we did not observe a tunnel diode behaviour as we were looking for. This could be explained by the device size (M2) and texturing (possible inhomogeneities across the surface), the shunt issues and especially the back-side of the structures (forming a hole contact).

Figure V.2-4 presents the “SHJ devices version” of test-structure **d**) (**Figure V.2-1**) and the corresponding dark J-V curves. We observed a resistance behaviour, $R_s = 0.95 \pm 0.02 \text{ Ohm} \cdot \text{cm}^2$, with high current at low voltage (the current limit of the equipment is reached around 75 mV). These measurements tend to prove that the diode behaviour observed in **Figure V.2-3** are not due to the $\mu\text{c-Si:H}$ (n^+/p^+) tunnel junction but rather to the back-side (c-Si (n)/ITO) of the structure which acts as a hole contact. Moreover, the J-V curves measured for test-structures **d**) are consistent with the addition of a tunnel diode and a resistance (see **Figure V.2-2 c**) at low voltage bias. However, the rapidly reached current limit does not allow us to observe a negative resistance region (see **Figure II.4-1**). In conclusion, test-structure **d**) seems more adapted to observe the tunnel effect than test-structure **g**).

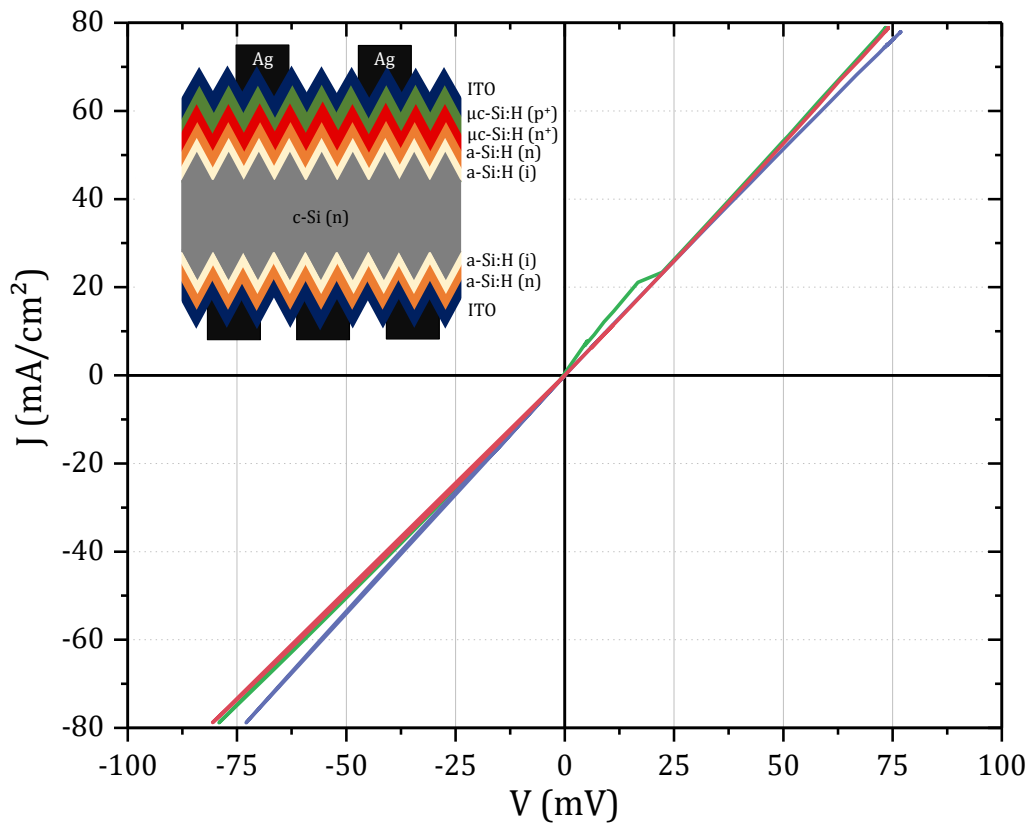


Figure V.2-4 J-V curves measured in the dark and structure of the “SHJ devices version” of test-structure d) (3 devices).

Secondly, in order to reduce the measured current and to observe the structures behaviour over a larger voltage range, we made smaller test-structures (Figure V.2-5).

- 1 • Substrate cleaning (see part III.1.1)
- 2 • aSi:H layers deposition in the PECVD industrial tool (see part III.1.2.a)
• μcSi:H layers deposition in the PECVD development tool (see part III.1.2.b)
- 3 • Substrate cutting (in 5 x 5 cm²) (see part III.1.5)
- 4 • Back-side 100 nm TCO by PVD (*Jusung* tool, see part III.1.3) with edge exclusion
• Front-side 100 nm TCO by PVD (*Jusung* tool, see part III.1.3) masked to form circular electrodes
- 5 • Front-side silver deposition by evaporation (thermal or e-beam, see parts III.1.4.b and III.1.4.a) using the same mask pattern than for the PVD
• Back-side silver deposition by evaporation (thermal or e-beam, see parts III.1.4.b and III.1.4.a) with edge exclusion

Figure V.2-5 Fabrication steps of the small test-structures, regardless of the starting substrate.

Then, we performed dark I-V measurements in the cryostat tool, presented in part III.3.4.b. We assume that it is dark measurements because we did not use special light

but it is important to note that the samples are not totally in the dark, a weak ambient light can reach the cell. However, the ambient light influence should be negligible for our experiments.

I-V curves of small test-structures **g**) (Figure V.2-1), presented in Figure V.2-6, have a completely different behaviour than with the “SHJ device version” (Figure V.2-3). At low voltage bias, the curves are almost linear with a very huge R_s , around 450 Ohm.cm^2 . Unfortunately, due to bad contacts and the influence of the ITO layers (see part V.3 for more details), test-structure **g**) does not allow us to measure the $\mu\text{-Si:H (n}^+/\text{p}^+)$ tunnel junction. To do this, it seems to be necessary to contact directly the front ($\mu\text{-Si:H (p}^+)$ layer) and back-side (c-Si (n) substrate), with a metal stack providing a good Ohmic contact with low contact resistivity, without the ITO layers. This type of adapted contact should be made with metallisation stacks, such as Ti/Pd/Ag ([185]), but we did not have the possibility to deposit Ti nor Pd layers.

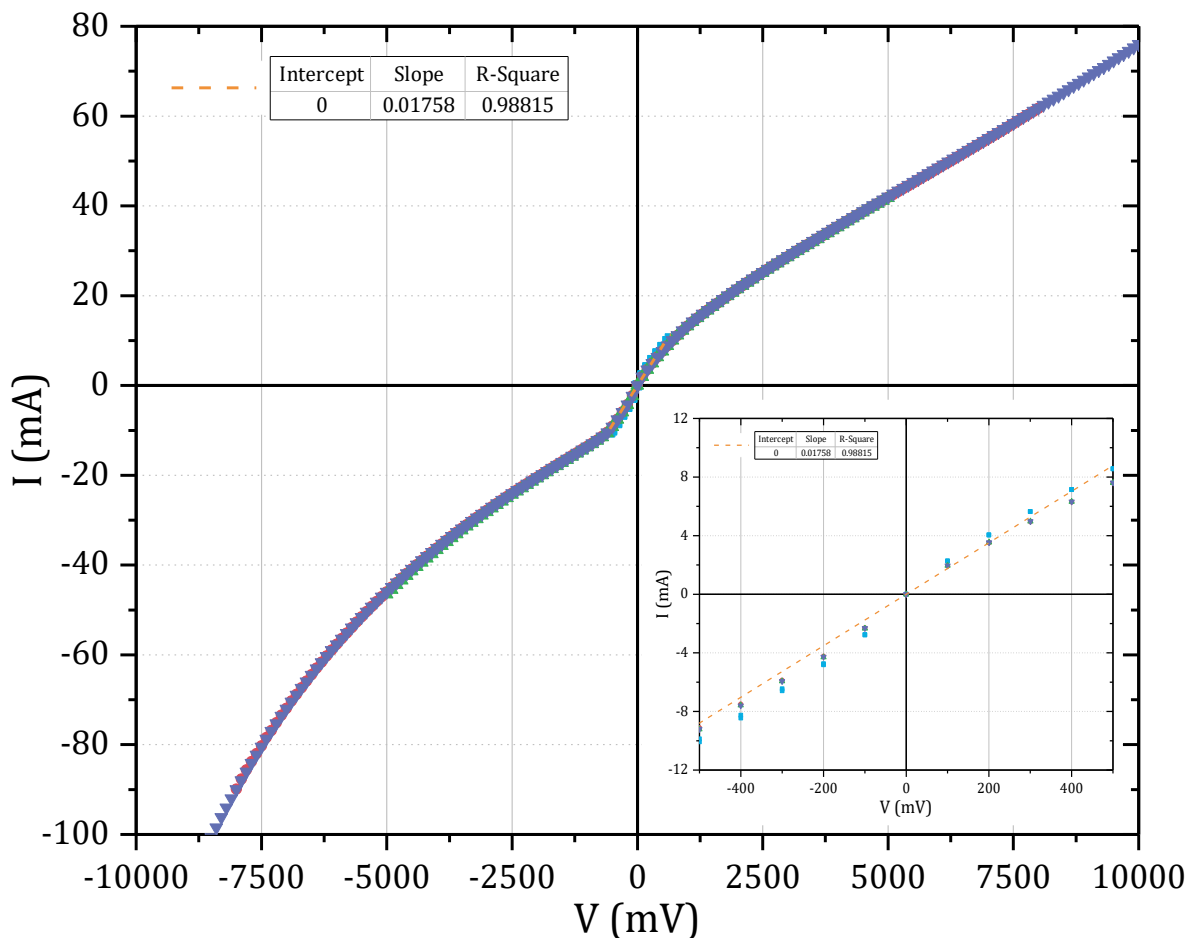


Figure V.2-6 I-V curves measured in the dark of double-side textured small test-structures **g**). The inset shows the curves at low voltage bias and the linear fitting curve.

Concerning small test-structures **a**), **b**) and **c**) (Figure V.2-1), based on SHJ solar cells, an expected diode behaviour is observed in Figure V.2-7, for all the structures. Moreover, shunt problems are also observed, despite edge exclusion. These shunts seem more important without the $\mu\text{-Si:H (p}^+)$ layer, which suggest that they are located on the front-side, the back-sides being identical. From 100 K to 200 K, test-structures **a**) and **c**) have very similar behaviour, with high R_s , contrary to test-structures **b**) which have a lower R_s . This difference is mainly explained by the contact with the front-side ITO. Indeed, at low temperature the contact $\mu\text{-Si:H (n}^+)/\text{ITO}$ is much better than the contacts $\mu\text{-Si:H (p}^+)/\text{ITO}$ and $\text{a-Si:H (n)}/\text{ITO}$ ([46], [186]). More generally, at all temperatures,

test-structures **b)** always present lower R_s than the other test-structures. At 250 K, test-structures **a)** have lower R_s than test-structures **c)**, but this trend is reversed by increasing the temperature. Thus, the main differences observed between test-structures **a)**, **b)** and **c)** are explained by the contact with the front-side ITO layer. Therefore, the $\mu\text{-Si:H (n}^+/\text{p}^+)$ tunnel junction influence seems negligible compared to the influence of the front-side ITO. These observations are positive concerning the developed tunnel junction but the test-structures did not allow us to characterise directly the tunnel junction. The influence of an ITO layer in the front-side electrode is discussed in the part **V.3**.

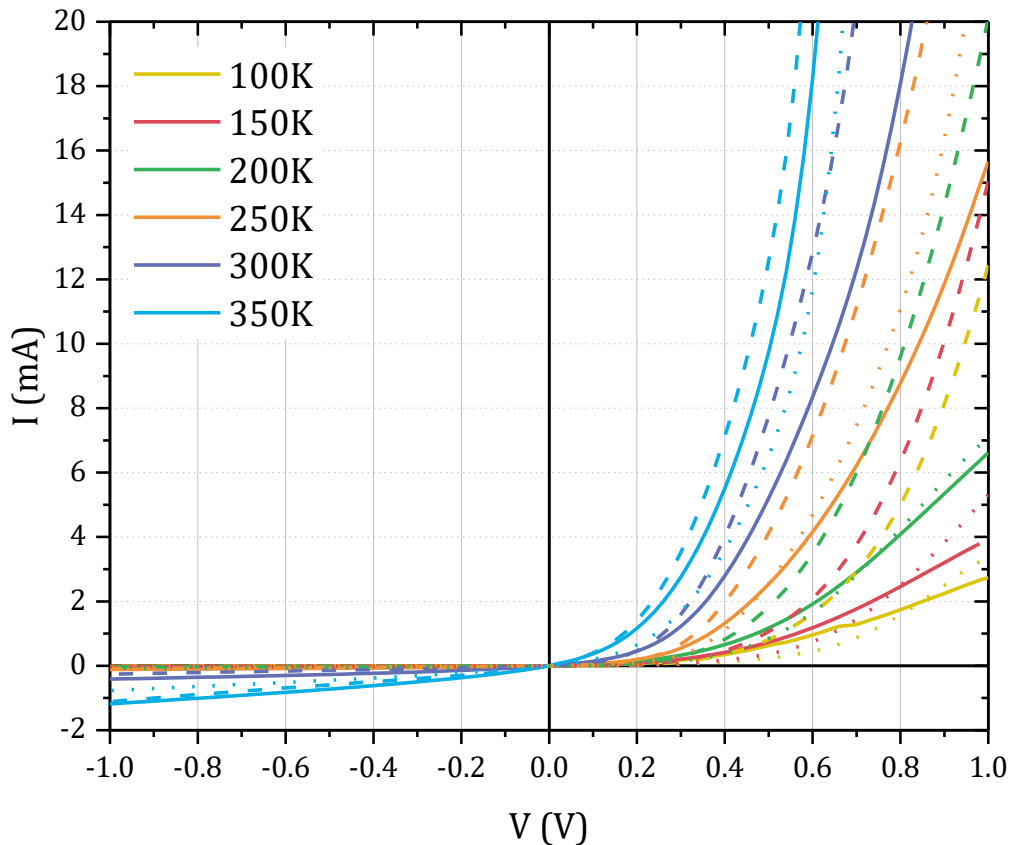


Figure V.2-7 Temperature dependent I-V curves, measured in the dark, of double-side textured test-structures **a)** (dotted lines), **b)** (dashed lines) and **c)** (solid lines).

V.2.2. Tunnel Diode Behaviour

In the previous part, we did not observe the I-V curve of the tunnel junction corresponding to a tunnel diode (**Figure II.4-1**). In this part, we perform dark I-V measurements under variable temperature, in the cryostat tool (**III.3.4.b**), of small test-structures **d)**, **e)** and **f)** made as presented in **Figure V.2-5**.

Figure V.2-8 shows the measured dark I-V curves of the isotype and symmetrical test-structures **f)** (**Figure V.2-1**), in solid lines, and those of test-structures with the developed $\mu\text{-Si:H (n}^+/\text{p}^+)$ junction on the front-side (**Figure V.2-1 d)**), in dotted lines. We observed that test-structures **f)** did not present linear I-V curves, as expected for this kind of device. The front-side contact a-Si:H (n)/ITO seems to form a diode, blocking the current at reverse bias. This could be explained by a degradation of the a-Si:H layers, during the e-beam evaporation (metallisation), which would be larger on the front-side, the ITO layer not protecting the entire a-Si:H layers surface (see **Appendix B**). However, with the $\mu\text{-Si:H (n}^+/\text{p}^+)$ tunnel junction, test-structures **d)** are less blocking for the current at reverse bias. Moreover, for these test-structures **d)**, the more the temperature

increases, the more linear the I-V curves are. At reverse bias, the front-side stack acts as a resistance at temperatures above 300 K, which tends to validate the tunnel diode behaviour of the developed $\mu\text{-Si:H}$ (n^+/p^+) junction.

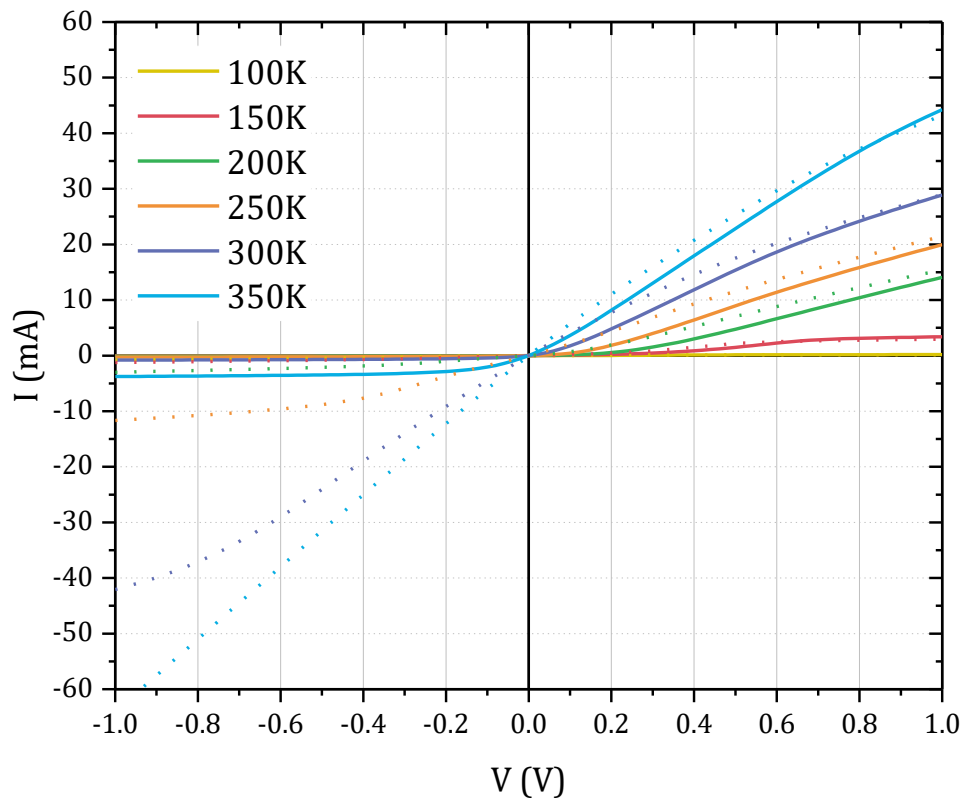


Figure V.2-8 Temperature dependent I-V curves, measured in the dark, of double-side textured test-structures **d**) (dotted lines) and **f**) (solid lines) made with e-beam evaporation metallisation.

In order to overcome the possible damage of the e-beam evaporation, we then made the same test-structures **d**), **e**) and **f**) (**Figure V.2-1**) with thermal evaporation metallisation. Resulting I-V curves are presented in **Figure V.2-9**. At reverse bias, a barrier is always observable at the front-side a-Si:H (n)/ITO contact (test-structures **f**) but it decreases with the temperature and a current is obtained at temperatures above 300 K. However, the measured I-V curves are still not symmetrical, which is probably not only due to the current spreading but also to a structural difference between the front stack and the back stack (e.g. different thermal budget due to the fabrication steps). Regarding the other test-structures: above 200 K test-structures **e**) are less resistive than test-structures **d**) which are less resistive than test-structures **f**). This tends to demonstrate that like for the test-structures **a**), **b**) and **c**), the behaviour is mainly influenced by the contact with the front-side ITO.

However, at forward bias, test-structures **d**) present peaks and valleys, with negative resistance region, at temperatures below 300 K, in **Figure V.2-10**. The negative resistance region oscillates. This shows that the transition between a conduction regime where the tunnel effect dominates and a regime where thermionic emission is the main transport mechanism is not instantaneous. Above 300 K, the current reaches the equipment limit before starting to decrease, thus the valleys are not observable. At 200 K and 210 K the valley currents are too weak and do not increase again directly, maybe due to a measurement artefact. Moreover, at 200 K, 210 K and 220 K, the conduction seems to be due only to the tunnel effect and varies very little with temperature. Furthermore, peak currents are much higher than the usual Perovskite/SHJ tandem

solar cells J_{sc} , which is required for a normal operation of the tunnel junction in multijunction solar cells, according to J. Yang *et al.* [173].

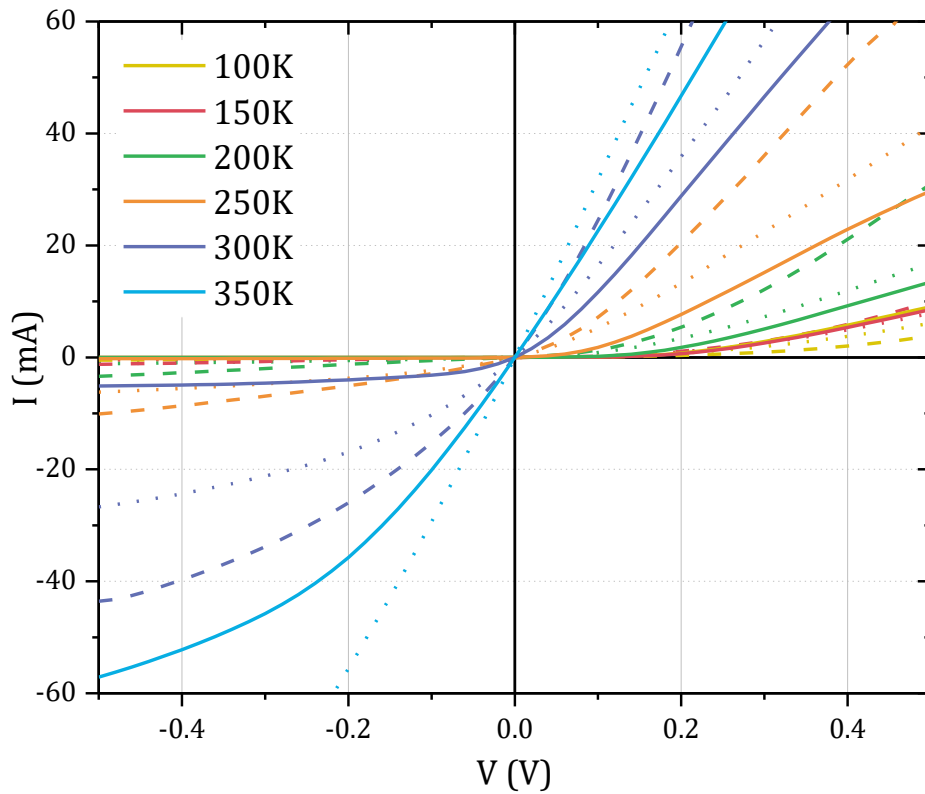


Figure V.2-9 Temperature dependent I-V curves, measured in the dark, of double-side textured test-structures **d**) (dotted lines), **e**) (dashed lines) and **f**) (solid lines) made with thermal evaporation metallisation.

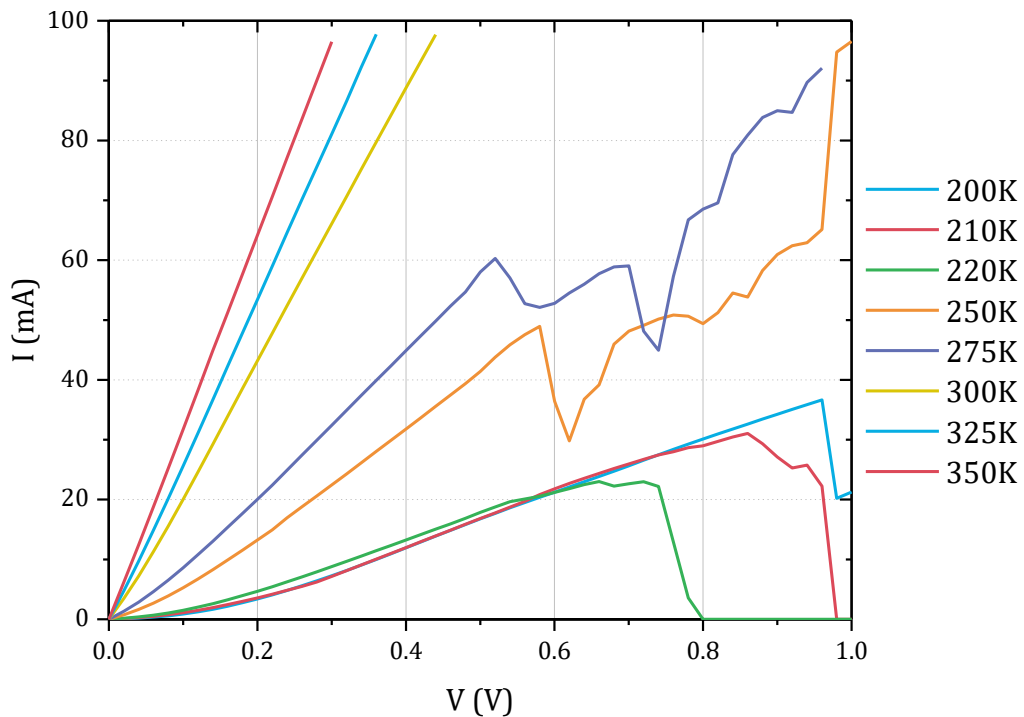


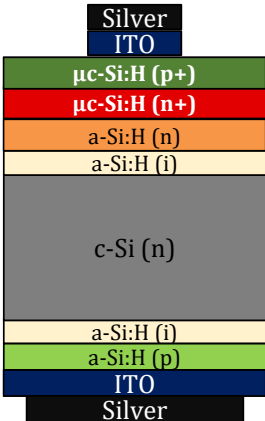
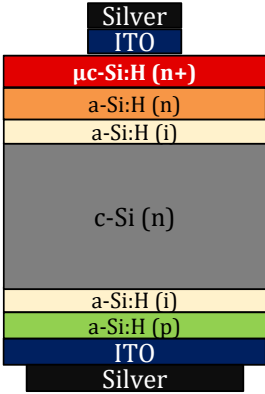
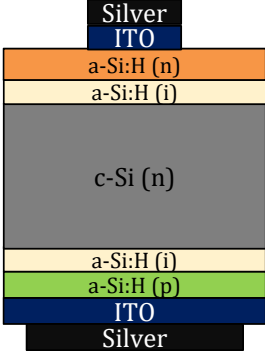
Figure V.2-10 Temperature dependent I-V curves, measured in the dark, of double-side textured test-structures **d**) made with thermal evaporation metallisation.

In conclusion, despite the non-ideal fabrication process (I-V curves of small test-structures **e**) are not symmetrical and the front-side ITO has a strong influence on

the measurements), test-structures **d)** seems to be suitable to observe the tunnel diode behaviour, as suggested in the previous part (see **Figure V.2-4**).

V.2.3. Conclusion

To conclude, we present a summary of the obtained results and our observations for each test-structures in **Table V.2-2**. In all cases, we observe a strong influence of the ITO layer composing the front-side electrode. Therefore, this issue is studied in the next part.

Test-Structure	Objective	Notes
 <p>Figure V.2-1 a)</p>	<p>To investigate the impact of the tunnel junction on the SHJ cell (see IV.3)</p>	<ul style="list-style-type: none"> → Diode behaviour with lower R_s than the reference (Figure V.2-1 c)) at temperatures below 250 K and a slightly higher R_s at temperatures above 300 K. This follows the trend of the $\mu\text{c-Si:H (p+)}/\text{ITO}$ contact resistance → No S-shape observed → Useful to compare the R_s with the reference and deduce if the RJ is lowly resistive or not
 <p>Figure V.2-1 b)</p>	<p>To compare to structure a): to investigate the impact of the P-type layer (additional R_s?)</p>	<ul style="list-style-type: none"> → Diode behaviour with lower R_s than the reference (Figure V.2-1 c)), as expected, thanks to a better contact with the front-side ITO
 <p>Figure V.2-1 c)</p>	<p>Reference for a) and b) structures</p>	<ul style="list-style-type: none"> → Expected diode/solar cell behaviour

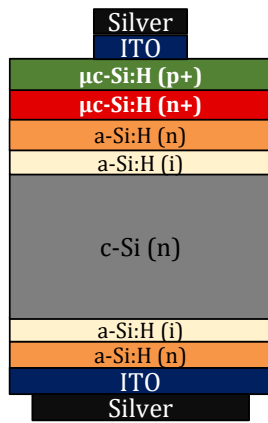


Figure V.2-1 d)

Alternative to **structure g)** to measure the I-V curve of the tunnel junction

- Low resistance behaviour (linear I-V curves and high current) at temperatures above 300 K
- Allows to observe the tunnel diode behaviour if the current is lower than the equipment limitation (at low temperatures or with very small electrodes)

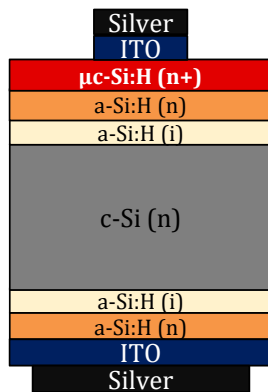


Figure V.2-1 e)

To compare this isotype structure with structure **d)** (second reference)

- Unexpected non-linear behaviour
- Less resistive front stack than the reference (**Figure V.2-1 f)**), thanks to a better contact with the front-side ITO

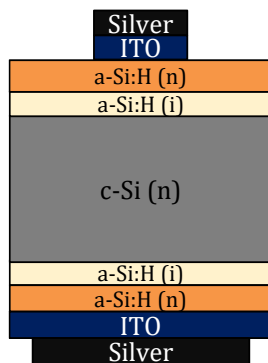


Figure V.2-1 f)

Reference for **d)** and **e)** structures

- Unexpected unsymmetrical and non-linear behaviour: structural difference between the front stack and the back stack (e.g. different thermal budget due to the fabrication steps)? Shunted back-side?

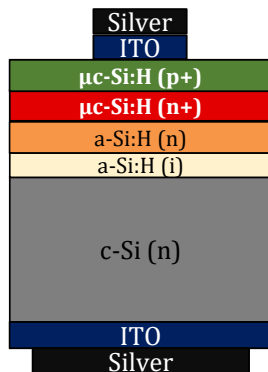


Figure V.2-1 g)

To measure the I-V curve of the tunnel junction

- Inconclusive because of the back-side ITO/Ag electrode

Table V.2-2 Reminder of the objectives of each test-structures and notes about the obtained results.

V.3. Transport Mechanisms Insight in NPN Junctions

In the previous part V.2, we defined and used several test-structures to characterise the $\mu\text{-Si:H (n}^+/\text{p}^+)$ tunnel junction (presented in chapter IV) with dark I-V measurements. We observed that the ITO layer in the front-side electrode has a strong influence on the measurements. Indeed, an N-type TCO layer (like the ITO used) forms a recombination junction with P-type amorphous or microcrystalline silicon layers (see **Figure V.3-1**), as explained in chapter II. In this part, we investigate the influence of this front-side TCO layer and try to replace the ITO/Silver electrode by an aluminium electrode (deposited by thermal evaporation, III.1.4.b).

The stack $\mu\text{-Si:H (n}^+)/\mu\text{-Si:H (p}^+)/\text{N-type TCO}$ forms a NPN junction with highly doped layers. Due to the P-type layer thickness, we think that electrons cannot directly tunnel from the conduction band of an N-type layer to the conduction band of the other N-type layer. In fact, in a closed circuit, if we assimilate each PN junction as a tunnel diode, one is in reverse bias while the other is in forward bias. Therefore, one NP junction acts as a recombination junction while the other acts as a separation junction, depending on the voltage bias, as defined by P. Procel *et al.* for P-type TLM structures [117]. **Figure V.3-2** shows the simplified band diagrams of the test-structures front-side with the NPN stack. At forward bias, by applying a small voltage, electrons in the conduction band of the $\mu\text{-Si:H (n}^+)$ layer tunnel to the empty states of the valence band in the $\mu\text{-Si:H (p}^+)$ layer (see **Figure II.4-2**, forward bias): there is recombination. In parallel, the $\mu\text{-Si:H (p}^+)/\text{TCO}$ junction is at reverse bias. Thus, electrons tunnel through the narrow space charge region from the valence band of the $\mu\text{-Si:H (p}^+)$ layer to the conduction band of the N-type TCO layer (see **Figure II.4-2**, reverse bias): there is separation. At reverse bias, the $\mu\text{-Si:H (n}^+/\text{p}^+)$ junction acts as a separation junction and the $\mu\text{-Si:H (p}^+)/\text{TCO}$ acts as a recombination junction. Therefore, the main transport mechanisms are direct band-to-band tunnelling (also named internal field-effect emission by L. Esaki [113]) and trap-assisted tunnelling.

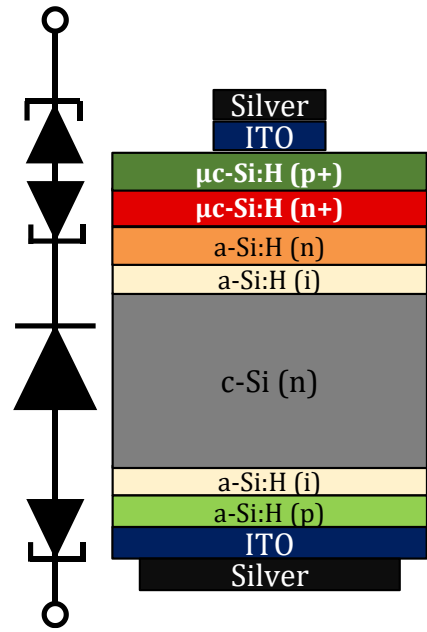


Figure V.3-1 Test-structure a) (**Figure V.2-1**) and its adjusted simplified circuit diagram.

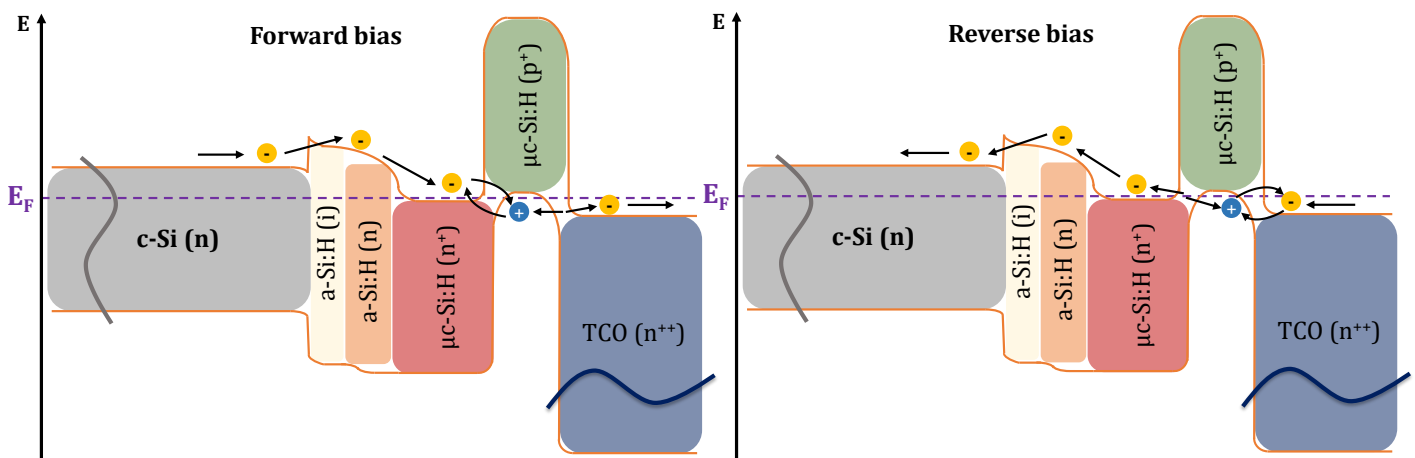


Figure V.3-2 Simplified band diagrams of the front-side stack of test-structures with a microcrystalline silicon tunnel junction and a TCO. At forward bias (regarding the $\mu\text{-Si:H (n}^+/\text{p}^+)$ tunnel junction) in the left and at reverse bias (regarding the $\mu\text{-Si:H (n}^+/\text{p}^+)$ tunnel junction) in the right.

In order to observe the influence of the N-type TCO layer in electrical characterisation (transversal measurements presented in the previous part V.2 or TLM measurements for examples [172]) of silicon tunnel junctions, we performed an experiment in collaboration with the *CSEM* (Swiss Center for Electronics and Microtechnology). We used two different ITO layers and one AZO layer as the N-type TCOs. Additionally, three different microcrystalline silicon tunnel junctions were processed. These tunnel junctions feature different thicknesses but low activation energies and nearly the same $X_{\mu\text{-Si}}$, presented in **Table V.3-1**.

Tunnel Junctions	$\mu\text{-Si:H (n}^+/\text{p}^+)$ ① (presented in chapter IV)	$\mu\text{-Si:H (n}^+/\text{p}^+)$ ② from <i>CSEM</i>	$\mu\text{-Si:H (n}^+/\text{p}^+)$ ③ from <i>CSEM</i>
Batch	Batch-2	Batch-1	Batch-1
Thickness	≈ 50 nm	≈ 80 nm	≈ 135 nm
Average $X_{\mu\text{-Si}}$	50 %	50 %	52 %

Table V.3-1 Thicknesses and average microcrystalline phase fractions of the tunnel junctions, extracted by SE and Raman spectroscopy.

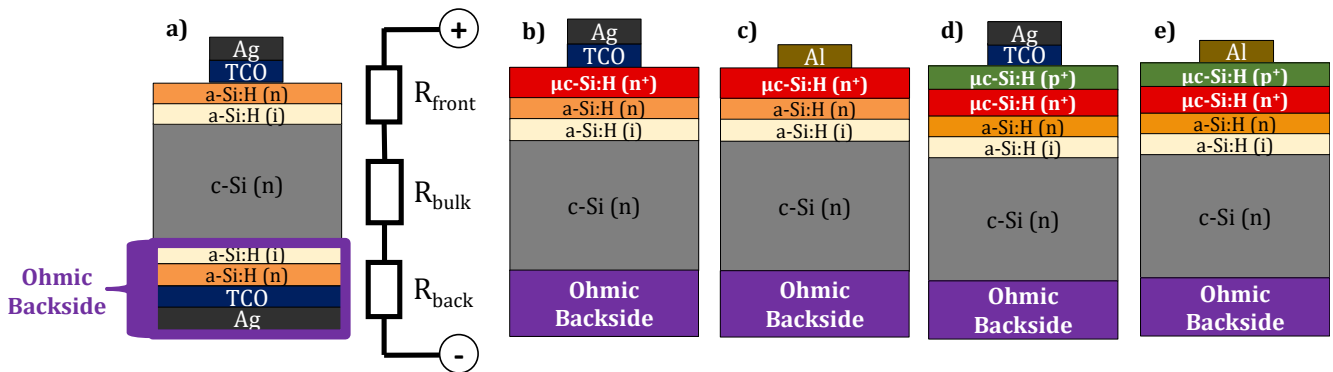


Figure V.3-3 Test-structures used in the experiment, based on test-structures **d)**, **e)** and **f)** from **Figure V.2-1**. The circuit diagram of the test-structures separated in three resistances (R_{front} for the studied front stack, R_{bulk} for the substrate and R_{back} for the Ohmic back-side) is also presented.

Moreover, we used the five test-structures presented in **Figure V.3-3** with known Ohmic back-sides (we used back stack, forming an Ohmic contact at ambient temperature, already studied in some previous experiments). We made sure that each test-structure had the same final thermal budget but some spent more time under air than others between fabrication steps. For each tunnel junction we made three test-structures **b)** and **d)** (**Figure V.3-3**), one for each TCO. Structures **a)** (**Figure V.3-3**) are symmetrical to measure the back-side, which is integrated in the other test-structures. Structures **b)** are composed at the front by a $\mu\text{-Si:H (n}^+)$ layer and a circular electrode of TCO and silver. Structures **c)** are similar to structures **b)** but with a circular electrode of aluminium. Furthermore, both structures **d)** and **e)** are similar to the **b)** and **c)** ones, but with an additional $\mu\text{-Si:H (p}^+)$ layer to form the tunnel junctions. Thus, the structures **d)** feature a NPN junction, whereas the structures **e)** feature only one NP junction. To study the structures, we decorrelated them in three resistances connected in series, as presented in **Figure V.3-3** and equation (V.3-1), where R_{tot} is the measured total resistance.

$$R_{\text{tot}} = R_{\text{front}} + R_{\text{bulk}} + R_{\text{back}} \quad (\text{V.3-1})$$

On top of that, experiments were performed on two batches of c-Si (n) textured wafers:

- Batch-1, with a c-Si (n) double-side textured substrate, featuring a thickness around 260 μm , a resistivity of 3.2 $\Omega\cdot\text{cm}$ (at 300 K) and an Ohmic back-side with an AZO layer,
- Batch-2, with a c-Si (n) double-side textured substrate, featuring a thickness around 185 μm , a resistivity of 0.82 $\Omega\cdot\text{cm}$ (at 300 K) and an Ohmic back-side with an ITO layer.

First, we performed dark I-V measurements from -0.3 V to 0.3 V, in the cryostat tool (III.3.4.b), under variable temperature, on structures **a)**. We obtained the expected symmetrical I-V curves. Thus, with the poor lateral conductivity and the small thickness of the amorphous silicon layers, compared to the crystalline bulk, we assume that the current spreading only occurs in the bulk. Therefore, we calculated the bulk resistance, R_{bulk} , with equation (V.3-2) ([187], [188]), where ρ is the bulk resistivity (extracted at each temperature with a calculator using D. B. M. Klaassen's mobility model, [189]), d the front-side circular electrode diameter and t the wafer thickness. For each sample, the diameter of the front-side electrode was calculated precisely with an optical microscope.

$$R_{\text{bulk}} = \frac{\rho}{d\pi} \arctan \frac{4t}{d} \quad (\text{V.3-2})$$

Then, as structures **a)** are fully symmetrical, we calculated their back-side resistances, R_{back} , with equation (V.3-3).

$$R_{\text{back}} = \frac{R_{\text{tot}} - R_{\text{bulk}}}{2} \quad (\text{V.3-3})$$

Next, we calculated the contact resistivity, ρ_c , for both back-sides (**Figure V.3-4**). In parallel, the same stacks were processed in TLM structures (see III.2.7) and the obtained ρ_c are consistent between both methods.

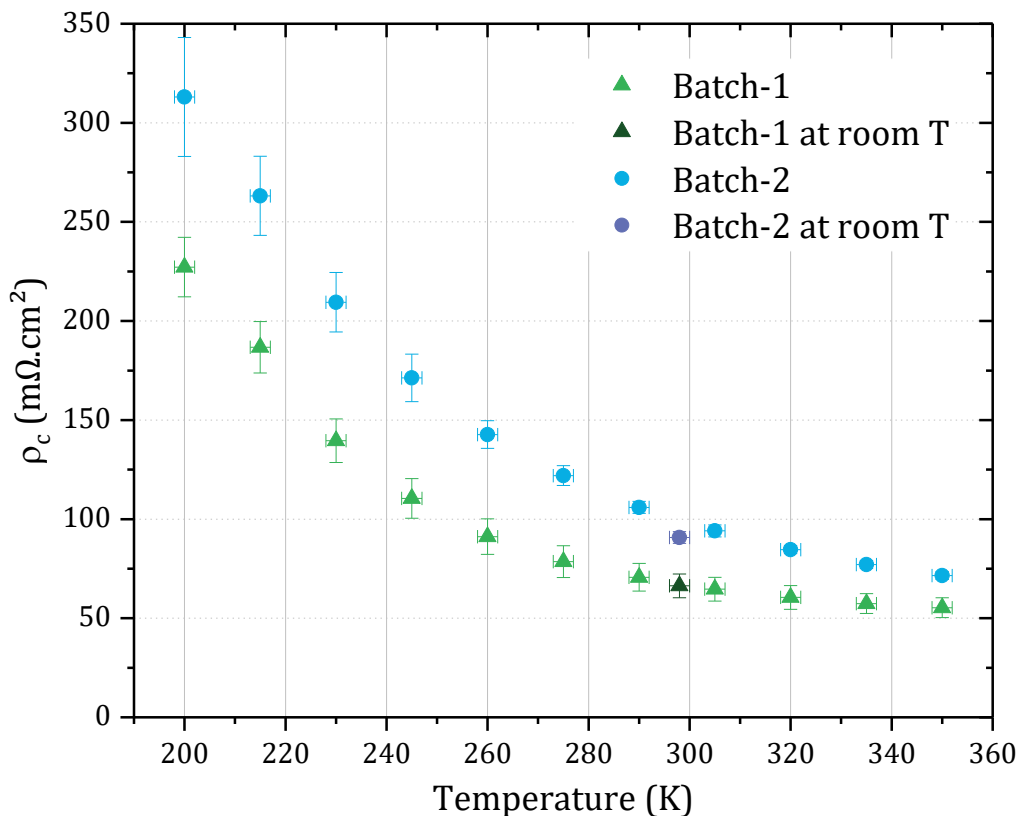


Figure V.3-4 Contact resistivity, ρ_c , from 200 K to 350 K calculated for both Ohmic back-sides. Batch-1 in green and Batch-2 in blue.

We observed that for the Batch-1, above 275 K, the total resistance, R_{tot} , is dominated by the bulk resistance. However, for the Batch-2, R_{bulk} stays low compared to R_{tot} .

Secondly, we also performed dark I-V measurements under variable temperature on the other structures and calculated the front resistance, R_{front} , with equation (V. 3-4), when the I-V curves were quite linear ($R^2 > 0.99$ from -0.1V to 0.1 V).

$$R_{front} = R_{tot} - R_{bulk} - R_{back} \quad (V.3-4)$$

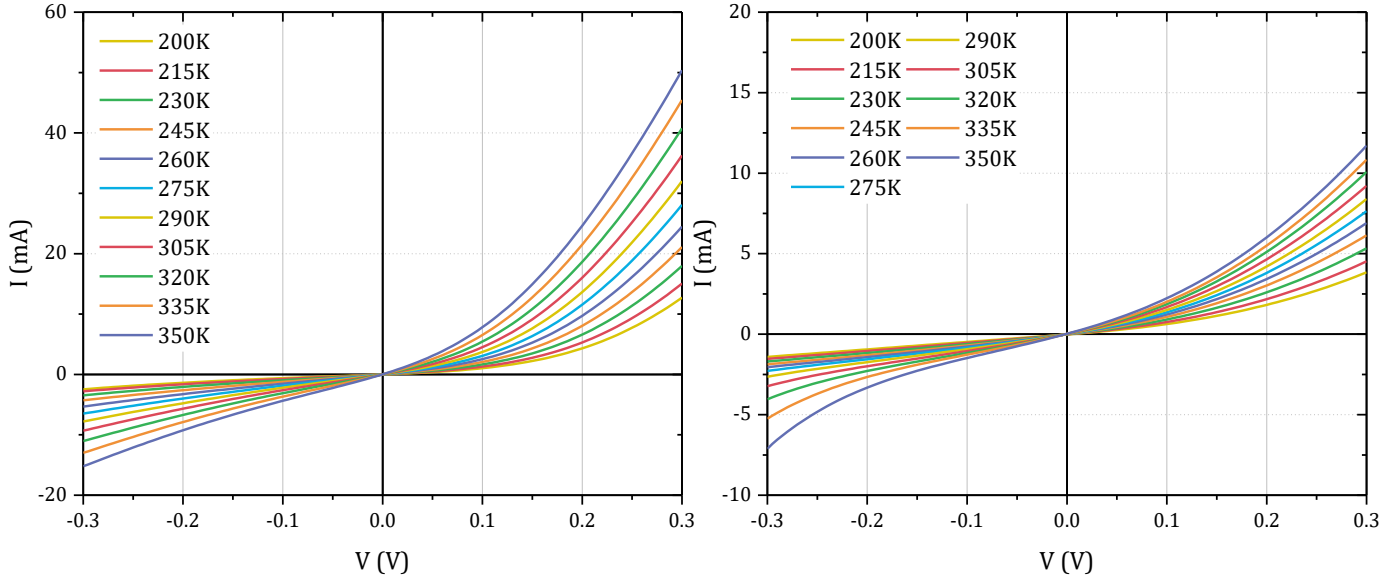


Figure V.3-5 I-V curves from 200 K to 350 K of structures **b)** (on the left) and **d)** (on the right), with the tunnel junction $\mu\text{-Si:H}$ (n^+/p^+) ① and the AZO layer, from Batch-2.

Figure V.3-5 is a good illustration of the importance of the front-side TCO layer in electrical measurements. Indeed, we observed that the $\mu\text{-Si:H}$ (n^+)/N-type AZO stack (on the left of **Figure V.3-5**) tends to act as a diode, probably due to a poor band alignment. By adding the $\mu\text{-Si:H}$ (p^+) (on the right of **Figure V.3-5**), the current is lower, thus we assume that the structure is more resistive. However, a diode behaviour is observed at forward and reverse bias, which highlights a NPN junction in structure **d)** (**Figure V.3-3**) with lowly efficient recombination/separation processes.

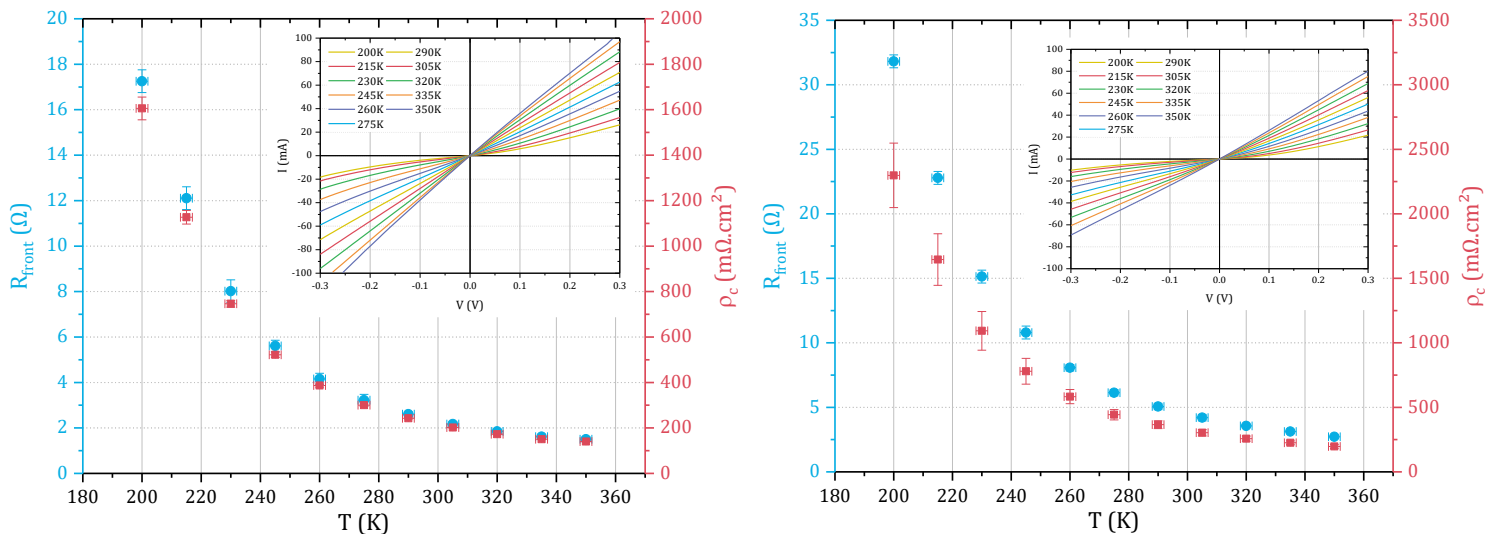


Figure V.3-6 R_{front} and ρ_c calculated for structures **b)** with the $\mu\text{-Si:H}$ (n^+) ① layer and the ITO layers (one on the left and the other on the right), from Batch-2. Measured I-V curves are presented in insets.

In the other cases, with both ITO layers, the obtained I-V curves had a more Ohmic behaviour, as presented in **Figure V.3-6** and **Figure V.3-7**, for the developed tunnel junction $\mu\text{-Si:H (n}^+/\text{p}^+)$ ①.

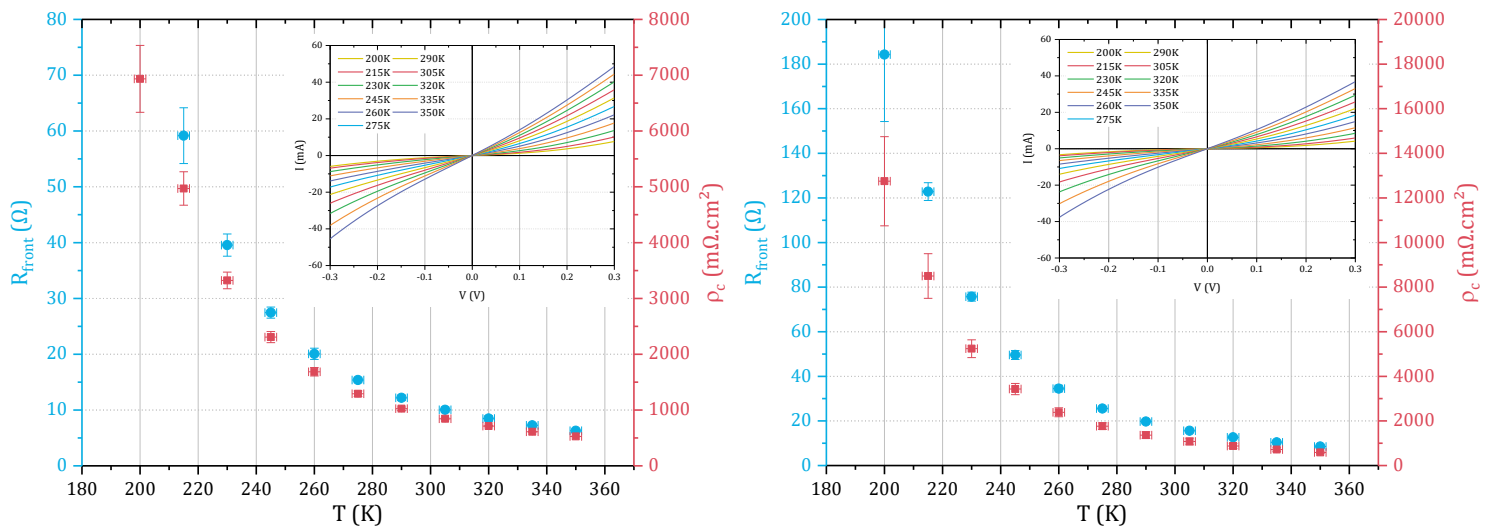


Figure V.3-7 R_{front} and ρ_c calculated for structures **d)** with the tunnel junction $\mu\text{-Si:H (n}^+/\text{p}^+)$ ① and the ITO layers (one on the left and the other on the right, as in **Figure V.3-6**), from Batch-2. Measured I-V curves are presented in insets.

We observed that for structures **b)** (**Figure V.3-3**), ρ_c is more important (33 ± 3 % higher) for the front stack including the second ITO (on the right of **Figure V.3-6**). However, ρ_c 's decrease with temperature is the same for both front stacks. Thus, by plotting ρ_c on an Arrhenius plot, this results in activation energies of 101 ± 1 meV for both front stacks (c-Si (n)/a-Si:H (i)/a-Si:H (n)/ $\mu\text{-Si:H (n}^+)$ /ITO/Ag). Therefore, regardless of the ITO layer, the contact $\mu\text{-Si:H (n}^+)$ /ITO changes in the same way with the temperature. On the contrary, with the $\mu\text{-Si:H (p}^+)$ layer, in structures **d)**, ρ_c is always more important for the front stack including the second ITO but decreases more rapidly with the temperature. This results in $E_a = 106 \pm 1$ meV for the front stack including the first ITO (on the left of **Figure V.3-7**) and $E_a = 125 \pm 1$ meV for the front stack including the second ITO (on the right of **Figure V.3-7**). Thus, the first ITO forms a less resistive junction with the $\mu\text{-Si:H (p}^+)$ layer.

Regarding the Batch-1 with the two others $\mu\text{-Si:H (n}^+/\text{p}^+)$ tunnel junctions (② and ③, **Table V.3-1**), we observed that the thicker the junction, the lower the ρ_c . However, the observations are the same: ρ_c and E_a are lower with the first ITO for structures **d)**. Moreover, it is impossible with these measurements to know if ρ_c and E_a are lower because the $\mu\text{-Si:H (n}^+/\text{p}^+)$ tunnel junction works better or because the $\mu\text{-Si:H (p}^+)$ /ITO contact is better. It is probably both, as the $\mu\text{-Si:H}$ layers thickness plays a role in the TCO growth [58], [190] and in the $\mu\text{-Si:H (n}^+/\text{p}^+)$ junction operation (see chapter IV). Finally, if we compare the results of structures **b)** with those of structures **d)**, the differences are very important depending on the TCO used. Thus, the resistance induced by the $\mu\text{-Si:H (n}^+/\text{p}^+)$ tunnel junctions appears negligible compared to the resistance induced by the contact with the TCO layer. Therefore, this type of electrodes and test-structures are interesting to characterise the total front stack, including the TCO, and ρ_c calculated with this method are consistent with those obtained by TLM. Nevertheless, it would be necessary to study deeply the $\mu\text{-Si:H (p}^+)$ /ITO contacts to decorrelate the front stack resistance and characterise the $\mu\text{-Si:H (n}^+/\text{p}^+)$ tunnel junctions. However, this would require more time and resources than directly testing the tunnel junction in a tandem solar cell. Structures **c)** and **e)** (**Figure V.3-3**) can perhaps help to overcome that.

In fact, structures **c)** and **e)**, with a front-side aluminium electrode instead of a TCO/Ag electrode, showed various results. We observed non Ohmic behaviours and high resistances when the thinnest $\mu\text{-Si:H}$ layers were in contact with the aluminium (see **Figure V.3-8**), maybe due to a degradation of these layers during the aluminium evaporation. However, for the samples with $\mu\text{-Si:H}$ films thicker than 60 nm, Ohmic behaviours and low resistances are obtained. For example, with the thickest tunnel junction ③ from Batch-1 (**Table V.3-1**), I-V curves are linear and symmetrical in reverse and forward bias (see **Figure V.3-9**) and ρ_c at 300 K is less than $5 \text{ m}\Omega\cdot\text{cm}^2$. Thus, according to these measurements, the tunnel junction $\mu\text{-Si:H}$ (n^+/p^+) ③ seems to operate well, the electrons can tunnel across the space charge region in both ways.

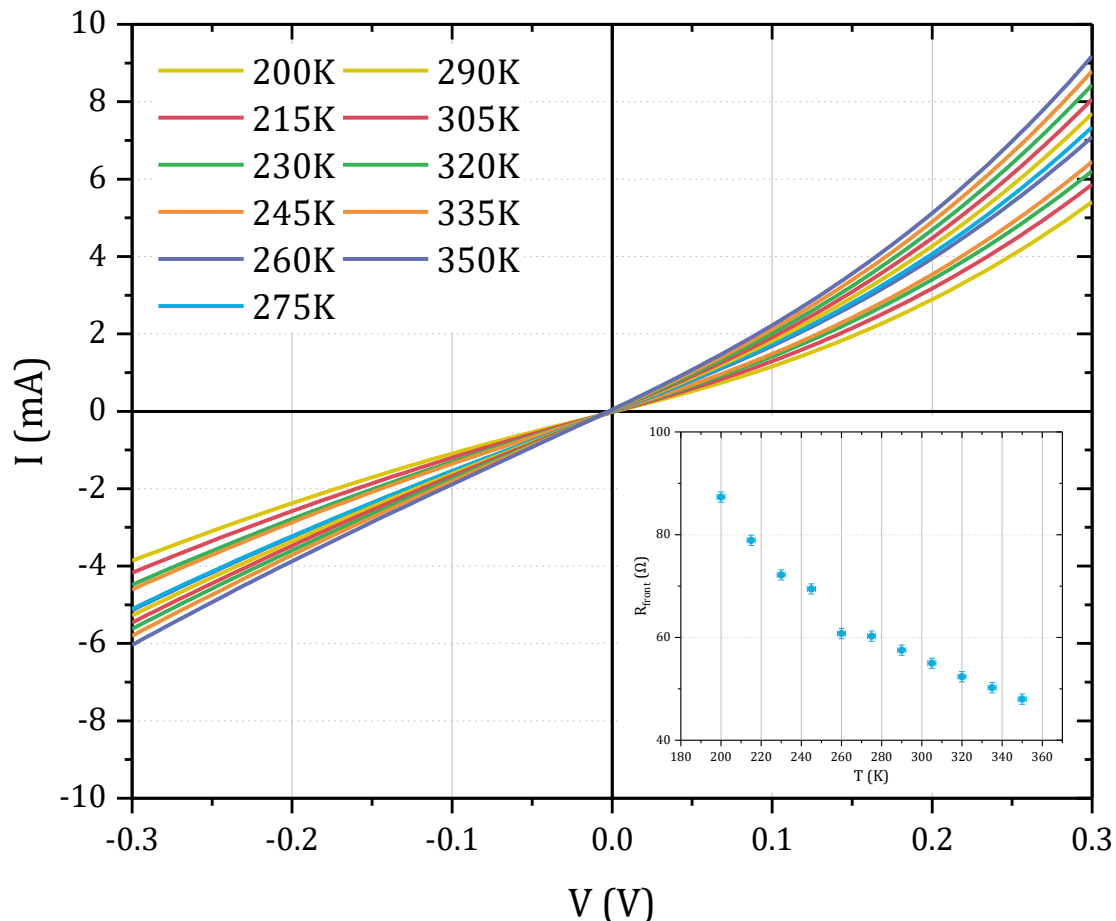


Figure V.3-8 I-V curves from 200 K to 350 K of structure **e)** with the tunnel junction $\mu\text{-Si:H}$ (n^+/p^+) ①, from Batch-2. Corresponding R_{front} are plot in inset.

In order to investigate further these direct contacts with an aluminium electrode, we performed STEM-EDX measurements (**III.2.8.b**) at the centre of the electrodes. **Figure V.3-10** and **Figure V.3-11** present the STEM-EDX analysis of structure **e)** with the previously developed junction ①. We observe a thick (almost 20 nm) oxide layer between the aluminium and the $\mu\text{-Si:H}$ (p^+). This and the oxide in the Al electrode (see **Figure V.3-11**) could explain the highly resistive front-side for this test-structure.

Finally, we think that these direct contacts with aluminium electrodes seem adapted to investigate thick silicon tunnel junction (in IBC solar cells for example, [172]). However, they are not the most suitable to characterise thin silicon recombination junction, like in our case. Indeed, for applications in multi-junction solar cells, the transparency of the

junction is important and linked to the layers thickness. Thus, the junction has to be thin and therefore cannot be contacted directly by aluminium for electrical measurements.

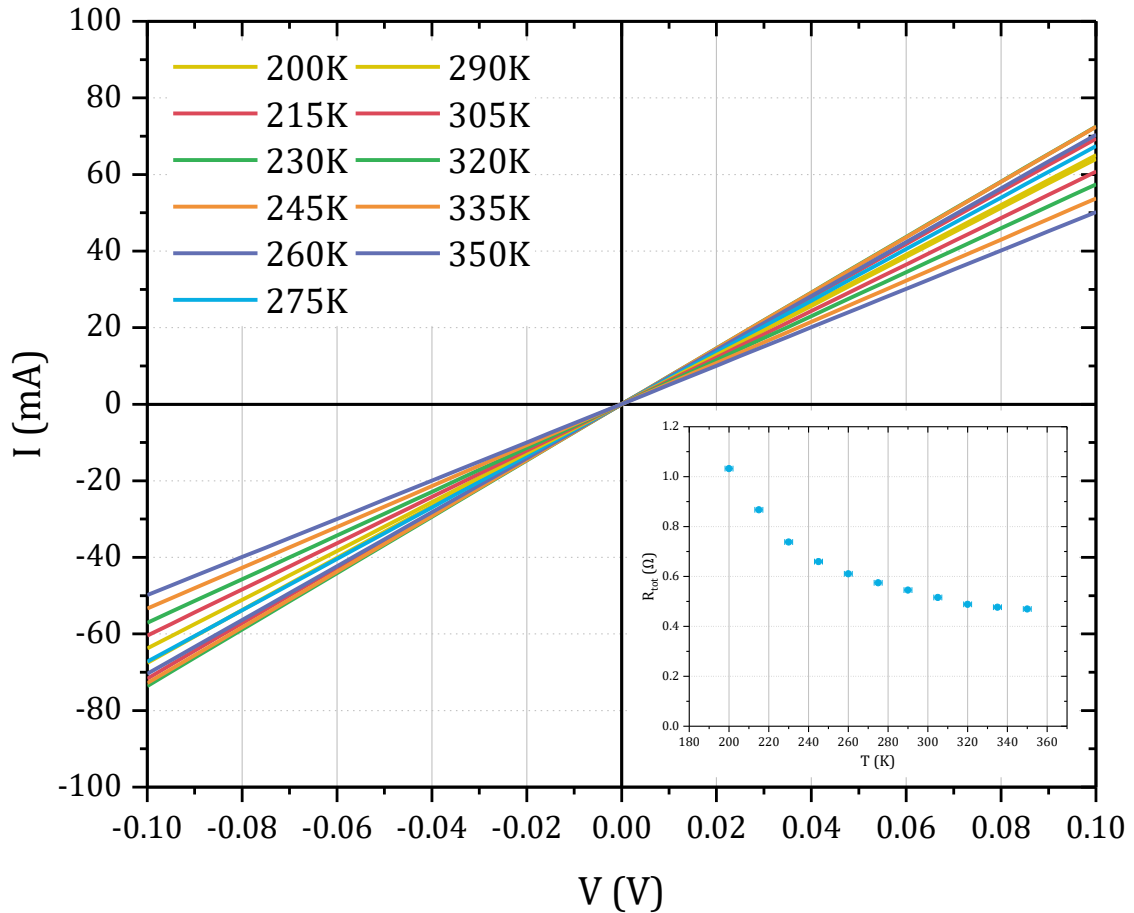


Figure V.3-9 I-V curves from 200 K to 350 K of structure **e**) with the tunnel junction $\mu\text{-Si:H}$ (n^+/p^+) ③, from Batch-1. Corresponding R_{front} are plot in inset.

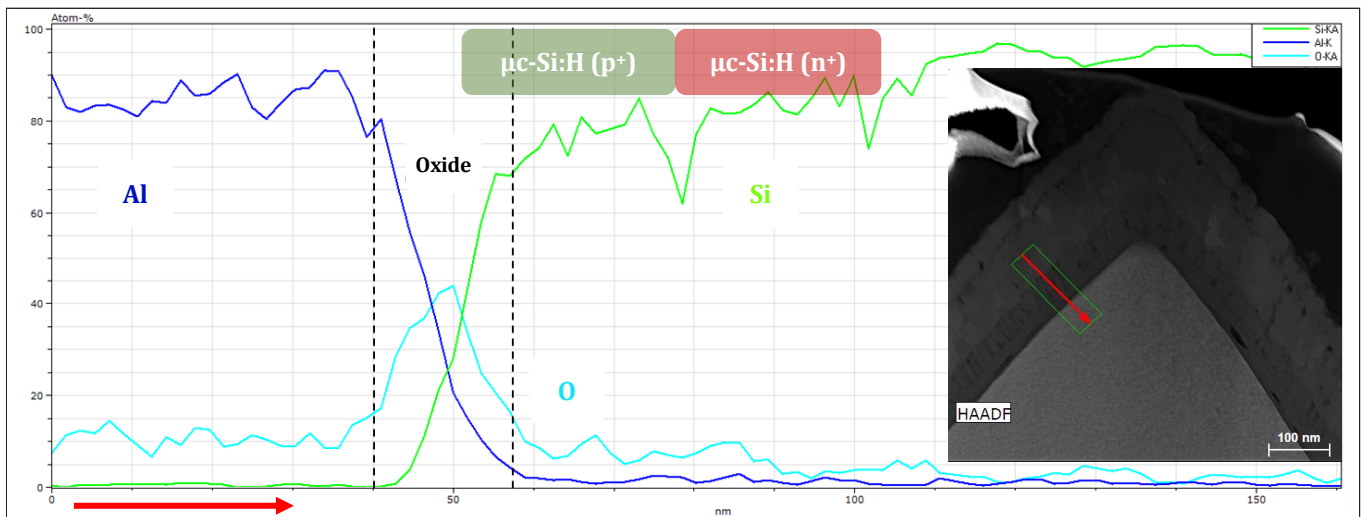


Figure V.3-10 Elemental EDX depth (nm) profile and corresponding STEM image of a cross section at the centre of the Al electrode of structure **e**) with the tunnel junction $\mu\text{-Si:H}$ (n^+/p^+) ①, from batch-2.

In conclusion, this experiment demonstrated that test-structures composed of a TCO layer in contact with the $\mu\text{-Si:H}$ (n^+/p^+) junction, like test-structures **d**) (Figure V.2-1; Figure V.3-1), do not allow to electrically characterise independently the $\mu\text{-Si:H}$ (n^+/p^+) junction. However, the developed method can be used to characterise the contact with TCO layers and obtain the contact resistivity of a stack (electron or hole contact of a SHJ

solar cell, for example). Moreover, test-structures composed of an aluminium electrode, like test-structures **e**) (**Figure V.3-1**) are not suitable either to electrically characterise independently $\mu\text{c-Si:H}$ (n^+/p^+) junctions thinner than 60 nm, without further developments.

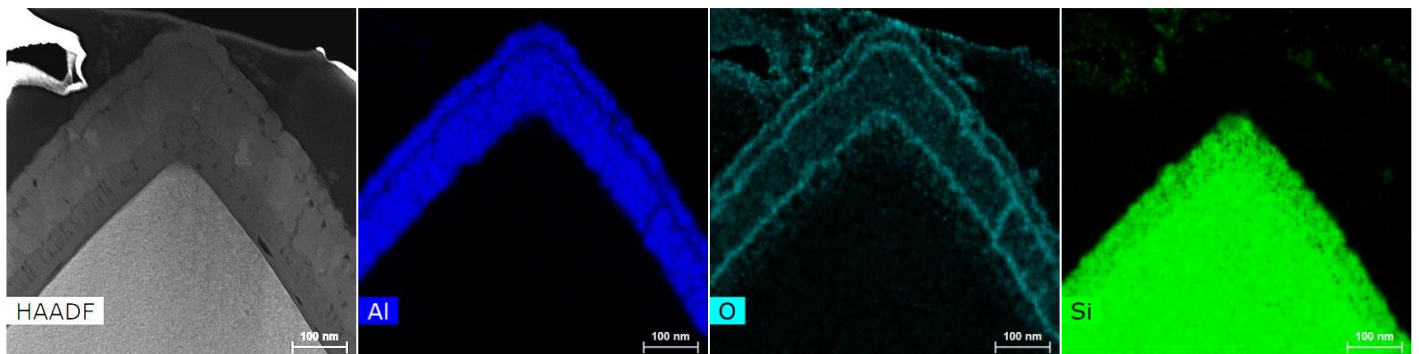


Figure V.3-11 STEM-EDX elemental mapping of a cross section at the centre of the Al electrode of structure **e**) with the tunnel junction $\mu\text{c-Si:H}$ (n^+/p^+) ①, from batch-2.

To sum up:

- A front-side metal electrode without TCO could be used but its deposition impact on $\mu\text{c-Si:H}$ layers has to be investigated first, validating that the layers are not damaged and that the contact is Ohmic and lowly resistive (no oxidation). Other metals than Al could be suitable, such as Ti or Pd.
- If a front-side electrode TCO/Metal is used, the results obtained are relative because the resistance induced by the contact with the TCO is often greater than that induced by the studied junction. However, this can be useful to compare and optimise a tunnel junction with varying parameters. Moreover, the performed transversal measurements allow determining the front stack ρ_c and E_a .

V.4. Characterisation of Recombination Junctions

In the previous parts, we investigated several test-structures, in order to perform electrical measurements of highly doped tunnel junctions. In this part, we use the presented method to characterise recombination junctions used in PK/SHJ tandem solar cells.

Firstly, even if the transversal dark I-V measurements method, presented in part **V.3**, did not allow us to measure the resistance of the $\mu\text{c-Si:H}$ (n^+/p^+), by knowing the resistances of the other layers of the stack we can get an idea of it. For example, **Figure V.4-1** shows the contact resistivity calculated with this method for the two presented stacks (based on the test-structures **b**) and **d**) from **Figure V.3-3**), on commercial N-type FZ (100) DSP (CMP) wafers (see **III.1.1**) used for PK/SHJ tandem solar cells. We observed that the measured ρ_c correspond well to the contact with the ITO layer ([46]). Thus, this tends to prove that the $\mu\text{c-Si:H}$ (n^+/p^+) developed junction is lowly resistive and therefore should not induce V_{oc} losses in tandem solar cells. On top of that, this method can be used to compare different highly doped tunnel junction of the same material (to keep similar contacts with the other layers composing the measured stack): for example, $\mu\text{c-Si:H}$ (n^+/p^+) tunnel junctions with different thicknesses.

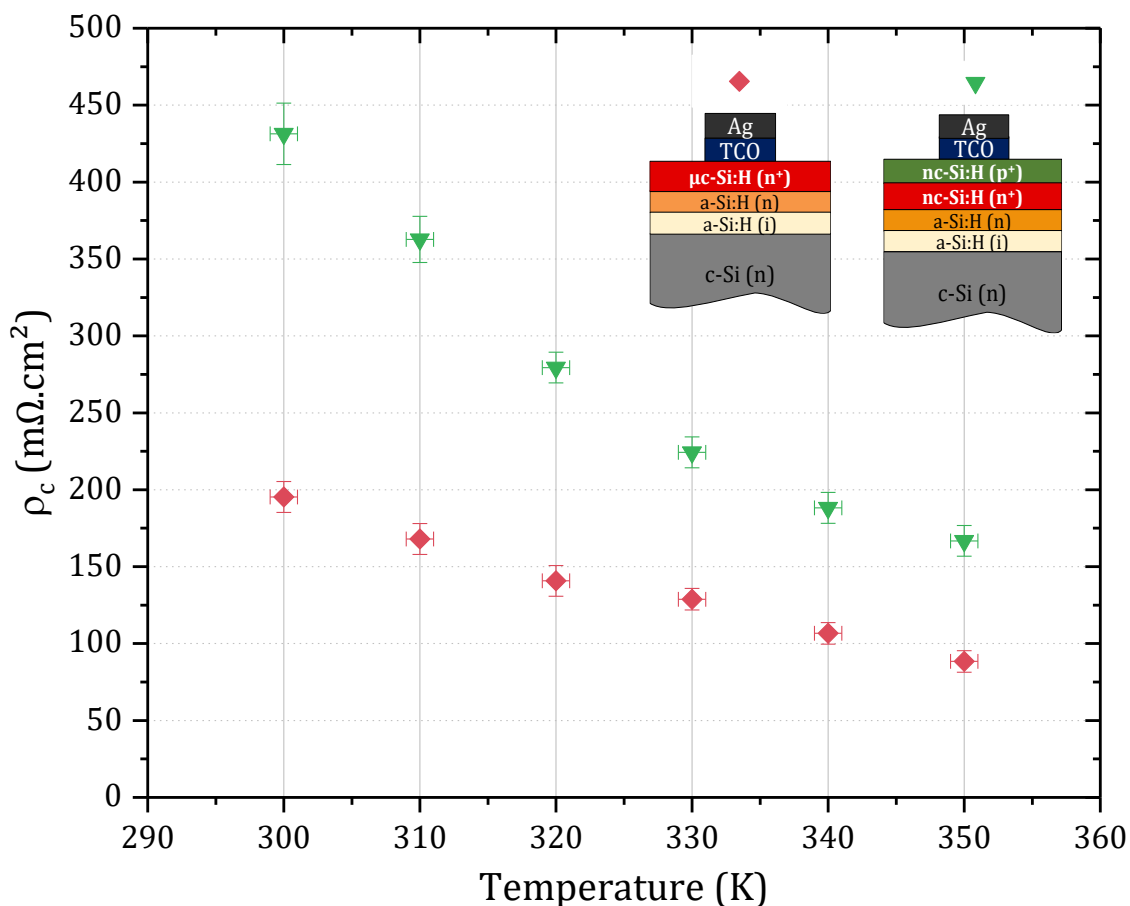


Figure V.4-1 Contact resistivity, ρ_c , from 300 K to 350 K, of the two presented stacks, extracted from transversal I-V measurements (see part V.3).

Secondly, for a recombination junction composed of a TCO layer, which is often thin for more transparency (see **Table II.3-1**), some issues can appear. Indeed, the TCO deposition can degrade the passivation of the SHJ bottom-cell or the contact with the amorphous layer may be worse than with a thicker TCO. In order to investigate these two issues for NIP PK/SHJ tandem solar cells, we made the four test-structures presented in **Figure V.4-2**.

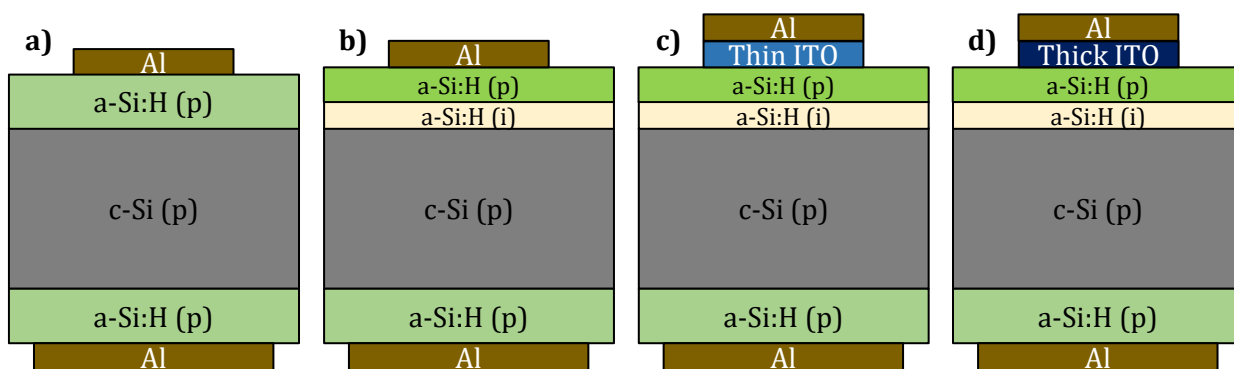


Figure V.4-2 Structures used to investigate the thin ITO recombination layer forming a recombination junction with the a-Si:H (p) layer of the SHJ bottom-cell in NIP tandem cells.

a) Symmetrical and isotype (P-type) structures with thick a-Si:H (p) layers (20 nm), **b)** Isotype (P-type) structures with the front a-Si:H layers of the SHJ NIP bottom-cell, structures **c)** are the same as structures **b)** but with the thin ITO RJ layer and structures **d)** are the same as structures **c)** but with a thick ITO layer.

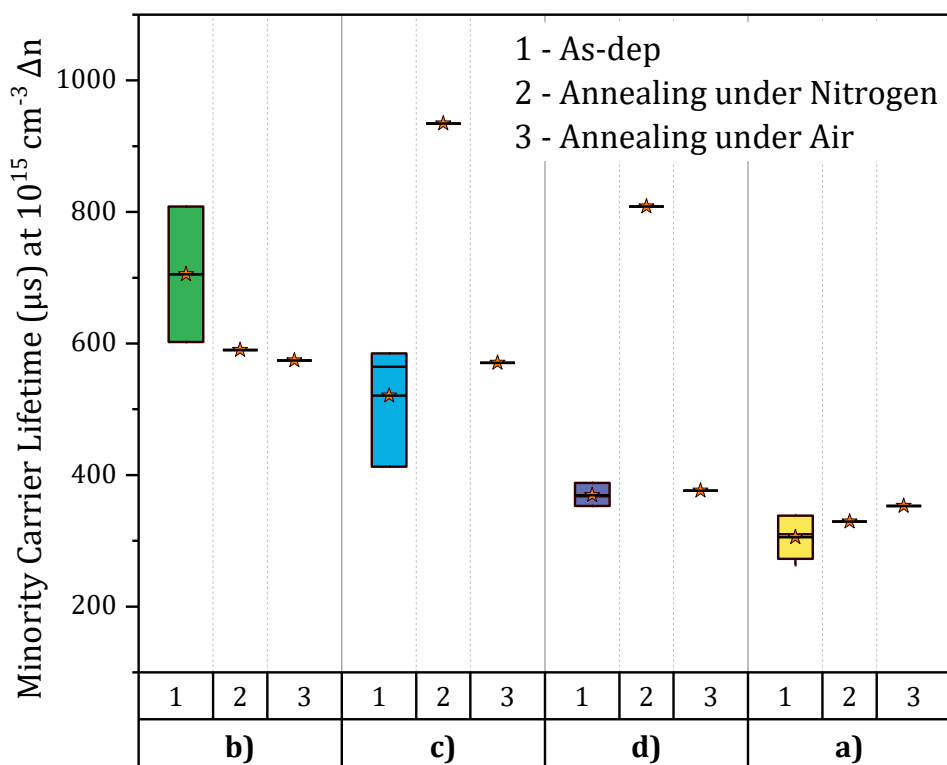


Figure V.4-3 Minority carrier lifetimes at $10^{15} \Delta n \text{ cm}^{-3}$ of structures **a)**, **b)**, **c)** and **d)** (**Figure V.4-2**) without metallisation, as-dep (1), after the annealing under nitrogen (2) or after the annealing under air (3). Annealing: one hour on a hot-plate at 100°C .

We used commercial P-type FZ (100) DSP (CMP) wafers and made an Ohmic back-side composed of a 20 nm a-Si:H (p) layer and a 200 nm aluminium layer. The main goal of this experiment was to observe if the annealing (one hour at 100°C) during the Perovskite top-cell deposition process (see **Figure III.1-5**, part **III.1.6**) heals the degradation induced by the thin ITO layer deposition. **Figure V.4-3** presents the minority carrier lifetime of the studied structures (**Figure V.4-2**) without the metallisation. Those lifetimes are low due to the lack of passivation in the back-sides of the structures but they are sufficient to observe the variations before and after an annealing. Comparing structures **b)** and structures **c)**: as expected, the lifetime is reduced after the ITO deposition. However, when there is an ITO layer in the structure (structures **c)** and **d)**), the lifetime is highly increased after the annealing under nitrogen atmosphere (in a glovebox, where the Perovskite top-cell deposition is usually performed). Yet, this is not the case for the same annealing performed under air. This tends to prove that an annealing under air is not useful after the ITO deposition because the deposition of the Perovskite top-cell and its annealing under nitrogen improve/heal the SHJ bottom-cell passivation.

Then, we performed dark I-V measurements in the cryostat tool (**III.3.4.b**) and used the method presented in part **V.3** on the P-type structures (**Figure V.4-2**). All measured I-V curves were linear. **Figure V.4-4** shows the front-side resistance of the measured structures (**Figure V.4-2**) before and after an annealing of one hour on a hot-plate at 100°C , under air. For all the structures, R_{front} is increased after the annealing, except the back-side reference structure **a)**. Moreover, this phenomenon is even more important with the thin ITO (structure **c)**). Thus, either the a-Si: H (p)/ITO contact has been deteriorated during the annealing, or the ITO/Al interface has been degraded. Without further experiment, it is hard to conclude. To sum up, this experiment demonstrates that

this type of measurements has to be performed with materials and stacks already studied and only the recombination layer as an unknown factor.

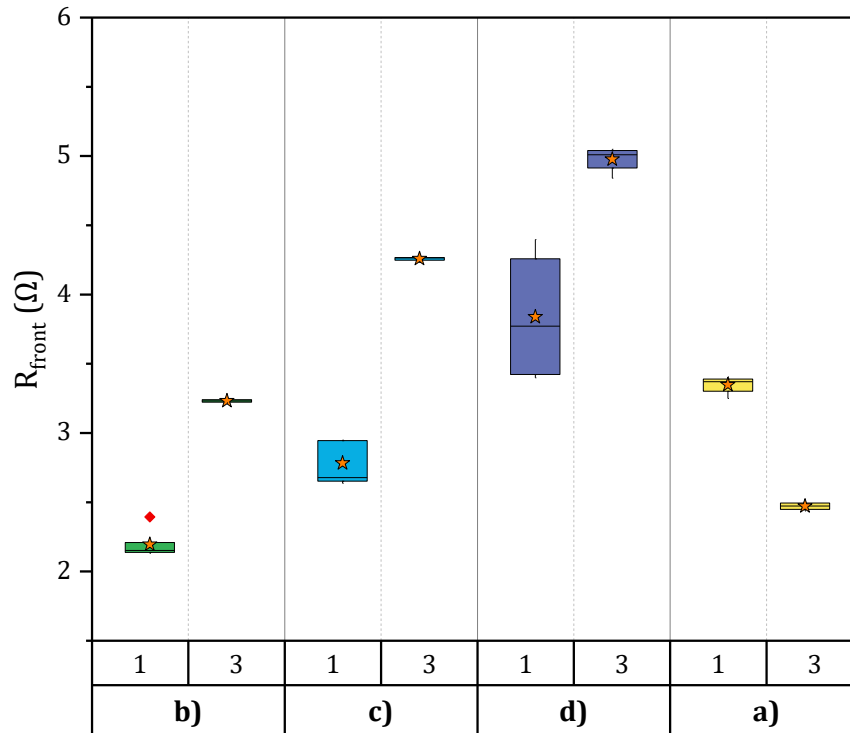


Figure V.4-4 R_{front} of structures a), b), c) and d) (Figure V.4-2), as-dep (1) and after the annealing under air (3).

V.5. Chapter Conclusion

In this chapter, we have presented different test-structures (Figure V.2-1, Figure V.3-3 and Figure V.4-2) composed of a c-Si substrate, the amorphous layers of the SHJ bottom-cell and the recombination junction. We have demonstrated that these structures preferably required a known Ohmic back-side stack and an already studied front electrode. Indeed, to facilitate the analysis and understanding of the results it is desirable if we study the recombination junction as the only unknown/variable factor.

Figure V.5-1 shows the architecture of the test-structures for NIP and PIN tandem solar cells. The ideal front electrode is a metal electrode that has a very good contact with the studied recombination junction (Ti/Pd/Ag for example). However, a well known TCO/Metal electrode can also be used to optimise highly doped tunnel recombination junctions. Moreover, if the contact resistance between the recombination junction and the TCO is known, such structures allow to observe quickly if the recombination junction is lowly resistive or highly resistive. Furthermore, if the electrode is very small or at low temperature (to have a low current and not to be impacted

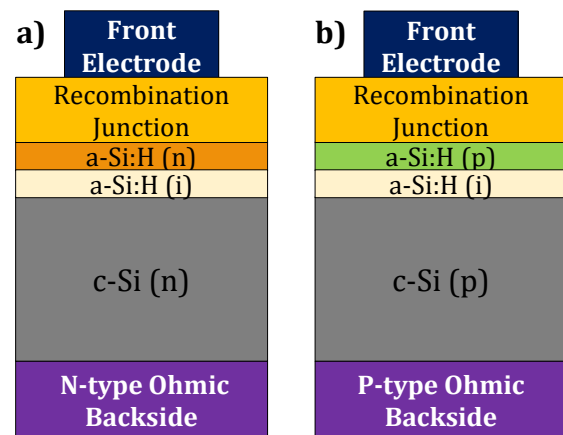


Figure V.5-1 Defined test-structures for transversal dark I-V measurements of recombination junctions. a) For PIN tandem solar cells and b) for NIP tandem solar cells.

by the current limit of the equipment), we can observe the tunnel diode behaviour (**Figure II.4-1**) of the highly doped tunnel junctions (**Figure V.2-10**).

On top of that, recombination junctions can be tested on top of SHJ solar cells (like in part **IV.3** and test-structures **a**) in **Figure V.2-1**) to validate that they are lowly resistive and do not induce accumulation of charge carriers (I-V curves with S-shape).

For more ease and speed of setting up the characterisation method, we have chosen in this chapter not to propose a structure for lateral measurements, e.g. **Figure V.1-1 b**). However, it is possible to use TLM type structures and TLM measurements (see **III.2.7**) to characterise the recombination junctions ([172], [191]), but this needs a more complicated fabrication process to obtain the right pattern ([149]).

In conclusion, we have demonstrated in this chapter that it is an extensive work to define and implement simple test-structures, isolating the junction behaviour from the complete device one. Interface and layer interactions are extremely sensitive to all analysis and need to be isolated in several batches and characterisation steps. Linking the junctions' properties with the materials electrical/optical/structural properties and annealing or subsequent steps is critical. In the next chapter, we complete this understanding with the investigation of the recombination junction influence on the Perovskite top-cell and the integration in the whole PK/SHJ tandem solar cell.

VI. TOWARDS PEROVSKITE ON SILICON HETEROJUNCTION TANDEM SOLAR CELLS INTEGRATION

In the previous chapters, we have presented and discussed the development and the characterisation of recombination junctions for PK/SHJ tandem solar cells. Moreover, we have studied their influence on the SHJ bottom-cell. In this chapter, first we present several results of optical simulations concerning recombination junctions. Then, we set up a new method to investigate the influence of the recombination junctions on the Perovskite top-cell. In conclusion, we integrate the developed $\mu\text{c-Si:H}$ (n^+/p^+) junction in PIN PK/SHJ tandem solar cells and discuss further optimisations.

VI.1. Introduction

In chapters IV and V, we studied the impact of recombination junctions on the SHJ bottom-cell. In this chapter, we focus on integrating the RJ in a complete PK/SHJ 2T device.

This chapter is divided in three parts. First, we investigate the influence of recombination junctions on the optical properties of PK/SHJ tandem solar cells. Then, we present and use a new method to study the influence (electrical and structural) of these junctions on the Perovskite top-cell. Finally, we integrate the developed $\mu\text{-Si:H}$ (n^+/p^+) in complete PIN PK/SHJ tandem solar cells.

Firstly, we performed optical simulation (see part III.4) to study the influence of the RJ in light-management. Indeed, light-management is very important in solar cells. Furthermore, in tandem solar cells, there are more layers and materials than in single-junction, which makes optical management more challenging but even more important, especially on 2T devices because of current-matching constraints. In the literature, many articles address the light-management and optical optimisation of PK/SHJ tandem solar cells, using optical simulations for dedicated structures ([93], [155], [192]–[194]...). Those simulations allow comparing several materials, layers thicknesses, stacks, architectures, texturing... However, optical simulations in the literature are based on the experimental materials of the research group or on the materials and structures already published by other research teams. Therefore, considering the variability of materials, it seems essential for each research group to carry out its own simulation work, according to the experimental possibilities. In this work, we made a focus on the recombination junctions, thus we present optical simulation studies concerning the impact of RJ.

Secondly, as the quality of the perovskite top-cell is dependent on the substrate (nature, surface, roughness, wettability), it seems important to characterise the Perovskite top-cell formed on structures mimicking as close as possible the bottom-cell and comprising the RJ. In part VI.3, we present a structure (“tandem-like”) that allows measuring only the Perovskite top-cell made in tandem conditions. Indeed, the Perovskite top-cell formation on the RJ is a key issue regarding final tandem performance, but this topic is often overlooked in literature.

Thirdly, we present the first integration results of PIN PK/SHJ solar cells with the developed $\mu\text{-Si:H}$ (n^+/p^+) junction (see chapter IV) as the recombination junction. These results demonstrate the viability of the developed junction and opens up several optimisation perspectives for this type of tandem devices that we also discuss.

Therefore, the objectives of this chapter are to complete this work on recombination junctions by investigating their influence on the Perovskite top-cell and the complete 2T PK/SHJ tandem solar cells.

VI.2. Optical Analysis of Recombination Junctions in PK/SHJ Tandem Solar Cells

In this part, we present the results of optical simulations performed with a variety of recombination junctions (first with a TCO layer and then with a highly doped tunnel junction).

VI.2.1. Transparent Conductive Oxides

TCO layers are the main used RJ in PK/SHJ tandem solar cells, associated with a modification of the bottom-cell layers (for optical matching) or not (see part II.4.3). In this part, we investigate the optical impact of the thin ITO layer usually used in our PK/SHJ devices.

First, in order to observe the impact of the ITO thickness, we performed optical simulations (with the method presented in part III.4) by varying the ITO thickness from 5 nm to 30 nm. We used the refractive indexes of deposited ITO layers with the corresponding thicknesses, except for the 5 nm which was simulated with the indexes of an ITO layer around 10 nm. For the other layers, the thicknesses (presented in **Table VI.2-1**) and the refractive indexes used correspond to our reference layers (see part III.4.2), with a double-cation Perovskite layer (see **Figure II.3-1**) and a front-side polished/back-side textured device. The obtained results were similar using a monocation Perovskite layer. **Figure VI.2-1** shows the current losses due to the parasitic absorption of the ITO layer used in the RJ. We observed that the thicker the ITO, the more its absorption causes current losses in the cell, regardless of the architecture. For the NIP architecture, losses are lower when the ITO thickness is superior to 15 nm surely, due to a better refractive indexes matching.

NIP Architecture	Thicknesses (nm)	PIN Architecture	Thicknesses (nm)
ITO front	100	ITO	100
PTAA	95	SnO ₂	40
Perovskite	415	Perovskite	415
SnO ₂	40	PTAA	95
ITO (RJ)	5 to 30	ITO (RJ)	5 to 30
a-Si:H (i)/ a-Si:H (p)	24	a-Si:H (i)/ a-Si:H (n)	13
c-Si	160000	c-Si	160000
a-Si:H (i)/ a-Si:H (n)	13	a-Si:H (i)/ a-Si:H (p)	24
ITO back	80	ITO	80
Ag	500	Ag	500

Table VI.2-1 Thicknesses of the different layers used in optical simulations with a varying ITO thickness.

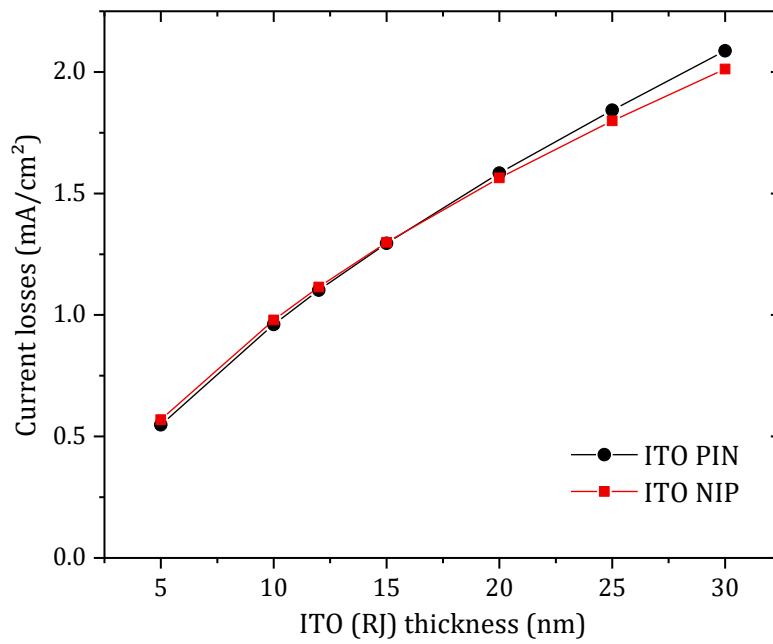


Figure VI.2-1 Current losses due to the parasitic absorption of the RJ ITO, depending on its thickness. In black for a PIN architecture and in red for a NIP architecture.

Secondly, we adjusted the thicknesses of the Perovskite top-cell layers, according to what is possible to do experimentally, to match the current between both subcells. We simulated both PIN and NIP architectures, with front-side polished and back-side textured, composed of a RJ ITO of 12 nm (thinner layers tend to degrade the electrical properties and the recombination potential of the RJ) and a double-cation Perovskite.

Layers	Thicknesses (nm)
ARC (SiO ₂)	100
ITO front	200
SnO ₂	40
Perovskite	230
PTAA	45
ITO (RJ)	12
a-Si:H (i)/ a-Si:H (n)	13
c-Si	160000
a-Si:H (i)/ a-Si:H (p)	24
ITO back	80
Ag	500

Table VI.2-2 Thicknesses of the different layers used in optical simulations with current-matching condition.

Table VI.2-2 presents the thicknesses used for these simulations and **Figure VI.2-2** shows the obtained absorption of each subcell. This gives us a glimpse of the current that can be achieved with minor optimisations (reduction of the thickness of the PTAA and the PK layers). For both architectures, NIP and PIN, current losses in the RJ ITO slightly exceed 1 mA/cm². If we assume realistic values of FF and V_{oc}, as V_{oc} = 1.85 V and FF = 75 %, the corresponding efficiencies are 24.7 % for the NIP architecture and 24.8 %

for the PIN architecture. Despite the PTAA parasitic absorption (observable comparing the PK absorption from 300 nm to 450 nm between PIN and NIP architectures, [195]), we observed very little optical differences between both NIP and PIN architectures. The lower parasitic absorption in the PIN architecture might be compensated by a higher reflectance. However, with a V_{oc} and a FF achievable in practice, these architectures do not allow us, optically speaking (because experimentally some physical and electrical factors can come to bring slight differences), to exceed 25 % efficiency considering these structures.

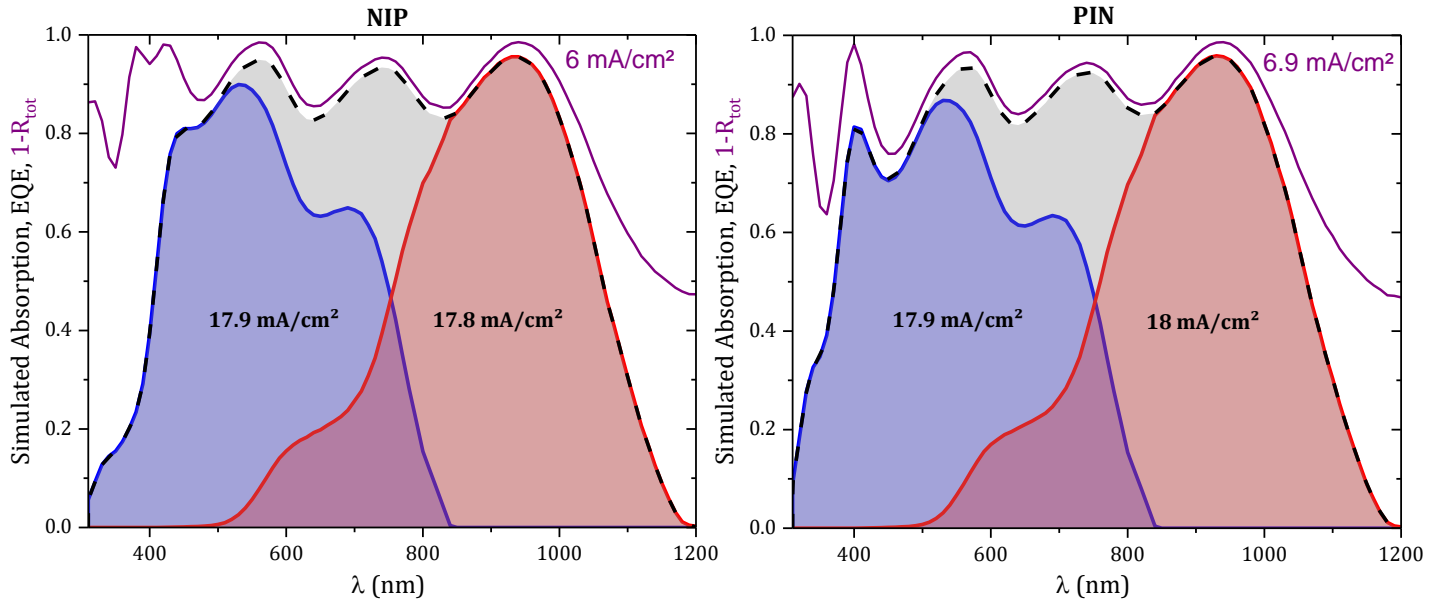


Figure VI.2-2 Simulated absorption and corresponding current in each subcell (top-cell in red and bottom-cell in blue). The EQE is presented in dashed lines and the losses by reflection in purple. NIP architecture on the left and PIN architecture on the right.

Thirdly, as ITO layers are N-type materials with tuneable properties according to their deposition recipe (III.1.3), we optically investigated tandem devices with a thin ITO acting as a selective layer (ETL) in one subcell and forming the RJ. The interest of these

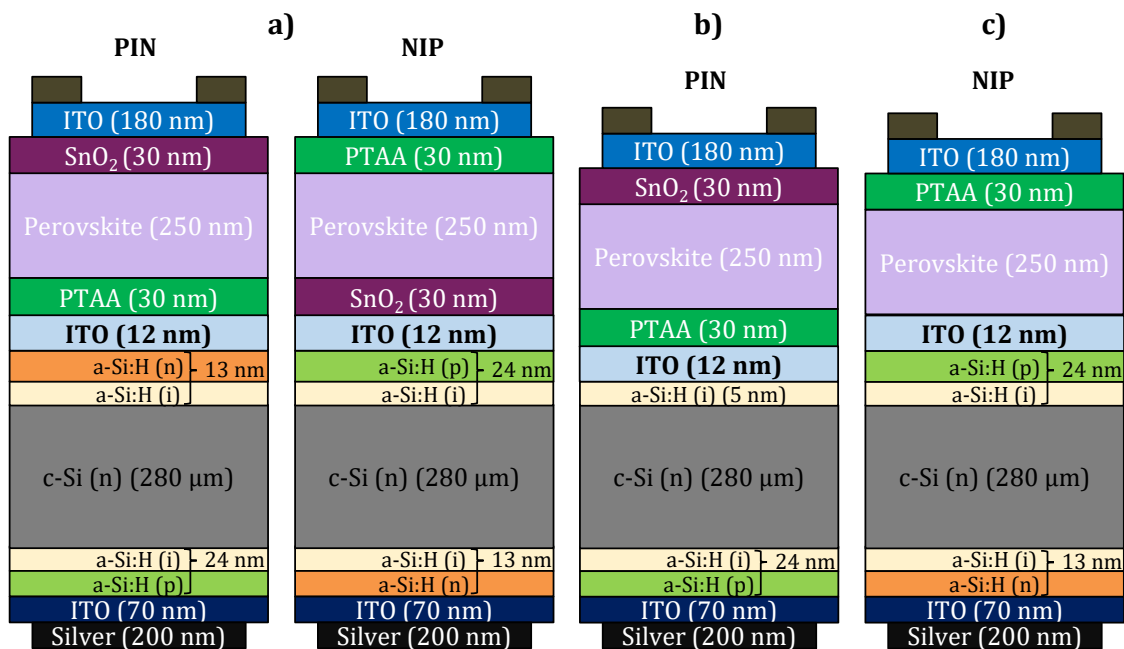


Figure VI.2-3 PK/SHJ tandem solar cell structures with a thin ITO at the junction between both subcells and the thicknesses used for optical simulations. **a)** Reference devices for NIP and PIN architectures. **b)** Device where the ITO replace the a-Si:H (n) layer. **c)** Device where the ITO replace the SnO_2 layer.

devices is the reduction of manufacturing costs by reducing the number of process steps. For this purpose, the RJ does not require the addition of an extra material between the two subcells. In these devices (**Figure VI.2-3 b**) and **c**), the thin ITO layer has two functions: both N-type contact for one of the two subcells (charge selection role), and highly doped N-type layer in a RJ formed with the P-type layer of the second subcell.

Optical simulations were performed using a double-cation Perovskite, with two different thicknesses to obtain a lower current difference between the subcells when the surface state is changed. Thus, the results presented are with a 250 nm thick Perovskite when the front surface is polished and 415 nm thick when the front surface is textured. The c-Si substrate is considered 280 μm thick, like the N-type FZ (100) DSP (CMP) wafers 4-inch sizes used experimentally (see part III.1.1).

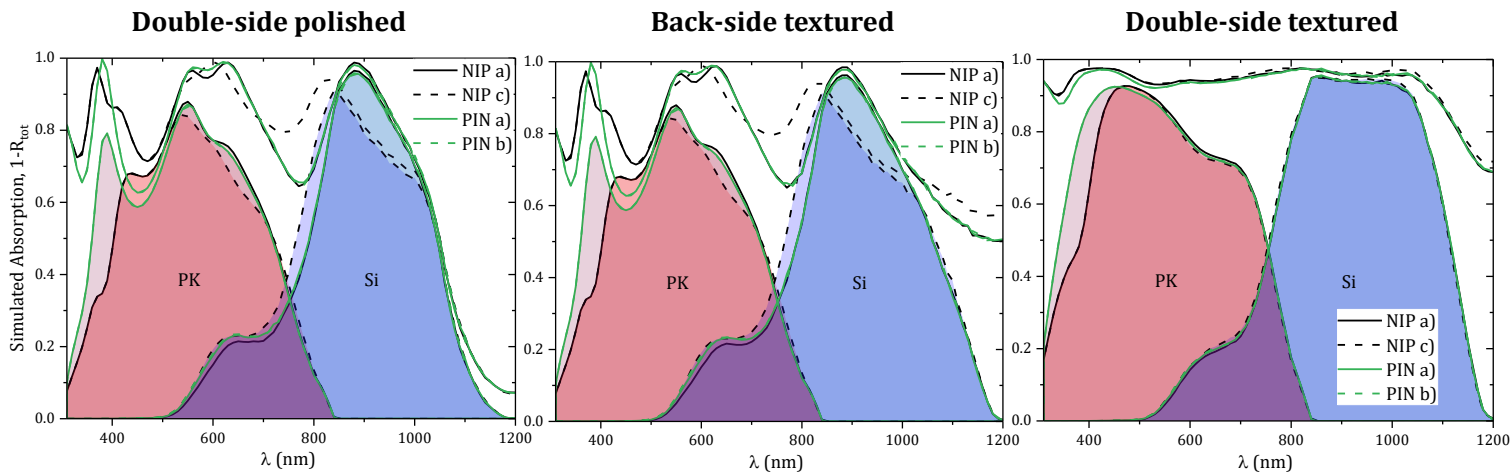


Figure VI.2-4 Simulated absorption of each subcell (top-cell in red and bottom-cell in blue) and $1-R_{\text{tot}}$ obtained by optical simulations, as a function of texturing and architecture (NIP in black and PIN in green) for each studied device (**Figure VI.2-3**).

Obtained results are summed up in **Figure VI.2-4** and **Table VI.2-3**. This optical study demonstrates that the simplified devices presented (**Figure VI.2-3 b**) and **c**) seem viable for both NIP and PIN architectures with a thin ITO junction, regardless of the texturing. Indeed, these simplified devices show very little optical difference from the conventional devices (**Figure VI.2-3 a**) and have the same optical potential, the resulting J_{sc} are very similar (**Table VI.2-3**). Moreover, we observed that with those materials, the NIP architectures have a better optical matching (less reflection losses thanks to a better refractive indexes matching) which compensate the PTAA parasitic absorption. Regarding the texturing, a double-side texturing tends to reduce significantly the impact of the optical parameters in a non-optimally optimised device.

Devices		NIP a)	NIP c)	PIN a)	PIN b)
Double-side polished (250 nm Perovskite layer)	PK J_{sc} (mA/cm^2)	16.95	16.58	16.93	16.91
	Si J_{sc} (mA/cm^2)	15.79	16.36	16.09	16.13
	PCE (%)	21.32	22.09	21.72	21.78
	R_{tot} Losses (mA/cm^2)	11.41	11.18	11.83	11.85
Back-side textured	PK J_{sc} (mA/cm^2)	16.95	16.58	16.93	16.91

(250 nm Perovskite layer)	Si J_{sc} (mA/cm²)	16.58	17.16	16.79	16.88
	PCE (%)	22.38	22.38	22.67	22.79
	R_{tot} Losses (mA/cm²)	9.2	8.73	9.69	9.67
Double-side Textured (415 nm Perovskite layer)	PK J_{sc} (mA/cm²)	19.67	19.42	19.99	19.99
	Si J_{sc} (mA/cm²)	20	20.32	20.1	20.12
	PCE (%)	26.55	26.22	26.99	26.99
	R_{tot} Losses (mA/cm²)	2.9	2.69	3.06	3.05

Table VI.2-3 J_{sc} in each subcell and R_{tot} obtained with optical simulations for the devices of **Figure VI.2-3**. The presented PCE are calculated assuming FF = 75% and V_{oc} = 1.8 V.

In conclusion, even a thin ITO layer (from 10 nm to 12 nm) leads to current losses around 1 mA/cm², which can result to losses in efficiency reaching 1 %. Moreover, the studied devices do not allow exceeding 25 % efficiency with the front-side polished, due to strong reflection losses. Indeed, important changes need to be made, for example adjusting the refractive indexes of the silicon layer in contact with the RJ ITO ([100]) and/or using textured ARC.

VI.2.2. Microcrystalline Silicon Tunnel Junction

In this part, we present a similar optical simulations work to the one carried out in the previous part **VI.2.1**, with the developed microcrystalline silicon tunnel junction (see chapter **IV**) instead of a thin ITO layer as the recombination junction.

Firstly, we performed optical simulations with adjusted thicknesses (presented in **Table VI.2-4**) of the Perovskite (double-cation) and the PTAA layers, to match the current between both subcells, similarly as the study presented in **Figure VI.2-2** (PIN and NIP architectures with front-side polished and back-side textured).

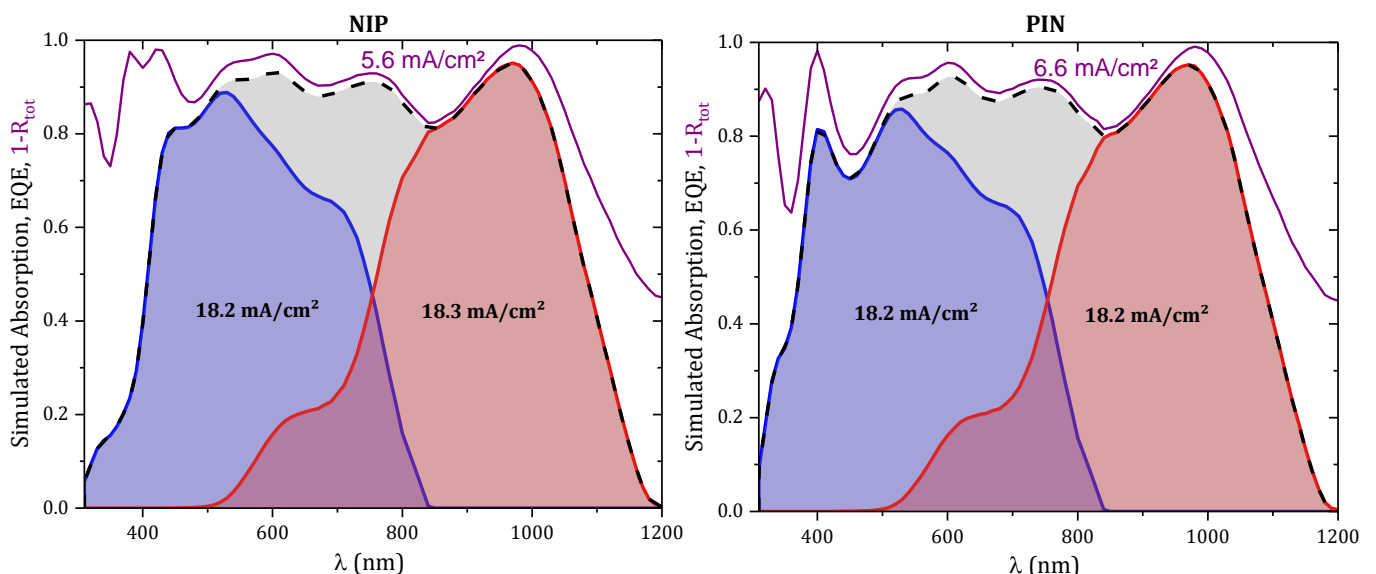


Figure VI.2-5 Simulated absorption and corresponding current in each subcell (top-cell in red and bottom-cell in blue). The EQE is presented in dashed lines and the losses by reflection in purple. NIP architecture on the left and PIN architecture on the right.

Layers	Thicknesses (nm)
ARC (SiO ₂)	100
ITO front	200
SnO ₂	40
Perovskite	260
PTAA	45
μc-Si:H (n⁺/p⁺) (RJ)	40
a-Si:H (i)/ a-Si:H (n)	13
c-Si	160000
a-Si:H (i)/ a-Si:H (p)	24
ITO back	80
Ag	500

Table VI.2-4 Thicknesses of the different layers used in optical simulations with current-matching condition.

Figure VI.2-5 presents the simulated absorption and the corresponding J_{sc} in each subcell. The simulated current losses in the μc -Si:H (n⁺/p⁺) tunnel junction are 0.4 mA/cm² for both architectures. With the same values of FF and V_{oc} used for the similar study with a RJ ITO, $V_{oc} = 1.85$ V and FF = 75 %, the corresponding efficiencies are 25.2 % for the NIP architecture and 25.3 % for the PIN architecture. This demonstrates that the developed μc -Si:H (n⁺/p⁺) tunnel junction is optically better than the thin ITO layer, for these PK/SHJ tandem solar cells: it reduces parasitic absorption and reflection losses.

Secondly, we performed a simulation study with simplified devices (similarly as these presented in **Figure VI.2-3**) composed of at least one microcrystalline silicon layer, a double-cation Perovskite (two different thicknesses depending on the texturing) and a

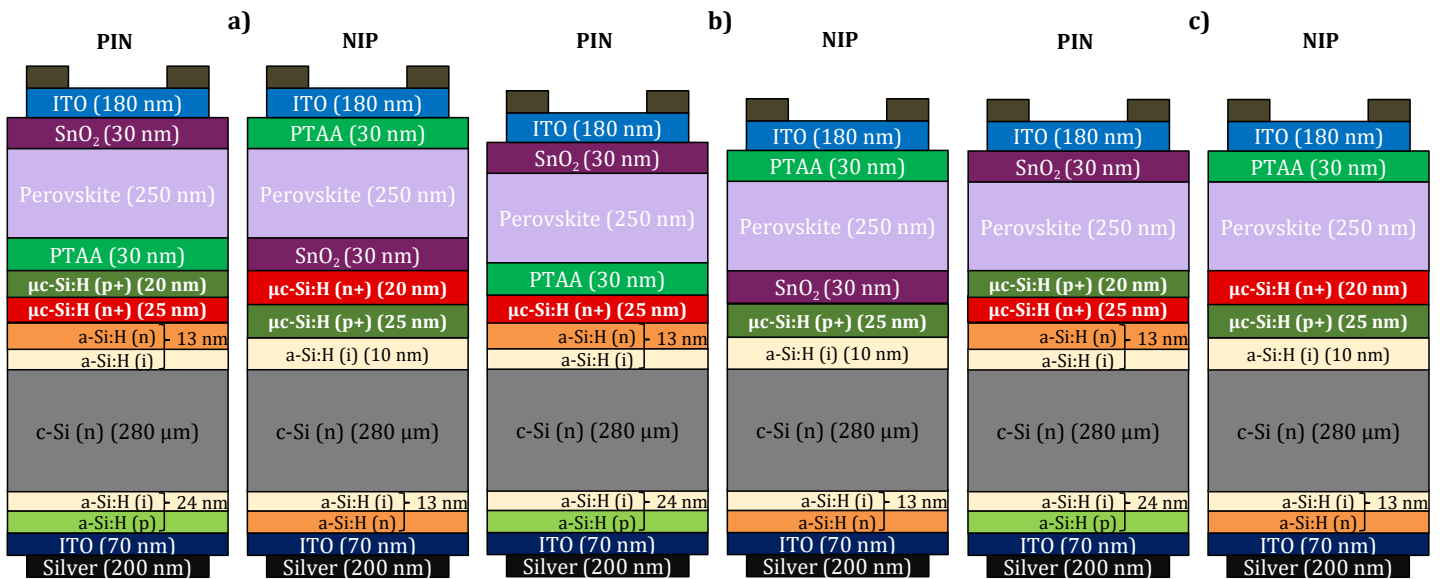


Figure VI.2-6 PK/SHJ tandem solar cell structures with a microcrystalline silicon-based tunnel junction and the thicknesses used for optical simulations. **a)** Reference devices for NIP and PIN architectures. **b)** Devices where a highly doped μc -Si:H layer forms a recombination junction with one of the charges transport layer of the top-cell. **c)** Devices where a highly doped μc -Si:H layer acts as a charges transport layer (ETL or HTL).

c-Si substrate 280 μm thick. The studied devices and the thicknesses used for the simulations are presented in **Figure VI.2-6**. For both architectures (PIN and NIP), the $\mu\text{c-Si:H}$ layers were simulated using the parameters of the developed layers (in chapter IV). Concerning the NIP architectures, we chose to simulate a thick (10 nm) intrinsic layer, combining the amorphous passivating layer and the incubation layer of the $\mu\text{c-Si:H}$ (p^+), to get closer of the experimental reality.

The results of this study are shown in **Figure VI.2-7** and **Table VI.2-5**. Again, we observed that the NIP architectures present less reflection losses, which results in similar J_{sc} to the PIN architectures, despite the front-side PTAA layer. However, microcrystalline silicon layers absorb less than the thin ITO layer, which results in stronger differences between a back-side polished or textured wafer. Indeed, having a back-side textured device is more profitable with $\mu\text{c-Si:H}$ layers instead of a thin ITO.

Devices		NIP a)	NIP b)	NIP c)	PIN a)	PIN b)	PIN c)
Double-side polished (250 nm Perovskite layer)	PK J_{sc} (mA/cm^2)	16.59	16.7	16.39	16.82	16.84	16.59
	Si J_{sc} (mA/cm^2)	17	16.75	16.98	16.47	16.47	16.6
	PCE (%)	22.4	22.55	22.13	22.23	22.23	22.4
	R_{tot} Losses (mA/cm^2)	10.92	11.21	11.1	11.85	11.87	11.91
Back-side textured (250 nm Perovskite layer)	PK J_{sc} (mA/cm^2)	16.59	16.7	16.39	16.82	16.84	16.59
	Si J_{sc} (mA/cm^2)	18.04	17.7	18.09	17.4	17.42	17.63
	PCE (%)	22.4	22.55	22.13	22.71	22.73	22.4
	R_{tot} Losses (mA/cm^2)	8.53	8.97	8.53	9.61	9.62	9.47
Double-side Textured (415 nm Perovskite layer)	PK J_{sc} (mA/cm^2)	19.44	19.55	19.25	19.94	19.91	19.74
	Si J_{sc} (mA/cm^2)	20.87	20.77	21.14	20.64	20.7	20.91
	PCE (%)	26.24	26.39	25.99	26.92	26.88	26.65
	R_{tot} Losses (mA/cm^2)	3.06	3.16	2.97	3.33	3.33	3.24

Table VI.2-5 J_{sc} in each subcell and R_{tot} obtained with optical simulations for the devices of **Figure VI.2-6**. The presented PCE are calculated assuming FF = 75% and V_{oc} = 1.8 V.

As for structures with a thin ITO layer (**Figure VI.2-3**), this study demonstrates that the simplified devices (**Figure VI.2-6 b)** and **c)** are viable for both NIP and PIN architectures. In fact, with some thickness optimisation to obtain a perfect current-matching, the optical potential of each studied structures is very similar.

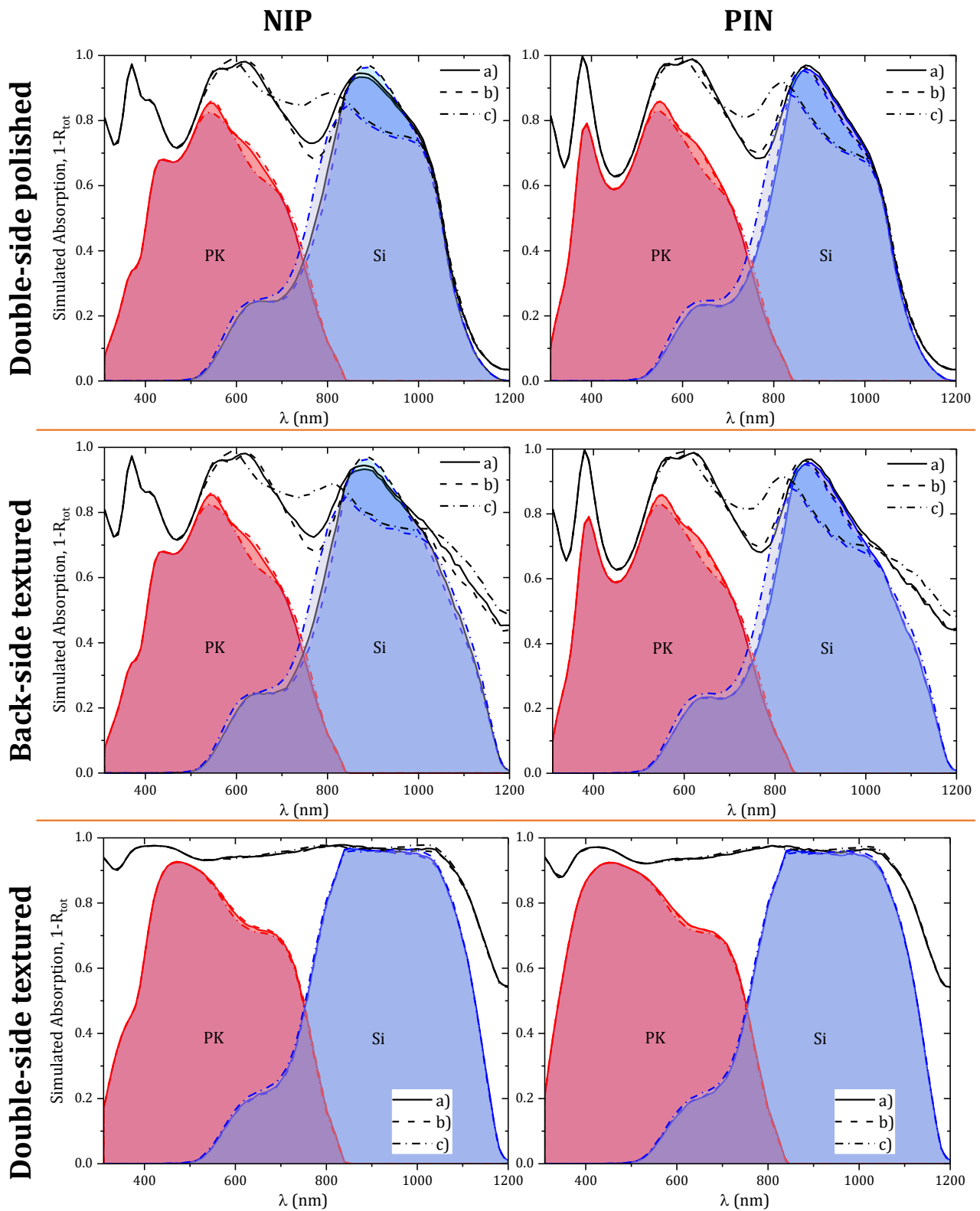


Figure VI.2-7 Simulated absorption of each subcell (top-cell in red and bottom-cell in blue) and $1-R_{tot}$ (in black) obtained by optical simulations, as a function of texturing and architecture, for each studied device (**Figure VI.2-6**).

To conclude, with a complete (PN) microcrystalline silicon tunnel junction, 25 % efficiency is reachable. Moreover, these materials could be optimised to form an efficient recombination junction with the ETL or the HTL of the top-cell (**Figure VI.2-6 b**), or to act as the ETL or the HTL (**Figure VI.2-6 c**). These are great options to reduce the manufacturing cost and time of PK/SHJ tandem solar cells at industrial scale.

VI.2.1. Conclusion

In this part, we have performed optical simulations on PK/SHJ tandem devices with a thin ITO layer or microcrystalline silicon layers as RJ. Those studies demonstrate that in all cases (no matter the architecture, texturing or device), the previously developed microcrystalline silicon tunnel junction (chapter IV) achieves better optical performances than the commonly used junction in thin ITO (12 nm).

Moreover, those studies also show that there is no significant difference between an NIP architecture and a PIN architecture, from an optical point of view, with our experimental materials. Indeed, the best J_{sc} obtained in both architectures are practically equal, whatever the texturing and despite an inequality of absorption between the ETM and the HTM of the Perovskite top-cell. Differences in absorption of the Perovskite top-cell between the NIP and PIN architectures, between 300 and 450 nm, are observed, due to the parasitic absorption of the PTAA (HTM) in the NIP case. However, the NIP architecture always presents less total reflection (R_{tot}), thanks to a better tuning of the refractive indexes. Nevertheless, the PIN architecture studied here is the reverse architecture of the NIP (same HTM and ETM materials). To compare the potential of both architectures, for real integration, interface materials for the PIN architecture have to be modelled and simulated but it was out of the scope of this work.

Furthermore, with the simplified devices **(b)** and **(c)** in **Figure VI.2-3** and **Figure VI.2-6**), very little differences are obtained in the case of double-side texturing. When the front-side is polished, devices **(c)** (without SnO_2) are found to be different from the other devices in terms of absorption distribution in the tandem solar cell. However, the resulting short circuit currents are very similar. In conclusion, all studied simplified devices **(b)** and **(c)** from **Figure VI.2-3** and **Figure VI.2-6**) are viable in tandem solar cell, and this for NIP and PIN architectures, with a thin ITO or microcrystalline silicon junction, regardless of the texturing.

Not surprisingly, **Figure VI.2-4** and **Figure VI.2-7** highlight the significant optical gain obtained with a textured substrate. Indeed, for a double-side polished device, the J_{sc} , obtained by optical simulation, of the tandem solar cell rarely exceeds 17 mA/cm^2 . It can slightly exceed 17.5 mA/cm^2 for a polished/textured device, while it is higher than 20 mA/cm^2 in the case of double-side textured devices. However, in the current state of developments on the implementation of Perovskite layers, the deposition of the Perovskite is very complicated on large textured surfaces. Thus, optimisations such as the addition of an anti-reflection layer and/or a textured foil, on the polished front-side, allow to reduce these differences ([99], [196]).

To conclude, optical simulations give us leads for optimising the RJ materials and their thicknesses. However, these simulations do not guarantee the electrical performance of those RJ materials. Thus, they must be combined with electrical characterisations, such as those presented in the previous chapter V or those comprising a complete tandem structure that we present in the next part VI.3.

VI.3. Investigation of the Recombination Junctions Influence on the Perovskite Top-Cell

In the previous part, we have studied tandem solar cells with optical simulations for different RJ. In this part, we present a method to investigate the influence of the RJ on Perovskite top-cell, electrically and structurally.

Playing on RJ materials to reduce parasitic absorption is important, but the Perovskite top-cell formation on the RJ is also a key factor. In this part, we use a “tandem-like” device to measure J-V curves of the Perovskite top-cell made in tandem conditions. This device is composed of an isotype bottom-stack, the RJ and the Perovskite top-cell. **Figure VI.3-1** shows “tandem-like” devices and the corresponding circuit diagram. In order to study a Perovskite top-cell in the NIP architecture, an N-type stack replaces the bottom-cells. Thus, the top-cell layers deposition (starting from the ETL) occurs the same way as in a PK/SHJ tandem solar cell, while the substrate behaves like a large N-type contact (represented by a resistance in the circuit diagram, **Figure VI.3-1**). In this work, we used these “tandem-like” devices with several possible RJ to investigate their impact on the Perovskite top-cell.

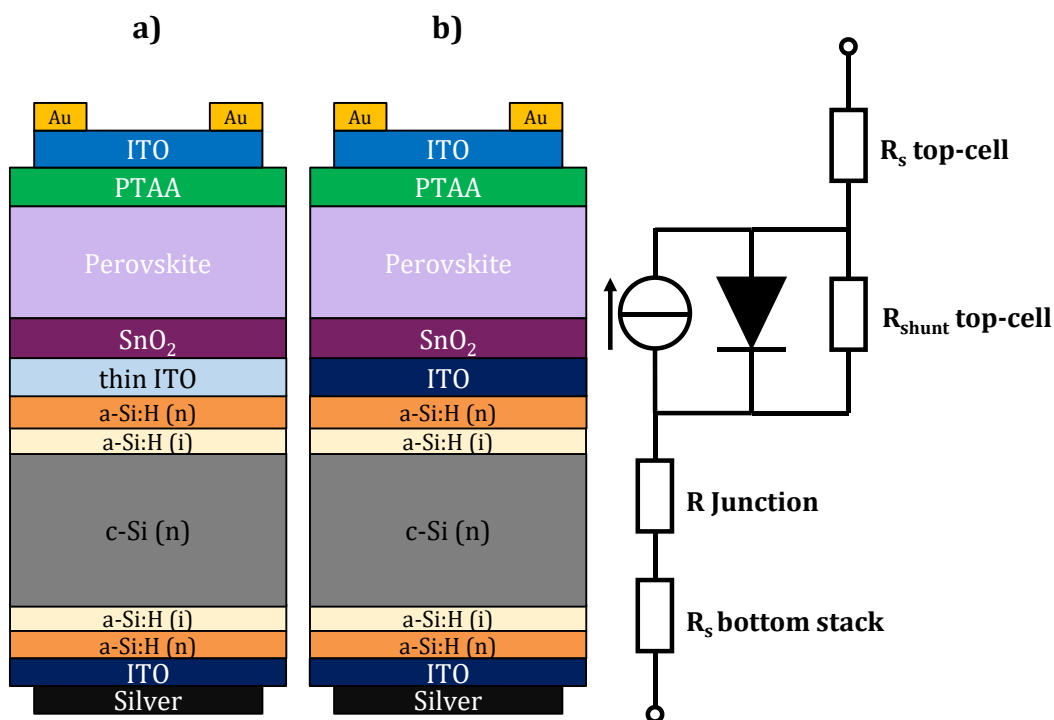


Figure VI.3-1 a) “Tandem-like” device with a thin ITO layer as the RJ, b) “Tandem-like” device with a thick ITO layer (70 nm) as the RJ and the corresponding circuit diagram of these devices (using the one-diode model for the Perovskite top-cell).

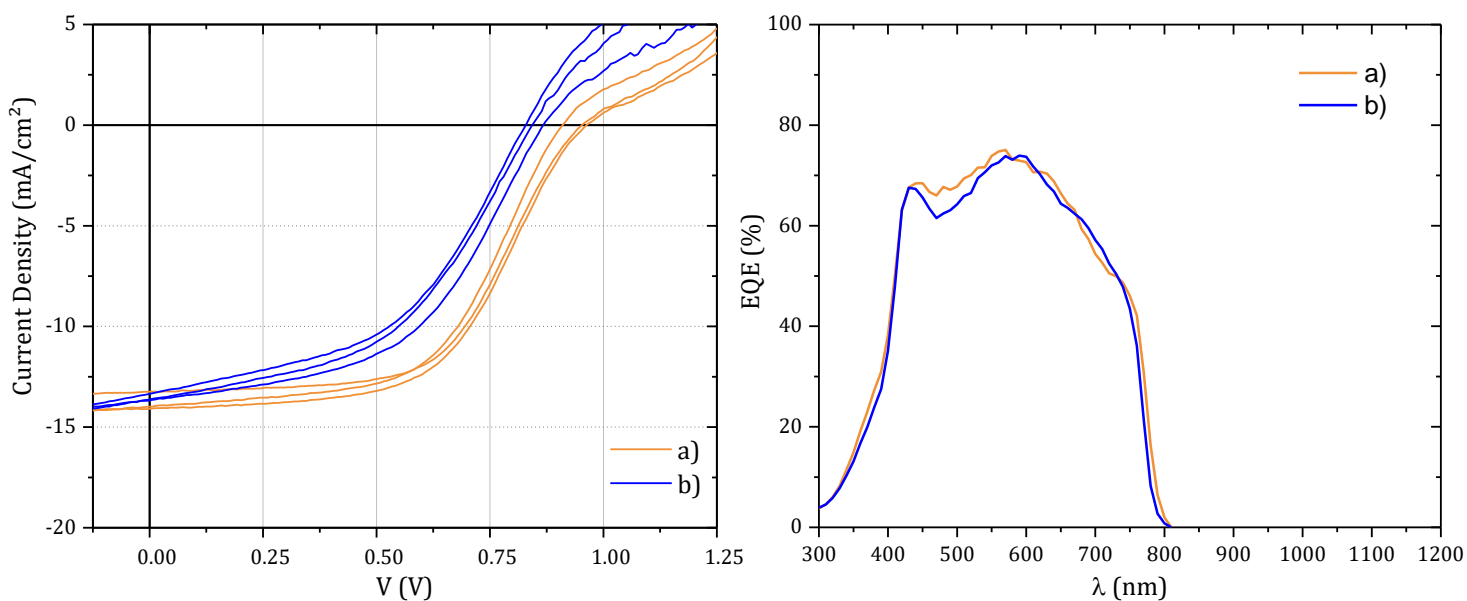


Figure VI.3-2 J-V curves in the left and EQE spectra in the right of the studied devices a) (in orange) and b) (in blue) from **Figure VI.3-1**.

Devices	a) 1	a) 2	a) 3	b) 1	b) 2	b) 3
J_{sc} (mA/cm ²)	16.11	17	17.1	16.6	16.22	16.56
V_{oc} (V)	0.953	0.910	0.964	0.869	0.828	0.844
PCE (%)	8.85	8.68	9.14	7.25	6.44	6.67
FF (%)	57.68	56.16	55.46	50.27	47.96	47.76

Table VI.3-1 J-V parameters of the studied devices **a)** and **b)** from **Figure VI.3-1** obtained with I-V measurements (3 samples of each device), after a shading correction on the J_{sc} (the shading induce by the metallisation is different for each sample, a correction is applied to compare the devices with the same active area).

Figure VI.3-2 and **Table VI.3-1** demonstrate that the “tandem-like” devices work well to measure the Perovskite top-cell only. Indeed, the measured EQE and V_{oc} correspond to a single-junction Perovskite solar cell and the J_{sc} are correlated with those obtained for the Perovskite top-cell by optical simulations of these “tandem-like” devices. Furthermore, we observed on the J-V curves the same trends as in our PK/SHJ tandem solar cells, which is different from a Perovskite single-junction on glass (see **Appendix C**). This confirms that the “tandem-like” device allows us to measure the Perovskite top-cell in tandem conditions.

Another way to assess the top-cell properties under illumination would be to saturate the bottom cell using an additional IR source, so as to force the tandem into the top-limited configuration (see **Appendix C**). However, the obtained I-V curve in that case would not directly correspond to the sole I-V curve of the Perovskite solar cell (because of voltage addition). The method proposed here therefore enables a direct measurement of the I-V curve of the Perovskite top cell.

Comparing the **a)** and **b)** devices from **Figure VI.3-1**, we observed that the **b)** devices present less V_{oc} and large shunt issues (which results in smaller FF and PCE). In order to investigate those differences, some structural characterisations can be performed on the Perovskite layer to compare the layers properties. In our case, we performed XRD and SEM measurements.

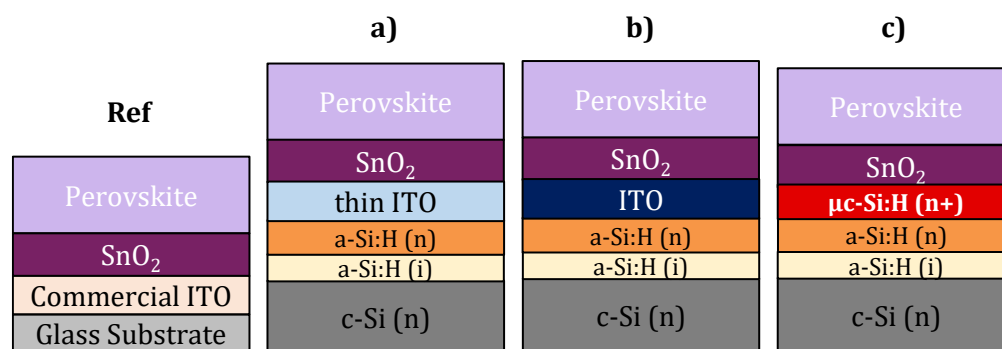


Figure VI.3-3 Substrates used to investigate the Perovskite layer: a **Ref** on commercial glass substrate (as the Perovskite single-junction solar cells), **a)** Simplified version of the “tandem-like” device with a thin ITO layer, **b)** “tandem-like” substrate with a thick ITO layer and **c)** “tandem-like” substrate with a $\mu\text{c-Si:H}$ (n^+) layer instead of an ITO.

Figure VI.3-4 shows SEM measurements of the Perovskite layer deposited on different substrates (presented in **Figure VI.3-3**). We observe “dark holes” (missing grains) in the layer, no matter the substrate. Moreover, in addition to the grains of Perovskite, we notice small bright grains in all the studied samples. These small grains correspond to

the PbI_2 (or $\text{PbI}_{1.5}\text{Br}_{0.5}$) in excess after the Perovskite crystallisation process ([197], [198]). Overall, no obvious differences are observed between the different substrates. However, the grains size is a bit larger in the **a)** and **b)** cases than for the **reference** on glass and in the **c)** case (substrate without ITO).

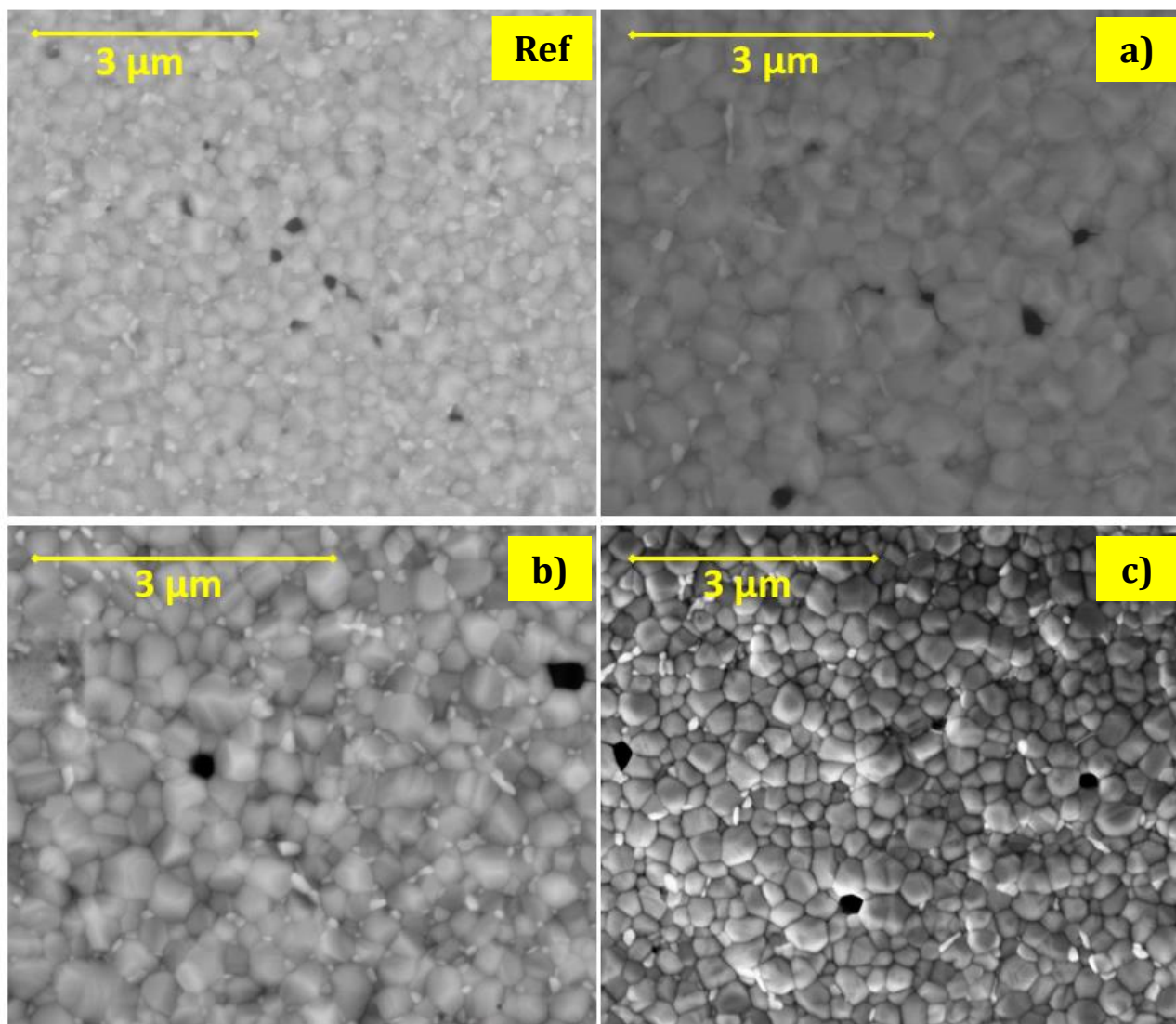


Figure VI.3-4 SEM images (III.2.8.a) of the Perovskite layer deposited on the substrates presented in **Figure VI.3-3**.

X-ray diffraction measurements (**Figure VI.3-5**) revealed more differences in the Perovskite layer composition than the SEM images. We observed that the ratio between the Perovskite peak and the PbI_2 (or $\text{PbI}_{1.5}\text{Br}_{0.5}$) peak seems to be dependent on the substrate. These results tend to show that there is less crystallised PbI_2 in excess in the **reference** sample and in the sample without ITO (**c)** **Figure VI.3-3**).

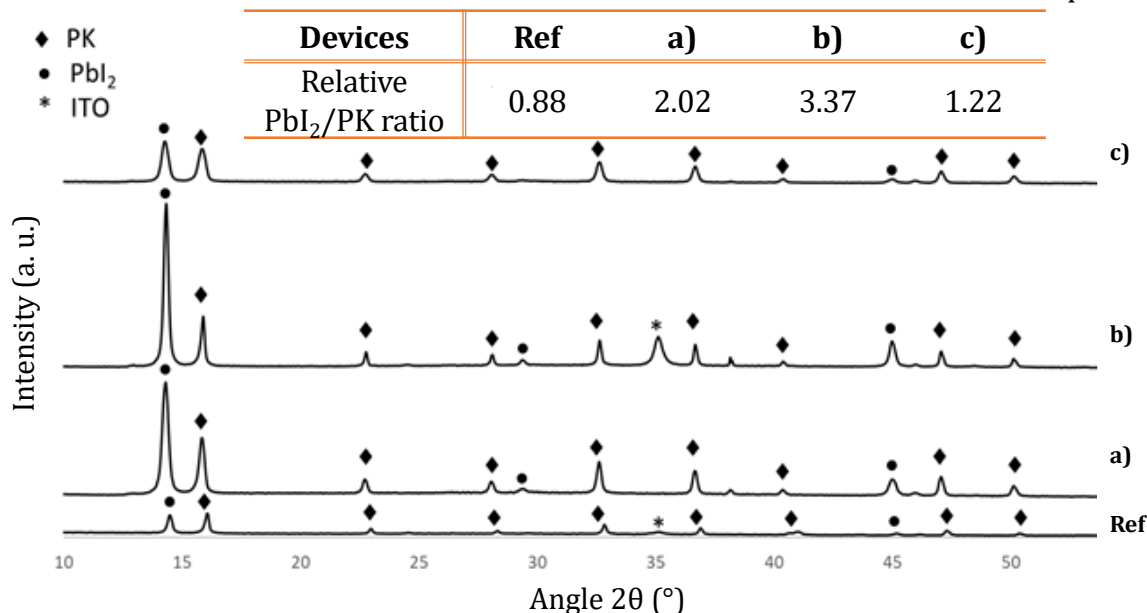


Figure VI.3-5 X-ray diffraction patterns (Bragg-Brentano geometry, Co source, see part (III.2.10) of the Perovskite layer deposited on the substrates presented **Figure VI.3-3**. The inset table shows the area ratios of low angle PbI₂ and Perovskite diffraction peaks.

After validating that “tandem-like” devices worked well, we did a more complete study using the devices presented in **Figure VI.3-6**. In order to avoid the formation of a tandem solar cell, we used fully symmetrical and isotype (N-type) bottom-stack, except for the device **e)** which acts as a reference compared to the previous test (**Figure VI.3-1 a)**). The main objective of this study is to observe if the shunt issues in our PK/SHJ tandem solar cells (see **Appendix C**), also observable in the previous test (**Figure VI.3-2**), are also obtained with a microcrystalline silicon junction (without ITO), or not.

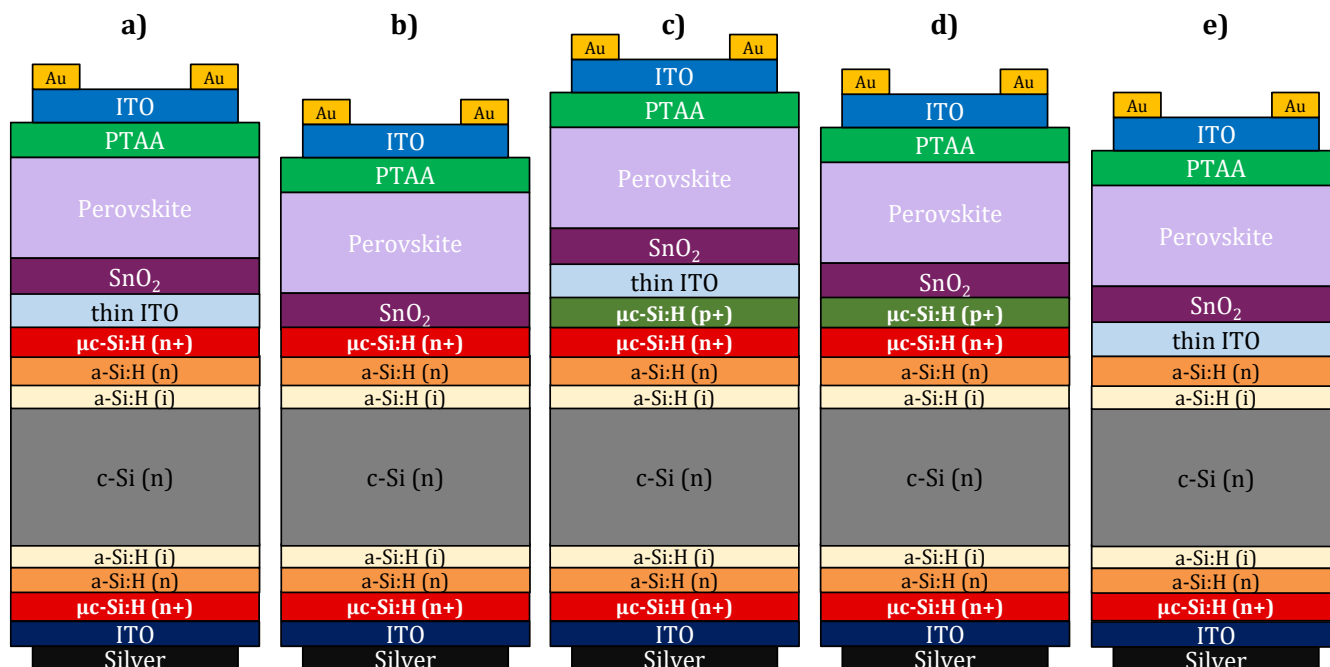


Figure VI.3-6 “tandem-like” devices with different junctions between the Perovskite top-cell and the N-type bottom-stack.

Devices **a)** and **e)** should lead to very similar results, except if the non-symmetrical bottom-stack of the device **e)** acts as a solar cell (and not a resistance) or if the thin ITO has very different properties when it is deposited on a $\mu\text{c-Si:H (n}^+)$ layer instead of the a-

Si:H (n) (which is possible [58]). Concerning the device **c)**, according to the $\mu\text{c-Si:H}$ (n^+/p^+) thickness, the thin ITO layer should be different than in the device **e)**. Moreover, the NPN junction (see part V.3) in the device **c)** could affect the measurement. Devices **b)** and **d)** have a junction only composed of microcrystalline silicon, but the device **d)** also presents a NPN junction ($\mu\text{c-Si:H}$ (n^+) / $\mu\text{c-Si:H}$ (p^+) / SnO_2).

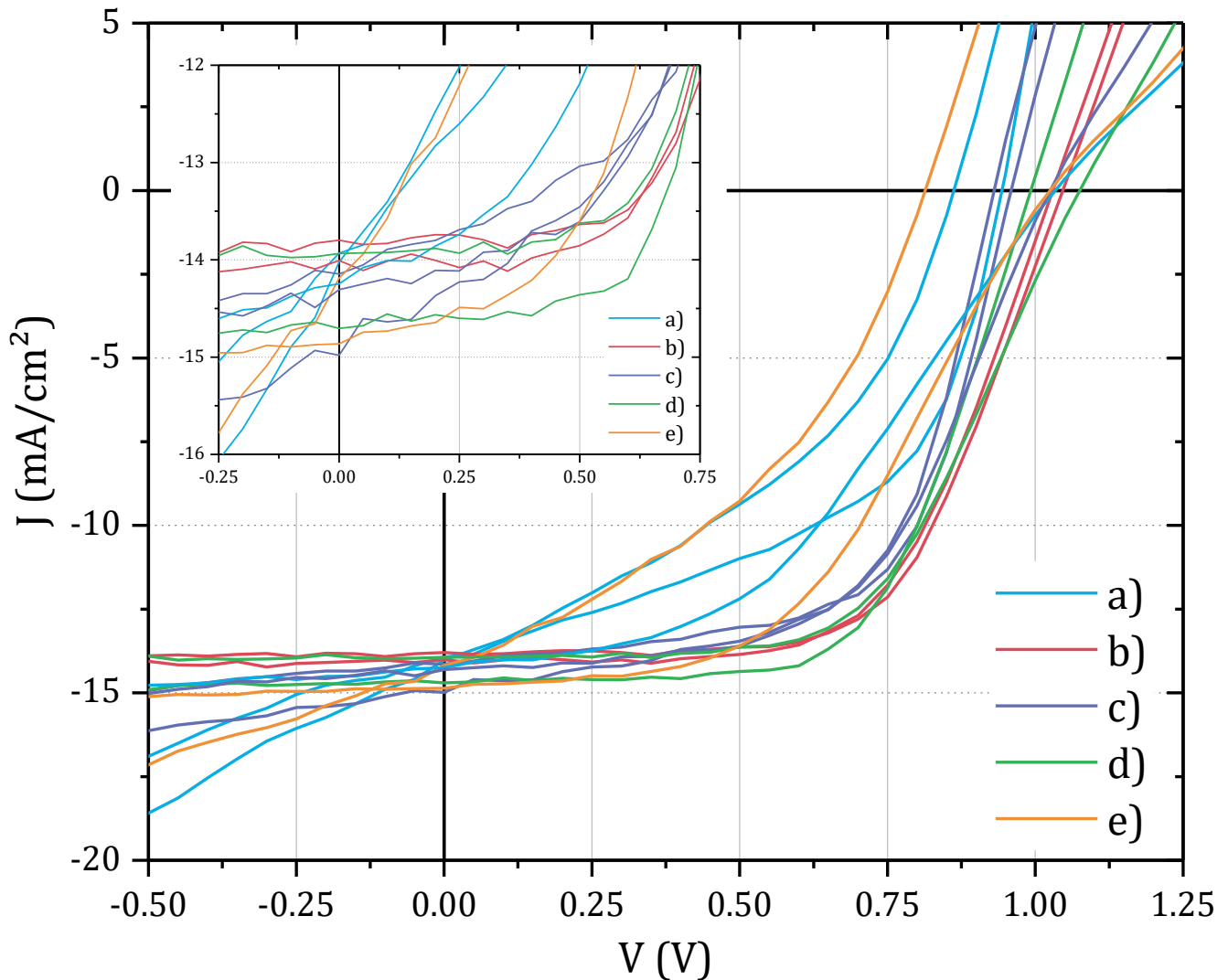


Figure VI.3-7 J-V curves of the “tandem-like” devices from **Figure VI.3-6** (2 or 3 samples per device type). A zoom is presented in inset to more easily differentiate the curves.

The measured J-V curves are presented in **Figure VI.3-7** and the corresponding parameters in **Figure VI.3-8**. We observed a large variability between the samples of devices **a)** and **e)**, probably due to more sensitivity to the process steps (the spin-coated layers vary according to the manual process conditions) compared to the other devices. Moreover, the observed J_{sc} variations for all devices are also due to the manual process conditions, which modify the Perovskite thickness. However, as expected according to the previous study, devices **a)**, **c)** and **e)** with a thin ITO layer present shunt issues, although devices **c)** seem less shunted (but as mentioned previously, ITO growth might differ from cases **a)** and **e)** and/or the NPN junction could help decreasing the shunt current). Regarding the devices **b)** and **d)**, with only microcrystalline silicon in the junction, no shunt issue was observed. This tends to demonstrate that the ITO layer plays a role in those shunt issues, probably mainly due to its high lateral conductivity ([13], [167]), but other factors can also play their role (e.g. a mix between the ITO and the SnO_2 layer, see **Appendix C**).

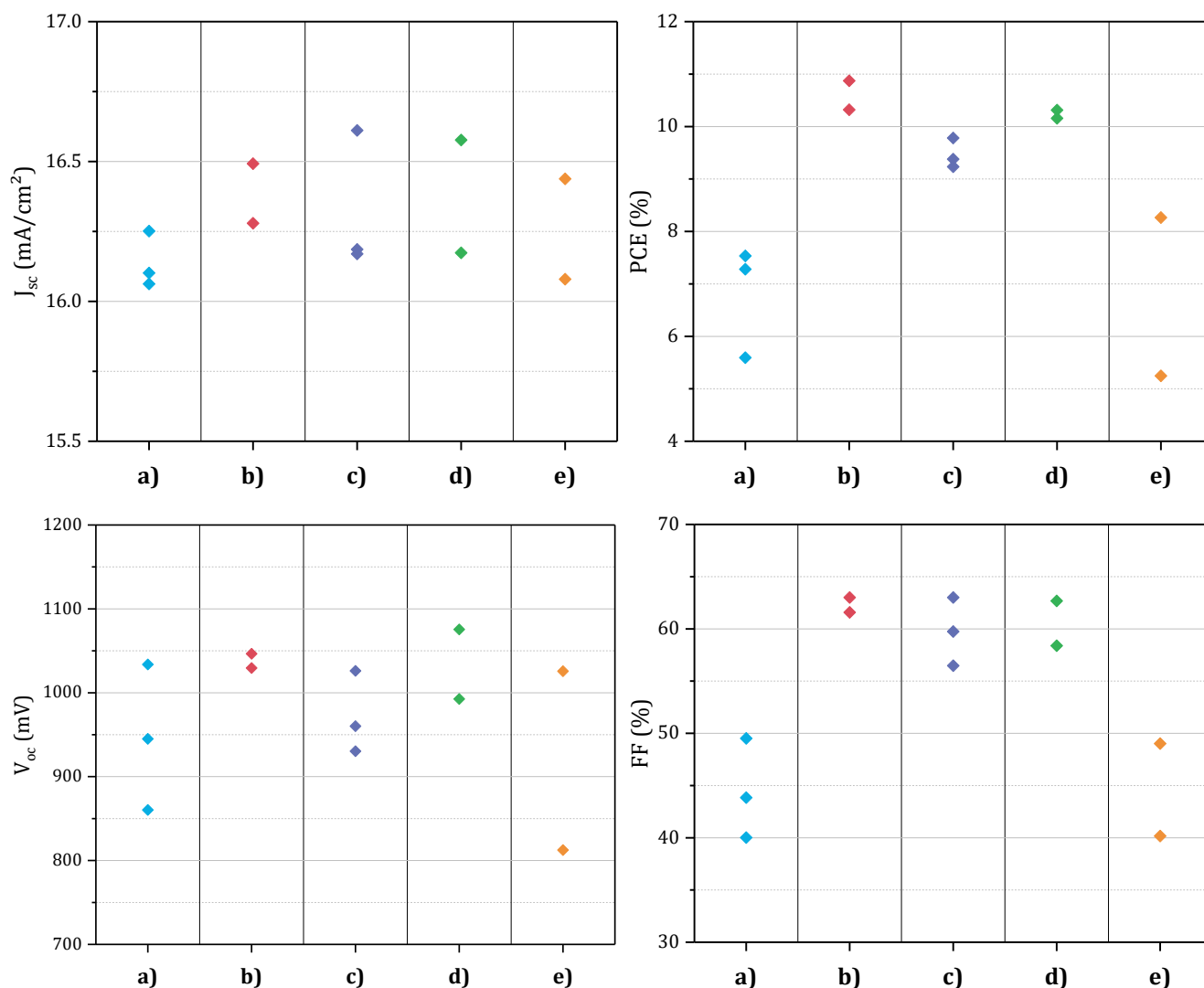


Figure VI.3-8 J-V parameters of the “tandem-like” devices from **Figure VI.3-6** obtained with I-V measurements, after a shading correction on the J_{sc} (the shading induce by the metallisation is different for each sample, a correction is applied to compare the devices with the same active area).

Regarding the J-V parameters, we observed that the devices **b)** **c)** and **d)**, without the thin ITO layer or with the $\mu\text{-Si:H}$ (n^+/p^+) junction, obtained better FF than the other devices. This is a promising result concerning the Perovskite top-cell quality on the developed microcrystalline silicon RJ (chapter IV).

Then, we performed STEM-EDX measurements (III.2.8.b) on the best devices **c)** and **d)** to look if we can observe some differences between the two Perovskite top-cells, which could explain the shunt issues. Nevertheless, we did not observe such differences (see Appendix C).

Next, in order to confirm experimentally that the $\mu\text{-Si:H}$ (n^+/p^+) junction is optically better than the thin ITO layer (see previous part VI.2.1), we performed spectrophotometry measurements (III.2.2) on the final devices and compared the result with optical simulations of the same devices. The results are presented in **Figure VI.3-9**. Firstly, we observe that the experimental results are consistent with the simulations, according to the possible variations in the layers thicknesses and properties during the fabrication process (reflectance peaks are reproduced and quite well adjusted to experimental data). Secondly, the devices **b)** (in red) and **e)** (in green), with only

microcrystalline silicon in the junction, have less total reflection (in particular from 800 nm to 950 nm) in both experimental and simulation cases. This demonstrates that the developed $\mu\text{c-Si:H}$ (n^+/p^+) junction is optically more adapted than a thin ITO layer for PK/SHJ tandem solar cells.

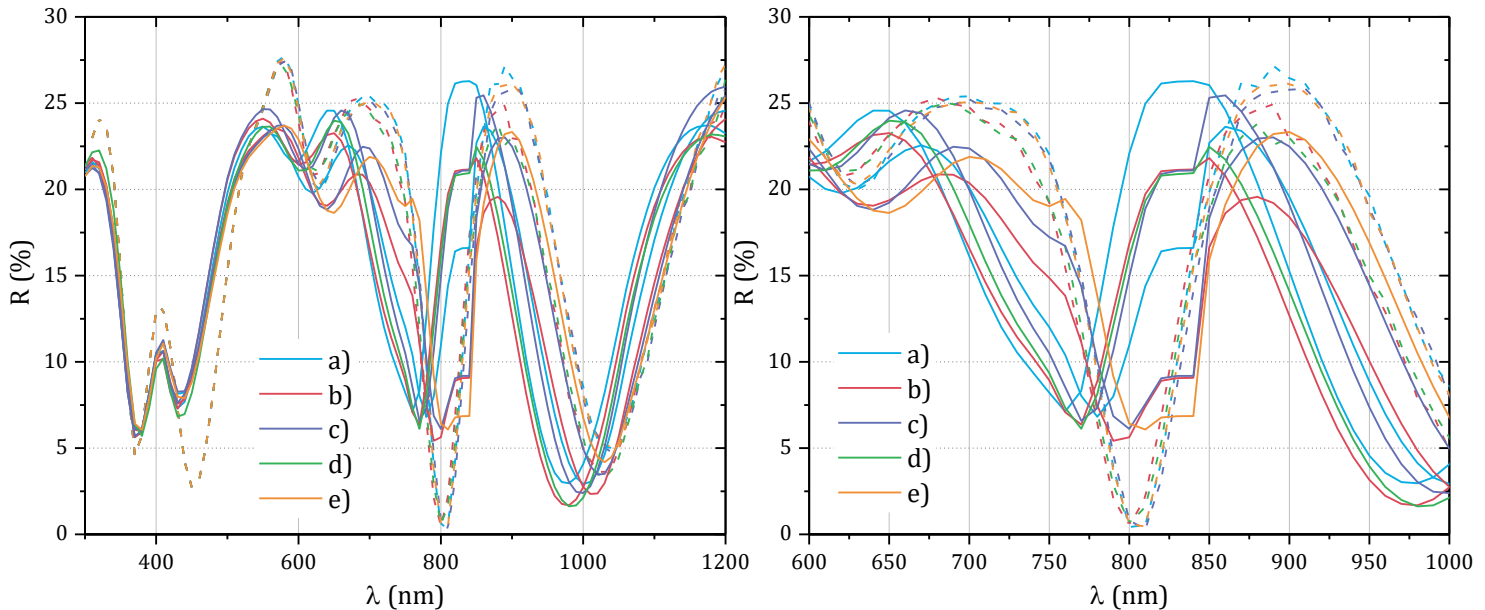


Figure VI.3-9 R_{tot} of the devices from **Figure VI.3-6**, measured by spectrophotometry in solid lines and obtained with optical simulations in dashed lines. On the right, a zoom is done to have a better view of each curve, from 600 nm to 1000 nm.

In conclusion, “tandem-like” devices, composed of an isotype bottom-stack, the RJ and the Perovskite top-cell, deposited in the same conditions as in PK/SHJ tandem solar cells, allow measuring I-V curves of the Perovskite top-cell only. Moreover, some characterisations (XRD, SEM, STEM-EDX, SE...) can be performed during the fabrication process of these “tandem-like” devices, which is useful to investigate and understand the substrate and the RJ influence on the Perovskite top-cell. Furthermore, these devices are important to optimise the matching between recombination junctions and the Perovskite top-cell.

VI.4. Tandem Solar Cells Integration

In chapter IV, we have developed a microcrystalline silicon tunnel junction for PK/SHJ tandem solar cells with the PIN architecture. Moreover, in chapters IV, V and in the previous parts, we have characterised this junction and investigated its influence on the top and bottom-cells separately. In this part, we integrate this developed $\mu\text{c-Si:H}$ (n^+/p^+) junction in PIN PK/SHJ tandem solar cells.

For technical reasons concerning the deposition of the Perovskite top-cell in the PIN configuration, we did not use the previously presented PTAA as the HTL but a PEDOT:PSS (Poly(3,4-EthyleneDiOxyThiophene) PolyStyrene Sulfonate) layer. Furthermore, we also tested a SAM as HTM in the device **e**) but the assembly of the molecule (with a process suitable for a deposition on an ITO layer) was not conclusive on the microcrystalline silicon (see **Figure VI.4-1** and **Table VI.4-1**). A complete study on this subject is mandatory for a better understanding of this behaviour (not in this work).

In order to avoid the degradation of the $\mu\text{-Si:H}$ layers during the UV/O₃ pretreatment (see part III.1.6) and highlight its impact, we tested the deposition of the PEDOT:PSS, by spin-coating in different conditions. First, with an UV/O₃ pretreatment for less than 3 min, the $\mu\text{-Si:H}$ surface was too hydrophobic, no PEDOT:PSS layer was obtained. Secondly, after an UV/O₃ pretreatment during 3 min, the device **a**) (in yellow in **Figure VI.4-1**) has a usual shape but a low V_{oc} due to the bad deposition of the PEDOT:PSS layer. This demonstrates that a 3 min UV/O₃ pretreatment seems acceptable for the $\mu\text{-Si:H}$ (no S-shape) but is not enough for the PEDOT:PSS deposition.

Finally, after a UV/O₃ pretreatment during 5 min, the first processed device (device **b**), in purple in **Figure VI.4-1**) obtained the expected V_{oc} and J_{sc} parameters (respectively the tensions addition of the subcells and a low J_{sc} because of a bad current-matching due to the strong absorption in the IR of the PEDOT:PSS, [199]). Moreover, this device **b**) exceeded 10 % efficiency, even with a very small S-shape at the V_{oc} (affecting the FF). However, the more time there has been between the UV/O₃ pretreatment (device **b**) then device **c**) then device **d**)) and the PEDOT:PSS deposition the larger the S-shape is at V_{oc} (see devices **b**), **c**) and **d**) in **Figure VI.4-1**). This tends to demonstrate that after the UV/O₃ pretreatment, the oxide layer continues growing and creates a barrier at the $\mu\text{-Si:H}$ (p⁺)/PEDOT:PSS interface, resulting in the S-shape.

Nevertheless, the most positive point is that the devices **a**), **b**), **c**) and **d**) do not seem to have any shunt issues, as expected with the $\mu\text{-Si:H}$ (n⁺/p⁺) junction. We also want to specify that the presented results were measured right after the solar cells fabrication and that they improve during cycling (light soaking) but also after storage in air for at least three days.

Devices	a)	b)	c)	d)	e)
Pretreatment / HTM	3 min UV/O ₃ PEDOT:PSS	5 min UV/O ₃ PEDOT:PSS			5 min UV/O ₃ SAM (2-PACz)
J_{sc} (mA/cm ²)	12.96	13.07	12.98	12.82	1.82
V_{oc} (V)	1.345	1.593	1.587	1.591	1.376
PCE (%)	7.35	10.10	7.53	5.23	0.25
FF (%)	42.16	48.51	35.55	25.64	N/A

Table VI.4-1 J-V parameters of PIN PK/SHJ tandem solar cells, with the developed $\mu\text{-Si:H}$ (n⁺/p⁺) junction (see **Figure IV.1-1**), extracted from I-V measurements with two different HTM (PEDOTS:PSS and a SAM), without shading correction on the J_{sc} .

In conclusion, these first integration results show three main observations:

- No shunt issues were observed with the $\mu\text{-Si:H}$ (n⁺/p⁺) junction as the RJ.
- The oxide layer formation during the UV/O₃ pretreatment on the $\mu\text{-Si:H}$ (n⁺/p⁺) junction impacts the electrical performances of the tandem solar cells (J-V curves have a S-shape depending on the pretreatment duration and the time between the pretreatment and the HTM deposition, which strongly affect the FF).
- If we want to avoid the parasitic absorption of the PEDOT:PSS layer (in order to increase the current) and, at the same time, improve the top-cell V_{oc} , another HTM has to be used in this PIN architecture. A SAM layer ([107]) might be a best choice

but its assembly on the $\mu\text{-Si:H}$ (n^+/p^+) junction should be studied beforehand ([200]).

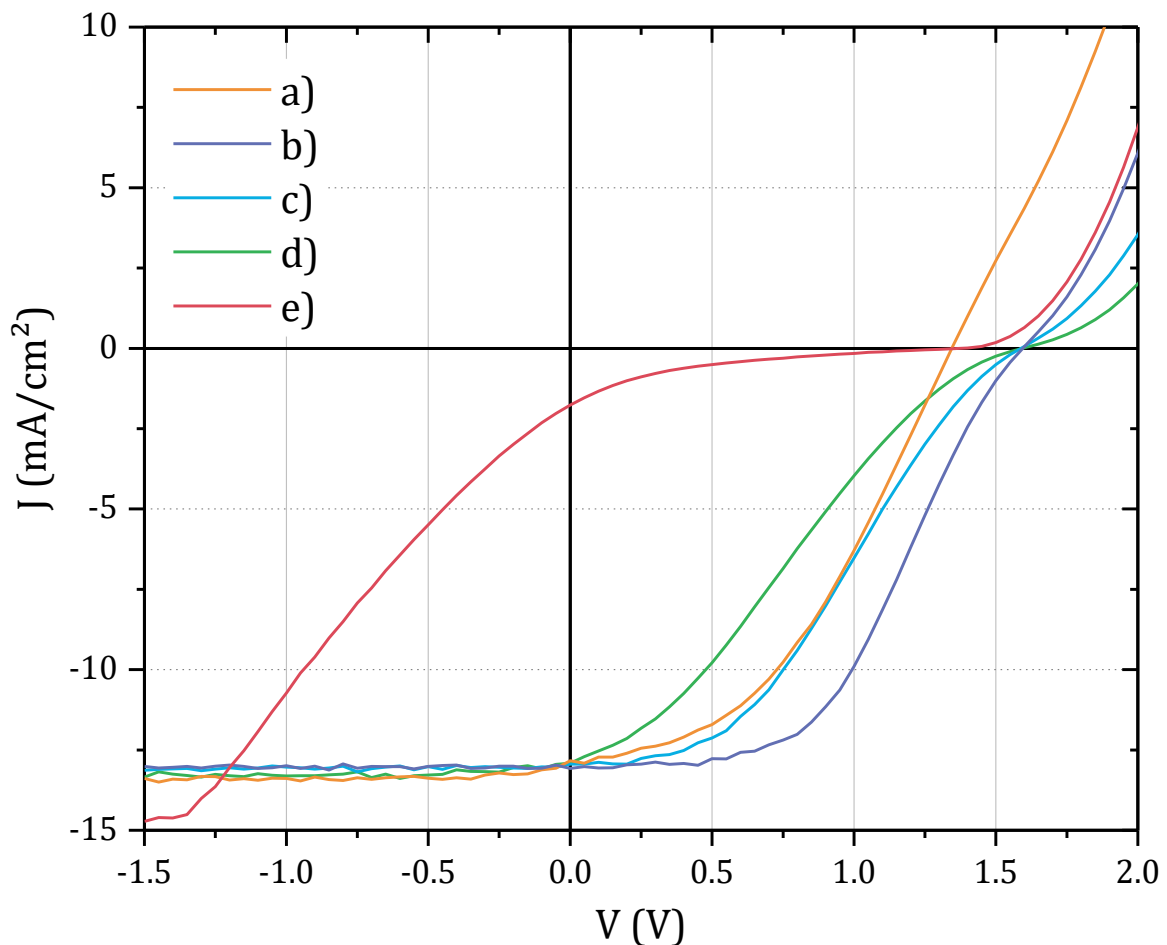


Figure VI.4-1 J-V curves of PIN PK/SHJ tandem solar cells, with the developed $\mu\text{-Si:H}$ (n^+/p^+) junction (**Figure IV.1-1**), with two different HTM and different pretreatment duration: **a)** 3 min UV/O₃ and PEDOT:PSS; **b), c) and d)** 5 min UV/O₃ and PEDOT:PSS; **e)** 5 min UV/O₃ and a SAM (2-PACz) HTM,

VI.5. Chapter Conclusion

In this chapter, we have used optical simulations, using the CROWM software (see part III.4), to compare the previously developed microcrystalline silicon tunnel junction (see chapter IV) to the usually thin ITO layer used as RJ in PK/SHJ tandem solar cells. Moreover, these optical simulations also allowed us to study the impact of this thin ITO layer according to its thickness and to investigate the viability of simplified PK/SHJ tandem solar cell structures. We found that, even below 15 nm, the ITO layer induces more than 0.5 mA/cm² of current losses due to its parasitic absorption, which is more than the developed $\mu\text{-Si:H}$ (n^+/p^+) junction. Other TCOs, more transparent, can also be used to replace the usual ITO (IZO, AZO...) but their development is needed. Furthermore, the optical simulations also demonstrated that the presented simplified devices (see **Figure VI.2-3** and **Figure VI.2-6**) have the same optical potential as the reference devices. This is interesting because with these simplified devices, we can

reduce the number of steps in the fabrication process, thus reducing the manufacturing cost.

In the second part, we demonstrated that “tandem-like devices”, presented in **Figure VI.5-1**, are important structures for the development of PK/SHJ tandem solar cells. In fact, they allow measuring the Perovskite top-cell, which has been deposited in the same conditions as in PK/SHJ tandem solar cells. This enables studying the influence of the bottom-cell substrate and the RJ on the Perovskite top-cell quality and optimising or adapting them (the RJ and both subcells) to each other.

Moreover, we used these “tandem-like” devices to compare the influence on the Perovskite top-cell of the previously developed microcrystalline silicon tunnel junction (see chapter IV) and of the thin ITO layer. We observed that with the $\mu\text{c-Si:H}$ (n^+/p^+) junction, the devices have much less shunt issues and less losses by reflection. Furthermore, the measured FF is also better with $\mu\text{c-Si:H}$ layers in the junction. In conclusion, a microcrystalline silicon tunnel junction seems to be the best choice of recombination junction, compared to an ITO layer.

To conclude this work, we integrated the developed $\mu\text{c-Si:H}$ (n^+/p^+) junction in PIN PK/SHJ tandem solar cells and obtained promising results, without shunt issues and exceeding 10 % efficiency. Moreover, these results demonstrated the importance of studying the deposition of the Perovskite top-cell (e.g. with “tandem-like” devices from **Figure VI.5-1**) on the RJ. Indeed, it is very important to find the best compromise between the different fabrication steps and to improve them jointly (e.g. pretreatments, annealing...). What improves one layer should not degrade another (at least at minimum possible).

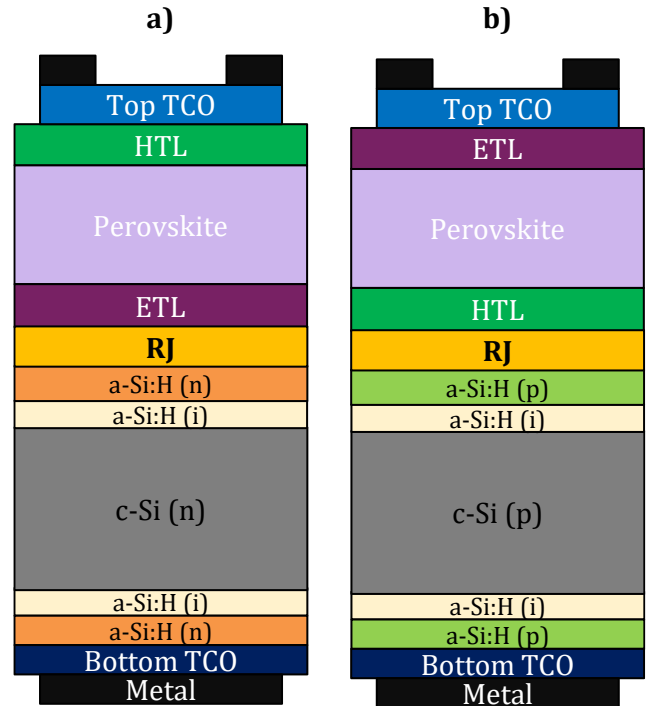


Figure VI.5-1 “tandem-like” devices to measure the Perovskite top-cell processed in tandem conditions (**a**) for NIP architecture and **b**) for PIN architecture).

VII. CONCLUSION AND PERSPECTIVES

In order to fulfil the three objectives of this work (development of a highly doped silicon tunnel junction, implementation of characterisation methods to optimise the recombination junctions, understanding the transport mechanisms), we presented an approach in three chapters. First, in chapter IV, we have presented the development of a microcrystalline silicon tunnel junction to be integrated as the recombination junction of PIN PK/SHJ tandem solar cells. Secondly, in chapter V, we have implemented and discussed methods to electrically characterise highly doped RJ, using the developed $\mu\text{c-Si:H}$ (n^+/p^+) junction as an example. Finally, in chapter VI, we have studied the integration of RJ in PK/SHJ tandem solar cells, using optical simulations and a new “tandem-like” structure allowing the measurement of the Perovskite top-cell, employing the developed $\mu\text{c-Si:H}$ (n^+/p^+) junction and the usual ITO layer as examples.

- Development of a highly doped silicon tunnel junction suitable for 2T PK/SHJ tandem solar cells

Firstly, in chapter IV, we have developed a highly doped tunnel junction, based on microcrystalline silicon, in order to replace the usual recombination junction based on ITO, in PK/SHJ PIN tandem solar cells. Thus, we have characterised the developed $\mu\text{c-Si:H}$ layers and validated that they fulfil the requirements, presented in part II.4, to form an efficient tunnel recombination junction. Indeed, the $\mu\text{c-Si:H}$ (n^+/p^+) junction features a thickness between 45 and 55 nm, with a high concentration of localised states due to high hydrogen content and an active dopant concentration in the order of 10^{20} at/cm³. Moreover, the layers are nearly transparent in the IR range and have small dark activation energies ($E_a < 30$ meV).

Then, we have integrated this $\mu\text{c-Si:H}$ (n^+/p^+) junction on SHJ solar cells and always observed an increase of minority carrier lifetime, which tends to demonstrate that the $\mu\text{c-Si:H}$ layers improve the SHJ bottom-cells chemical passivation and field effect. Furthermore, we have demonstrated that no additional R_s seems to be created by the addition of the developed $\mu\text{c-Si:H}$ (n^+/p^+) junction and that the I-V curves are classic, without S-shape. Therefore, we have concluded that the developed $\mu\text{c-Si:H}$ (n^+/p^+) junction seems to have the structural, optical and electrical requirements to fulfil its role of recombination junction.

Secondly, in chapter V, we have demonstrated that the developed $\mu\text{-Si:H (n}^+/\text{p}^+)$ junction is lowly resistive and acts as a tunnel diode with band-to-band tunnelling (B2BT). Furthermore, we have observed its tunnel diode characteristic and validated that the peak current is sufficient for a normal operation of the tunnel junction in PK/SHJ tandem solar cells.

Finally, in chapter VI, the performed optical simulations have confirmed that the developed $\mu\text{-Si:H (n}^+/\text{p}^+)$ junction reduces, by more than half, the losses by parasitic absorption in the RJ of PK/SHJ tandem solar cells, compared to the usual thin ITO. Furthermore, the first integration results have demonstrated that the PIN PK/SHJ tandem solar cells with the $\mu\text{-Si:H (n}^+/\text{p}^+)$ junction worked and reached more than 10 % efficiency. Indeed, the observed issues are not directly linked to the developed microcrystalline silicon junction, which fulfils its recombination junction role. Moreover, thanks to a predominantly vertical transport of the charge carriers, the developed $\mu\text{-Si:H (n}^+/\text{p}^+)$ junction seems to lower the shunt issues as compared to the usual ITO.

In conclusion, we have developed and integrated a highly doped, silicon-based, tunnel junction suitable for PK/SHJ tandem solar cells in the PIN architecture. With an optimisation of the Perovskite top-cell, this $\mu\text{-Si:H (n}^+/\text{p}^+)$ junction should make it possible to obtain PIN PK/SHJ tandem solar cells with better efficiencies than with the usual thin ITO layer as RJ (in particular, better current and FF are expected). However, according to the optical simulations, presented in chapter V, the NIP architecture also looks viable and interesting. Therefore, this opens up the perspective to adapt the developed $\mu\text{-Si:H}$ layers, in order to obtain a $\mu\text{-Si:H (p}^+/\text{n}^+)$ tunnel junction suitable for PK/SHJ tandem solar cells in the NIP architecture. This implies new challenges, related to the growth of the P-type layer in first, surely requiring the development of a lightly doped incubation layer (as boron is disrupting the growth of the microcrystalline layer) preserving the high passivation and V_{oc} of SHJ technology.

- Implementation of characterisation methods to optimise the recombination junctions

In chapter IV, we have started by demonstrating that integrating the recombination junction on SHJ solar cells and performing lifetime and I-V measurements is an essential first step to validate that the RJ and its deposition process do not degrade the future bottom-cell.

Then, in chapter V, we have defined several test-structures, rather simple to set up, to perform transversal dark I-V measurements of highly doped PN recombination junctions. To characterise the PN junctions as close as they are in the tandem solar cells, we kept the substrate and the layers preceding the junction, namely a-Si:H (i)/a-Si:H (n) for the PIN architecture. Furthermore, we have demonstrated that isolating the junction behaviour from the complete device one is hard and that taking into account annealing or subsequent steps is critical. Therefore, we have shown that these test-structures preferably require a known Ohmic back-side stack and an already studied front electrode, ideally a metal electrode that allows a good contact with the RJ material. Nevertheless, we have demonstrated that in order to optimise and/or compare the studied PN junctions, a TCO/Metal electrode can be used if the influence of the addition of a TCO layer is taken into account.

The defined test-structures allowed us to know quickly if the studied PN junction is lowly or highly resistive. Moreover, for highly doped PN tunnel junctions, such structures permitted us to observe the tunnel diode behaviour.

Next, in chapter VI, we have presented “tandem-like” devices composed of an isotype bottom-cell. Then, we have demonstrated that these devices allow performing I-V measurements of the Perovskite top-cell deposited in PK/SHJ tandem conditions. Therefore, the implementation of these “tandem-like” devices allow comparing and/or optimising the recombination junctions depending on the Perovskite top-cell.

To conclude, in this work we have defined, tested and used several characterisation methods, in order to optimise recombinations junctions or validate their properties, depending on the RJ type/material. These new implemented methods are combined with existing characterisation techniques, detailed in chapter III, and can be used routinely in the PK/SHJ tandem solar cells development process to study and optimise different RJ separately from complete tandem devices.

- Understanding the transport mechanisms in 2T PK/SHJ tandem solar cells and the influence of their RJ

As a starting point, in chapter IV, we have studied the developed $\mu\text{-Si:H (n}^+/\text{p}^+)$ junction influence on the SHJ bottom-cell, by performing lifetime and I-V measurements. We have observed that the SHJ passivation seems to be improved by the addition of the $\mu\text{-Si:H (n}^+/\text{p}^+)$ junction and that this junction works well in the electron contact of SHJ solar cells, thus demonstrating a B2BT transport mechanism.

Afterwards, in chapter V, we also have investigated the transport mechanisms in highly doped, silicon-based RJ, especially when a NPN junction is formed with an N-type TCO. Overall, we have stated that if the RJ is composed of an N-type TCO layer, the recombination mechanisms at the interface with the hole contact of the adjacent subcell are the same that at hole contact of single-junction solar cells (with N-type TCO electrodes), mainly TAT and B2BT. However, in the case of an optimised highly doped PN recombination junction, B2BT is probably the main transport mechanism.

For a deeper investigation, in chapter VI, we have used optical simulations, to observe the optical influence of both types of RJ. Therefore, we have demonstrated that the transparency and the optical matching of the RJ is an important factor to reduce optical losses. This opens up the perspective of optical indexes adaption of the bottom-cell and the RJ, in order to obtain a better matching with the Perovskite top-cell and reduce the reflection losses. For example, with $\text{nc-SiO}_x\text{:H}$ layers instead of the amorphous one, as already presented in the literature ([92]).

Then, we have used “tandem-like” devices to study the influence of the bottom-cell substrate and the RJ on the Perovskite top-cell quality. Such a question has rarely ever been addressed in literature and the first observations we made provide a good starting point for further studies, for example on Perovskite layer formation as a function of the underlying layers. We have observed that some shunt issues (which play a non-negligible role in the PK/SHJ tandem solar cells FF and performances) seems to be linked to the RJ properties. Indeed, with the developed $\mu\text{-Si:H (n}^+/\text{p}^+)$ junction, the devices have much less shunt issues than with a thin ITO layer. Moreover, the integration of the $\mu\text{-Si:H (n}^+/\text{p}^+)$ junction in PIN PK/SHJ tandem solar cells has also shown that. This tends to demonstrate that those shunt issues are enhanced by high lateral transport in the RJ, as already assumed in the literature ([13], [167]) but, never clearly compared experimentally within the same batch of devices.

To summarise, we have performed various studies during this work to understand and investigate the influence of the RJ and the transport mechanisms in monolithic PK/SHJ

tandem solar cells. Moreover, we have highlighted the observed differences between both types of RJ, demonstrating the different dominant recombination mechanisms presented in chapter II.

This work and related scientific contributions highlight the importance of the recombination junction in monolithic Perovskite on silicon tandem solar cells. By presenting development and characterisation methods to improve the RJ and the subcells most efficiently (taking into account the influence of each other), this work brings essential leads to the scientific community for the improvement of this tandem technology (to exceed 30 % efficiency and to prepare for large-area mass-production).

Finally, this work opens up many perspectives:

- Firstly, as discussed previously, the adaptation of the developed microcrystalline silicon layers, in order to obtain a $\mu\text{c-Si:H}$ (p+/n+) tunnel junction for PK/SHJ tandem solar cells in the NIP architecture, seems to be a great option. Indeed, the performed optical simulations demonstrated that the NIP architecture is also viable and the NIP Perovskite top-cells reached better performances than the PIN ones at CEA-INES. The main issue will be the presence of boron dopants to grow the $\mu\text{c-Si:H}$ (p+) layer first. Thus, the development of a new incubation layer is surely required, maybe with very low dopant concentration, preserving the high performances of the SHJ bottom-cell.
- Secondly, an adapted metal electrode, ensuring low contact resistivity, has to be developed to improve the test-structures defined in chapter V. For example, an electrode with a thin titanium layer topped by a thicker silver layer, preferably deposited by thermal evaporation. Furthermore, the test-structures are useful to test the stack bottom-cell/RJ/ETL or HTL. Thus, this is important to make sure the first layer of the Perovskite top-cell is electrically compatible with the bottom-cell and the RJ.
- Thirdly, for a better optical matching, the optical indexes of the subcells layers should be taken into account for the recombination junction optimisation. Indeed, to reduce absorption and reflection losses, the optical properties of the RJ have to be optimised (transparency in the IR region and refractive indexes matching with the adjacent layers). For example, the refractive indexes of the layer can be tuned by adding other gases (e.g. CO_2) during the PECVD deposition process of the amorphous or microcrystalline silicon layers. Moreover, using optical simulations to define the right thicknesses of such layers seems an efficient way to improve the optical matching in PK/SHJ tandem solar cells.
- Fourthly, the Perovskite layer formation (deposition and crystallisation) on different sub-layers (e.g. ITO and $\mu\text{c-Si:H}$ + HTL or ETL, with or without surface pretreatment) and the observed shunt issues have to be further investigated. The “tandem-like” devices, presented in chapter VI, are essential for this type of study.
- At last, the simplified devices, presented in chapter VI, being viable according to the optical simulations, are worth being developed and tested in device. For that purpose, the materials properties have to be modified in order to obtain the best selectivity for the charge carriers while allowing efficient recombination.

SCIENTIFIC CONTRIBUTION

Publications

Apolline Puaud, Anne-Sophie Ozanne, Laurie-Lou Senaud, Delfina Muñoz, Charles Roux, *Microcrystalline Silicon Tunnel Junction for Monolithic Tandem Solar Cells Using Silicon Heterojunction Technology*, IEEE Journal of Photovoltaics, Volume 11, 58-64, 2021. [159]

Contributions in Conferences

Apolline Puaud, Martin Vandenbossche, Anthony Valla, Carine Roux, Mathieu Manceau, Delfina Muñoz, Solenn Berson, Anis Jouini, *Chemically Polished Silicon Cells ready for Large Area printed Perovskite/Silicon 2T Tandem devices*, 4th International Conference on Perovskite Solar Cells and Optoelectronics (PSCO-2018), Lausanne (Suisse), 2018 -> **Poster Presentation**.

Apolline Puaud, Solenn Berson, Delfina Muñoz, *Development and Characterization of Microcrystalline Silicon Tunnel Junction for Monolithic Perovskite/Silicon-Heterojunction Tandem Solar Cells*, 28th International Conference on Amorphous and Nanocrystalline Semiconductors (ICANS-2019), Palaiseau (France), 2019 -> **Oral Presentation**.

Apolline Puaud, Muriel Matheron, Olivier Dupré, Daniel Saponi, Solenn Berson, Delfina Muñoz, *Junction engineering for Monolithic Perovskite/Silicon Tandem Solar Cells*, 5th International Conference on Perovskite Solar Cells and Optoelectronics (PSCO-2019), Lausanne (Suisse), 2019 -> **Oral Presentation**.

Apolline Puaud, Daniel Saponi, Muriel Matheron, Benoit Marie, Romain Couderc, Carine Roux, Nathalie Nguyen, Matthieu Manceau, Giuseppe Condorelli, Marina Foti, Cosimo Gerardi, Olivier Dupré, Solenn Berson and Delfina Muñoz, *Investigation of the Junction Influence in Perovskite/Silicon Tandem Solar Cells*, 37th European Photovoltaic Solar Energy Conference and Exhibition (EU PVSEC-2020), 2020, Online -> **Oral Presentation**.

Apolline Puaud, Laurie-Lou Senaud, Bertrand Paviet-Salomon and Delfina Muñoz, *Nanocrystalline Silicon Tunnel Junctions in High Efficiency Solar Cells: Characterization and Deep Insight*, A Meeting of the Materials Research Society (MRS Spring-2021), 2021, Online -> **Oral and Video Presentation**.

Apolline Puaud, Laurie-Lou Senaud, Bertrand Paviet-Salomon and Delfina Muñoz, *Deep Insight of Nanocrystalline Silicon Tunnel Junctions for High Efficiency Solar Cells*, 11th International Conference on Crystalline Silicon Photovoltaics (SiliconPV-2021), 2021, Online -> **Poster Video Presentation**.

Registered Patents

Apolline Puaud, Daniel Saponi, Delfina Muñoz, *Procédé de caractérisation d'une cellule solaire dans des conditions similaires à celles d'un dispositif solaire a architecture tandem*, 2020.

Apolline Puaud, Muriel Matheron, Delfina Muñoz, *Structure simplifiée de cellules solaires tandem à deux terminaux*, 2020.

Apolline Puaud, Muriel Matheron, Delfina Muñoz, *Structure simplifiée de cellules solaires tandem à deux terminaux ayant un matériau de jonction en oxyde transparent conducteur*, 2020.

REFERENCES

- [1] 'Global Warming of 1.5°C', IPCC, 2018. [Online]. Available: <https://www.ipcc.ch/sr15/>
- [2] 'State of the Global Climate 2020', World Meteorological Organization, WMO-No. 1264, 2021.
- [3] 'Carbon Dioxide, DIRECT MEASUREMENTS: 2005-PRESENT', NASA. Accessed: Jun. 20, 2021. [Online]. Available: <https://climate.nasa.gov/vital-signs/carbon-dioxide/>
- [4] International Energy Agency, *World Energy Outlook 2019*. 2019.
- [5] 'World Energy Scenarios 2019', World Energy Council, 2019. Accessed: Jun. 20, 2021. [Online]. Available: https://www.worldenergy.org/assets/downloads/European_Scenarios_FINAL_for_website_v2.pdf
- [6] J. Fatet, 'Recreating Edmond Becquerel's', *Arch. Sci.*, p. 10, 2005.
- [7] *Renewables 2021 Global Status Report*. 2021. Accessed: Jun. 20, 2021. [Online]. Available: https://www.ren21.net/wp-content/uploads/2019/05/GSR2021_Full_Report.pdf
- [8] 'Global installed solar PV capacity by scenario, 2010-2030', IEA, 2020. Accessed: Jun. 20, 2021. [Online]. Available: <https://www.iea.org/data-and-statistics/charts/global-installed-solar-pv-capacity-by-scenario-2010-2030>
- [9] 'International Technology Roadmap for Photovoltaic (ITRPV) 2020 Results', VDMA, 2021. Accessed: Jun. 22, 2021. [Online]. Available: <https://itrpv.vdma.org/>
- [10] L. Zhu *et al.*, 'Conversion efficiency limits and bandgap designs for multi-junction solar cells with internal radiative efficiencies below unity', *Opt. Express*, vol. 24, no. 10, p. A740, May 2016, doi: 10.1364/OE.24.00A740.
- [11] S. Albrecht *et al.*, 'Monolithic perovskite/silicon-heterojunction tandem solar cells processed at low temperature', *Energy Environ. Sci.*, vol. 9, no. 1, pp. 81–88, 2016, doi: 10.1039/C5EE02965A.
- [12] J. Werner *et al.*, 'Efficient Monolithic Perovskite/Silicon Tandem Solar Cell with Cell Area >1 cm²', *J. Phys. Chem. Lett.*, vol. 7, no. 1, pp. 161–166, Jan. 2016, doi: 10.1021/acs.jpcllett.5b02686.
- [13] F. Sahli *et al.*, 'Improved Optics in Monolithic Perovskite/Silicon Tandem Solar Cells with a Nanocrystalline Silicon Recombination Junction', *Adv. Energy Mater.*, vol. 8, no. 6, p. 1701609, Feb. 2018, doi: 10.1002/aenm.201701609.
- [14] K. A. Bush *et al.*, '23.6%-efficient monolithic perovskite/silicon tandem solar cells with improved stability', *Nat. Energy*, vol. 2, no. 4, p. 17009, Apr. 2017, doi: 10.1038/nenergy.2017.9.
- [15] R. Fan *et al.*, 'Toward Full Solution Processed Perovskite/Si Monolithic Tandem Solar Device With PCE Exceeding 20%', *Sol. RRL*, vol. 1, no. 11, p. 1700149, Nov. 2017, doi: 10.1002/solr.201700149.
- [16] G. L. Pearson, 'Conversion of Solar to Electrical Energy', *Am. J. Phys.*, vol. 25, no. 9, pp. 591–598, Dec. 1957, doi: 10.1119/1.1934565.
- [17] A. D. Vos, 'Detailed balance limit of the efficiency of tandem solar cells', *J. Phys. Appl. Phys.*, vol. 13, no. 5, pp. 839–846, May 1980, doi: 10.1088/0022-3727/13/5/018.
- [18] R. L. Moon, L. W. James, H. A. VanderPlas, and N. J. Nelson, 'Performance of an Al_{0.92}Ga_{0.08}As/Al_{0.14}Ga_{0.86}As solar cell in concentrated sunlight', *Appl. Phys. Lett.*, vol. 33, no. 2, pp. 196–198, Jul. 1978, doi: 10.1063/1.90272.

- [19] S. M. Bedair, M. F. Lamorte, and J. R. Hauser, 'A two-junction cascade solar-cell structure', *Appl. Phys. Lett.*, vol. 34, no. 1, pp. 38–39, Jan. 1979, doi: 10.1063/1.90576.
- [20] F. T. Si, O. Isabella, and M. Zeman, 'Too Many Junctions? A Case Study of Multijunction Thin-Film Silicon Solar Cells', *Adv. Sustain. Syst.*, vol. 1, no. 10, p. 1700077, Oct. 2017, doi: 10.1002/adsu.201700077.
- [21] J. Werner, B. Niesen, and C. Ballif, 'Perovskite/Silicon Tandem Solar Cells: Marriage of Convenience or True Love Story? - An Overview', *Adv. Mater. Interfaces*, vol. 5, no. 1, p. 1700731, Jan. 2018, doi: 10.1002/admi.201700731.
- [22] W. Shockley and H. J. Queisser, 'Detailed Balance Limit of Efficiency of p-n Junction Solar Cells', p. 11.
- [23] F. Dimroth and S. Kurtz, 'High-Efficiency Multijunction Solar Cells', *MRS Bull.*, vol. 32, no. 3, pp. 230–235, Mar. 2007, doi: 10.1557/mrs2007.27.
- [24] W. E. McMahon, D. J. Friedman, and J. F. Geisz, 'Multijunction solar cell design revisited: disruption of current matching by atmospheric absorption bands: Disruption of current matching by atmospheric absorption bands', *Prog. Photovolt. Res. Appl.*, vol. 25, no. 10, pp. 850–860, Oct. 2017, doi: 10.1002/pip.2899.
- [25] J. F. Geisz *et al.*, 'Six-junction III–V solar cells with 47.1% conversion efficiency under 143 Suns concentration', *Nat. Energy*, vol. 5, no. 4, pp. 326–335, Apr. 2020, doi: 10.1038/s41560-020-0598-5.
- [26] R. S. Ohl, 'Light-Sensitive Electric Device Including Silicon', 2.443.542, May 27, 1941
- [27] R. S. Ohl, 'Light-Sensitive Electric Device', 2.402.662, May 27, 1941
- [28] L. M. Fraas, 'History of Solar Cell Development', in *Low-Cost Solar Electric Power*, Cham: Springer International Publishing, 2014, pp. 1–12. doi: 10.1007/978-3-319-07530-3_1.
- [29] M. A. Green, 'The path to 25% silicon solar cell efficiency: History of silicon cell evolution', *Prog. Photovolt. Res. Appl.*, vol. 17, no. 3, pp. 183–189, May 2009, doi: 10.1002/pip.892.
- [30] M. A. Green, 'Silicon solar cells: evolution, high-efficiency design and efficiency enhancements', *Semicond. Sci. Technol.*, vol. 8, no. 1, pp. 1–12, Jan. 1993, doi: 10.1088/0268-1242/8/1/001.
- [31] J. Zhao, A. Wang, and M. A. Green, '24.5% Efficiency Silicon PERT Cells on MCZ Substrates and 24.7% Efficiency PERL Cells on FZ Substrates', p. 4, 1999.
- [32] A. Richter, 'n-Type Si solar cells with passivating electron contact_ Identifying sources for efficiency limitations by wafer thickness and resistivity variation', *Sol. Energy Mater. Sol. Cells*, p. 10, 2017.
- [33] T. G. Allen, J. Bullock, X. Yang, A. Javey, and S. De Wolf, 'Passivating contacts for crystalline silicon solar cells', *Nat. Energy*, vol. 4, no. 11, pp. 914–928, Nov. 2019, doi: 10.1038/s41560-019-0463-6.
- [34] W. Fuhs, K. Niemann, and J. Stuke, 'Heterojunctions of Amorphous Silicon and Silicon Single Crystals', in *TETRAHEDRALLY BONDED AMORPHOUS SEMICONDUCTORS: International Conference*, Yorktown Heights, New York (USA), 1974, pp. 345–350. doi: 10.1063/1.2945985.
- [35] 'HITTM cells—high-efficiency crystalline Si cells with novel structure', p. 11, 1999.
- [36] M. Tanaka *et al.*, 'Development of New a-Si/c-Si Heterojunction Solar Cells: ACJ-HIT (Artificially Constructed Junction-Heterojunction with Intrinsic Thin-Layer)', *Jpn. J. Appl. Phys.*, vol. 31, no. 11R, pp. 3518–3522, 1992.
- [37] M. Taguchi *et al.*, '24.7% Record Efficiency HIT Solar Cell on Thin Silicon Wafer', *IEEE J. Photovolt.*, vol. 4, no. 1, pp. 96–99, Jan. 2014, doi: 10.1109/JPHOTOV.2013.2282737.

- [38] D. Adachi, J. L. Hernández, and K. Yamamoto, 'Impact of carrier recombination on fill factor for large area heterojunction crystalline silicon solar cell with 25.1% efficiency', *Appl. Phys. Lett.*, vol. 107, no. 23, p. 233506, Dec. 2015, doi: 10.1063/1.4937224.
- [39] K. Yamamoto *et al.*, 'High-efficiency heterojunction crystalline Si solar cell and optical splitting structure fabricated by applying thin-film Si technology', *Jpn. J. Appl. Phys.*, vol. 54, no. 8S1, p. 08KD15, Aug. 2015, doi: 10.7567/JJAP.54.08KD15.
- [40] X. Ru *et al.*, '25.11% efficiency silicon heterojunction solar cell with low deposition rate intrinsic amorphous silicon buffer layers', *Sol. Energy Mater. Sol. Cells*, vol. 215, p. 110643, Sep. 2020, doi: 10.1016/j.solmat.2020.110643.
- [41] K. Yoshikawa *et al.*, 'Silicon heterojunction solar cell with interdigitated back contacts for a photoconversion efficiency over 26%', *Nat. Energy*, vol. 2, no. 5, p. 17032, May 2017, doi: 10.1038/nenergy.2017.32.
- [42] F. Haase *et al.*, 'Laser contact openings for local poly-Si-metal contacts enabling 26.1%-efficient POLO-IBC solar cells', *Sol. Energy Mater. Sol. Cells*, vol. 186, pp. 184–193, Nov. 2018, doi: 10.1016/j.solmat.2018.06.020.
- [43] A. Danel *et al.*, 'SILICON HETEROJUNCTION SOLAR CELLS WITH OPEN-CIRCUIT-VOLTAGE ABOVE 750MV', p. 4.
- [44] J. P. Seif *et al.*, 'Strategies for Doped Nanocrystalline Silicon Integration in Silicon Heterojunction Solar Cells', *IEEE J. Photovolt.*, vol. 6, no. 5, pp. 1132–1140, Sep. 2016, doi: 10.1109/JPHOTOV.2016.2571619.
- [45] K. Ding, U. Aeberhard, F. Finger, and U. Rau, 'Silicon heterojunction solar cell with amorphous silicon oxide buffer and microcrystalline silicon oxide contact layers', *Phys. Status Solidi RRL - Rapid Res. Lett.*, vol. 6, no. 5, pp. 193–195, May 2012, doi: 10.1002/pssr.201206030.
- [46] G. Nogay *et al.*, 'Nanocrystalline Silicon Carrier Collectors for Silicon Heterojunction Solar Cells and Impact on Low-Temperature Device Characteristics', *IEEE J. Photovolt.*, vol. 6, no. 6, pp. 1654–1662, Nov. 2016, doi: 10.1109/JPHOTOV.2016.2604574.
- [47] L. Mazarella, S. Kirner, B. Stannowski, L. Korte, B. Rech, and R. Schlatmann, 'p-type microcrystalline silicon oxide emitter for silicon heterojunction solar cells allowing current densities above 40 mA/cm²', *Appl. Phys. Lett.*, vol. 106, no. 2, p. 023902, Jan. 2015, doi: 10.1063/1.4905906.
- [48] F. Li *et al.*, 'Silicon Heterojunction Solar Cells with MoO_x Hole-Selective Layer by Hot Wire Oxidation–Sublimation Deposition', *Sol. RRL*, vol. 4, no. 3, p. 1900514, Mar. 2020, doi: 10.1002/solr.201900514.
- [49] Y. Wan *et al.*, 'Conductive and Stable Magnesium Oxide Electron-Selective Contacts for Efficient Silicon Solar Cells', *Adv. Energy Mater.*, vol. 7, no. 5, p. 1601863, Mar. 2017, doi: 10.1002/aenm.201601863.
- [50] J. Wang, H. Lin, Z. Wang, W. Shen, J. Ye, and P. Gao, 'Hard mask processing of 20% efficiency back-contacted silicon solar cells with dopant-free heterojunctions', *Nano Energy*, vol. 66, p. 104116, Dec. 2019, doi: 10.1016/j.nanoen.2019.104116.
- [51] C. Battaglia *et al.*, 'Hole Selective MoO_x Contact for Silicon Solar Cells', *Nano Lett.*, vol. 14, no. 2, pp. 967–971, Feb. 2014, doi: 10.1021/nl404389u.
- [52] E. Ros *et al.*, 'Improved Electron Selectivity in Silicon Solar Cells by Cathode Modification with a Dipolar Conjugated Polyelectrolyte Interlayer', *ACS Appl. Energy Mater.*, vol. 2, no. 8, pp. 5954–5959, Aug. 2019, doi: 10.1021/acsaem.9b01055.
- [53] M. Gao *et al.*, 'Bifunctional Hybrid a-SiO_x (Mo) Layer for Hole-Selective and Interface Passivation of Highly Efficient MoO_x /a-SiO_x (Mo)/n-Si Heterojunction Photovoltaic Device', *ACS Appl. Mater. Interfaces*, vol. 10, no. 32, pp. 27454–27464, Aug. 2018, doi: 10.1021/acsami.8b07001.

- [54] D. Sacchetto *et al.*, 'ITO/MoOx/a-Si:H(i) Hole-Selective Contacts for Silicon Heterojunction Solar Cells: Degradation Mechanisms and Cell Integration', *IEEE J. Photovolt.*, vol. 7, no. 6, pp. 1584–1590, Nov. 2017, doi: 10.1109/JPHOTOV.2017.2756066.
- [55] G. Nogay, 'Full-Area Passivating Contacts with High and Low Thermal Budgets: Solutions for High Efficiency c-Si Solar Cells', 2018, doi: 10.5075/EPFL-THESIS-8707.
- [56] L.-L. Senaud *et al.*, 'Aluminium-Doped Zinc Oxide Rear Reflectors for High-Efficiency Silicon Heterojunction Solar Cells', *IEEE J. Photovolt.*, vol. 9, no. 5, pp. 1217–1224, Sep. 2019, doi: 10.1109/JPHOTOV.2019.2926860.
- [57] M. Morales-Masis, S. Martin De Nicolas, J. Holovsky, S. De Wolf, and C. Ballif, 'Low-Temperature High-Mobility Amorphous IZO for Silicon Heterojunction Solar Cells', *IEEE J. Photovolt.*, vol. 5, no. 5, pp. 1340–1347, Sep. 2015, doi: 10.1109/JPHOTOV.2015.2450993.
- [58] A. Cruz *et al.*, 'Influence of Silicon Layers on the Growth of ITO and AZO in Silicon Heterojunction Solar Cells', *IEEE J. Photovolt.*, pp. 1–7, 2019, doi: 10.1109/JPHOTOV.2019.2957665.
- [59] K. Nakamura, K. Muramatsu, T. Nishihara, A. Ogura, and Y. Ohshita, 'Development of Transparent Conductive Oxide for Silicon Heterojunction Solar Cell', *36th Eur. Photovolt. Sol. Energy Conf. Exhib. 527-529*, p. 3 pages, 2145 kb, 2019, doi: 10.4229/EUPVSEC20192019-2DV.1.40.
- [60] D. B. Mitzi, C. A. Feild, W. T. A. Harrison, and A. M. Guloy, 'Conducting tin halides with a layered organic-based perovskite structure', *Nature*, vol. 369, no. 6480, pp. 467–469, Jun. 1994, doi: 10.1038/369467a0.
- [61] A. Kojima, K. Teshima, Y. Shirai, and T. Miyasaka, 'Organometal Halide Perovskites as Visible-Light Sensitizers for Photovoltaic Cells', *J. Am. Chem. Soc.*, vol. 131, no. 17, pp. 6050–6051, May 2009, doi: 10.1021/ja809598r.
- [62] M. M. Lee, J. Teuscher, T. Miyasaka, T. N. Murakami, and H. J. Snaith, 'Efficient Hybrid Solar Cells Based on Meso-Superstructured Organometal Halide Perovskites', *Science*, vol. 338, no. 6107, pp. 643–647, Nov. 2012, doi: 10.1126/science.1228604.
- [63] H.-S. Kim *et al.*, 'Lead Iodide Perovskite Sensitized All-Solid-State Submicron Thin Film Mesoscopic Solar Cell with Efficiency Exceeding 9%', *Sci. Rep.*, vol. 2, no. 1, p. 591, Dec. 2012, doi: 10.1038/srep00591.
- [64] X. Zhao and N.-G. Park, 'Stability Issues on Perovskite Solar Cells', *Photonics*, vol. 2, no. 4, pp. 1139–1151, Nov. 2015, doi: 10.3390/photonics2041139.
- [65] W. S. Yang *et al.*, 'High-performance photovoltaic perovskite layers fabricated through intramolecular exchange', *Science*, vol. 348, no. 6240, pp. 1234–1237, Jun. 2015, doi: 10.1126/science.aaa9272.
- [66] M. Jeong *et al.*, 'Stable perovskite solar cells with efficiency exceeding 24.8% and 0.3-V voltage loss', p. 7, 2020.
- [67] P. A. Basore, D. Chung, and T. Buonassisi, 'Economics of future growth in photovoltaics manufacturing', in *2015 IEEE 42nd Photovoltaic Specialist Conference (PVSC)*, New Orleans, LA, Jun. 2015, pp. 1–4. doi: 10.1109/PVSC.2015.7355620.
- [68] N. Kour and R. Mehra, 'Recent Advances in Photovoltaic Technology based on Perovskite Solar Cell- A Review', vol. 04, no. 07, p. 13.
- [69] S. De Wolf *et al.*, 'Organometallic Halide Perovskites: Sharp Optical Absorption Edge and Its Relation to Photovoltaic Performance', *J. Phys. Chem. Lett.*, vol. 5, no. 6, pp. 1035–1039, Mar. 2014, doi: 10.1021/jz500279b.
- [70] R. Sheng *et al.*, 'Monolithic Wide Band Gap Perovskite/Perovskite Tandem Solar Cells with Organic Recombination Layers', *J. Phys. Chem. C*, vol. 121, no. 49, pp. 27256–27262, Dec. 2017, doi: 10.1021/acs.jpcc.7b05517.

- [71] D. Zhao *et al.*, 'Efficient two-terminal all-perovskite tandem solar cells enabled by high-quality low-bandgap absorber layers', *Nat. Energy*, vol. 3, no. 12, pp. 1093–1100, Dec. 2018, doi: 10.1038/s41560-018-0278-x.
- [72] R. Lin, 'Monolithic all-perovskite tandem solar cells with 24.8% efficiency exploiting comproportionation to suppress Sn(ii) oxidation in precursor ink', *Nat. Energy*, vol. 4, p. 12, 2019.
- [73] A. F. Palmstrom *et al.*, 'Enabling Flexible All-Perovskite Tandem Solar Cells', *Joule*, vol. 3, no. 9, pp. 2193–2204, Sep. 2019, doi: 10.1016/j.joule.2019.05.009.
- [74] Y. Wang *et al.*, 'Recent progress in developing efficient monolithic all-perovskite tandem solar cells', *J. Semicond.*, vol. 41, no. 5, p. 051201, May 2020, doi: 10.1088/1674-4926/41/5/051201.
- [75] M. Soldera, A. Koffman-Frischknecht, and K. Taretto, 'Optical and electrical optimization of all-perovskite pin type junction tandem solar cells', *J. Phys. Appl. Phys.*, vol. 53, no. 31, p. 315104, Jul. 2020, doi: 10.1088/1361-6463/ab8851.
- [76] X. Luo *et al.*, 'Progress of all-perovskite tandem solar cells: the role of narrow-bandgap absorbers', p. 10.
- [77] B. Joon Lee, H. Jung Kim, W. Jeong, and J.-J. Kim, 'A transparent conducting oxide as an efficient middle electrode for flexible organic tandem solar cells', *Sol. Energy Mater. Sol. Cells*, vol. 94, no. 3, pp. 542–546, Mar. 2010, doi: 10.1016/j.solmat.2009.11.021.
- [78] A. Hadipour, B. de Boer, and P. W. M. Blom, 'Organic Tandem and Multi-Junction Solar Cells', *Adv. Funct. Mater.*, vol. 18, no. 2, pp. 169–181, Jan. 2008, doi: 10.1002/adfm.200700517.
- [79] J. Sakai *et al.*, 'Efficient organic photovoltaic tandem cells with novel transparent conductive oxide interlayer and poly (3-hexylthiophene): Fullerene active layers', *Sol. Energy Mater. Sol. Cells*, vol. 94, no. 2, pp. 376–380, Feb. 2010, doi: 10.1016/j.solmat.2009.08.008.
- [80] A. Louwen, 'A cost roadmap for silicon heterojunction solar cells', *Sol. Energy Mater.*, p. 20, 2016.
- [81] H. J. Snaith, 'Perovskites: The Emergence of a New Era for Low-Cost, High-Efficiency Solar Cells', *J. Phys. Chem. Lett.*, vol. 4, no. 21, pp. 3623–3630, Nov. 2013, doi: 10.1021/jz4020162.
- [82] P. Löper *et al.*, 'Organic–inorganic halide perovskite/crystalline silicon four-terminal tandem solar cells', *Phys. Chem. Chem. Phys.*, vol. 17, no. 3, pp. 1619–1629, 2015, doi: 10.1039/C4CP03788J.
- [83] J. P. Mailoa *et al.*, 'A 2-terminal perovskite/silicon multijunction solar cell enabled by a silicon tunnel junction', *Appl. Phys. Lett.*, vol. 106, no. 12, p. 121105, Mar. 2015, doi: 10.1063/1.4914179.
- [84] J. Werner *et al.*, 'Efficient Near-Infrared-Transparent Perovskite Solar Cells Enabling Direct Comparison of 4-Terminal and Monolithic Perovskite/Silicon Tandem Cells', *ACS Energy Lett.*, vol. 1, no. 2, pp. 474–480, Aug. 2016, doi: 10.1021/acsenenergylett.6b00254.
- [85] D. Kirk, 'OXFORD PV Perovskite Silicon Tandem Cells, Reliable, efficient and cost effective'. Oct. 11, 2016.
- [86] J. Werner *et al.*, 'Zinc tin oxide as high-temperature stable recombination layer for mesoscopic perovskite/silicon monolithic tandem solar cells', *Appl. Phys. Lett.*, vol. 109, no. 23, p. 233902, Dec. 2016, doi: 10.1063/1.4971361.
- [87] Y. Wu *et al.*, 'Monolithic perovskite/silicon-homojunction tandem solar cell with over 22% efficiency', *Energy Environ. Sci.*, vol. 10, no. 11, pp. 2472–2479, 2017, doi: 10.1039/C7EE02288C.

- [88] R. Swartwout, M. T. Hoerantner, and V. Bulović, 'Scalable Deposition Methods for Large-area Production of Perovskite Thin Films', *ENERGY Environ. Mater.*, vol. 2, no. 2, pp. 119–145, Jun. 2019, doi: 10.1002/eem2.12043.
- [89] T. Duong *et al.*, 'Rubidium Multication Perovskite with Optimized Bandgap for Perovskite-Silicon Tandem with over 26% Efficiency', *Adv. Energy Mater.*, vol. 7, no. 14, p. 1700228, Jul. 2017, doi: 10.1002/aenm.201700228.
- [90] J. Macey White, M. Low, and L. Marshall, 'Oxford PV hits new world record for solar cell', Dec. 21, 2020. <https://www.oxfordpv.com/news/oxford-pv-hits-new-world-record-solar-cell>
- [91] F. Hou *et al.*, 'Monolithic Perovskite/Silicon-Heterojunction Tandem Solar Cells with Open-Circuit Voltage of over 1.8 V', *ACS Appl. Energy Mater.*, vol. 2, no. 1, pp. 243–249, Jan. 2019, doi: 10.1021/acsaem.8b00926.
- [92] L. Mazzarella *et al.*, 'Infrared photocurrent management in monolithic perovskite/silicon heterojunction tandem solar cells by using a nanocrystalline silicon oxide interlayer', *Opt. Express*, vol. 26, no. 10, p. A487, May 2018, doi: 10.1364/OE.26.00A487.
- [93] M. Jošt *et al.*, 'Textured interfaces in monolithic perovskite/silicon tandem solar cells: advanced light management for improved efficiency and energy yield', *Energy Environ. Sci.*, vol. 11, no. 12, pp. 3511–3523, 2018, doi: 10.1039/C8EE02469C.
- [94] K. A. Bush *et al.*, 'Compositional Engineering for Efficient Wide Band Gap Perovskites with Improved Stability to Photoinduced Phase Segregation', *ACS Energy Lett.*, vol. 3, no. 2, pp. 428–435, Feb. 2018, doi: 10.1021/acseenergylett.7b01255.
- [95] F. Sahli *et al.*, 'Fully textured monolithic perovskite/silicon tandem solar cells with 25.2% power conversion efficiency', *Nat. Mater.*, vol. 17, no. 9, pp. 820–826, Sep. 2018, doi: 10.1038/s41563-018-0115-4.
- [96] S. Zhu *et al.*, 'Transparent electrode for monolithic perovskite/silicon-heterojunction two-terminal tandem solar cells', *Nano Energy*, vol. 45, pp. 280–286, Mar. 2018, doi: 10.1016/j.nanoen.2017.12.043.
- [97] E. Köhnen *et al.*, 'Highly efficient monolithic perovskite silicon tandem solar cells: analyzing the influence of current mismatch on device performance', *Sustain. Energy Fuels*, vol. 3, no. 8, pp. 1995–2005, 2019, doi: 10.1039/C9SE00120D.
- [98] B. A. Kamino *et al.*, 'Low-Temperature Screen-Printed Metallization for the Scale-Up of Two-Terminal Perovskite-Silicon Tandems', *ACS Appl. Energy Mater.*, vol. 2, no. 5, pp. 3815–3821, May 2019, doi: 10.1021/acsaem.9b00502.
- [99] F. Hou *et al.*, 'Inverted pyramidally-textured PDMS antireflective foils for perovskite/silicon tandem solar cells with flat top cell', *Nano Energy*, vol. 56, pp. 234–240, Feb. 2019, doi: 10.1016/j.nanoen.2018.11.018.
- [100] L. Mazzarella *et al.*, 'Infrared Light Management Using a Nanocrystalline Silicon Oxide Interlayer in Monolithic Perovskite/Silicon Heterojunction Tandem Solar Cells with Efficiency above 25%', *Adv. Energy Mater.*, vol. 9, no. 14, p. 1803241, Apr. 2019, doi: 10.1002/aenm.201803241.
- [101] B. Chen *et al.*, 'Grain Engineering for Perovskite/Silicon Monolithic Tandem Solar Cells with Efficiency of 25.4%', *Joule*, vol. 3, no. 1, pp. 177–190, Jan. 2019, doi: 10.1016/j.joule.2018.10.003.
- [102] D. Kim *et al.*, 'Efficient, stable silicon tandem cells enabled by anion-engineered wide-bandgap perovskites', *Science*, vol. 368, no. 6487, pp. 155–160, Apr. 2020, doi: 10.1126/science.aba3433.
- [103] Y. Hou *et al.*, 'Efficient tandem solar cells with solution-processed perovskite on textured crystalline silicon', *Science*, vol. 367, no. 6482, pp. 1135–1140, Mar. 2020, doi: 10.1126/science.aaz3691.

- [104] J. Xu *et al.*, 'Triple-halide wide-band gap perovskites with suppressed phase segregation for efficient tandems', *Science*, vol. 367, no. 6482, pp. 1097–1104, Mar. 2020, doi: 10.1126/science.aaz5074.
- [105] A. J. Bett *et al.*, 'Two-terminal Perovskite silicon tandem solar cells with a high-Bandgap Perovskite absorber enabling voltages over 1.8 V', *Prog. Photovolt. Res. Appl.*, p. pip.3208, Nov. 2019, doi: 10.1002/pip.3208.
- [106] C. O. Ramírez Quiroz *et al.*, 'Interface Molecular Engineering for Laminated Monolithic Perovskite/Silicon Tandem Solar Cells with 80.4% Fill Factor', *Adv. Funct. Mater.*, p. 1901476, Aug. 2019, doi: 10.1002/adfm.201901476.
- [107] A. Al-Ashouri *et al.*, 'Monolithic perovskite/silicon tandem solar cell with >29% efficiency by enhanced hole extraction', p. 10, 2020.
- [108] E. Aydin *et al.*, 'Interplay between temperature and bandgap energies on the outdoor performance of perovskite/silicon tandem solar cells', *Nat. Energy*, Sep. 2020, doi: 10.1038/s41560-020-00687-4.
- [109] A. S. Subbiah *et al.*, 'High-Performance Perovskite Single-Junction and Textured Perovskite/Silicon Tandem Solar Cells via Slot-Die Coating', *ACS Energy Lett.*, p. acsenergylett.0c01297, Aug. 2020, doi: 10.1021/acsenergylett.0c01297.
- [110] P. S. C. Schulze *et al.*, '25.1% High-Efficiency Monolithic Perovskite Silicon Tandem Solar Cell with a High Bandgap Perovskite Absorber', *Sol. RRL*, p. 2000152, May 2020, doi: 10.1002/solr.202000152.
- [111] B. Chen *et al.*, 'Blade-Coated Perovskites on Textured Silicon for 26%-Efficient Monolithic Perovskite/Silicon Tandem Solar Cells', *Joule*, p. S2542435120300350, Jan. 2020, doi: 10.1016/j.joule.2020.01.008.
- [112] J. A. Willemen, 'Modelling of amorphous silicon single- and multi-junction solar cells', s.n.], S.l., 1998.
- [113] L. Esaki, 'New Phenomenon in Narrow Germanium p – n Junctions', *Phys. Rev.*, vol. 109, no. 2, pp. 603–604, Jan. 1958, doi: 10.1103/PhysRev.109.603.
- [114] T. Ameri, G. Dennler, C. Lungenschmied, and C. J. Brabec, 'Organic tandem solar cells: A review', *Energy Environ. Sci.*, vol. 2, no. 4, p. 347, 2009, doi: 10.1039/b817952b.
- [115] M. Jošt, L. Kegelmann, L. Korte, and S. Albrecht, 'Monolithic Perovskite Tandem Solar Cells: A Review of the Present Status and Advanced Characterization Methods Toward 30% Efficiency', *Adv. Energy Mater.*, p. 1904102, May 2020, doi: 10.1002/aenm.201904102.
- [116] D. Di Carlo Rasi *et al.*, 'Solution-Processed Tin Oxide-PEDOT:PSS Interconnecting Layers for Efficient Inverted and Conventional Tandem Polymer Solar Cells', *Sol. RRL*, vol. 3, no. 4, p. 1800366, Apr. 2019, doi: 10.1002/solr.201800366.
- [117] P. Procel *et al.*, 'The role of heterointerfaces and subgap energy states on transport mechanisms in silicon heterojunction solar cells', *Prog. Photovolt. Res. Appl.*, vol. 28, no. 9, pp. 935–945, Sep. 2020, doi: 10.1002/pip.3300.
- [118] C. Messmer, M. Bivour, C. Luderer, L. Tutsch, J. Schon, and M. Hermle, 'Influence of Interfacial Oxides at TCO/Doped Si Thin Film Contacts on the Charge Carrier Transport of Passivating Contacts', *IEEE J. Photovolt.*, vol. 10, no. 2, pp. 343–350, Mar. 2020, doi: 10.1109/JPHOTOV.2019.2957672.
- [119] T. F. Schulze, L. Korte, E. Conrad, M. Schmidt, and B. Rech, 'Electrical transport mechanisms in a-Si:H/c-Si heterojunction solar cells', *J. Appl. Phys.*, vol. 107, no. 2, p. 023711, Jan. 2010, doi: 10.1063/1.3267316.
- [120] A. Kanevce and W. K. Metzger, 'The role of amorphous silicon and tunneling in heterojunction with intrinsic thin layer (HIT) solar cells', *J. Appl. Phys.*, vol. 105, no. 9, p. 094507, May 2009, doi: 10.1063/1.3106642.

- [121] L. Mazzarella, A. Morales-Vilches, L. Korte, R. Schlatmann, and B. Stannowski, 'Versatility of Nanocrystalline Silicon Films: from Thin-Film to Perovskite/c-Si Tandem Solar Cell Applications', *Coatings*, vol. 10, no. 8, p. 759, Aug. 2020, doi: 10.3390/coatings10080759.
- [122] H. Shen *et al.*, 'In situ recombination junction between p-Si and TiO₂ enables high-efficiency monolithic perovskite/Si tandem cells', *Sci. Adv.*, vol. 4, no. 12, p. eaau9711, Dec. 2018, doi: 10.1126/sciadv.aau9711.
- [123] J. Zheng *et al.*, 'Large area efficient interface layer free monolithic perovskite/homo-junction-silicon tandem solar cell with over 20% efficiency', *Energy Environ. Sci.*, vol. 11, no. 9, pp. 2432–2443, 2018, doi: 10.1039/C8EE00689J.
- [124] A. Faes *et al.*, 'Metallization and interconnection for high-efficiency bifacial silicon heterojunction solar cells and modules', p. 12.
- [125] A. Danel *et al.*, 'VERSATILE PILOT LINE TO SUPPORT THE HETEROJUNCTION SOLAR CELL INDUSTRIAL DEVELOPMENT: BUSBAR AND BUSBAR-LESS CONFIGURATIONS', p. 4.
- [126] P. Roca i Cabarrocas, 'New approaches for the production of nano-, micro-, and polycrystalline silicon thin films: New approaches for the production of silicon thin films', *Phys. Status Solidi C*, vol. 1, no. 5, pp. 1115–1130, Mar. 2004, doi: 10.1002/pssc.200304328.
- [127] R. E. I. Schropp and M. Zeman, *Amorphous and Microcrystalline Silicon Solar Cells: Modeling, Materials and Device Technology*. Boston, MA: Springer US, 1998. doi: 10.1007/978-1-4615-5631-2.
- [128] P. Carroy, D. Muñoz, F. Ozanne, A. Valla, P. Mur, and G. Rodriguez, 'ANALYSIS OF DIFFERENT FRONT AND BACK TCO ON HETEROJUNCTION SOLAR CELLS', p. 6.
- [129] R. Patidar, D. Burkitt, K. Hooper, D. Richards, and T. Watson, 'Slot-die coating of perovskite solar cells: An overview', *Mater. Today Commun.*, vol. 22, p. 100808, Mar. 2020, doi: 10.1016/j.mtcomm.2019.100808.
- [130] S. Uličná *et al.*, 'Scalable Deposition of High-Efficiency Perovskite Solar Cells by Spray-Coating', *ACS Appl. Energy Mater.*, vol. 1, no. 5, pp. 1853–1857, May 2018, doi: 10.1021/acsaem.8b00328.
- [131] X. Peng *et al.*, 'Perovskite and Organic Solar Cells Fabricated by Inkjet Printing: Progress and Prospects', *Adv. Funct. Mater.*, vol. 27, no. 41, p. 1703704, Nov. 2017, doi: 10.1002/adfm.201703704.
- [132] S. Wang, X. Li, J. Wu, W. Wen, and Y. Qi, 'Fabrication of efficient metal halide perovskite solar cells by vacuum thermal evaporation: A progress review', *Curr. Opin. Electrochem.*, vol. 11, pp. 130–140, Oct. 2018, doi: 10.1016/j.coelec.2018.10.006.
- [133] M. R. Leyden, Y. Jiang, and Y. Qi, 'Chemical vapor deposition grown formamidinium perovskite solar modules with high steady state power and thermal stability', *J. Mater. Chem. A*, vol. 4, no. 34, pp. 13125–13132, 2016, doi: 10.1039/C6TA04267H.
- [134] J. A. Raiford, S. T. Oyakhire, and S. F. Bent, 'Applications of atomic layer deposition and chemical vapor deposition for perovskite solar cells', *Energy Environ. Sci.*, vol. 13, no. 7, pp. 1997–2023, 2020, doi: 10.1039/D0EE00385A.
- [135] G. Longo, L. Gil-Escrig, M. J. Degen, M. Sessolo, and H. J. Bolink, 'Perovskite solar cells prepared by flash evaporation', *Chem. Commun.*, vol. 51, no. 34, pp. 7376–7378, 2015, doi: 10.1039/C5CC01103E.
- [136] Q. Chen *et al.*, 'Planar Heterojunction Perovskite Solar Cells via Vapor-Assisted Solution Process', *J. Am. Chem. Soc.*, vol. 136, no. 2, pp. 622–625, Jan. 2014, doi: 10.1021/ja411509g.

- [137] T. Soto-Montero, W. Soltanpoor, and M. Morales-Masis, 'Pressing challenges of halide perovskite thin film growth', *APL Mater.*, vol. 8, no. 11, p. 110903, Nov. 2020, doi: 10.1063/5.0027573.
- [138] M. Losurdo *et al.*, 'Spectroscopic ellipsometry and polarimetry for materials and systems analysis at the nanometer scale: state-of-the-art, potential, and perspectives', *J Nanopart Res*, p. 34, 2009.
- [139] G. E. Jellison and F. A. Modine, 'Parameterization of the optical functions of amorphous materials in the interband region', *Appl. Phys. Lett.*, vol. 69, no. 3, pp. 371–373, Jul. 1996, doi: 10.1063/1.118064.
- [140] HORIBA, 'Tauc-Lorentz Dispersion Formula'. 2008.
- [141] M. Losurdo *et al.*, 'Parametrization of optical properties of indium–tin–oxide thin films by spectroscopic ellipsometry: Substrate interfacial reactivity', *J. Vac. Sci. Technol. Vac. Surf. Films*, vol. 20, no. 1, pp. 37–42, Jan. 2002, doi: 10.1116/1.1421596.
- [142] HORIBA, 'Classical Dispersion Model'. 2008.
- [143] HORIBA, 'Lorentz Dispersion Model'. 2008.
- [144] HORIBA, 'New Amorphous Dispersion Formula'. 2008.
- [145] S. Kim *et al.*, 'The recorded open-circuit voltage and fill factor achievement of a-Si:H p-i-n/HIT-type tandem solar cells by tuning up the crystalline in tunneling recombination junction layer', *Semicond. Sci. Technol.*, vol. 34, no. 6, p. 065004, Jun. 2019, doi: 10.1088/1361-6641/ab118a.
- [146] E. Bustarret, M. A. Hachicha, and M. Brunel, 'Experimental determination of the nanocrystalline volume fraction in silicon thin films from Raman spectroscopy', *Appl. Phys. Lett.*, vol. 52, no. 20, pp. 1675–1677, May 1988, doi: 10.1063/1.99054.
- [147] P. Blood and J. W. Orton, 'The electrical characterisation of semiconductors', p. 102.
- [148] H. M. Dyalsingh and J. Kakalios, 'Thermopower and conductivity activation energies in hydrogenated amorphous silicon', p. 4.
- [149] L. Basset, 'Contact electrodes for heterojunction silicon solar cells: Evaluations and optimizations of the electron contact', Université Lille Nord de France, Bourget-du-Lac, 2020.
- [150] D. Lachenal *et al.*, 'Heterojunction and Passivated Contacts: A Simple Method to Extract Both n/tco and p/tco Contacts Resistivity', *Energy Procedia*, vol. 92, pp. 932–938, Aug. 2016, doi: 10.1016/j.egypro.2016.07.104.
- [151] T. Oku, 'Crystal Structures of CH₃NH₃PbI₃ and Related Perovskite Compounds Used for Solar Cells', in *Solar Cells - New Approaches and Reviews*, L. A. Kosyachenko, Ed. InTech, 2015. doi: 10.5772/59284.
- [152] R. A. Sinton and A. Cuevas, 'A QUASI-STEADY-STATE OPEN-CIRCUIT VOLTAGE METHOD FOR SOLAR CELL CHARACTERIZATION', presented at the 16th European Photovoltaic Solar Energy Conference, Glasgow, UK, May 2000. [Online]. Available: <https://www.sintoninstruments.com/wp-content/uploads/sinton-epvsc16-pcd.pdf>
- [153] A. Khanna, T. Mueller, R. A. Stangl, B. Hoex, P. K. Basu, and A. G. Aberle, 'A Fill Factor Loss Analysis Method for Silicon Wafer Solar Cells', *IEEE J. Photovolt.*, vol. 3, no. 4, pp. 1170–1177, Oct. 2013, doi: 10.1109/JPHOTOV.2013.2270348.
- [154] B. Lipovšek, J. Krč, and M. Topič, 'CROWM User Manual'. University of Ljubljana, 2019. [Online]. Available: http://lpvo.fe.uni-lj.si/fileadmin/files/programi/CROWM_v3_User_Manual.pdf
- [155] D. T. Grant, K. R. Catchpole, K. J. Weber, and T. P. White, 'Design guidelines for perovskite/silicon 2-terminal tandem solar cells: an optical study', *Opt. Express*, vol. 24, no. 22, p. A1454, Oct. 2016, doi: 10.1364/OE.24.0A1454.

- [156] F. A. Rubinelli, J. K. Rath, and R. E. I. Schropp, 'Microcrystalline n-i-p tunnel junction in a-Si:H/a-Si:H tandem cells', *J Appl Phys*, vol. 89, no. 7, p. 10, 2001.
- [157] R. E. I. Schropp, R. Carius, and G. Beaucarne, 'Amorphous Silicon, Microcrystalline Silicon, and Thin-Film Polycrystalline Silicon Solar Cells', *MRS Bull.*, vol. 32, no. 3, pp. 219–224, Mar. 2007, doi: 10.1557/mrs2007.25.
- [158] M. N. Kateb, S. Tobbeche, and A. Merazga, 'Influence of $\mu\text{c-Si:H}$ tunnel recombination junction on the performance of a-Si:H/ $\mu\text{c-Si:H}$ tandem solar cell', *Optik*, vol. 139, pp. 152–165, Jun. 2017, doi: 10.1016/j.ijleo.2017.03.099.
- [159] A. Puaud, A.-S. Ozanne, L.-L. Senaud, D. Munoz, and C. Roux, 'Microcrystalline Silicon Tunnel Junction for Monolithic Tandem Solar Cells Using Silicon Heterojunction Technology', *IEEE J. Photovolt.*, pp. 1–7, 2020, doi: 10.1109/JPHOTOV.2020.3038600.
- [160] H. Fujiwara, M. Kondo, and A. Matsuda, 'Real-time spectroscopic ellipsometry studies of the nucleation and grain growth processes in microcrystalline silicon thin films', *Phys. Rev. B*, vol. 63, no. 11, p. 115306, Feb. 2001, doi: 10.1103/PhysRevB.63.115306.
- [161] B. Demaurex *et al.*, 'Low-temperature plasma-deposited silicon epitaxial films: Growth and properties', *J. Appl. Phys.*, vol. 116, no. 5, p. 053519, Aug. 2014, doi: 10.1063/1.4892095.
- [162] P. R. i Cabarrocas, T. Nguyen-Tran, Y. Djeridane, A. Abramov, E. Johnson, and G. Patriarche, 'Synthesis of silicon nanocrystals in silane plasmas for nanoelectronics and large area electronic devices', *J. Phys. Appl. Phys.*, vol. 40, no. 8, pp. 2258–2266, Apr. 2007, doi: 10.1088/0022-3727/40/8/S04.
- [163] K.-H. Kim, E. V. Johnson, A. G. Kazanskii, M. V. Khenkin, and P. Roca i Cabarrocas, 'Unravelling a simple method for the low temperature synthesis of silicon nanocrystals and monolithic nanocrystalline thin films', *Sci. Rep.*, vol. 7, no. 1, p. 40553, Feb. 2017, doi: 10.1038/srep40553.
- [164] U. Kroll, J. Meier, A. Shah, S. Mikhailov, and J. Weber, 'Hydrogen in amorphous and microcrystalline silicon films prepared by hydrogen dilution', *J. Appl. Phys.*, vol. 80, no. 9, pp. 4971–4975, Nov. 1996, doi: 10.1063/1.363541.
- [165] A. Matsuda, 'Growth mechanism of microcrystalline silicon obtained from reactive plasmas', *Thin Solid Films*, vol. 337, no. 1–2, pp. 1–6, Jan. 1999, doi: 10.1016/S0040-6090(98)01165-1.
- [166] A. Rolland *et al.*, 'Computational analysis of hybrid perovskite on silicon 2-T tandem solar cells based on a Si tunnel junction', *Opt. Quantum Electron.*, vol. 50, no. 1, p. 21, Jan. 2018, doi: 10.1007/s11082-017-1284-0.
- [167] C. Blaga, G. Christmann, M. Boccard, C. Ballif, S. Nicolay, and B. A. Kamino, 'Palliating the efficiency loss due to shunting in perovskite/silicon tandem solar cells through modifying the resistive properties of the recombination junction', *Sustain. Energy Fuels*, vol. 5, no. 7, pp. 2036–2045, 2021, doi: 10.1039/D1SE00030F.
- [168] P. Roca i Cabarrocas, 'Plasma enhanced chemical vapor deposition of silicon thin films for large area electronics', *Curr. Opin. Solid State Mater. Sci.*, vol. 6, no. 5, pp. 439–444, Oct. 2002, doi: 10.1016/S1359-0286(02)00112-2.
- [169] T. Masuda, N. Sotani, H. Hamada, Y. Matsuki, and T. Shimoda, 'Fabrication of solution-processed hydrogenated amorphous silicon single-junction solar cells', *Appl. Phys. Lett.*, vol. 100, no. 25, p. 253908, Jun. 2012, doi: 10.1063/1.4730614.
- [170] P. Procel, G. Yang, O. Isabella, and M. Zeman, 'Theoretical evaluation of contact stack for high efficiency IBC-SHJ solar cells', *Sol. Energy Mater. Sol. Cells*, vol. 186, pp. 66–77, Nov. 2018, doi: 10.1016/j.solmat.2018.06.021.
- [171] A. Banerjee, J. Yang, T. Glatfelter, K. Hoffman, and S. Guha, 'Experimental study of p layers in "tunnel" junctions for high efficiency amorphous silicon alloy

- multijunction solar cells and modules', *Appl. Phys. Lett.*, vol. 64, no. 12, pp. 1517–1519, Mar. 1994, doi: 10.1063/1.111877.
- [172] A. Tomasi *et al.*, 'Simple processing of back-contacted silicon heterojunction solar cells using selective-area crystalline growth', *Nat. Energy*, vol. 2, no. 5, p. 17062, May 2017, doi: 10.1038/nenergy.2017.62.
- [173] J. Yang, J. Goguen, and R. Kleiman, 'Silicon Solar Cell With Integrated Tunnel Junction for Multijunction Photovoltaic Applications', *IEEE Electron Device Lett.*, vol. 33, no. 12, pp. 1732–1734, Dec. 2012, doi: 10.1109/LED.2012.2217391.
- [174] D. Jung, C. A. Parker, J. Ramdani, and S. M. Bedair, 'AlGaAs/GaInP heterojunction tunnel diode for cascade solar cell application', *J. Appl. Phys.*, vol. 74, no. 3, pp. 2090–2093, Aug. 1993, doi: 10.1063/1.354753.
- [175] M. Baudrit and C. Algora, 'Modeling of GaInP/GaAs Dual-Junction solar cells including Tunnel Junction', in *2008 33rd IEEE Photovoltaic Specialists Conference*, San Diego, CA, USA, May 2008, pp. 1–5. doi: 10.1109/PVSC.2008.4922476.
- [176] S. Lü and X. Qu, 'AlGaAs/GaAs tunnel junctions in a 4-J tandem solar cell', *J. Semicond.*, vol. 32, no. 11, p. 112003, Nov. 2011, doi: 10.1088/1674-4926/32/11/112003.
- [177] J. F. Wheeldon *et al.*, 'AlGaAs tunnel junction for high efficiency multi-junction solar cells: Simulation and measurement of temperature-dependent operation', in *2009 34th IEEE Photovoltaic Specialists Conference (PVSC)*, Philadelphia, PA, Jun. 2009, pp. 000106–000111. doi: 10.1109/PVSC.2009.5411723.
- [178] A. Rolland *et al.*, 'Design of a lattice-matched III–V–N/Si photovoltaic tandem cell monolithically integrated on silicon substrate', *Opt. Quantum Electron.*, vol. 46, no. 10, pp. 1397–1403, Oct. 2014, doi: 10.1007/s11082-014-9909-z.
- [179] A. Fave, J.-F. Lelièvre, T. Gallet, Q. Su, and M. Lemitte, 'Fabrication of Si tunnel diodes for c-Si based tandem solar cells using proximity rapid thermal diffusion', *Energy Procedia*, vol. 124, pp. 577–583, Sep. 2017, doi: 10.1016/j.egypro.2017.09.281.
- [180] P. Bellanger, A. Minj, A. Fave, Z. Djebbour, S. Roques, and A. Slaoui, 'Silicon Tunnel Junctions Produced by Ion Implantation and Diffusion Processes for Tandem Solar Cells', *IEEE J. Photovolt.*, vol. 8, no. 6, pp. 1436–1442, Nov. 2018, doi: 10.1109/JPHOTOV.2018.2864632.
- [181] Jinli Wang, D. Wheeler, Y. Yan, Jialin Zhao, S. Howard, and A. Seabaugh, 'Silicon tunnel diodes formed by proximity rapid thermal diffusion', *IEEE Electron Device Lett.*, vol. 24, no. 2, pp. 93–95, Feb. 2003, doi: 10.1109/LED.2002.807706.
- [182] G. J. Bauhuis, P. Mulder, and J. J. Schermer, 'Ultra-thin, high performance tunnel junctions for III-V multijunction cells: Ultra-thin, high performance tunnel junctions for III-V multijunction cells', *Prog. Photovolt. Res. Appl.*, vol. 22, no. 6, pp. 656–660, Jun. 2014, doi: 10.1002/pip.2333.
- [183] J. Kim, Y. Takiguchi, and S. Miyajima, 'Characterization of p-type nitrogen-doped cuprous oxide/n-type hydrogenated microcrystalline silicon tunnel recombination junction for perovskite/crystalline silicon tandem solar cells', *Jpn. J. Appl. Phys.*, vol. 57, no. 8S3, p. 08RB05, Aug. 2018, doi: 10.7567/JJAP.57.08RB05.
- [184] M. Baudrit and C. Algora, 'Tunnel Diode Modeling, Including Nonlocal Trap-Assisted Tunneling: A Focus on III–V Multijunction Solar Cell Simulation', *IEEE Trans. Electron Devices*, vol. 57, no. 10, pp. 2564–2571, Oct. 2010, doi: 10.1109/TED.2010.2061771.
- [185] C. Luderer, C. Reichel, F. Feldmann, M. Bivour, and M. Hermle, 'Passivating and low-resistive poly-Si tunneling junction enabling high-efficiency monolithic perovskite/silicon tandem solar cells', *Appl. Phys. Lett.*, vol. 115, no. 18, p. 182105, Oct. 2019, doi: 10.1063/1.5120552.

- [186] S.-Y. Lee *et al.*, 'Analysis of a-Si:H/TCO contact resistance for the Si heterojunction back-contact solar cell', *Sol. Energy Mater. Sol. Cells*, vol. 120, pp. 412–416, Jan. 2014, doi: 10.1016/j.solmat.2013.06.026.
- [187] R. H. Cox and H. Strack, 'OHMIC CONTACTS FOR GaAs DEVICES', p. 8.
- [188] W. Wang *et al.*, 'An Expanded Cox and Strack Method for Precise Extraction of Specific Contact Resistance of Transition Metal Oxide/ *n*- Silicon Heterojunction', *IEEE J. Photovolt.*, vol. 9, no. 4, pp. 1113–1120, Jul. 2019, doi: 10.1109/JPHOTOV.2019.2917386.
- [189] PV Lighthouse: Resistivity calculator, *Resistivity calculator*. [Online]. Available: <https://www.pvlighthouse.com.au/resistivity>
- [190] K. Ji, H. Syn, J. Choi, H.-M. Lee, and D. Kim, 'The Emitter Having Microcrystalline Surface in Silicon Heterojunction Interdigitated Back Contact Solar Cells', *Jpn. J. Appl. Phys.*, vol. 51, p. 10NA05, Oct. 2012, doi: 10.1143/JJAP.51.10NA05.
- [191] M. De Bastiani, A. S. Subbiah, E. Aydin, F. H. Isikgor, T. G. Allen, and S. De Wolf, 'Recombination junctions for efficient monolithic perovskite-based tandem solar cells: physical principles, properties, processing and prospects', *Mater. Horiz.*, vol. 7, no. 11, pp. 2791–2809, 2020, doi: 10.1039/D0MH00990C.
- [192] F. E. Subhan, A. D. Khan, A. D. Khan, N. Ullah, M. Imran, and M. Noman, 'Optical optimization of double-side-textured monolithic perovskite–silicon tandem solar cells for improved light management', *RSC Adv.*, vol. 10, no. 45, pp. 26631–26638, 2020, doi: 10.1039/D0RA04634E.
- [193] S. Manzoor *et al.*, 'Optical modeling of wide-bandgap perovskite and perovskite/silicon tandem solar cells using complex refractive indices for arbitrary-bandgap perovskite absorbers', *Opt. Express*, vol. 26, no. 21, p. 27441, Oct. 2018, doi: 10.1364/OE.26.027441.
- [194] K. Jäger, L. Korte, B. Rech, and S. Albrecht, 'Numerical optical optimization of monolithic planar perovskite-silicon tandem solar cells with regular and inverted device architectures', *Opt. Express*, vol. 25, no. 12, p. A473, Jun. 2017, doi: 10.1364/OE.25.00A473.
- [195] D. B. Khadka, Y. Shirai, M. Yanagida, J. W. Ryan, and K. Miyano, 'Exploring the effects of interfacial carrier transport layers on device performance and optoelectronic properties of planar perovskite solar cells', *J. Mater. Chem. C*, vol. 5, no. 34, pp. 8819–8827, 2017, doi: 10.1039/C7TC02822A.
- [196] B. Lipovsek, J. Krc, and M. Topic, 'Microtextured Light-Management Foils and Their Optimization for Planar Organic and Perovskite Solar Cells', *IEEE J. Photovolt.*, vol. 8, no. 3, pp. 783–792, May 2018, doi: 10.1109/JPHOTOV.2018.2810844.
- [197] Y. Peng *et al.*, 'The Influence of PbI₂ on Characteristic of Organic-Inorganic Hybrid Perovskite Thin Films', *Model. Numer. Simul. Mater. Sci.*, vol. 07, no. 04, pp. 47–57, 2017, doi: 10.4236/mnsms.2017.74004.
- [198] D. Luo *et al.*, 'Enhanced photovoltage for inverted planar heterojunction perovskite solar cells', *Science*, vol. 360, no. 6396, pp. 1442–1446, Jun. 2018, doi: 10.1126/science.aap9282.
- [199] B. J. Bruijnaers, E. Schiepers, C. H. L. Weijtens, S. C. J. Meskers, M. M. Wienk, and R. A. J. Janssen, 'The effect of oxygen on the efficiency of planar p–i–n metal halide perovskite solar cells with a PEDOT:PSS hole transport layer', *J. Mater. Chem. A*, vol. 6, no. 16, pp. 6882–6890, 2018, doi: 10.1039/C7TA11128B.
- [200] D. K. Aswal, S. Lenfant, D. Guerin, J. V. Yakhmi, and D. Vuillaume, 'Self assembled monolayers on silicon for molecular electronics', *Anal. Chim. Acta*, p. 25, 2006.

APPENDICES

Appendix A. Chemically polished silicon wafers study for large-area printed PK

A great way to reduce the cost and prepare for mass-production PK/SHJ tandems solar cells is the deposition of the Perovskite top-cell with large-scale solution-based process (e.g. printing process). Thus, the substrates must be polished in order to allow a homogeneous deposition. In this work, we investigated different chemical polishing (CP) processes, on N type CZ (100) “as cut” wafers, M2 size, with the objective to find an enough polished surface for the PK deposition. The tested PC process, from PC1 to PC5, are KOH-based and have different etching time and temperature.

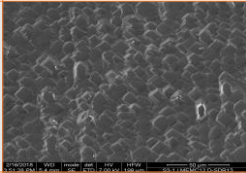
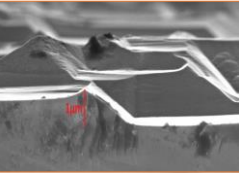
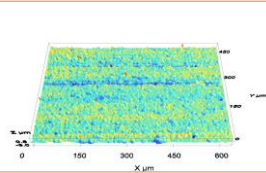
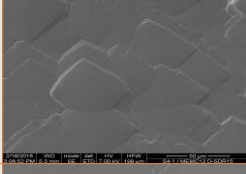
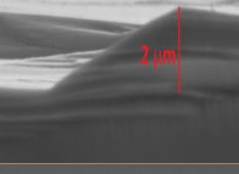
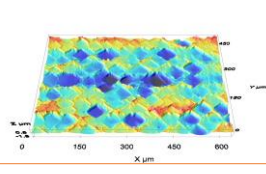
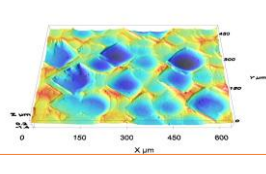
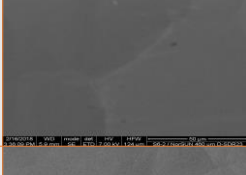
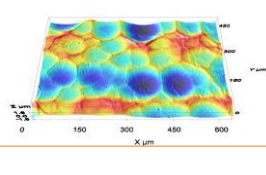
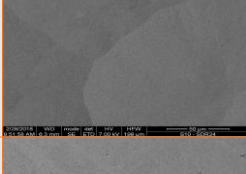
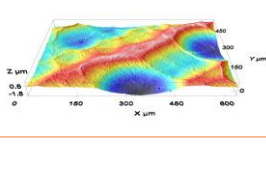
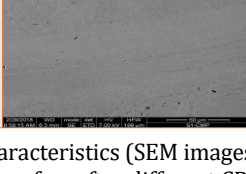
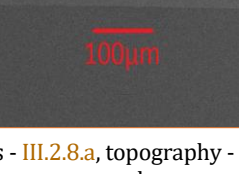
CP	SEM Images (x1500)	Cross-section SEM Images	Confocal Microscopy (x20) – Topography	Diffuse Reflectance (%) at 800 nm
CP1 - 4 $\mu\text{m}/\text{side}$				23
CP2 - 16 $\mu\text{m}/\text{side}$				9,8
CP3 - 32 $\mu\text{m}/\text{side}$				4,8
CP4 - 62 $\mu\text{m}/\text{side}$				1,5
CP5 - 123 $\mu\text{m}/\text{side}$				1
CMP (commercial)			Too smooth	0,4

Figure A-1 Characteristics (SEM images - III.2.8.a, topography - III.2.9 and diffuse Reflectance - III.2.2) of the wafers after different CP processes and commercial CMP wafer presented as a flat-surface reference.

Figure A-1 shows the different properties of the wafers after the CP processes. The more the surface is etched, the smoother it looks.

Then, we deposited a Perovskite top-cell on those wafers, by spin-coating (see III.1.6). The deposition worked well for the wafers with the CP4 and CP5 processes, the Perovskite layer appeared homogeneous in SEM images. However, the CP1, CP2 and CP3 processes seem to be not sufficient, the Perovskite layer did not cover well the substrates.

Nevertheless, CP4 and CP5 processes etched more than 60 $\mu\text{m}/\text{side}$, which is too much from an economic point of view (wafers have to be thick and too much material is wasted). Thus, other industrially viable methods have to be tested, in order to print the Perovskite top-cell on large-area substrates.

Appendix B. Passivation degradation after e-beam evaporation of silver electrodes

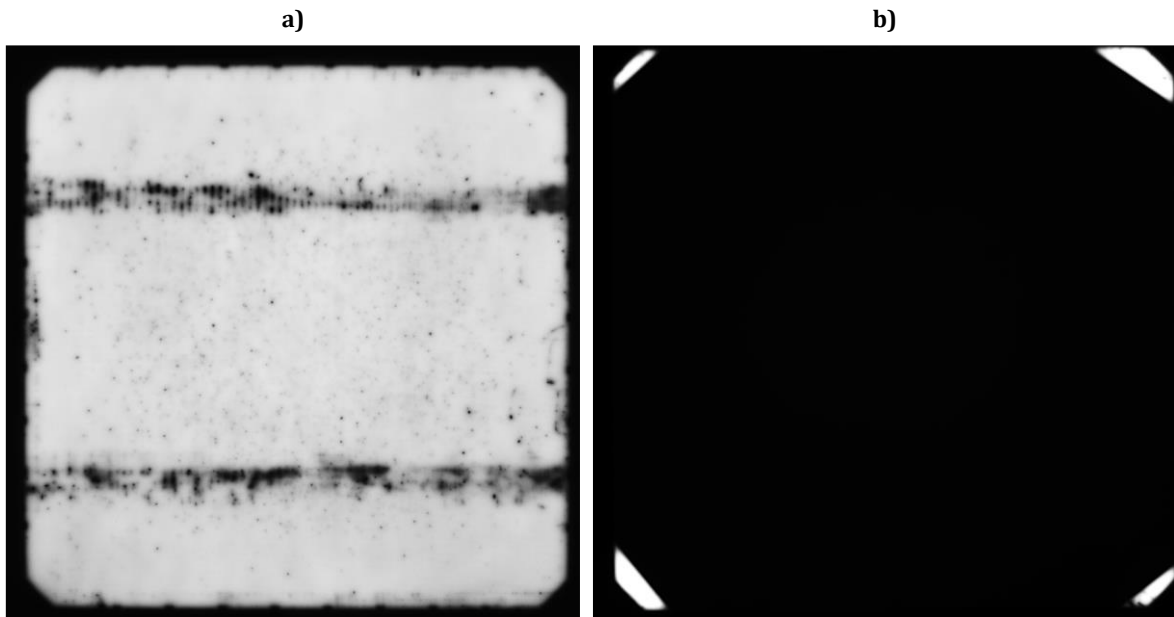


Figure B-1 a) Photoluminescence image of a 1N/1N M2 size wafer (see **Figure IV.2-1 f**) after the PECVD process, b) after a deposit of silver on the whole back-side by e-beam evaporation (except in the white corners).

Figure B-1 demonstrates the degradation on the a-Si:H layers due to e-beam evaporation of silver without protection (e.g. a thick ITO layer on the a-Si:H layers). Moreover, we tried to heal the samples by an annealing during 10 min at 200 °C and/or a light soaking during 15 hours but nothing was conclusive.

However, we did not observe such a degradation with thermal evaporation. This explains why we chose this type of metallisation (thermal evaporation) in chapters **V** and **VI**.

Appendix C. Investigation of shunt issues in PK/SHJ tandem solar cells

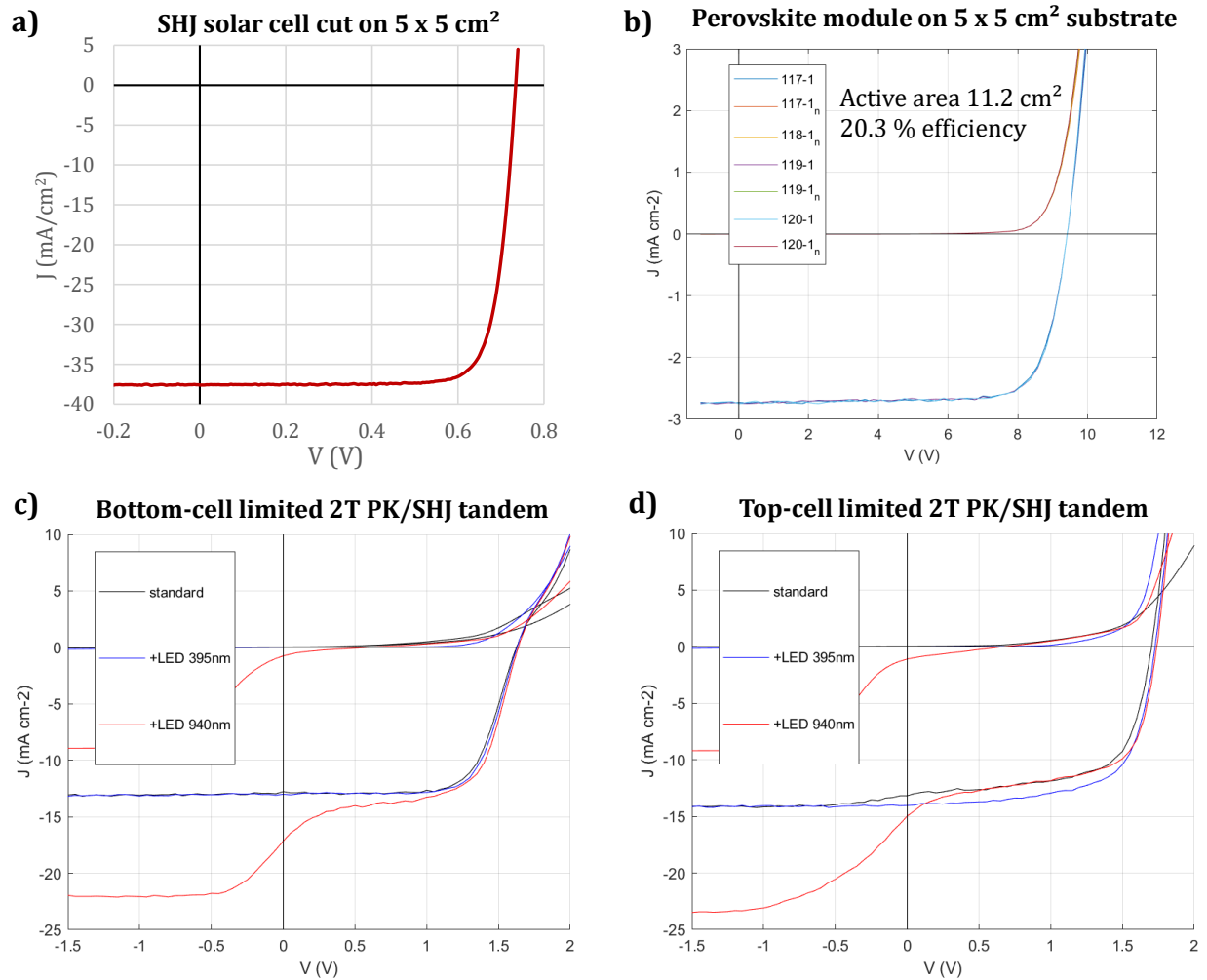


Figure C-1 J-V curves of **a)** single-junction SHJ cut on 5 x 5 cm², **b)** single-junction Perovskite module on a 5 x 5 cm² substrate, **c)** bottom-cell limited 2T PK/SHJ tandem solar cell and **d)** top-cell limited 2T PK/SHJ tandem solar cell.

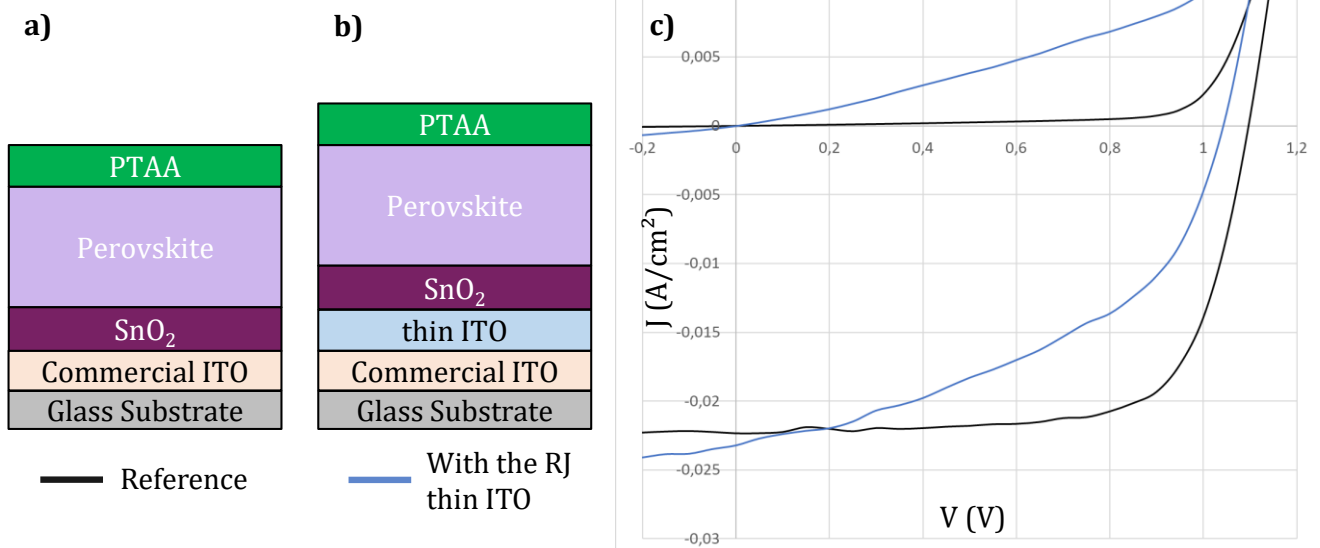


Figure C-2 **a)** Reference single-junction Perovskite solar cell structure, **b)** single-junction Perovskite solar cell structure with the thin ITO layer (used in RJ) on top of the commercial ITO and **c)** the corresponding J-V curves of structures **a)** and **b)**.

As mentioned in this work, PK/SHJ tandem solar cells with a thin ITO layer in the recombination junction have shunt issues. Indeed, we observed that I-V curves of both SHJ and Perovskite cells, in single-junction solar cells (**Figure C-1 a) and b)** and **Figure C-2 c)** have a plane shape, without apparent shunts. However, in PK/SHJ tandem solar cells, we observe large shunt issues in the Perovskite top-cell in **Figure C-1 c) and d)**, in the top-cell limited condition (red curves). Moreover, those shunt issues are also observable in J-V curves of single-junction Perovskite solar cells when the Perovskite cell is deposited on the thin ITO layer (see **Figure C-2 c)**).

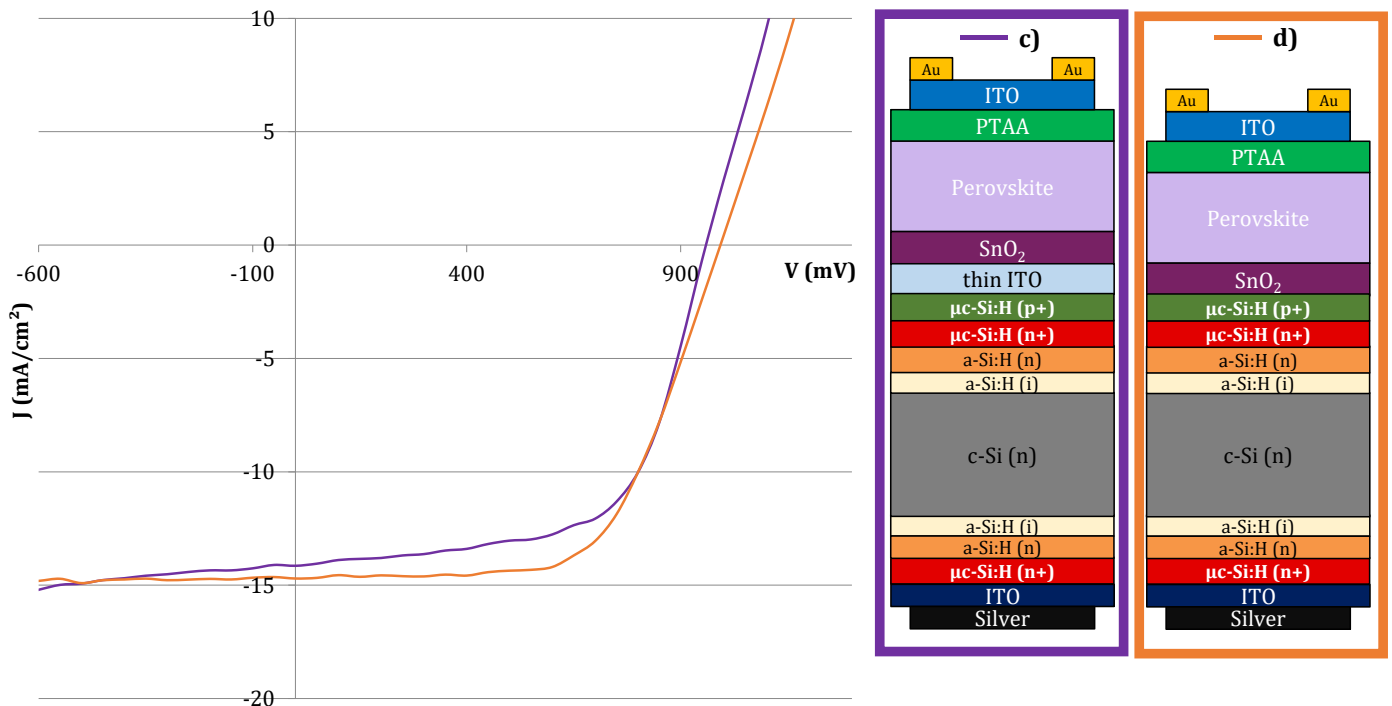


Figure C-3 J-V curves and the corresponding structures of the “tandem-like” devices **c)** (in purple) and **d)** (in orange) from part VI.3 (**Figure VI.3-6**).

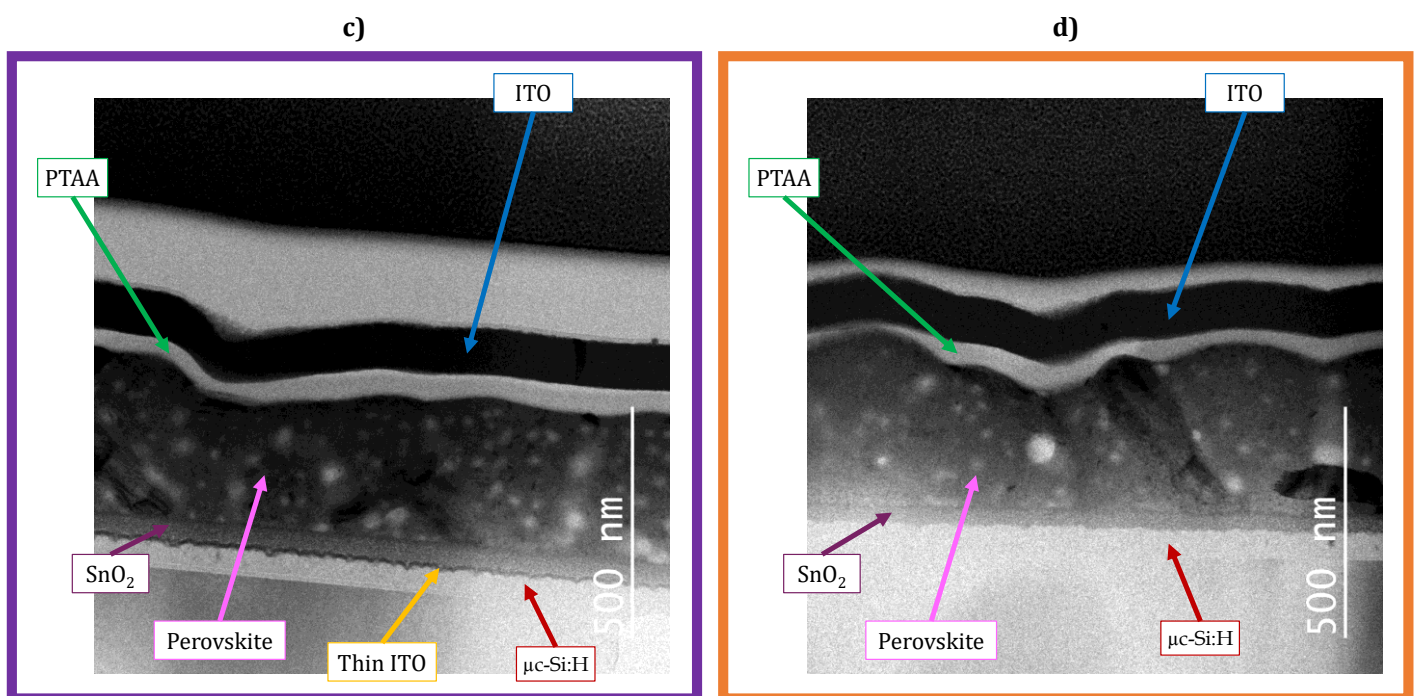


Figure C-4 Cross-section STEM images in bright field of the devices **c)** and **d)** (**Figure C-3**).

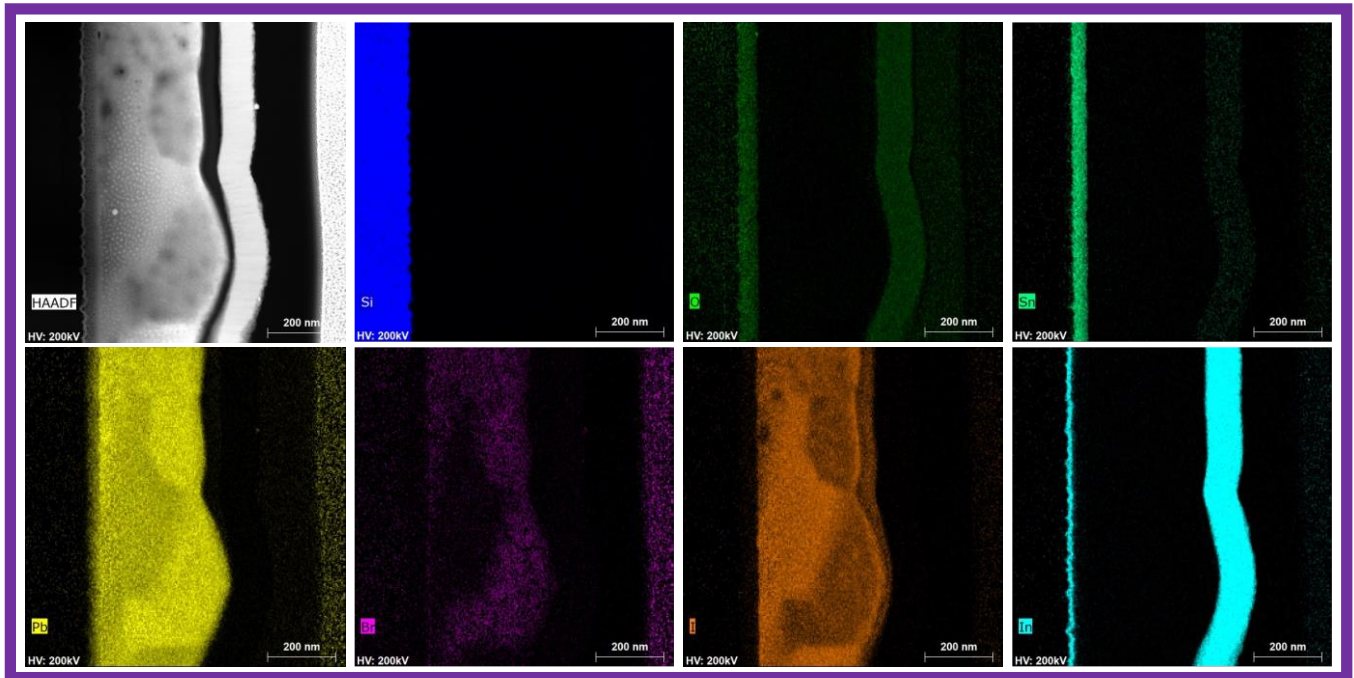


Figure C-5 STEM-EDX elemental mapping of a cross section of the device **c)** (Figure C-3).

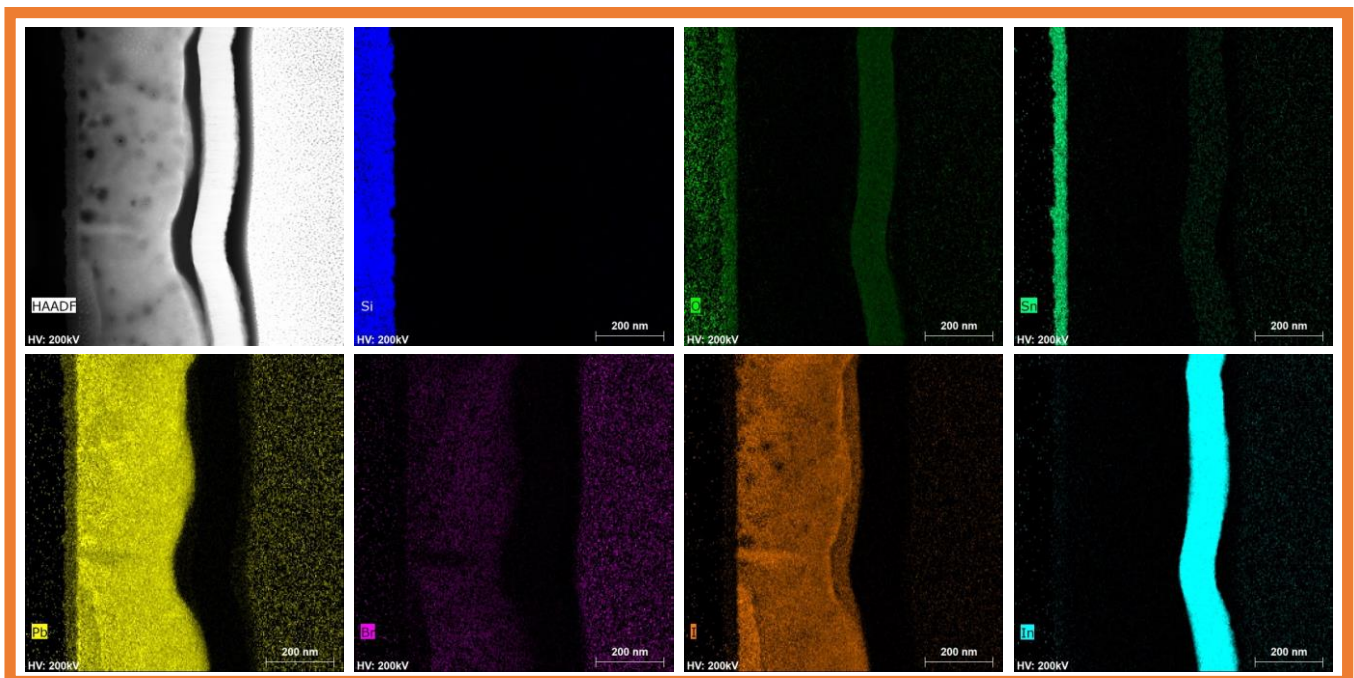


Figure C-6 STEM-EDX elemental mapping of a cross section of the device **d)** (Figure C-3).

In order to observe differences (mix between the thin ITO and the SnO₂ or different Perovskite layer), linked to the thin ITO in the RJ, which can explain those shunt issues, we performed STEM and EDX measurements on the “tandem-like” devices **c)** and **d)** from Figure VI.3-6 (Figure C-3). However, the Perovskite layer seems to be similar in both cases in the Figure C-4, the same different phases are observed and in similar proportions. Moreover, the EDX elemental mapping (Figure C-5 and Figure C-6) tends to demonstrate that the thin ITO does not mix with the SnO₂ layer (Figure C-5). Indeed, in both cases (device **c)** and **d)**), the SnO₂ and the thin ITO cover the $\mu\text{c-Si:H}$ (p⁺) layer roughness, but the Sn material seems to diffuse more in the $\mu\text{c-Si:H}$ (Figure C-6) than in the ITO (Figure C-5). In conclusion, the shunt issues seem related to the electrical (e.g. lateral conductivity) of the thin ITO layer and not to structural or chemical differences.

RÉSUMÉ ÉTENDU

I. Contexte et Objectifs

Cette thèse prend place dans le contexte de la crise environnementale, présentant le photovoltaïque comme un élément essentiel de la lutte contre le réchauffement climatique.

Le réchauffement climatique ([1], [2]) nous amène à repenser nos émissions de gaz à effet de serre. En effet, il est désormais connu que cette crise climatique d'origine humaine ne cesse de s'aggraver. Notre façon de consommer et de produire doit donc changer. Ce changement passe nécessairement par la réduction des émissions de CO₂ dans l'atmosphère et pour cela, l'électrification des modes de consommation d'énergie, notamment via des sources d'énergie renouvelables, dont l'énergie photovoltaïque ([4], [5]), est indispensable.

L'énergie photovoltaïque est produite par des dispositifs appelées cellules solaires, grâce à l'effet photovoltaïque démontré par E. Becquerel en 1839 [6]. Depuis la découverte de cet effet, la recherche et l'industrie du photovoltaïque ont connu une croissance rapide. Au début de cette thèse (fin 2017), la capacité solaire photovoltaïque installée cumulée dépassait 400 GW et elle a atteint 760 GW à la fin 2020 [7]. Selon certaines estimations, cette capacité mondiale devrait dépasser les 1000 GW au cours des 2 prochaines années [8]. Le facteur clé de cette augmentation est la baisse des coûts de production, associée à l'augmentation des rendements des cellules solaires. Ces travaux de thèse s'inscrivent dans cette course, en proposant des études de développement et de compréhension d'une technologie prometteuse de cellules solaires à haut rendement et à potentiel bas coût.

En effet, la part de marché mondiale du solaire photovoltaïque est actuellement dominée par les cellules solaires en silicium cristallin élaborées à haute température (PERC, PERL ou à contacts passivés), mais les technologies dites « tandem » à base de silicium devraient entrer sur le marché dans les 5 prochaines années [9]. Ces technologies ont une limite d'efficacité théorique plus élevée que celle des cellules à simple jonction [10]. Elles sont composées d'une cellule inférieure à base de silicium associée à une cellule supérieure dans un matériau ayant une bande interdite plus large. Du point de vue économique, l'ajout de cette cellule supérieure doit être le moins coûteux possible. Ces travaux de thèse se concentrent donc sur les cellules solaires tandem Pérovskite sur hétérojonction de silicium (PK/SHJ), une technologie capable de dépasser les rendements de conversion actuels, tout en limitant l'augmentation des coûts de production et l'impact environnemental.

De 2015 à 2017, plusieurs preuves de concept de cellules solaires tandem PK/SHJ ont été présentées dans la littérature ([11]–[15]). Ces dispositifs, impliquant la mise en série d'une cellule solaire Pérovskite et d'une cellule solaire SHJ, ont ainsi démontré des rendements supérieurs à 20 %, sur de petites surfaces, rivalisant avec les rendements des cellules à simple-jonction en silicium. Par ailleurs, plusieurs types d'architecture (NIP et PIN), de texturation (poli/poli, poli/texturé et texturé/texturé) et de jonctions de recombinaison (RJ) ont été proposés dans les expériences et les simulations. Cependant, ces premières études ont également montré qu'il est essentiel de réduire les pertes pour augmenter les rendements, qu'elles soient optiques (dues à l'absorption parasite des

différentes couches) ou liées au transport des charges, notamment dans la jonction de recombinaison.

Néanmoins, même si cette RJ entre les deux sous-cellules semble être un facteur clé, les études publiées ne se sont pas attardées sur ce sujet. Elles ont démontré la possibilité d'utiliser une couche d'ITO ou une jonction PN en silicium fortement dopé dans les preuves de concept mais sans proposer de perspectives de caractérisation et d'amélioration. Ceci justifie ces travaux, qui consistent à caractériser, comprendre et optimiser la jonction de recombinaison entre les sous-cellules, en développant des méthodes adaptées.

Les objectifs de ces travaux de thèse sont donc les suivants :

- Développement d'une jonction tunnel en silicium fortement dopé adaptée aux cellules solaires tandem PK/SHJ à 2-terminaux (2T),
- Mise en œuvre de méthodes de caractérisation pour optimiser les jonctions de recombinaison,
- Compréhension des mécanismes de transport dans les cellules solaires tandem PK/SHJ 2T et l'influence de leur RJ.

II. Jonction de recombinaison en $\mu\text{c-Si}$

Déjà présentées dans la littérature ([13], [95]), les jonctions tunnel fortement dopées peuvent être utilisées comme RJ dans les cellules tandem. Cette jonction doit être suffisamment fine, transparente et conductrice pour permettre la recombinaison des porteurs de charge. En outre, dans le cas d'une cellule inférieure SHJ, les couches de la RJ ne doivent pas dégrader les couches et interfaces a-Si:H, qui sont très sensibles aux variations de température. Dans ce contexte, le silicium microcristallin qui peut être déposé par PECVD (comme les couches de silicium amorphes) à basse température (≤ 200 °C) semble être un bon choix. Il présente également les avantages d'être assez transparent dans le domaine IR et d'avoir des indices optiques adaptés [155]. De plus, ce type de RJ est déjà utilisé dans plusieurs cellules solaires multijonctions ([156]–[158]) et possède toutes les qualités requises.

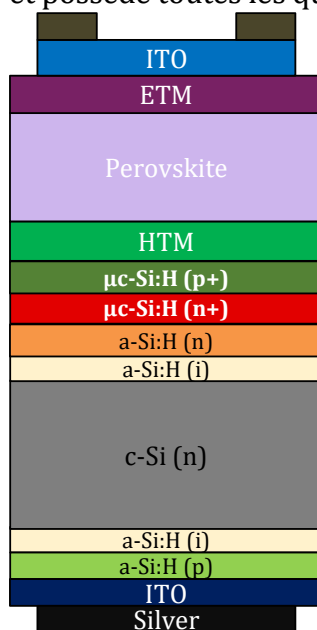


Fig. 1 Cellule solaire tandem PIN PK/SHJ avec une RJ en silicium microcristallin.

Nous avons donc choisi de développer une RJ en silicium microcristallin, déposé à basse température pour préserver la cellule SHJ, dans la configuration PIN, comme représenté sur la **Fig. 1**. Cette RJ est développée pour être intégrée sur un substrat poli afin de permettre la fabrication de la cellule supérieure en Pérovskite par dépôt par centrifugation. Le temps de dépôt de cette jonction a ensuite été adapté pour conserver des épaisseurs similaires dans les résultats et études présentés sur des surfaces texturées.

Pour le développement des couches, nous avons utilisé l'ellipsométrie spectroscopique (SE) et des mesures 4-pointes comme méthodes de caractérisation de référence. Les mesures SE ont été ajustées avec un modèle supposant un mélange de $\mu\text{c-Si:H}$, a-Si:H et de vide (pour la rugosité de la couche, en appliquant les approximations du milieu effectif de Bruggeman [160]). Le matériau $\mu\text{c-Si:H}$ est basé sur un matériau polysilicium à petits grains et représente la phase microcristalline de la couche. Le processus d'ajustement SE

nous a permis de déterminer les épaisseurs des couches et les pourcentages de fraction de phase microcristalline ($X_{\mu\text{-Si}}$). Les mesures 4-pointes ont été réalisées pour contrôler la R_{sheet} et la conductivité latérale, σ , des couches déposées sur des substrats en verre.

Nous avons fait varier les paramètres de dépôt PECVD jusqu'à obtenir les caractéristiques de couches souhaitées : une épaisseur cumulée de 50 nm avec un pourcentage de phase microcristalline élevée ($X_{\mu\text{-Si}} > 50\%$) et une conductivité presque 10^4 fois plus élevée que des couches amorphes ($\sigma \approx 8 \text{ S/cm}$). Le **Tableau 1** présente les paramètres finaux sélectionnés pour les couches $\mu\text{-Si:H}$ de type N et de type P développées.

Pression dans la chambre (Torr)	Puissance RF (Watt)	Vitesse du suscepteur (mm/sec)	Position du suscepteur (mm)
9	1100	3	21
$\mu\text{-Si:H}$	R	R_N ou R_P	Temps de dépôt
N-type	0.0025	1	100 s
P-type	0.0025	1.2	80 s

Tableau 1. Paramètres PECVD utilisés pour le dépôt des couches de silicium microcristallin.

$$R = \frac{\text{SiH}_4}{\text{SiH}_4 + \text{H}_2} \quad R_N = \frac{\text{PH}_3}{\text{SiH}_4} \quad R_P = \frac{\text{B}_2\text{H}_6}{\text{SiH}_4}$$

Ensuite, nous avons caractérisé les propriétés optiques, électriques et structurales des couches développées et validé qu'elles présentent les conditions requises pour former une RJ efficace. En effet, le pourcentage de phase microcristalline obtenu par mesures SE correspond à celui mesuré par spectroscopie Raman et l'épaisseur extraite a été vérifiée avec des images STEM (**Fig. 2**). Nous avons également obtenu de faibles énergies d'activation, $E_a \leq 30 \text{ meV}$, en comparaison des couches amorphes habituellement utilisées dans les cellules SHJ ([118]). De plus, nous avons observé une augmentation de la durée de vie des porteurs minoritaires, ce qui démontre que les couches $\mu\text{-Si:H}$ améliorent la passivation chimique et l'effet de champ des cellules solaires SHJ. En sus, la jonction $\mu\text{-Si:H}$ (n^+/p^+) développée est presque transparente dans le domaine IR, ce qui affecte donc peu l'absorption de la cellule SHJ inférieure dans la configuration tandem. Enfin, nous avons fabriqué des cellules solaires SHJ avec l'ajout de la jonction $\mu\text{-Si:H}$ (n^+/p^+) et observé qu'aucune résistance série, R_s , supplémentaire n'est créée et que les courbes I-V ne présentent pas de forme en S (caractéristique de phénomènes parasites d'accumulation de charges).

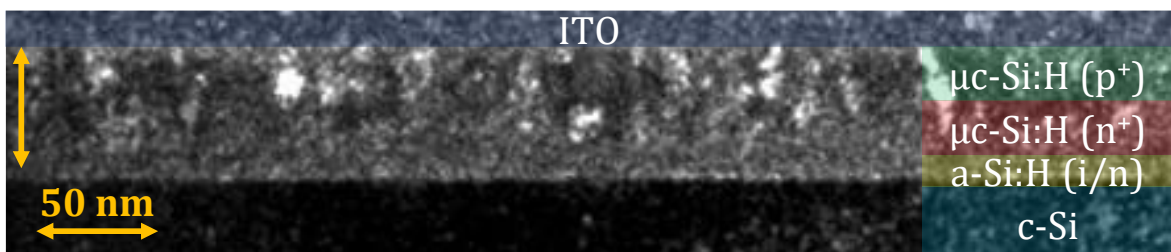


Fig. 2 Image STEM de la jonction $\mu\text{-Si:H}$ (n^+/p^+) sur un substrat poli.

En conclusion, la RJ en silicium microcristallin développée présente toutes les exigences structurales, optiques et électriques pour remplir son rôle dans des cellules solaires tandem.

III. Caractérisation des jonctions de recombinaisons

Suite au développement de la RJ fortement dopée et à son intégration dans des cellules solaires SHJ, nous avons cherché à caractériser électriquement l'effet recombinant de cette RJ. Pour ce faire, les RJ fortement dopées étant très similaires aux diodes tunnel, nous avons proposé et étudié plusieurs façons de les caractériser, en les assimilant à des diodes tunnel. Dans la littérature, des jonctions tunnel à base de GaAs ont souvent été isolées sur un substrat avec des électrodes à l'avant et à l'arrière pour obtenir les courbes I-V caractéristiques des diodes tunnel [174]–[176]. Par ailleurs, d'autres structures avec des électrodes uniquement à l'avant, ont aussi été utilisées, mais le principe reste le même [177]. De même, de telles structures de test ont également été utilisées pour des jonctions en silicium dopé par diffusion [173], [178]–[180], ainsi que pour les diodes tunnel en silicium [181].

Dans notre cas, l'objectif est de définir une structure de test où la RJ est similaire à celle qu'elle sera dans la cellule solaire tandem, comme l'ont fait G. J. Bauhuis et al. et J. Kim et al. [182], [183], par exemple. Ainsi, pour obtenir la même croissance des couches, nous avons conservé le même substrat que dans les cellules tandem et les couches a-Si:H sous-jacentes. De plus, pour des raisons pratiques, la structure de test doit être plus facile à mettre en œuvre et à mesurer que la fabrication et les mesures des cellules solaires tandem complètes, tout en étant représentative du comportement du dispositif final.

Premièrement, nous avons mesuré différentes structures de test composées d'un substrat c-Si, des couches amorphes de la cellule SHJ et de la RJ en silicium microcristallin. Nous avons démontré que ces structures nécessitent de préférence un empilement arrière ohmique et une électrode avant déjà étudiés. En effet, pour faciliter l'analyse et la compréhension des résultats, il est souhaitable que la RJ soit le seul facteur inconnu/variable. Avec une structure isotype (de type N, **Fig. 3**), à laquelle nous avons ajouté la RJ développée et des électrodes ITO/Ag, nous avons mesuré la caractéristique de diode tunnel de la RJ avec des mesures I-V dans l'obscurité à différentes températures, **Fig. 3**. Ceci démontre que la RJ $\mu\text{c-Si:H}$ (n^+/p^+) développée se comporte bien comme une diode tunnel, avec un courant tunnel élevé à faible tension.

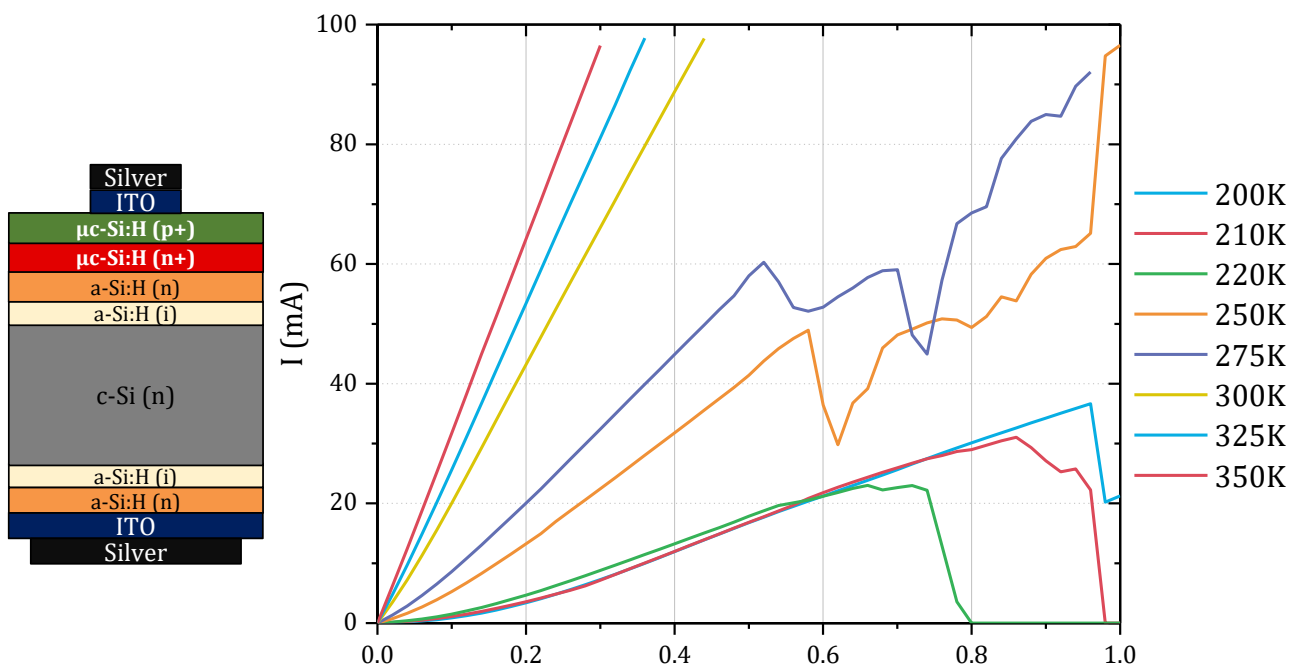


Fig. 3 Courbes I-V dans l'obscurité, mesurées à différentes températures, de la structure de test présentée à gauche.

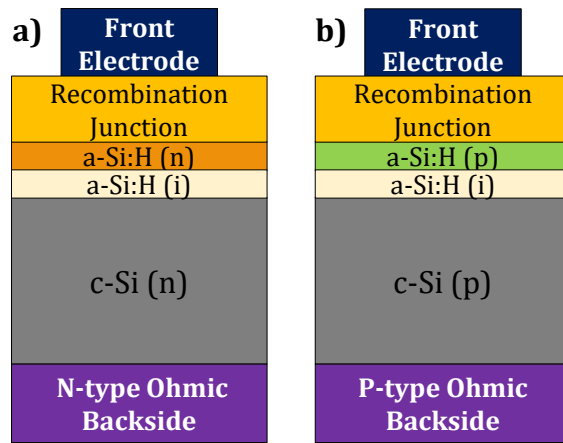


Fig. 4 Structures de tests pour les mesures I-V dans l'obscurité des jonctions de recombinaison. **a)** Pour les cellules solaires tandem PIN et **b)** pour les cellules solaires tandem NIP.

Néanmoins, nous avons également observé que la présence d'ITO dans l'électrode avant forme une jonction NPN avec la RJ, ce qui influence de façon non négligeable les mesures et doit être pris en compte dans leur interprétation. La **Fig. 4** montre l'architecture des structures de test définies pour caractériser les RJ des cellules solaires tandem NIP et PIN. L'électrode frontale idéale est une électrode métallique qui a un très bon contact avec la RJ étudiée (Ti/Pd/Ag par exemple). Cependant, une électrode TCO/Métal bien connue peut également être utilisée pour optimiser les RJ fortement dopées. De plus, si la résistance

de contact entre la RJ et le TCO est connue, de telles structures permettent d'observer rapidement si la RJ est faiblement ou fortement résistive. Nous avons également conclu que si l'électrode est très petite ou que les mesures sont réalisées à basse température (pour avoir un faible courant et ne pas être impacté par la limite de l'équipement), on peut observer le comportement de diode tunnel RJ fortement dopées (**Fig. 3**).

En conclusion, nous avons démontré que définir et mettre en œuvre des structures de test simples, isolant le comportement de la RJ de celui du dispositif complet, est un travail considérable et important. Les interactions entre les interfaces et les couches sont extrêmement sensibles à toute analyse et doivent être isolées en plusieurs lots et étapes de caractérisation pour interpréter au mieux les résultats. De plus, il est essentiel de relier les propriétés des RJ aux propriétés électriques/optiques/structurales des matériaux et au budget thermique ou aux étapes ultérieures.

IV. Vers des tandems Pérovskite sur hétérojonction de silicium

Après avoir développé, caractérisé et étudié l'impact des RJ sur la cellule inférieure SHJ, nous nous sommes concentrés sur l'intégration de la RJ dans un dispositif tandem complet PK/SHJ 2T. Tout d'abord, nous avons étudié l'influence des RJ sur les propriétés optiques des cellules solaires tandem PK/SHJ, avec des simulations optiques. Ensuite, nous avons présenté et utilisé une nouvelle méthode pour étudier l'influence de ces RJ sur la cellule supérieure en Pérovskite. Enfin, nous avons intégré la RJ $\mu\text{-Si:H}$ (n^+/p^+) développée dans des cellules solaires tandem PIN PK/SHJ complètes.

Premièrement, nous avons effectué des simulations optiques des cellules solaires tandem PK/SHJ avec différentes RJ, à l'aide du logiciel CROWM. En effet, la gestion de la lumière est très importante dans les cellules solaires. De plus, dans les cellules solaires tandem PK/SHJ, il y a beaucoup de couches et de matériaux, ce qui rend la gestion optique plus difficile mais encore plus importante, notamment sur les dispositifs 2T en raison des contraintes d'adaptation au courant. Dans la littérature, de nombreux articles traitent de la gestion de la lumière et de l'optimisation optique des cellules solaires tandem PK/SHJ, en utilisant des simulations optiques pour des structures dédiées ([93], [155], [192]–[194]). Ces simulations permettent de comparer plusieurs matériaux, épaisseurs de couches, empilements, architectures, textures... Cependant, les simulations optiques dans la littérature sont basées sur les matériaux expérimentaux du groupe de recherche ou sur les matériaux et structures déjà publiés par d'autres équipes de

recherche. Ainsi, compte tenu de la variabilité des matériaux, il semble essentiel pour chaque groupe de réaliser ses propres travaux de simulation, en fonction des possibilités expérimentales. Concernant la RJ habituellement utilisée en ITO, nous avons constaté que, même en dessous de 15 nm d'épaisseur, la couche d'ITO induit plus de $0,5 \text{ mA/cm}^2$ de pertes de courant dues à son absorption parasite, ce qui est supérieur à la RJ $\mu\text{-Si:H}$ (n^+/p^+) développée. D'autres TCOs, plus transparents, peuvent être utilisés pour remplacer l'ITO (IZO, AZO...) mais leur développement est nécessaire. En outre, les simulations optiques ont également démontré que des dispositifs tandem simplifiés (avec formation d'une RJ entre les deux sous-cellules, sans ajout de couche) ont le même potentiel optique que les dispositifs de référence. Ceci est intéressant car avec ces dispositifs simplifiés, nous pouvons réduire le nombre d'étapes dans le processus de fabrication, réduisant ainsi le coût total.

Deuxièmement, la qualité de la cellule supérieure en Pérovskite étant dépendante du substrat (nature, surface, rugosité, mouillabilité), il semble important de la caractériser sur des structures répliquant au mieux la cellule inférieure et comprenant la RJ. En effet, la formation de la cellule supérieure en Pérovskite sur la RJ est une question clé concernant les performances finales de la cellule tandem, mais ce sujet est souvent négligé dans la littérature. Nous avons mis en place et démontré que des dispositifs de test « type tandem », présentés dans la **Fig.5**, sont des structures importantes pour le développement des cellules solaires tandem PK/SHJ. En effet, ils permettent de mesurer la cellule supérieure en Pérovskite, qui a été déposée dans les mêmes conditions que

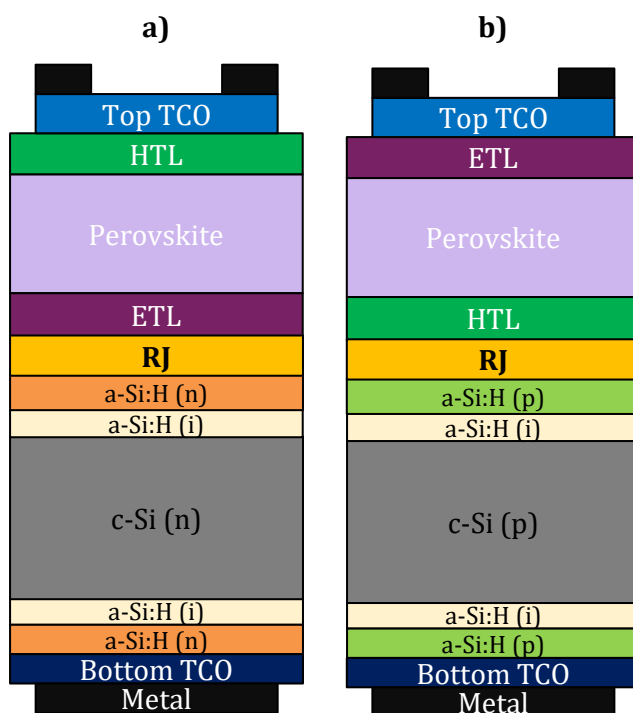


Fig. 5 Dispositifs de test "type tandem" pour mesurer la cellule supérieure en Pérovskite dans des conditions de tandem (a) pour l'architecture NIP et (b) pour l'architecture PIN).

dans les cellules solaires tandem PK/SHJ. Cela permet d'étudier l'influence du substrat de la cellule inférieure et de la RJ sur la qualité de la cellule supérieure et de les optimiser, ou de les adapter (la RJ et les deux sous-cellules), les unes par rapport aux autres.

De plus, nous avons utilisé ces dispositifs « type tandem » pour comparer l'influence, sur la cellule en Pérovskite, de la RJ en silicium microcristallin développée précédemment et de la RJ à base d'ITO. Nous avons observé qu'avec la RJ $\mu\text{-Si:H}$ (n^+/p^+), les dispositifs ont beaucoup moins de problèmes de shunt et moins de pertes par réflexion. De plus, le FF mesuré est également meilleur avec les couches $\mu\text{-Si:H}$ dans la jonction. En conclusion, une RJ en silicium microcristallin semble être le meilleur choix, comparé à une couche d'ITO.

Troisièmement, nous avons intégré la RJ $\mu\text{-Si:H}$ (n^+/p^+) développée dans des cellules solaires PIN PK/SHJ. La **Fig.6** présente les premiers résultats de mesures I-V obtenus. Trois observations principales en découlent :

- Aucun problème de shunt n'a été observé avec la RJ $\mu\text{-Si:H}$ (n^+/p^+),

- La formation d'une couche d'oxyde pendant le prétraitement UV/O₃ sur la RJ a un impact sur les performances électriques des cellules (les courbes J-V ont une forme en S qui dépend de la durée du prétraitement et du temps entre le prétraitement et le dépôt HTM, ce qui affecte fortement le FF),
- Si nous voulons éviter l'absorption parasite de la couche PEDOT:PSS (afin d'augmenter le courant) et, en même temps, améliorer le V_{oc} de la cellule supérieure, un autre HTM doit être utilisé dans cette architecture PIN. Une couche SAM ([107]) pourrait être un meilleur choix mais son assemblage sur la jonction $\mu\text{-Si:H}$ (n⁺/p⁺) doit être étudié au préalable ([200]).

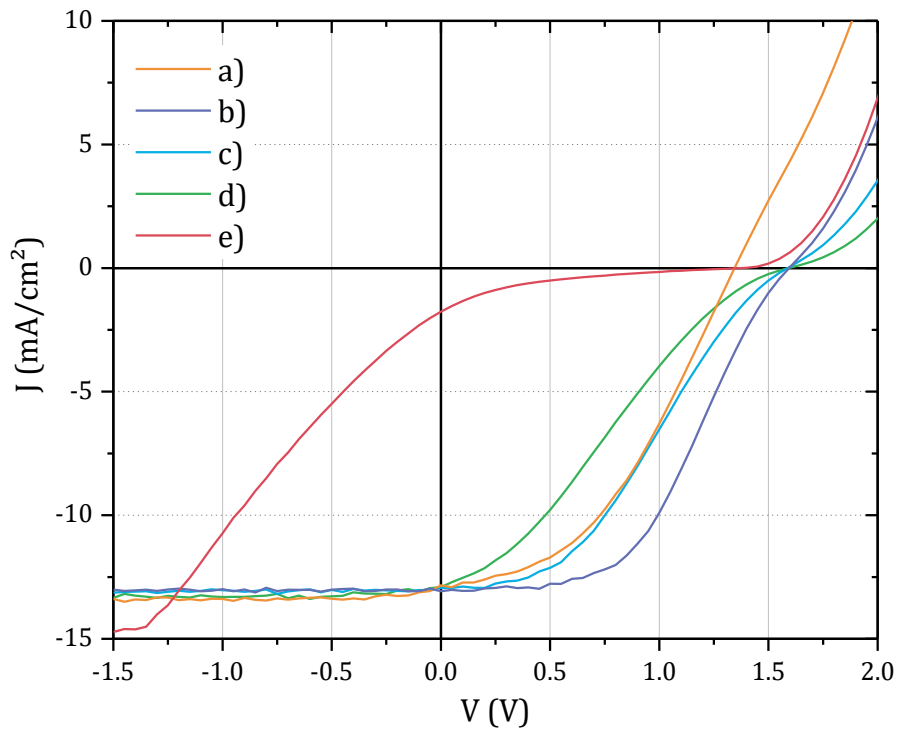


Fig. 6 Courbes J-V des cellules solaires tandem PIN PK/SHJ, avec la RJ $\mu\text{-Si:H}$ (n⁺/p⁺) développée, deux HTM différents et différentes durées de prétraitement UV/O₃: **a)** 3 min UV/O₃ et PEDOT:PSS ; **b), c) et d)** 5 min UV/O₃ et PEDOT:PSS ; **e)** 5 min UV/O₃ et un HTM SAM (2-PACz).

En conclusion, nous avons obtenu des résultats prometteurs, sans problèmes de shunt et dépassant 10 % d'efficacité, ce qui démontre la viabilité de la RJ en silicium microcristallin développée. De plus, ces résultats ont illustré l'importance d'étudier préalablement le dépôt de la cellule supérieure (par exemple avec les dispositifs de test « type tandem ») sur la RJ. En effet, il est très important de trouver le meilleur compromis entre les différentes étapes de fabrication et de les améliorer conjointement (prétraitements, recuits...), ce qui améliore une couche ne doit pas en dégrader une autre (du moins au minimum possible).

V. Conclusions et Perspectives

Afin de remplir les trois objectifs de cette thèse, nous avons mis en place une approche en trois parties. Premièrement, nous avons présenté le développement d'une jonction tunnel en silicium microcristallin destinée à être intégrée comme jonction de recombinaison dans des cellules solaires tandem PIN PK/SHJ. Deuxièmement, nous avons mis en œuvre et discuté des méthodes pour caractériser électriquement les RJ, en utilisant la jonction $\mu\text{-Si:H}$ (n⁺/p⁺) précédemment développée comme exemple. Enfin,

nous avons étudié l'intégration de la RJ dans les cellules solaires tandem PK/SHJ, avec des simulations optiques et en utilisant une nouvelle structure de test (permettant la mesure de la cellule supérieure Pérovskite), en utilisant la jonction $\mu\text{-Si:H}$ (n^+/p^+) et une couche d'ITO fin comme exemples.

- Développement d'une jonction tunnel en silicium fortement dopé adaptée aux cellules solaires tandem PK/SHJ à 2-terminaux (2T)

Tout d'abord, dans le chapitre IV, nous avons présenté le développement d'une jonction tunnel hautement dopée, à base de silicium microcristallin, afin de remplacer la RJ habituelle en ITO, dans les cellules solaires tandem PK/SHJ en configuration PIN. Nous avons caractérisé les couches $\mu\text{-Si:H}$ développées et validé qu'elles remplissent les conditions pour former une RJ efficace. Ensuite, nous avons intégré cette jonction $\mu\text{-Si:H}$ (n^+/p^+) dans des cellules solaires SHJ et nous avons conclu que la jonction semble avoir toutes les exigences structurales, optiques et électriques pour remplir correctement son rôle de RJ.

Ensuite, dans le chapitre V, nous avons démontré que la RJ développée est faiblement résistive. De plus, nous avons observé sa caractéristique de diode tunnel et validé que le courant de pointe est suffisant pour un fonctionnement normal de la RJ dans les cellules solaires tandem PK/SHJ.

Enfin, dans le chapitre VI, les simulations optiques réalisées ont confirmé que la RJ développée réduit, de plus de la moitié, les pertes par absorption parasite dans la RJ, par rapport à la couche d'ITO habituellement utilisée. En outre, les premiers résultats d'intégration ont démontré que les cellules solaires tandem PIN PK/SHJ avec la jonction $\mu\text{-Si:H}$ (n^+/p^+) ont fonctionné correctement (avec un rendement supérieur à 10 %). Les problèmes observés ne sont pas directement liés à la RJ développée, qui remplit son rôle. De plus, grâce à un transport vertical prédominant des porteurs de charge, la jonction $\mu\text{-Si:H}$ (n^+/p^+) développée semble réduire les problèmes de shunt par rapport à l'ITO habituellement utilisé.

En conclusion, nous avons développé et intégré une RJ à base de silicium fortement dopé, adaptée aux cellules solaires tandem PK/SHJ PIN. Avec une optimisation de la cellule supérieure en Pérovskite, cette jonction devrait permettre d'obtenir des cellules solaires tandem PIN PK/SHJ avec de meilleurs rendements qu'avec la couche d'ITO habituellement utilisée comme RJ (en particulier, de meilleurs courant et FF sont attendus).

- Mise en œuvre de méthodes de caractérisation pour optimiser les jonctions de recombinaison

Premièrement, dans le chapitre IV, nous avons démontré que l'intégration de la RJ dans des cellules solaires SHJ et la réalisation de mesures de durée de vie et de mesures I-V est une première étape essentielle pour valider que la RJ et son procédé de dépôt ne dégradent pas la future cellule-inférieure.

Deuxièmement, dans le chapitre V, nous avons défini plusieurs structures de test, simples à mettre en place, pour réaliser des mesures I-V transversales dans l'obscurité de RJ fortement dopées. De plus, nous avons démontré qu'il est difficile d'isoler le comportement de la jonction de celui du dispositif complet et que la prise en compte du recuit et des étapes ultérieures est critique. Par conséquent, nous avons montré que ces structures de test nécessitent de préférence un empilement arrière ohmique connu et une électrode avant déjà étudiée, idéalement une électrode métallique qui permet un bon contact avec le matériau RJ. Néanmoins, nous avons démontré que pour optimiser et/ou comparer les jonctions PN étudiées, une électrode TCO/Métal peut être utilisée si

l'influence de l'ajout d'une couche de TCO est prise en compte. Les structures de test définies nous ont permis de savoir rapidement si la jonction étudiée est faiblement ou fortement résistive. De plus, pour les jonctions PN fortement dopées, ces structures nous ont permis d'observer le comportement de la diode tunnel.

Troisièmement, dans le chapitre VI, nous avons présenté des dispositifs de test « type tandem » composés d'une cellule inférieure isotype. Nous avons ensuite démontré que ces dispositifs permettent de réaliser des mesures I-V de la cellule supérieure en Pérovskite déposée dans des conditions de cellule tandem PK/SHJ. Par conséquent, la mise en œuvre de ces dispositifs de test « type tandem » permet de comparer et/ou d'optimiser les RJ en fonction de la cellule supérieure et inversement.

Pour conclure, nous avons défini, testé et utilisé plusieurs méthodes de caractérisation, afin d'optimiser les RJ ou de valider leurs propriétés, en fonction du type/matériau de RJ. Ces nouvelles méthodes mises en œuvre sont combinées avec des techniques de caractérisation existantes et peuvent être utilisées en routine dans le processus de développement des cellules solaires tandem PK/SHJ.

- Compréhension des mécanismes de transport dans les cellules solaires tandem PK/SHJ 2T et l'influence de leur RJ

Comme point de départ, dans le chapitre IV, nous avons étudié l'influence de la jonction $\mu\text{-Si:H}$ (n^+/p^+) développée sur la cellule inférieure SHJ, en réalisant des mesures de durée de vie et I-V. Nous avons observé que la passivation semble être améliorée par l'ajout de la jonction et que cette RJ fonctionne bien dans le contact électronique des cellules solaires SHJ, démontrant ainsi un mécanisme de transport par effet tunnel bandes à bandes.

Par la suite, dans le chapitre V, nous avons également étudié les mécanismes de transport dans les RJ à base de silicium fortement dopé, en particulier lorsqu'une jonction NPN est formée avec un TCO de type N. Dans l'ensemble, nous avons constaté que si la RJ est composée d'une couche de TCO de type N, les mécanismes de recombinaison à l'interface avec le contact de trou de la sous-cellule adjacente sont les mêmes qu'au contact de trou des cellules solaires à simple jonction.

Pour une investigation plus approfondie, dans le chapitre VI, nous avons utilisé des simulations optiques, pour observer l'influence optique des deux types de RJ. Nous avons ainsi démontré que la transparence et les indices optiques de la RJ sont des facteurs importants pour réduire les pertes. Ensuite, nous avons utilisé des dispositifs de test « type tandem » pour étudier l'influence du substrat de la cellule inférieure et de la RJ sur la qualité de la cellule supérieure en Pérovskite. Une telle question a rarement été abordée dans la littérature et les premières observations que nous avons faites constituent un bon point de départ pour des études ultérieures, par exemple sur la formation des couches de Pérovskite en fonction des couches sous-jacentes. Nous avons observé que certains problèmes de shunt (qui jouent un rôle non négligeable dans le FF et les performances des cellules solaires tandem PK/SHJ) semblent être liés aux propriétés de la RJ. En effet, avec la RJ $\mu\text{-Si:H}$ (n^+/p^+) développée, les dispositifs présentent beaucoup moins de problèmes de shunt qu'avec la couche d'ITO habituellement utilisée.

En résumé, nous avons réalisé diverses études au cours de ces travaux pour comprendre et étudier l'influence de la RJ et les mécanismes de transport dans les cellules solaires tandem monolithiques PK/SHJ.

Ces travaux de thèse et les différentes contributions scientifiques produites soulignent l'importance de la jonction de recombinaison dans les cellules solaires tandem

monolithiques Pérovskite sur silicium. En présentant des méthodes de développement et de caractérisation pour améliorer la RJ et les sous-cellules le plus efficacement possible (en tenant compte de l'influence des unes sur les autres), ce travail apporte des pistes essentielles à la communauté scientifique pour l'amélioration de cette technologie tandem.

Ces travaux ouvrent également plusieurs perspectives :

- Premièrement, l'adaptation des couches de silicium microcristallin développées, afin d'obtenir une jonction $\mu\text{-Si:H}$ (p^+/n^+) pour les cellules solaires tandem PK/SHJ en configuration NIP, semble être une option valide. En effet, les simulations optiques réalisées ont démontré que la configuration NIP est également viable et les cellules en Pérovskite NIP ont atteint de meilleures performances que les cellules PIN au CEA-INES. Le principal problème sera la présence de dopants au bore pour faire croître la couche $\mu\text{-Si:H}$ (p^+) en premier. Ainsi, le développement d'une nouvelle couche d'incubation est sûrement nécessaire, peut-être avec une très faible concentration de dopants, préservant les hautes performances de la cellule inférieure SHJ.
- Deuxièmement, une électrode métallique adaptée, assurant une faible résistivité de contact, doit être développée pour améliorer les structures de test présentées. Par exemple, une électrode avec une fine couche de titane surmontée d'une couche d'argent plus épaisse, de préférence déposée par évaporation thermique.
- Troisièmement, pour une meilleure correspondance optique, les indices optiques des couches des sous-cellules doivent être pris en compte pour l'optimisation de la RJ. En effet, pour réduire les pertes par absorption et par réflexion, les propriétés optiques de la RJ peuvent être optimisées (transparence dans la région IR et correspondance des indices de réfraction avec les couches adjacentes). Par exemple, les indices de réfraction de la couche peuvent être accordés en ajoutant d'autres gaz pendant le processus de dépôt PECVD des couches de silicium amorphe ou microcristallin. En outre, l'utilisation de simulations optiques pour définir les bonnes épaisseurs de ces couches semble être un moyen efficace d'améliorer l'adaptation optique dans les cellules solaires tandem PK/SHJ.
- Quatrièmement, la formation de la couche de Pérovskite (dépôt et cristallisation) sur différentes sous-couches (par exemple ITO et $\mu\text{-Si:H}$ + HTL ou ETL, avec ou sans prétraitement de surface) et les problèmes de shunts observés doivent être étudiés plus en détail. Les dispositifs test « type tandem », présentés au chapitre VI, sont essentiels pour ce type d'étude.
- Enfin, les structures tandems simplifiées présentées au chapitre VI, viables selon les simulations optiques, méritent d'être développées et testées. Pour cela, les propriétés des matériaux doivent être modifiées afin d'obtenir la meilleure sélectivité des porteurs de charge en permettant une recombinaison efficace.